Optimization of the interfaces of encapsulated OPV devices

Sacha Juillard

Communauté
UNIVERSITÉ Grenoble Alpes

THÈSE

Pour obtenir le grade de

DOCTEUR DE LA COMMUNAUTE UNIVERSITE GRENOBLE ALPES

Spécialité : **Matériaux, Mécanique, Génie civil, Electrochimie**

Arrêté ministériel : 25 mai 2016

Présentée par

Sacha JUILLARD

Thèse dirigée par **Lionel FLANDIN**, Professeur, Université Savoie-Mont-Blanc,
Co-dirigée par **Emilie PLANES**, Maître de conférence, Université Savoie-Mont-Blanc,
Muriel MATHERON, Ingénieur de recherche, CEA/LITEN,
et **Solenn BERSON**, Ingénieur de recherche, CEA/LITEN.

préparée au sein du **Laboratoire d'Electrochimie et de Physico-Chimie des Matériaux et Interfaces (LEPMI)**
et au CEA/LITEN/Laboratoire des Modules Photovoltaïques Organiques (LMPO)
dans **l'École Doctorale IMEP-2 – Ingénierie – Matériaux, Mécanique, Environnement, Energétique, Procédés, Production**

Optimisation des interfaces de systèmes PV organiques encapsulés

Thèse soutenue publiquement le **5 avril 2018**,
devant le jury composé de :

Monsieur Jean-Charles MAJESTE Professeur des universités, IMP, Université de Saint-Etienne (Président du jury)
Monsieur Fabrice GOUBARD Professeur des universités, LPPI, Université de Cergy-Pontoise, (Rapporteur)
Monsieur Bernard, RATIER Professeur des universités, XLIM, Université de Limoges, (Rapporteur)
Monsieur Jean-Jacques, SIMON Professeur des universités, IM2NP, Université d'Aix-Marseille (Examinateur)
Madame Muriel MATHERON Ingénieur Recherche, CEA-LITEN-LMPO (Examinateur)
Madame Solenn BERSON Ingénieur Recherche, CEA-LITEN-LMPO (Examinateur)
Monsieur Lionel FLANDIN Professeur des universités, LEPMI, Université Savoie-Mont-Blanc (Directeur de thèse)
Madame Emilie PLANES Maître de Conférences, LEPMI, Université Savoie-Mont-Blanc (Co-directeur de thèse)

Communauté
UNIVERSITÉ Grenoble Alpes

Remerciements

Je remercie tout d'abord mes encadrants : Lionel Flandin, mon directeur de thèse, Emilie Planès, Solenn Berson et Muriel Matheron pour leur travail, leur soutien et leur guidance durant ces trois années.

Je tiens également à remercier sincèrement Fabrice Goubard ainsi que Bernard Ratier de m'avoir accordé l'honneur d'être rapporteurs de ces travaux. Je remercie également Jean-Charles Majesté et Jean-Jacques Simon pour leur participation en tant que jury de thèse.

Je me dois ensuite de remercier particulièrement chaleureusement Muriel ainsi que Amal Chabli qui sont allées bien au-delà de leurs responsabilités en m'apportant une véritable aide humaine dans des moments singulièrement compliqués. Je m'excuse de trahir votre humilité en vous disant que ce travail ne serait surement pas allé au bout sans vous.

Un grand merci à mes collègues du LMOPS : Nicolas pour son aide, Lara pour sa bonne humeur, Ali pour son naturel, Gilles pour son dynamisme, Florence pour sa gentilesse et Marjorie pour son phare dans mon épais brouillard administratif. Je souhaite également un bon courage aux thésards restants : Thibault et Manon mes camarades de double nationalité, Marwen que je n'ai malheureusement pas assez connu, Quentin pour son humour, et Zeinab avec qui j'ai hâte de refaire une bouffe!

Egalement un grand merci au LMPO qui a égayé mon quotidien : Vincent « la cascade » et Marco-Antonio « moins fort ! » (ça avance bien la rédac ? ;-)), Guillaume « La Such' », Coolette et son rire, Marion ma camarade de dépit devant l'EL, Marion « La gouj », Clement « La botte », Patrick a.k.a. « The Boston Watchtower » , Carine, Pia, Bobo, Soumsoum, Mélo et Fabinou, antho... j'en passe et des meilleures (pardon pour les oubliés !) !

Un gros merci également aux permanents : Noella pour m'avoir permis de découvrir mes premières galères de recherche, Mattieu pour nos discussions scientifico-ésotériques, Stephane pour sa râlerie communicative et son bon gout vestimentaire ;-), Caro et Flo pour leur bienveillance ainsi que Pascal, et les deux Nathalies pour leur aide précieuse.

Une grand merci également pour mes autres camarades de L'INES, du LOCIE jusqu'à l'accueil, des thésards jusqu'aux permanents, pour les multiples repas, soirées, apéros, coups de mains, sourires... Une pensée particulière pour Severine Bailly avec qui ces longs après-midi de

MEB semblaient passer en quelques instants grâce à sa bonne compagnie.

I also have to thank the Biomolecular and Organic Electronics team, especially Pr. Inganäs, Fengling and Deping who gave me some of their valuable time, at Linkoping University for their warm welcome which allowed me to discover their unique culture.

Je remercie également ma famille et mes amis qui ont réussi à me supporter et me motiver malgré une humeur des plus variables.

Contents

List of Units

Units and contants	Complete name (quantity measured)
°C	Celcius degree (0°C = 273.15 Kelvin)
A	Amps (electrical current)
C	Coulomb (electrical charge)
eV	Electron-volt (energy = qV)
g	Gramm (mass)
h	Hour (time)
k	Boltzmann constant = $1.381.10^{-23} m^2.kg.s^{-2}.K^{-1}$
K	Kelvin (temperature)
m	Meter (distance)
mol	mole (amount of substance)
N	Newton (force)
$N.m^{-1}$	Newton per meter (normalized peeling force)
q	Electron electrical charge = $1.60.10^{-19}$ C
S	Siemens (conductivity)
V	Volts (potential difference)
W	Watt (power)

List of abbreviations

Abbreviation	Complete name
μ_{PL}	Mean photo-luminescence intensity
σ_{PL}	Standard deviation of the photo-luminescence intensity
Ag	Silver
AL	Active layer
AM1.5G	1.5 Atmosphere standardized illumination
B2B	Band-to-band
BHJ	Bulk hetero-junction
C	Carbon
Ca	Calcium
CT	Charge transfer
D:A	(Electron) Donnor:acceptor
DCB	Double cantilever-beam
E_F	Fermi energy (in eV)
EL(I)	Electro-luminescence (imaging)
ETL	Electron transport layer
FF	Fill-factor
FTIR	Fourier-transform infrared spectroscopy
H	Hydrogen
HOMO	Highest occupied molecular orbital
HTL	Holt-transport layer
I	Current (in A)
IR	Infrared
J	Current density (in $A.m^{-2}$)
J_{ph}	Photo-generated current density (in $A.m^{-2}$)
J_{SC}	Short-circuit current density (in $A.m^{-2}$)
J_mpp	Current-density at maximum power point
LBIC	Laser-beam induced current
LED	Light-emitting diode
LUMO	Lowest unoccupied molecular orbital
NIR	Near infrared
NP	Nanoparticles
O	Oxygen
OC	Open circuit
OPV	Organic photovoltaics
OTR	Oxygen transmission rate (in $g.m^{-2}.day^{-1}$)

Abbreviation	Complete name
P_mpp	Maximum power output
P3HT	Poly-3-hexylthiophene
PCBM or $PC_{60}BM$	Phenyl-C61-butyric acid methyl ester
PCE	Power conversion efficiency
PEDOT:PSS	poly(3,4-ethylenedioxythiophene):polystyrene sulfonate
PET	Polyethylene terephthalate
PL(I)	Photo-luminescence (imaging)
PS	Poly-styrene
PSA	Pressure sensitive adhesive
PTFE	Polytetrafluoroethylene
PV	Photovoltaic
R_{SH}	Shunt resistance (in $\Omega.m^2$)
R_S	Series resistance (in $\Omega.m^2$)
R2R	Roll-to-roll
RH	Relative humidity
S	Sulphur
S2S	Sheet-to-sheet
SEM-EDX	Scanning electron microscopy with energy dispersive X-ray spectroscopy
Si-CCD	Silicon charge coupled device
SMU	Source-measure unit
T_g	Glass transition temperature (in K)
TCO	Transparent conductive oxide
TP	Thermoplastic
UV	Ultra-violet
UVO_3	ultraviolet + ozone treatment
UV-Vis	Ultra-violet (absorption spectroscopy)
V_{OC}	Open-circuit voltage (in V)
V_mpp	Voltage at maximum power point
vbPL	Voltage -biased photoluminescence
W_a or W_c	Work of adhesion or cohesion, respectively
WO_3	Tungsten trioxide
WVTR	Water vapor transmission rate (in $g.m^{-2}.day^{-1}$)
XPS	X-ray photo-electron spectroscopy
Zn	Zinc
ZnO	Zinc Oxide

Introduction

Energy supply is among the most important challenges to meet for humanity in the XXI century. Fig.1 represents the world total energy supply according to the International Energy Agency [1], in millions of tons of oil equivalent (Mtoe), by fuel since 1971.

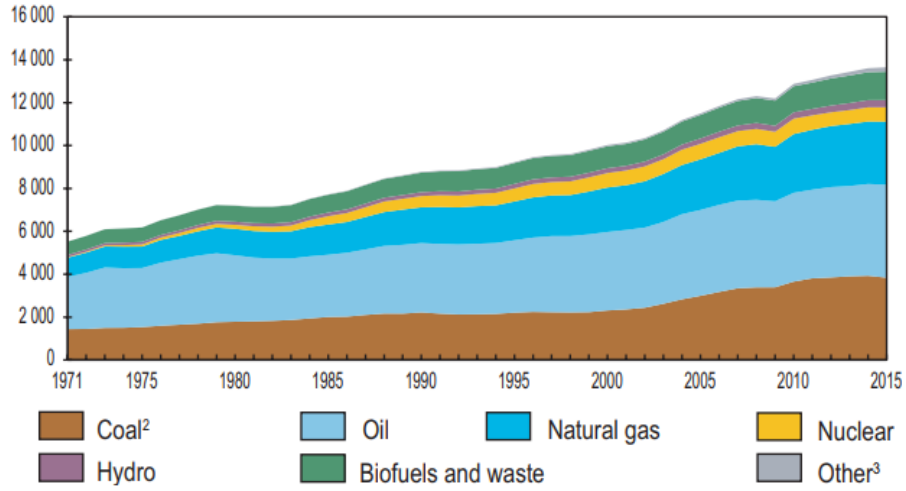

Figure 1: *World total primary energy supply by fuel according to the International Energy Agency. The "other" grey category includes geothermal, solar, wind, tide/wave/ocean, heat and other energy sources. Reproduced from [1].*

The humanity energy demand is steadily increasing but currently, its supply relies for 86.3 % on finite resources which will eventually be exhausted.

Assuming 65% absorption losses by atmosphere and clouds, the yearly solar energy received by the emerged continents covers more than a thousand times the energy demand in the same period [2]. As such, this energy source is a solid candidate to answer the increasing need for energy. Nowadays, photovoltaic technologies represents 2% of the worldwide electricity demand in the end of 2016 [3]. According to almost all scenarios, the renewable share of the energetic mix will be steadily increased during the next decades [4].

The photovoltaic effect was first observed in 1839 by Edmond Becquerel [5]. This led to the invention of the first actual solar cell, made of selenium covered by a thin gold film, which was first patented in 1888 [6].

Several developments led to the invention of the first generation photovoltaic (PV) panels made of crystalline silicon. Such technologies are still among the most efficient PV modules.

Thereafter, the second generation called thin film PV technologies, mostly made of amor-

phous silicon and rare post-transition metals, was created. Such cells are generally produced at a lower cost but have lower performances than crystalline silicon cells.

Finally, the third PV generation called organic solar cells, on which this work focuses, are currently developed in order to further decrease the production cost of PV panels.

In 1977, Hideki Shirakawa, Alan J. Heeger and Alan G. MacDiarmid dicovered that the polyacetylene polymer can be doped with halogens in order to produce high conducting materials [7]. This discovery made them to earn a Nobel prize of chemistry in 2000. Such discovery opened the way for a range of new conductive materials ultimately leading to the development of organic electronics and notably the organic photovoltaics.

Among the large number of competing solar photovoltaic technologies, organic photovoltaics (OPV) have many unique characteristics that are unreachable by classical (e.g silicon) or even other thin-film technologies. It includes lightweight (10 $W.g^{-1}$) [8], semi-transparency [9], tunable colors [10] and designs [11], use of flexible substrates and high-speed manufacturing under ambient conditions through roll-to-roll processing [12]. These characteristics allow the OPV technology to reach new fields of applications such as portable devices [13] or building-integrated PV modules [14].

The first OPV solar cells were developed in the early 1980's [15]. Such cells had a structure close to that of the first inorganic cells with a polyacetylene layer sandwiched by graphite and aluminum electrodes. Since then, several developments have been implemented in order to boost the efficiency of the cells from below 0.1% to 13.2 % recently. The record cell, produced by Heliatek [16], are based on multi-junction architectures made of evaporated small molecules. Fig.2 represents the United States National Renewable Energy Laboratory (NREL) chart plotting record yields (at laboratory scale) of many photovoltaic technologies as a function of time. Organic photovoltaic technologies are shown in plain red triangles and discs. The 13.2% OPV record set by Heliatek was authenticated by a different institute than NREL (Fraunhofer ISE [17]) and is not shown here.

A major drawback of this technology is its degradation induced by water and oxygen [19]. To protect the flexible devices from the atmospheric species and thus increase their lifetime, they are encapsulated between gas barrier films. which are held by encapsulant materials. Currently, little work studied the lifetime of the flexible solar cells. Indeed, the most of the results quoted in the literature are obtained on glass substrates. Furthermore, despite its potential cost and its importance for both the devices as-prepared performances and their lifetime, encapsulation design and optimization are scarcely described in the literature [20], even in studies treating of aging in accelerated conditions. In recent years, significant progress, both for cell structure and for encapsulation materials, has considerably improved the stability of OPV modules to the point that some devices reported in the litterature [21–23] pass european normalization standards [24] which are expected to guarantee a ten year lifetime on the field. However significant limitations remain. In particular, the problems of damage at the interfaces are often neglected. The entire manufacture and encapsulation processes as well as use of the flexible devices can generate

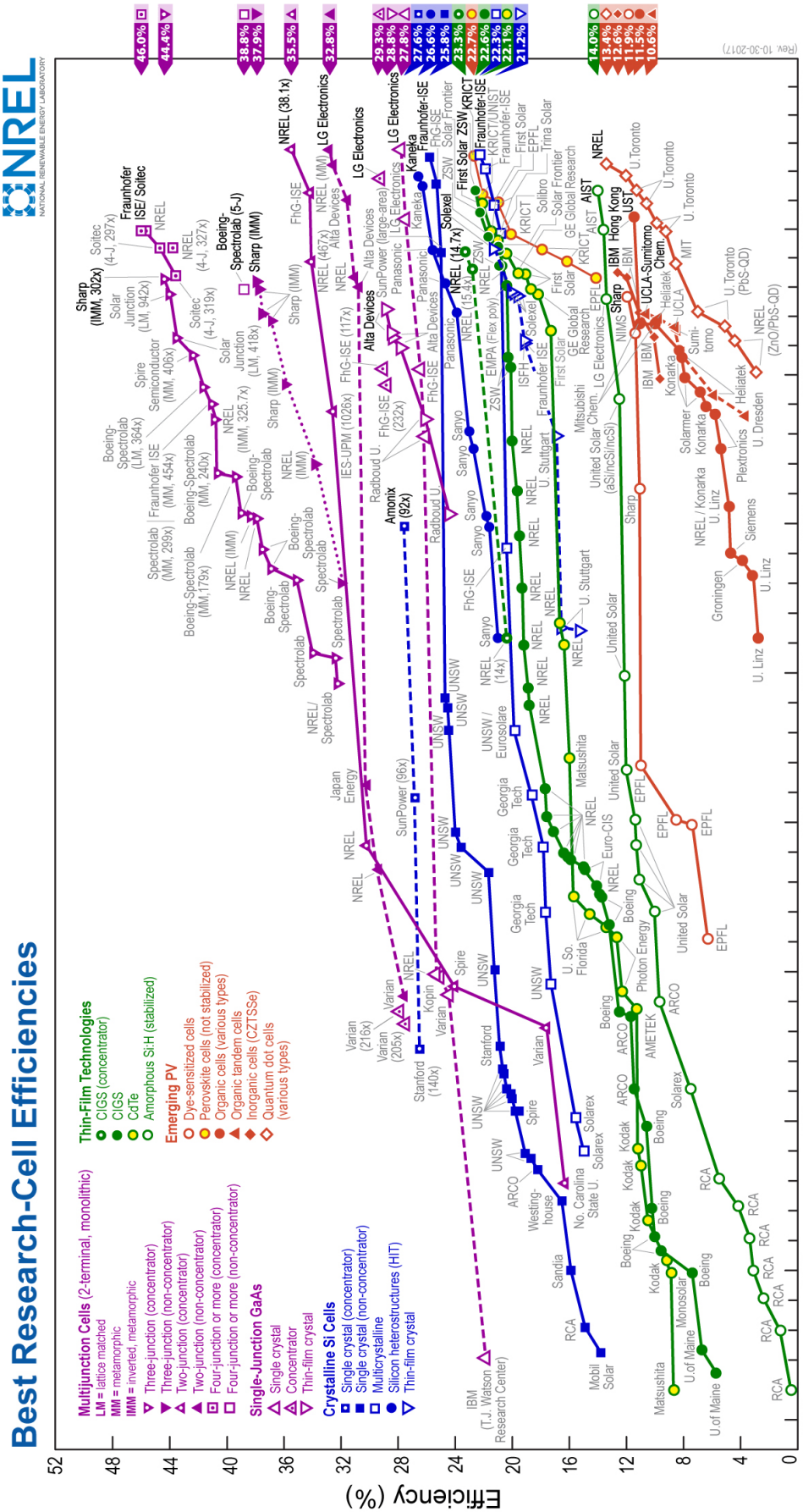

Figure 2: *NREL's record efficiency chart for various photovoltaic technologies. Reproduced from [18]. This plot is courtesy of the National Renewable Energy Laboratory, Golden, CO.*

constraints likely to propagate inherent defects [25]. The resulting delaminations often lead to irreversible damage and a decrease in performance. Such mechanical failures are reported in several field studies as a prime degradation factor[26, 27].

The aim of this work is the optimization and study of the interfaces of flexible OPV devices. From a technological point of view, one of the objectives of this thesis work is to develop tools for characterization and understanding of interfacial fractures developing within the OPV stack. These experiments are conducted on complete encapsulated devices. Conventional adhesion measurement techniques such as 180° peel methods have been implemented and associated with innovative characterization means for the identification of the weakest interfaces (photo-luminescence imaging, SEM-EDX, IR spectroscopy, etc.). Other characterization methods to evaluate the impact of these delaminations on optoelectronic properties on a more local scale are developed during this PhD : electro-luminescence, photo-luminescence, voltage-biased photoluminescence and laser beam induced current measurement.

As mentioned previously, the study of the encapsulation of OPV device is the main objective of this research work. Several aspects have been discussed. Firstly, the impact of two traditional encapsulation strategies (roll-to-roll (R2R) lamination of a pressure sensitive adhesive (PSA) and the lamination under vacuum of a hotmelt thermoplastic (TP)) on mechanical reliability and optoelectronic properties of devices has been studied. Solutions allowing the improvement of two interfaces identified as mechanically weak were sought and then evaluated with respect to the photovoltaic performances of the reference devices. Secondly, the durability of these encapsulated systems was studied. Previously developed imaging techniques have proved to be valuable tools for this study. Thanks to the complementarity of several characterization techniques and a suitable sampling, allowing to identify the type of degradation (optical or electrical), a degradation mechanism , explaining the inhomogeneity of the degradation on the cell surface and symptoms suffered by the device, could be highlighted.

In order to answer these problems, this work is divided in six chapters:

I A state of the art review is first performed. It will cover the basic working principle and architectures of organic photovoltaic devices. Their degradation mechanisms and the strategies employed to prevent them will then be discussed. A particular focus will then be performed on the characterization and improvement of the devices mechanical properties. Finally, non-destructive imaging characterization will be presented and their use will be highlighted.

II In the second chapter, our reference device materials as well as the fabrication and characterization protocols employed in this work will be precised.

III The third chapter will cover the development of imaging characterizations and mechanical characterizations performed in the frame of this work.

IV In the fourth chapter, the impact of our encapsulation protocols on the OPV cells as-prepared performances will be studied. With the help of imaging characterizations devel-

oped previously, the hypothesis of a mechanical degradation occurring during encapsulation will be given. Thus, the adhesion of all the interfaces comprised in our reference stack will be quantified. From those results, mechanically weak interfaces will be identified. Thereafter, the adhesion improvement strategies performed on such weak interfaces will be presented and discussed according to both the mechanical properties and PV performances of the resulting device architectures.

V In the fifth chapter, cells encapsulated according to our reference protocols were aged under several heat and moisture conditions. Imaging characterizations were employed along the cells aging. From such data, possible permeation and degradation mechanisms will be proposed.

VI Finally, the sixth chapter will summarize the main results of this work and outlooks for this work will be proposed.

Chapter 1

State of the art

This work will focus on the encapsulation processes, the aging and the characterization techniques for study of encapsulated OPV devices. To this end, this chapter will review the literature covering such topics.

In a first time, the OPV devices operating principles and their performance measurement will be presented in Sec.1.1. In Sec.1.2, their main degradation mechanisms and the encapsulation methods employed to protect them will be described. Then, mechanical degradation of the devices will be further discussed in Sec.1.3. Finally, advanced imaging characterizations adapted for study of encapsulated devices will be described in Sec.1.4.

1.1 Principle of organic photovoltaics

1.1.1 Physical processes occurring during organic solar cells operation

The goal of all solar cells is to generate an electrical current from incident light. To do so, photons are absorbed by an active layer (AL) where they are converted to free (unbound) charges: negatively charged electrons and their positively charged counterparts called holes. They must then be driven to its cathode and its anode, respectively.

Band diagrams. The optoelectronic properties of materials used in OPV devices are generally described by the semi-conductor models [28, 29]. In solid semi-conductors, molecular orbitals are degenerated and form a continuum called energy bands. Fig. 1.1 depicts a simple band diagram of an intrinsic (i.e. non-doped) excited semi-conductor.

At 0 Kelvin, the range of occupied molecular orbitals energies forms the "valence band" and the energetically range of unoccupied molecular orbitals forms the "conduction band". By analogy with the molecular-orbitals theory's terminology, the maximal energy level available in the valence band E_v is the highest occupied molecular orbital (HOMO) energy level and the minimum energy level available of the conduction band E_c is the lowest unoccupied molecular orbital (LUMO) energy level.

These energy levels are separated by a band-gap energy E_g, which is the minimal energy needed for an electron to be promoted from the valence band to the conduction band.

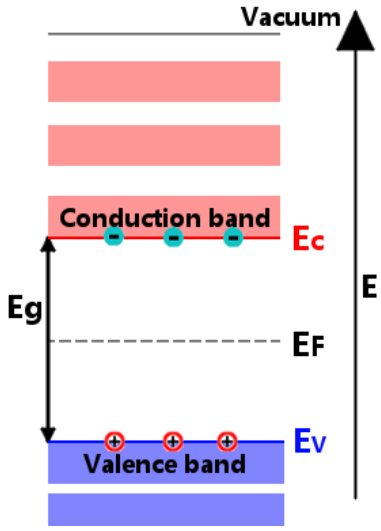

Figure 1.1: *Schematic energy-band diagram of an excited intrinsic semi-conductor.*

Electrons excited (by thermal or optical processes) with sufficient energy can cross the band gap to the conduction band. Conversely, holes in the conduction band move to the valence band. These excited charges, in minor proportion compared to those left on their original band, are mobile and are thus responsible for conductivity in semi-conductors.

The stakes of photovoltaics is to separate and extract these excited charges before they go back to their ground states.

In opposition to inorganic photovoltaics, the low relative permittivity of the organic materials used in OPV cells ($\approx$ 2-4), makes the Coulomb attraction between both charges much stronger (in the 350 - 500 meV range) than kT (the thermal energy = 25.7 meV at 300 K) [30]. Therefore, the active layer is made of a blend of two materials, an electron-acceptor and an electron-donor, in order to assist the charge pair dissociation [31].

The PV mechanism of organic devices. Here, we will consider a simple bi-layer solar cell composed of an active layer framed between a cathode and an anode.

In this example, the active layer was made of poly-3-hexylthiophene (P3HT) electron-donor polymer and phenyl-C_{61}-butyric acid methyl ester (PCBM or $PC_{60}BM$) fullerene electron-acceptor molecules.

Fig. 1.2 summarizes, in chronological order from left to right, band diagrams of the most widely accepted photovoltaic mechanisms occurring during operation of OPV cells. Loss mechanisms, expanding energy, are also described. They are called "recombinations".

– **Light absorption (1)**

  Photons are absorbed by the active-layer's donor polymers. Electrons are promoted to excited states in the conduction band thus creating electron-hole pairs, named "excitons", bound by Coulomb electrostatic attraction [32].

  For simplification we consider that photons are absorbed by the donor polymer only. Actually, PCBM also contributes to the light harvesting and the subsequent mechanisms

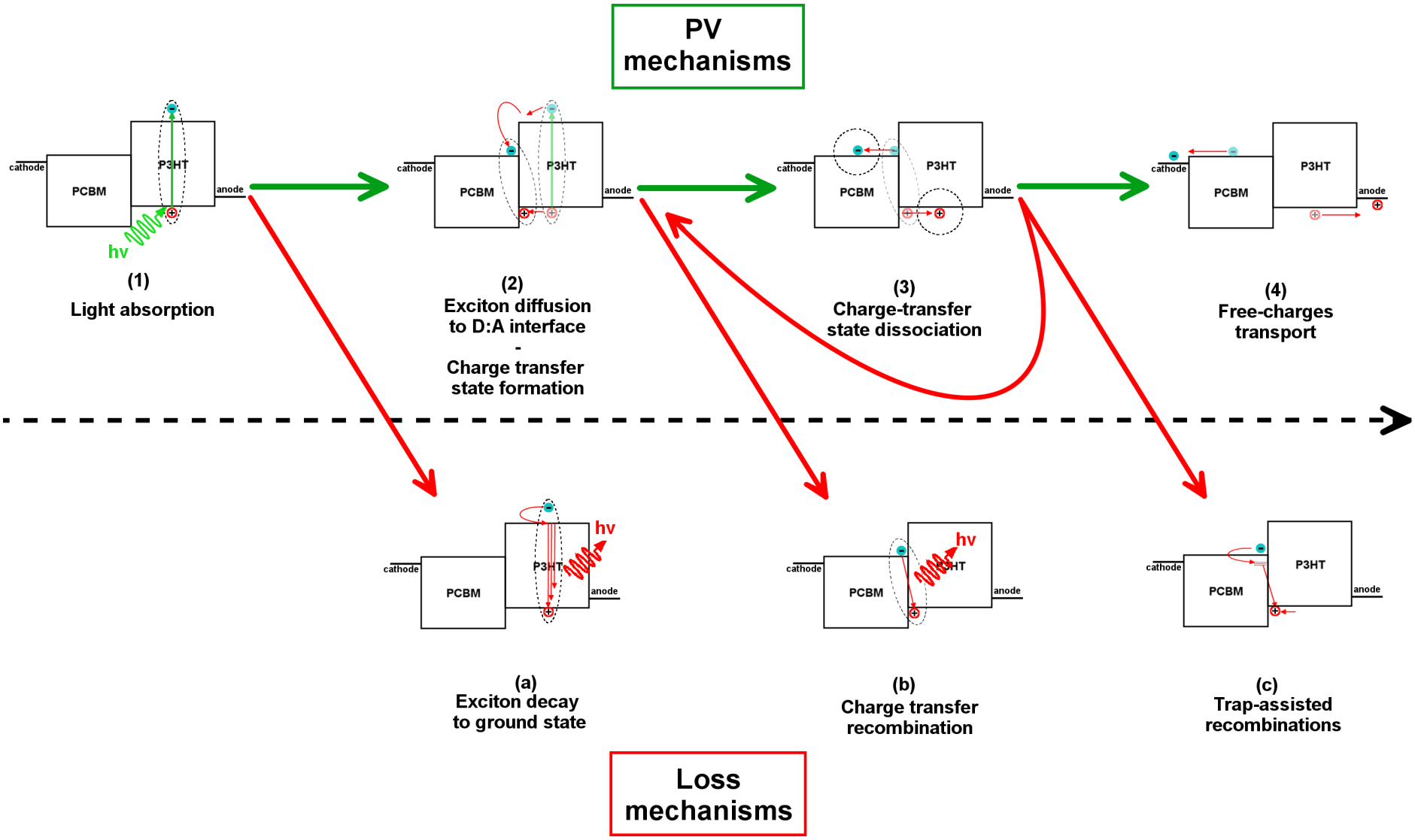

Figure 1.2: *Band diagrams of the main mechanisms occurring during operation of OPV devices, in chronological order from left to right. Mechanisms favorable for photo-conversion are depicted in the top row and connected by green arrows. Terminal loss mechanisms are depicted in the bottom row. Red arrows represent unfavorable mechanisms for photo-conversion. Electrons are represented as blue discs in the conduction bands and holes are represented as red circles in the valence bands. Dashed lines represent the Coulomb radius of interaction of the charge-carriers.*

but to a lesser extent, due to its absorption spectrum poorly matched with the sun emission spectrum.

- **Exciton diffusion to a Donor:Acceptor (D:A) interface and charge-transfer state formation (2) Versus Exciton decay to ground state (a)**
  Bound excitons then thermally diffuse within the polymer phase. During diffusion, they lose some excess kinetic energy through thermalization (i.e. distribution of vibrational energy through the lattice) [33].
  If they encounter an interface between the two materials of the active layer, the electrons can move to the electron-acceptor's conduction band while the holes will remain on the electron-donor's valence band [34, 35]. These electron-hole pairs, although delocalized on two different materials, are still coulombically bound but weakly as compared to the localized excitons; this is most commonly known as the charge-transfer (CT) state [32, 36].
  However, the excitons have a finite lifetime. If the exciton does not reach a D:A interface in time, it will eventually decay to its ground state [37].
- **Charge-transfer state dissociation (4) Versus Geminate charge-transfer recombination (b)**
  If the weakened coulombic forces bounding the exciton are surpassed, the charges separate; they are then called "free" charges.

  However, if the free charges cannot escape their mutual coulombic field, they could eventually recombine. Because both charges come from the same photon, this process is called a "geminate" recombination [37].

  If the bounding energy of the CT state is superior to kT, the thermal energy, additional energy is necessary in order to successfully dissociate the excitons. The mechanism of charges separation, although this was the subject of extensive research, is not yet completely understood [38, 39]. Nevertheless, it has been proven by CT-photoluminescence [37], time-delayed collection field [40] and transient photo-conductivity [41] experiments that CT dissociation, at least of P3HT:PCBM blends, is field independent.
  On one hand, "Hot" CT-states, formed by not completely thermalized excitons, which would be more delocalized and therefore weaker than "cold" ones, have been proposed as possible dissociation mediators [42, 43].
  On the other hand, an energy gradient is thought to form between the disordered interfaces and the ordered, crystalline, pristine materials. After formation at the interface, this gradient would further delocalize the exciton until complete dissociation [44–46].
- **Free charges transport (5) Versus CT re-formation and Trap-assisted recombinations (c)**
  Once the charges are separated from each other, they drift, according to the electric field applied by the anode and the cathode, in their respective affinity-material phases. Once they reach the electrodes, they may be collected in an external electrical circuit and partici-

pate to the electrical current output of the cell.

If during the transport, the charges come close to a D:A interface, they may enter the Coulomb attraction radius of an opposite charge carrier and form again a CT-state. This CT-state as well has a probability to either dissociate or recombine. In the latter case, recombination is "non-geminate" because each charge originates from different photons [47].

Mobile charges may also recombine with stationary, "trapped" charges at interfaces. It is still unclear whether such traps are caused by disorder in polymer chains, inducing tail energy states below transport levels [48, 49], or impurities and structural defects, causing deep potential wells in the electronic landscape [50–52].

1.1.2 OPV devices concepts

From the early concepts of OPV solar cells, several developments have been implemented in order to boost the efficiency of the cells from below 0.1% to 13.2 % recently [16]. Such concepts widely in use nowadays will be reviewed here.

The bulk-heterojunction active layer. In the active layer, the excitons average diffusion length before decay L_D is small ($\approx$ 10 nm) [53]. Therefore, in order to limit their decay and favor the formation of CT-states, the bulk-heterojunction (BHJ) concept was introduced [54, 55]. It consists of a fine blend of the two materials composing the active layer, distributed in the all layer volume. On the one hand, in order for every photo-generated exciton to have a maximal probability of reaching an interface, both phases should not be larger than twice the exciton diffusion length. On the other hand, in order to limit the probability of CT reformation after its dissociation, percolated pathways of each material to their respective electrodes must exist [56, 57].

Thus the bulk morphology of the active layer must be balanced between a high interfacial area between both material phases and the growth of large percolated pathways of each material. Fig. 1.3 describes the ideal and a more realistic morphology of a solution-processed active layer. For the ideal morphology, each "tooth" of the heterojunction comb have a 20 nm width equal to twice the exciton diffusion length.

In practice, to create a BHJ for solution processed layers, both materials are blended in a single solution before deposition. To further control the morphology of the active layer, a thermal annealing, which will favor growth of larger material phases, is often performed after its deposition [58].

Electrodes design. In order to break the symmetry of the devices and create an electric field driving the free charges toward their respective electrode, the cathode and anode energy levels must be asymmetric. Ideally, they match the energy level of the electron-acceptor conduction

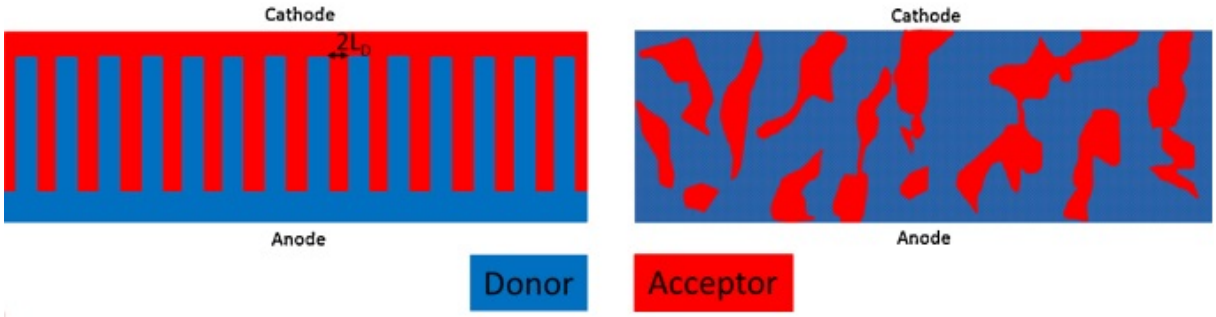

Figure 1.3: *(left) Ideal morphology of a BHJ layer, (right) Typical morphology of a solution-processed active layer. Reproduced from [30].*

band and the electron-donor valence band, respectively. Therefore, the organic photovoltaic devices behave like diodes in the dark, allowing only one drift direction for each charge type.

Furthermore, in the case where the electrodes are located on both sides of the cells, at least the front electrode must be transparent to allow incoming photons to reach the active layer.

Finally, for opaque OPV cells, in order to extend the photons travel path through the active layer, the back electrode should be reflective [59].

Interfacial layers. Commonly, interfacial layers, called electron or hole transport layers (ETL and HTL, respectively), are introduced between the active layer and the electrodes. These layers can play many roles [60–62]:

- They can improve charge extraction by pinning the electrodes energy level to that of their respective active layer material.
- They can limit parasitic leakage currents, by conducting a single charge type and preventing the other from being transported in the same electrode.
- They can limit diffusion of electrode materials into the polymeric active layer thus preventing shorting of the devices [63]

Device configurations. The two cells architectures most-used in OPV are presented in Fig. 1.4. The standard configuration is represented in Fig 1.4a whereas Fig. 1.4b depicts the inverted architecture.

In the standard architecture, holes are collected by the transparent electrode (most often with a hole transportlayer (HTL) to align its energy level) and electrons are collected to a low work function metal electrode.

In the inverted structure, electrons are collected by the transparent electrode with the help of an electron transport layer (ETL) and holes are collected by a high work function metal electrode and a HTL [64, 65]. The high work function electrode (most often silver) exposed at the top of the inverted device has the advantage to be less vulnerable to oxidation. As a result, inverted devices lifetimes in damp-heat conditions has often been shown to be superior to those in conventional configurations [66].

In this work, only inverted devices were studied as a superior lifetime in damp aging conditions is expected for such configurations.

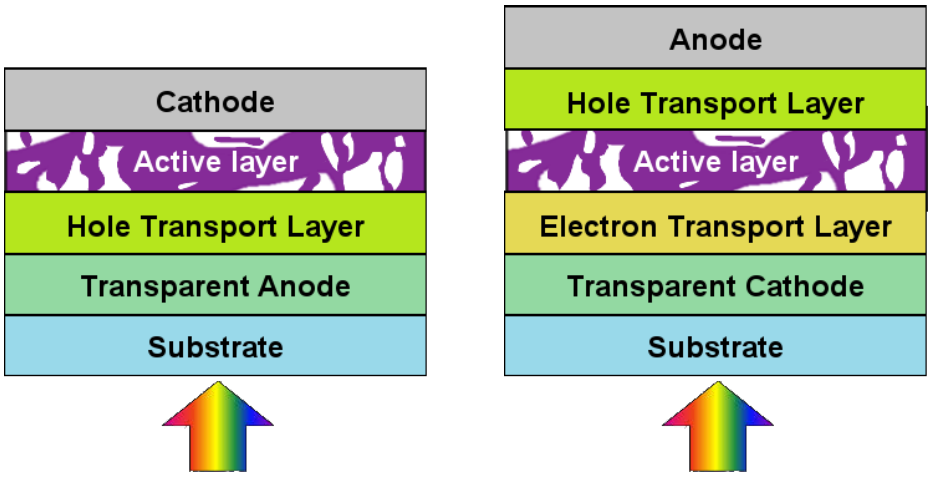

(a) *Standard architecture* ***(b)*** *Inverted architecture*

Figure 1.4: *Most widespread architectures of OPV devices.*

.

1.1.3 Current-Voltage characteristics

The most classical characterization tool used for measuring the performance of solar cells is to plot the current density versus voltage J(V) curve under illumination. By convention, extracted current will be represented as negative J values and injected current as positive J values. In this section, an ideal cell was firstly studied in the dark, then several non-ideality terms were implemented and finally the case of the real cell under illumination was studied.

The J(V) curve in the dark. Without illumination, the cell is considered as a classic semiconductor diode. It will allow current to flow in one direction only. The current flowing through the cell as a function of the applied voltage at its terminals follows the ideal diode law [67]:

$$J = J_0 \left[exp\left(\frac{qV}{kT}\right) - 1 \right]$$

With J the net current density flowing at the cell terminals, J_0 the reverse saturation current, i.e. the current flowing through the diode under reverse voltage bias, q the elementary charge, k the Boltzmann constant, T the temperature of the cell and V the bias voltage applied at the cell terminals.

Implementation of non-ideal recombinations In the case of the ideal diode, the reverse saturation current is assumed to be independent of the applied voltage or the illumination intensity [68]. However, on real OPV cells, such dependence is observed when trap-assisted recombinations are considered. In order to model this deviation from the ideal exponential law, an ideality factor n is commonly introduced:

$$J = J_0 \left[exp\left(\frac{qV}{nkT}\right) - 1 \right] \tag{1.1}$$

For an ideal system with only CT recombinations, whether they are geminate or non-geminate, this factor will be unity. However, when trap-assisted recombinations are dominant, the n-factor

will tend to 2 [48, 69].

The ideality factor is often used as a tool to determine the main mechanisms of recombination in OPV solar cells [48, 49, 70–72]. However, several methods are employed to determine them and they occasionally lead to contradictory results.

For P3HT:PCBM cells, ideality factors are generally comprised between 1.2 and 1.7 [48, 70, 72].

Implementation of series resistances and leakage currents In order to further address the differences between the ideal and the real diodes, additional resistances are implemented to the model [73, 74].
A series resistance, R_s, will take into account any Joule losses between the probes of the measurement apparatus; this includes the bulk resistances of the layers, the contact resistances at their interfaces and also the internal resistance of the apparatus. The ideal voltage term in the ideal diode equation is thus replaced by the "effective" voltage V_{eff} applied to the cell such as: $V_{eff} = V - JR_s$ with V the voltage applied to the cell terminals and J the current flowing through the circuit.

A shunt resistance R_{sh} bypassing the diode can also be used to model parasitic leakage current. It models any current which is not driven by the cell potential gradient, i.e. any current which does not follow the diode direction.
The diode equation is now:

$$J = J_0 \left[exp\left(\frac{q(V - JR_s)}{nkT} \right) - 1 \right] + \frac{V - JR_s}{R_{sh}} \tag{1.2}$$

The J(V) curve under illumination. To complete the model of the solar cell under operation, a generator representing the photon-to-charge conversion of the cell is implemented.
Figure 1.5 schemes the equivalent circuit of the solar cells according to the model described in this section.

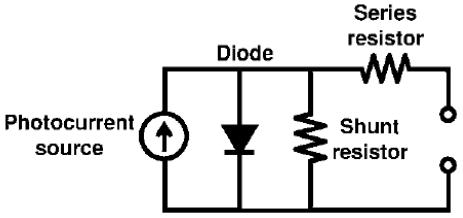

Figure 1.5: *One-diode equivalent circuit from [73].*

This model, known as the one-diode model, fits well the behavior of inorganic solar cells. More complex models exist for OPV cells [75, 76], but their parameters are more complicated to assess and to relate to physical meanings.

Mathematically, according to the one-diode model, the J(V) curve is modeled by the equation :

$$J = \underbrace{J_0\left[exp\left(\frac{q(V-JR_s)}{nkT}\right)-1\right]}_{\text{Diode current}} + \underbrace{\frac{V-JR_s}{R_{sh}}}_{\text{Shunt current}} - \underbrace{J_{ph}}_{\substack{\text{Photogenerated}\\ \text{current}}} \tag{1.3}$$

Where the term J_{ph} describes the photo-current generated by the cell. In this model, it is taken as a constant value for a given illumination power. Compared to the J(V) curves in the dark, the J(V) curve under illumination will be shifted downward by a negative J_{ph} value and R_s effects will shift the exponential knee to lower bias voltages.

Fig. 1.6 represents an experimental J(V) curve of one of our cells in the dark and under illumination.

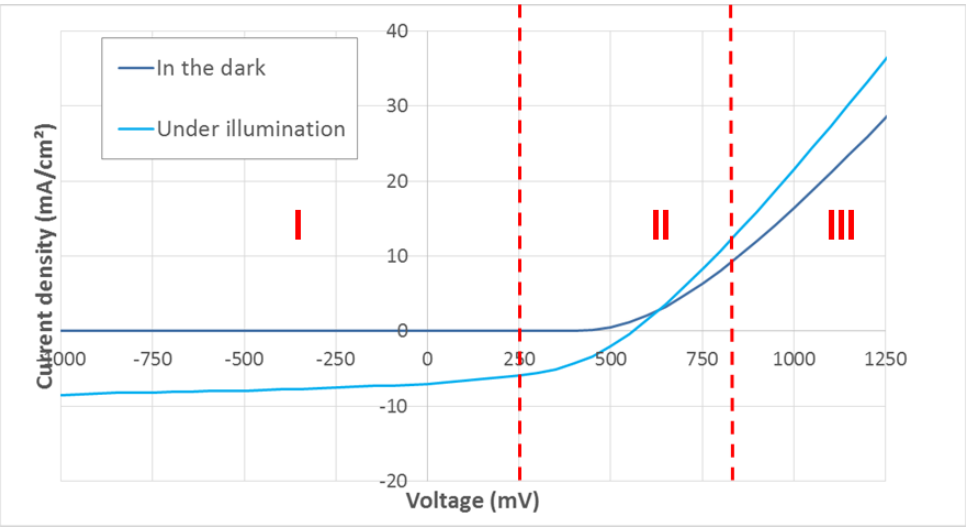

Figure 1.6: *J(V) curve of a P3HT:PCBM cell in the dark and under illumination.*

According to Eq. 1.2, the curve recorded in the dark can be divided into three regions:

I. In the first region, below $\approx 250mV$, the diode is in blocking mode. The slope of the J(V) curve is primarily influenced by the shunt current ($J \approx J_{sh} = V/R_{sh}$) bypassing the diode.

II. In the second region, the knee around 500 mV, the diode is at its turn-on voltage. The J(V) is influenced by the diode rectification properties, expressed by the parameters J_0 and n and also by its characteristic resistances.

III. In the third region, above the turn-on voltage (>800 mV), the diode behaves like a conductive wire characterized by its series resistance R_s.

According to Eq. 1.3, the illuminated curve should be equivalent to the dark curve shifted by a constant J_{ph} value. However, on our samples, a few differences are observed:

Firstly, the shunt resistance dominated region I shows a voltage dependence of the cell output current once under illumination; it means that the internal voltage of the cell, induced by the energy levels gradient between the layers, is not sufficient in order to extract all the photo-generated charges.

Secondly, the series resistance dominated region III shows a slope less affected by series resistance upon illumination of the cell; this is likely due to the increased conductivity of our

ETL, zinc oxide nanoparticles, once under illumination [77].

1.1.4 Photovoltaic parameters

The photovoltaic efficiency of a cell under illumination can be assessed by a performance indicator called the power conversion efficiency (PCE). It is defined as the ratio of the output electrical power of the cell on the incident illumination power. Most of the data, found in the literature, as well as ours, is given for a standard 1 sun illumination i.e. a power of 100 $mW.cm^2$ distributed over a simulated AM 1.5G spectrum at 25 °C [78].

$$PCE = \frac{P_{output}}{P_{incident}} = \frac{V_{OC} * J_{SC} * FF}{P_{incident}} \tag{1.4}$$

The output power is calculated from three characteristic parameters discussed below :

– **The open-circuit voltage (V_{OC})**

V_{OC} is the measured biasing voltage under a 1-sun illumination when no current flows out of the cell, i.e. when the biasing voltage compensates for the built-in voltage of the cell induced by the energy levels gradient between each electrode.

Its absolute value is therefore equal to the cell built-in voltage.

Its origin is still debated [79–82] but an empirical formula can be used to link it to the difference between the electron acceptor's LUMO and the donor's HOMO [30] :

$$V_{OC} \approx \frac{E_{CT}}{q} - 0.3 \tag{1.5}$$

with $E_{CT} = E_{HOMO}^{Donor} - E_{LUMO}^{Acceptor}$ and q defined as the electronic charge.

This empirical formula suggests that the V_{OC} is linked to the CT state energy.

This can be explained by the fact that, unlike in classical metal-insulator-metal systems, the V_{OC} is not set by the work function difference between the anode and the cathode. Instead, because of the ohmic contact between the electrodes, the transport layers and the active layer, effective charge transfer occurs, thus pinning the electrodes work functions to the LUMO of the acceptor and HOMO of the donor [28].

The $-0.3\ V$ loss of Eq. 1.5 is thought to be related to disorder in the organic semiconductors [30, 81, 83], in particular with trap-assisted recombination via band-tail states located in their band gap [84, 85].

Equation 1.6 shows the J(V) curve formula at $V = V_{OC}$.

$$J(V_{OC}) = J_0 \left[exp\left(\frac{q(V_{OC})}{nkT} \right) - 1 \right] + \frac{V_{OC}}{R_{sh}} - J_{ph} = 0 \tag{1.6}$$

This formula implies that the V_{OC} is independent of any series resistance effect. However, this parameter is sensitive to any shunt resistance decrease, notably occurring during the cells shunting.

– **The short-circuit current density (J_{sc})**

J_{SC} is the the current-density measured in short-circuit conditions under 1-sun illumination,

i.e. without biasing the cell. Therefore, it is the current-density output of the cell under its own built-in voltage.

With a cell having relatively low series resistance values ($R_s < 10\ \Omega.cm^2$), the short circuit-current is mainly dependent on the shunt and the photo-generated current. At higher values, the series resistance decreases the J_{SC} value as well.

– **The fill-factor *(FF)***

FF is the fill factor. It is defined as:

$$FF = \frac{P_{mpp}}{P_{max}} = \frac{V_{mpp} * J_{mpp}}{V_{OC} * J_{SC}} \tag{1.7}$$

With P_{mpp} and P_{max} the power output at the maximum power point and the ideal one (i.e. for an ideal diode), respectively. V_{mpp} and J_{mpp} are the voltage and current, respectively, for which their product P_{mpp} is the highest. The fill factor is a measure of the deviation of the cell from the ideal behavior. Such deviation is affected by the recombination parameters J_0 and n as well as both the shunt and series resistances.

Fig. 1.7 displays an example J(V) curve of an OPV cell under illumination. Its characteristic parameters are indicated in red.

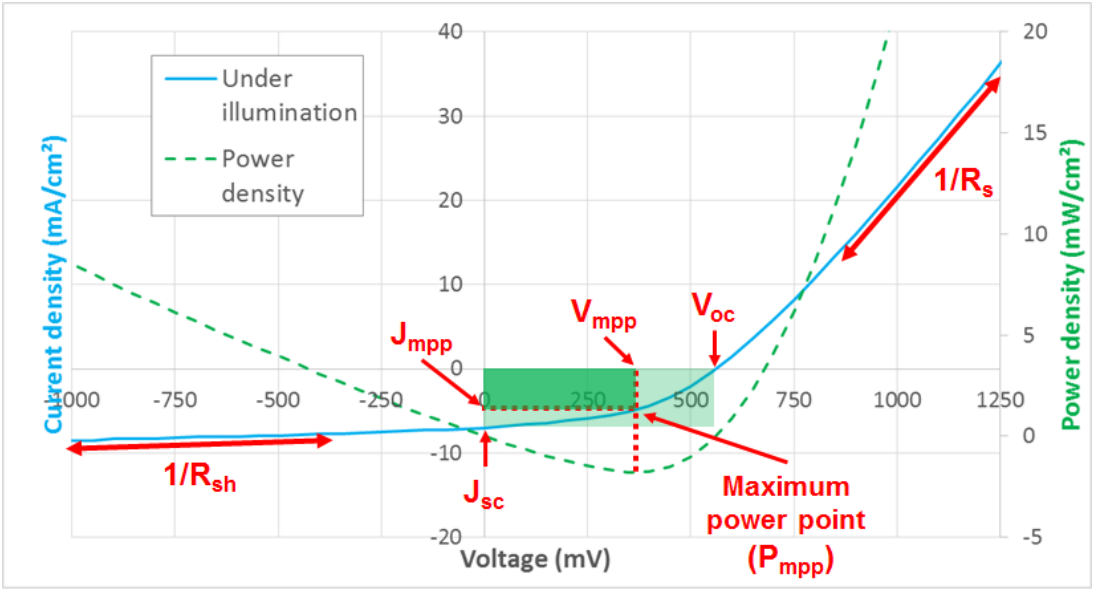

Figure 1.7: *J(V) curve of a typical OPV cell under illumination.*

Fill-factor (FF) is defined as the area ratio of the dark-green rectangle over the light-green one. Series resistance R_s and shunt resistance R_{sh} are calculated as the inverse of the slopes where their respective influence is dominant.

1.2 Aging of OPV devices

In order to allow commercial usefulness of a technology, one must make sure it will survive long enough in its end-user environment. In order to study aging of the devices in a limited time, accelerated aging experiments are conducted and the lifetimes under these conditions are extrapolated to real-environment aging. Standardized accelerated aging tests are commonly used

in the field of inorganic solar cells. Based on the experience in the field, modules passing these tests are reasonably expected to survive 20-30 years in the end-user environment. For OPV devices however, the current lack of outdoor aging experiments which have been conducted for more than a few years does not allow to accurately extrapolate accelerated aging lifetimes to end-user lifetime [20]. However, accelerated aging studies are useful in order to investigate degradation mechanisms of OPVs and design rules for more stable devices.

In this section, the degradation mechanisms of OPV devices occurring during their aging and their effect on the devices performance will be displayed. Then, a focus will be made on the strategies applied to improve the lifetime of the modules.

1.2.1 Aging mechanisms of inverted OPV devices

Aging regimes. Figure 1.8 displays a typical aging curve for OPV devices under illumination.

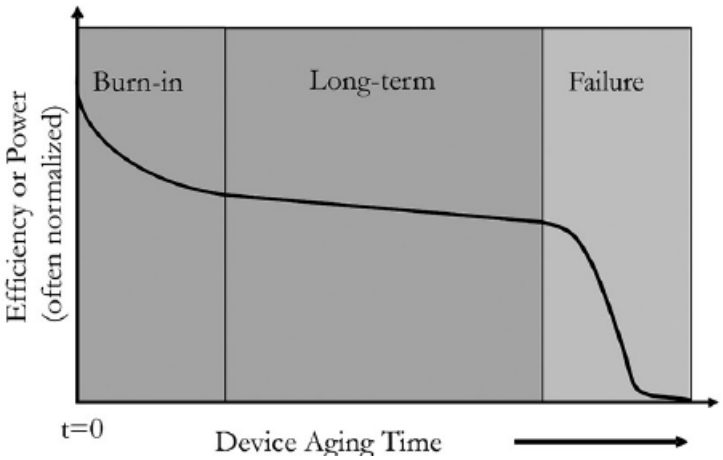

Figure 1.8: *Typical aging study of the performance of an OPV cell under illumination as a function of its aging time. Reproduced from [86]*

Aging studies of OPV devices can generally be broken down in three different regimes [86]:

– The "burn-in" regime - The term makes reference to an unstable state immediately after device fabrication. This term comes from a typical practice in inorganic electronics which consists in a thermal treatment applied to a large batch of fresh devices, before shipping to the customer. Devices performances are generally lowered by the treatment, but devices with high failure rates can be identified and rejected quickly. This allows for a better reliability of the devices and this burn-in loss is generally considered as an initial performance loss.

  Considering the OPV technology, immature compared to their inorganic counterparts, the initial "burn-in" loss of performance can occur for long times (up to a thousand hours before stabilization), and to a significant magnitude (mostly 10 to 50 % efficiency loss). In addition, their performances are generally considered as a blocking point for their commercialization. Therefore, for the research community, this regime is still highly relevant to study, in order to mitigate this loss. Recently, guidelines, defined for reporting

devices lifetime, advise to specify whether the starting point of an aging study is the stabilized time or the just-finished time [20, 66, 87].

– The "long-term" regime - Coming after the burn-in regime, a stabilized, linear, degradation behavior over a large period of time is generally observed. This is the time-frame given to a customer by the term "lifetime"; it must therefore be as long as possible and generally last for tens of thousands hours.
– The "failure" regime - Finally, the devices are quickly degraded in a few hours; this is categorized as the failure regime.

We will now have a look at the degradation mechanisms occurring within the devices during their lifetime. Such degradation factors can be categorized in two groups: the intrinsic factors, where the layers themselves and their interfaces with each other degrade spontaneously, at a given temperature or under illumination and the extrinsic factors, where external species such as moisture or oxygen induce an additional decay of the devices performances. This work was performed on cells with a P3HT:PCBM active layer in inverted configuration. As a consequence, we mainly focused our review on studies made on similar samples.

Thermal degradation.

Active layer degradation The active layer is composed of a blend of a donor polymer and acceptor molecules in most OPV cells. As covered in Sec. 1.1.1, the nano-morphology of this blend is of prime importance in order to optimize the PV efficiency. However, the blend is thermodynamically unstable. As a consequence, the performances of the device may evolve according to the temperature. This is commonly exploited in order to optimize the initial morphology of the cells by performing thermal annealing steps.

The thermal instability of the donor:accepor (D:A) blends is illustrated in th following work. OPV cells made of P3HT:$PC_{60}BM$ as well as other D:A blends were aged at different temperatures [88].

As shown on Fig.1.9a, V_{OC} is decreasing as a function of time at 57 °C but not at 47 °C. In the same article, cells made of poly[N- 9'-heptadecanyl-2,7-carbazole-alt-5,5-4,7-di-2-thienyl-2',1',3'-benzothiadiazole] (PCDTBT):$PC_{70}BM$ were shown to be stable at temperatures up to 127 °C. Interestingly, the glass transition temperatures T_g of P3HT and PCDTBT are 56 and 135 °C, respectively. Another blend, composed of poly[[2,3-bis(3-octyloxyphenyl)-5,8-quinoxalinediyl]-2,5-thiophenediyl] (TQ1):$PC_{60}BM$, with TQ1 having a T_g of $\approx$ 110 °C has shown the a similar behavior [89]. Transmission electron micrographs in Fig.1.9b and Fig.1.9c show domain sizes growth during annealing from a few nanometer wide to micrometer-scale $PC_{60}BM$ crystals.

Furthermore, vertical phase separation, inducing aggregation at the interfaces, is a possible degradation factor. Experimental [90, 91] studies evidence the phase-separation of P3HT:$PC_{60}BM$ cells during film drying. A P3HT-rich phase forms at the surface of the samples. This P3HT-rich phase at the top of the active layer is beneficial for inverted devices because the P3HT (donor polymer)/HTL interface is maximized in this case while it is detrimental

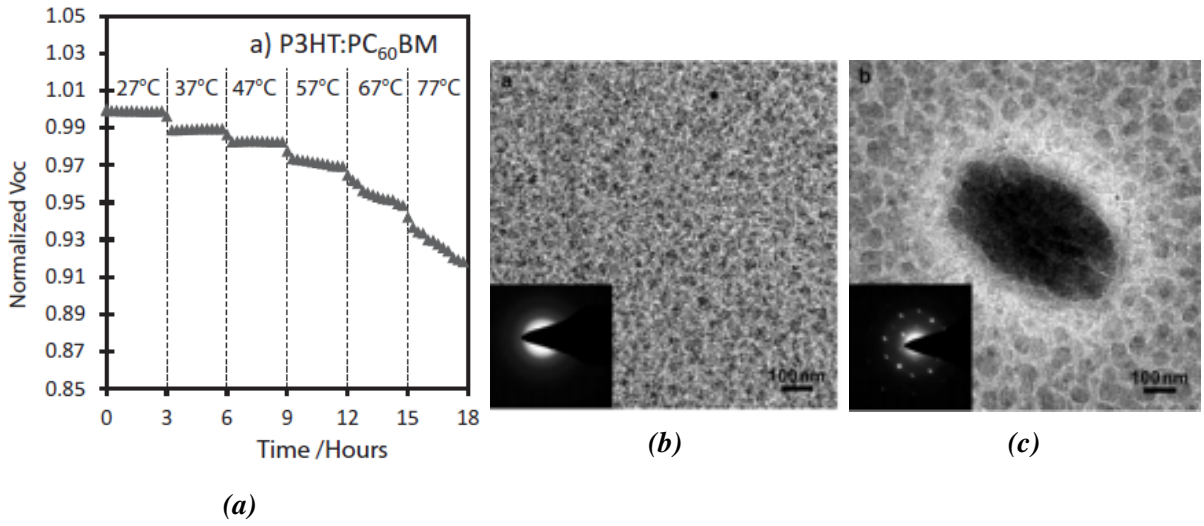

(a) *(b)* *(c)*

Figure 1.9: *(a) P3HT:PCBM (standard architecture) cells' V_{OC} along thermal aging at various temperatures . Reproduced from [88]. (b) and (c) Transmission electron micrographs and electron diffraction patterns (insets) of poly[[2,3-bis(3-octyloxyphenyl)-5,8-quinoxalinediyl]-2,5-thiophenediyl] (TQ1) :$PC_{60}BM$ films before and after annealing at 130 °C, respectively. Reproduced from [89].*

in conventional geometry with the formation of an energetic barrier at the top electrode (or ETL if present)/P3HT interface. This phase separation is expected to evolve with temperature: theoretical work [92] based on the interaction energies between P3HT:$PC_{60}BM$ active layer and poly(3,4-ethylenedioxythiophene):polystyrene sulfonate (PEDOT:PSS) HTL predicts the thermodynamically favorable formation of a $PC_{60}BM$/PEDOT electronic barrier at the interface between the active layer and the HTL.

To improve the thermal stability, cross-linking the polymer, the fullerene or using copolymers are possible strategies [86]. However these strategies often lead to lower initial performances of the cells. High-T_g polymers such as PCDTBT do not suffer from thermal degradation and are relevant when considering thermal stability [88].

Transport layers degradation Other layers, notably the HTL and the metal electrodes have been shown to migrate during thermal aging [93–95]. V_{OC} losses for ZnO/P3HT:$PC_{60}BM$-/MoO_3/Ag cells occurred in a few hours of aging at 85 °C. The direct contact between the low work function Ag electrode and the active layer through the MoO_3, observed by X-ray photoelectron spectroscopy (XPS) of mechanically fractured devices, explains the loss of performance. Replacing the silver by an aluminum electrode limited the diffusion and the subsequent V_{OC} loss.

PEDOT:PSS has also been shown to thermally degrade with an exponential degradation of conductance over time, with a half time of 55 h at 120 °C [96].

Illumination-induced degradation. P3HT:$PC_{60}BM$ devices performances were monitored as a function of exposition time under 1 sun illumination in inert atmosphere [97].

As shown on Fig.1.10a, a significant V_{OC} and J_{SC} loss was shown to occur in the first hundred hours of exposition, during the "burn-in" regime.

The V_{OC} loss was proven to be dependent on the interface materials, as shown on Fig . 1.10b.

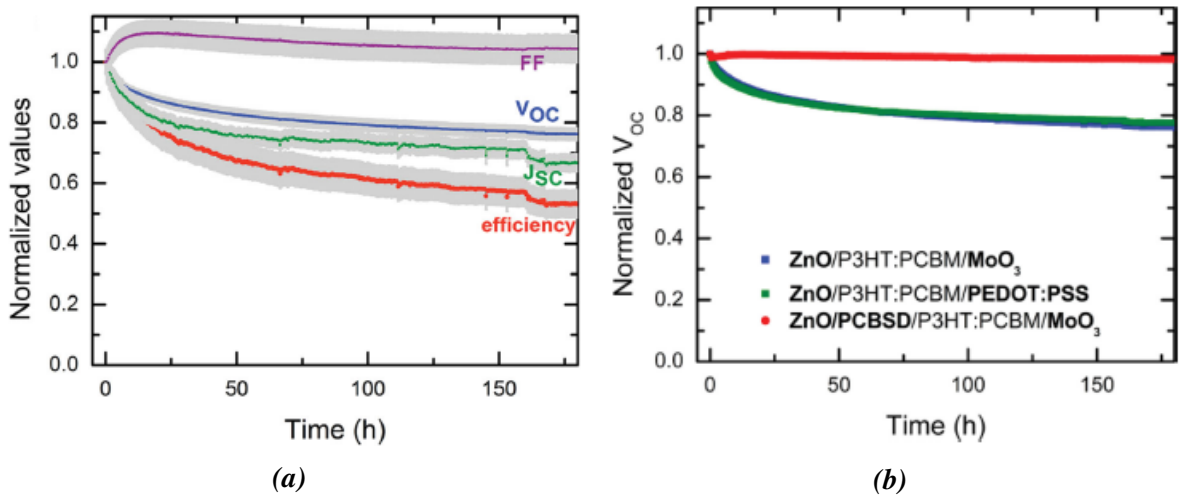

Figure 1.10: *(a) Performances of inverted P3HT:$PC_{60}BM$ devices as a function of aging time under 1-sun illumination. (b) V_{OC} of inverted P3HT:$PC_{60}BM$ devices as a function of aging time under 1-sun illumination with different interfacial layers. Reproduced from [97].*

Replacing the PEDOT:PSS by an MoO_3 had limited influence but adding a [6,6]-phenyl-C(61)-butyric styryl dendron ester (PCBSD) layer as a second ETL layer between the active and the ZnO layers almost totally limited this loss. This is in agreement with other studies which suggest the formation of trapping energy levels even without illumination of UV-light [52].

The J_{SC} loss was linked to the presence of $PC_{60}BM$ dimers [98].

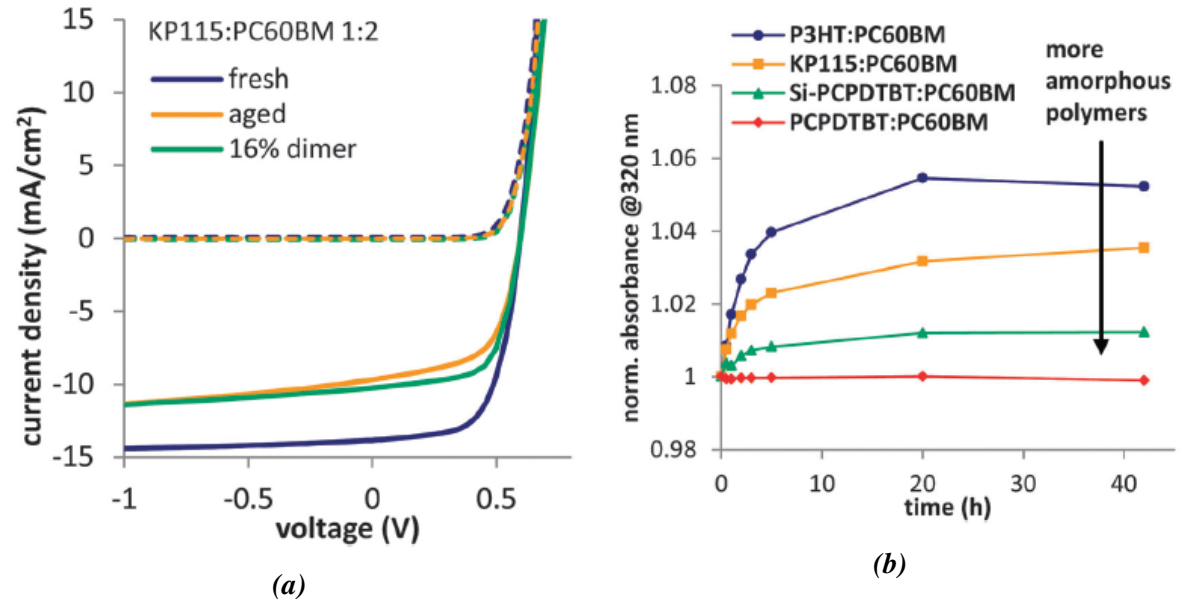

Figure 1.11: *(a) Dark (dashed lines) and illuminated (plain lines) J(V) curves of fresh and aged (120 h under 1-sun illumination) inverted KP115:$PC_{60}BM$ devices along with a fresh device with a 16 % $PC_{60}BM$ dimers added to the active layer during cell production. (b) Normalized absorbance at 320 nm, representative of the $PC_{60}BM$ dimer concentration, for different donor polymers (with a 1:2 donor/acceptor ratio), plotted as a function of aging time under 1-sun illumination. Reproduced from [98].*

As shown in Fig. 1.11a, a 16% addition of $PC_{60}BM$ dimers to the pristine solution of poly [(4,4'- bis (2-ethylhexyl) dithieno [3,2-b:2',3'-d] silole) -2,6-diyl-alt-(2,5-bis 3-tetradecylthiophen-2-yl thiazolo 5,4-d thiazole)-2,5diyl] (KP115):$PC_{60}BM$ almost yield the same losses than 120 h of aging under 1-sun illumination of the pristine active layer, integrated into inverted

devices.
Furthermore, J_{sc} losses were shown to be more important for crystalline-polymer-based active layers than those based on more amorphous ones. As shown in Fig. 1.11b, the dimer concentration, investigated by plotting the absorbance of the cells at 320 nm, was shown to increase more during aging under illumination when blended to more crystalline polymers, which favor the crystallization of the fullerenes, than for amorphous ones.
Therefore, the J_{SC} burn-in loss was associated to $PC_{60}BM$ dimerization favored by the presence of large, crystalline phases of donor polymer.

Several strategies were developed in order to tackle burn-in performance degradation: the use of non-fullerene acceptors [99], the use of fullerene triplet (which eventually leads to fullerene dimerization) quenchers [100] or the use of active layers made of evaporated small molecules[101] .

Oxygen-induced degradation.

Adsorption on ETL leading to conductivity decrease. Freshly prepared devices in air were shown to have strong S-shaped J(V) curves [77, 102].

After exposition to UV-light (as shown on Fig. 1.12a) or after several J(V) measurements [103], the curves shifted to more satisfactory J-shaped curves. However, the inflexion point was shown to re-appear to a lesser extent after days of dark storage (Fig. 1.12b). This was ascribed to the photo-conductivity dependence of the ZnO nanoparticles toward adsorbed oxygen on their free surface [104]. The S-shaped behavior is originating from the unbalanced conductivity of holes and electrons in the device, produced by the formation of mid-gap energy levels from adsorbed O_2^- species. During exposition under UV-light or upon injection of charges into the device, these trap states are quenched by free holes, allowing for the J(V) performances to recover upon exposition.

Active polymer photo-bleaching In addition, polyalkylthiophene compounds were found to bleach under the influence of oxygen and illumination [105].

As shown on Fig. 1.13, this mechanism is achieved by the side chain oxidation ultimately leading to carboxylic compounds. Fortunately, the addition of fullerenes to the blend significantly limits polymer bleaching; fullerenes are thought to be able to capture free radicals, thus slowing down the photo-oxidation process [106]. On a larger study of a range of polymers, alkyl side chains were indeed identified as the weak point for photo-chemical stability of the polymers [107].
To improve the stability of polymers without suppressing the side chains, which would limit their solubility, thermally labile groups can be inserted [108] leaving only the polymer backbone after deposition and subsequent thermal treatment. However, cleavage temperatures are still above 150 °C, which limits this application to glass devices.

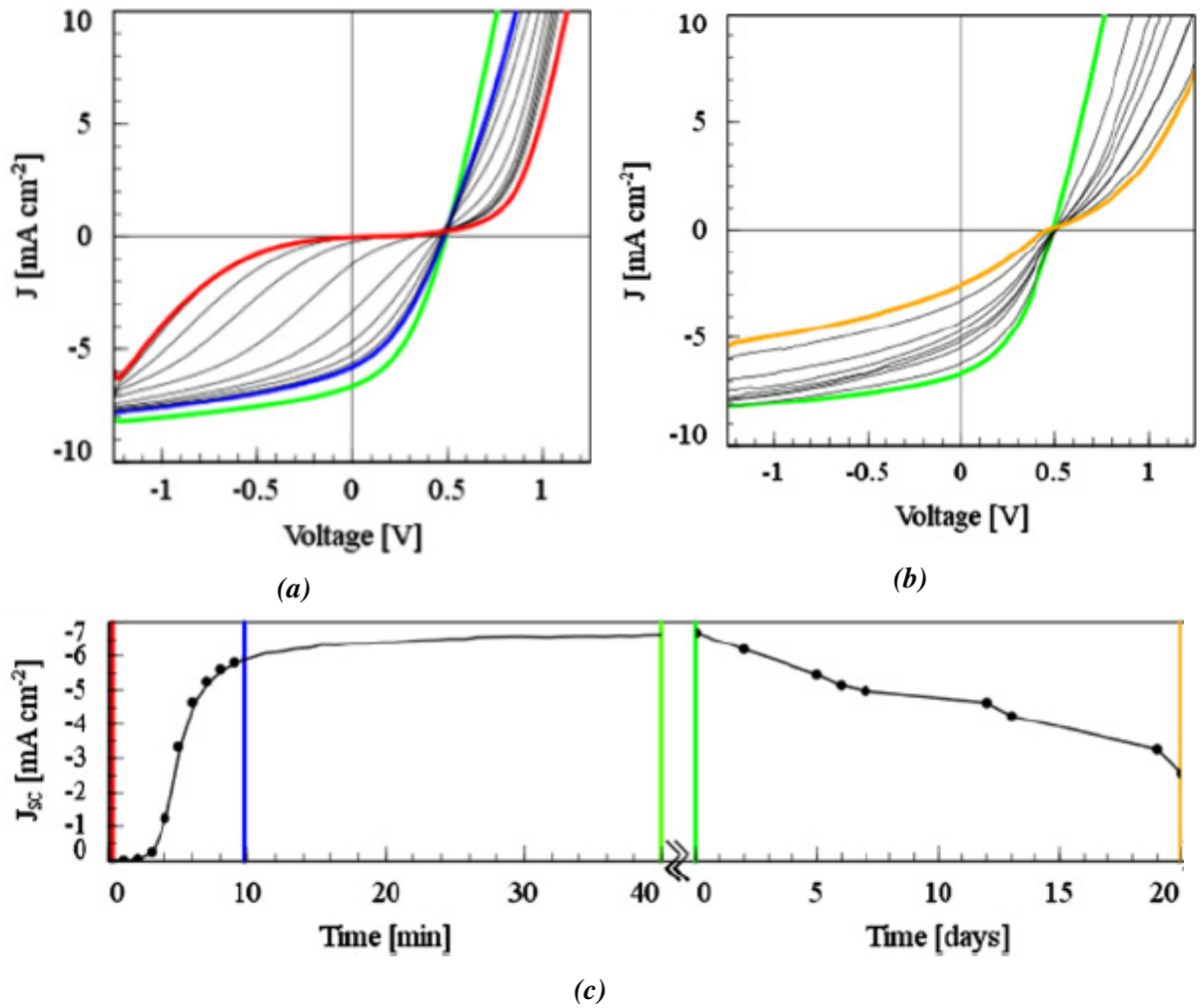

Figure 1.12: *J(V) curves of devices (a) freshly prepared, during exposition to UV-light, (b) device left in dark storage after UV exposure. The J_{SC} evolution as a function of time is plotted on (c). Colors of figures (a) and (b) correspond to times marked in (c). Reproduced from [102].*

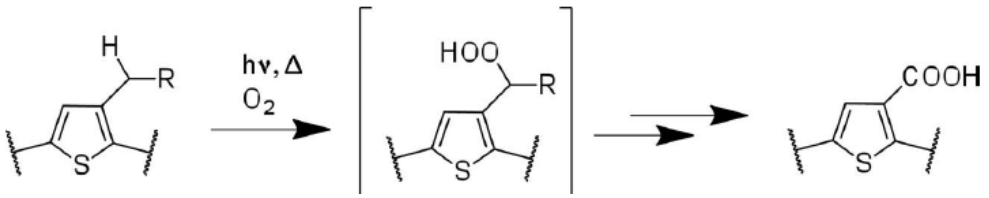

Figure 1.13: *Photo-oxidation mechanism of poly-alkylthiophene compounds. Reproduced from [105].*

Moisture-induced degradation. Low work-function electrodes, such as calcium or aluminum, used in conventional-architecture devices are known to easily oxidize in contact with water vapor [109]. Oxidation alters both the conductivity as well as the work function of the electrodes, thus causing degradation of the performances of the devices. On conventional-architecture devices, the active layer / metal interface was identified as a weak point for the stability of the devices [110–112]. It was shown that water preferentially diffuses between the aluminum grains while oxygen diffuses through microscopic pinholes [110]. This leads to the formation of an electrically resistive aluminum oxide layer for the former and the delamination of aluminum for the latter, as shown on Fig. 1.14.

Permeation of water and oxygen within the devices can be tracked by imaging techniques; it

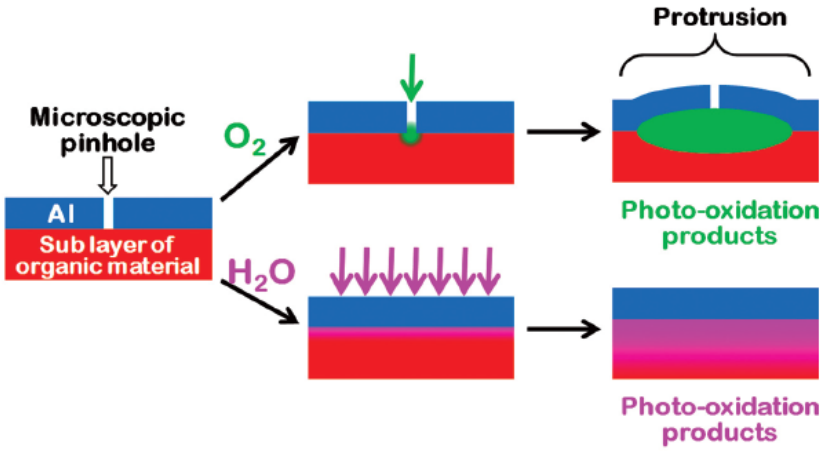

Figure 1.14: *Permeation of oxygen and water vapor through the aluminum electrode. Reproduced from [113].*

will be covered in Sec. 1.4.

These low work-function metals can be replaced with higher ones, notably in inverted-architecture devices.

In both structures, the use of PEDOT:PSS as HTL was identified as an accelerating degradation factor because of its hygroscopic nature [114, 115].
Significantly higher lifetimes can be achieved by substituting PEDOT:PSS by other HTLs such as MoO_3 [93, 95, 115], WO_3 [93], NiO [116], V_2O_5 [117, 118], polyaniline [119] or even a silver oxide layer, spontaneously formed after seven days in ambient conditions of a bare Ag electrode [120]. However, cells made of such materials generally yield lower initial performances.

Mechanical degradation. Several research groups identified the mechanical failure of complete OPV devices as a prime concern even over efficiency and photo-chemical stability issues: in 2010, in the "Lighting Africa" framework, which consisted in the installation in rural Zambia of white-LED lamps powered by roll-to-roll manufactured OPV devices; Krebs *et al.* reported that mechanical issues were dominant during the field test before the photo-chemical stability of the solar cells became a problem [26]. In 2012, during the "Workshop on Key Scientific and Technological Issues for Development of Next-Generation Organic Solar Cells", it was emphasized that there was no knowledge of the mechanical behavior of OPV cells under thermal cycling and that no strategies were identified to prevent mechanical failure [27].

Mechanical degradation studies, covering both the characterization and the improvement of such properties will be the main focus of Sec.1.3.

1.2.2 Encapsulation for enhancing stability

Encapsulation has been naturally implemented to photovoltaic devices according to their sensibility toward water and oxygen. It consists in the packaging of the cells in between oxygen and water barrier layers. Such barrier layers are held by encapsulant layers. This packaging

also improves the scratch resistance of the devices. Finally UV-cutoff filters can be added in the encapsulation materials in order to protect the cell from the most harmful radiations [113].

In inorganic PV modules, encapsulation consists of two rigid glass layers held with an ethylene vinyl acetate hotmelt encapsulant [121]. This technique offers the advantages of an almost zero nocive species orthogonal permeation (i.e. through the glass layers) and a good protection against outdoor conditions, notably hail damage [122]. However, such rigid glass encapsulation systems are not suitable for flexible devices such as most organic devices are expected to be.

Encapsulation systems adapted to OPV devices - Permeation pathways. Fig.1.15 shows a typical encapsulation system for an OPV device. Possible permeation pathways are shown with red arrows.

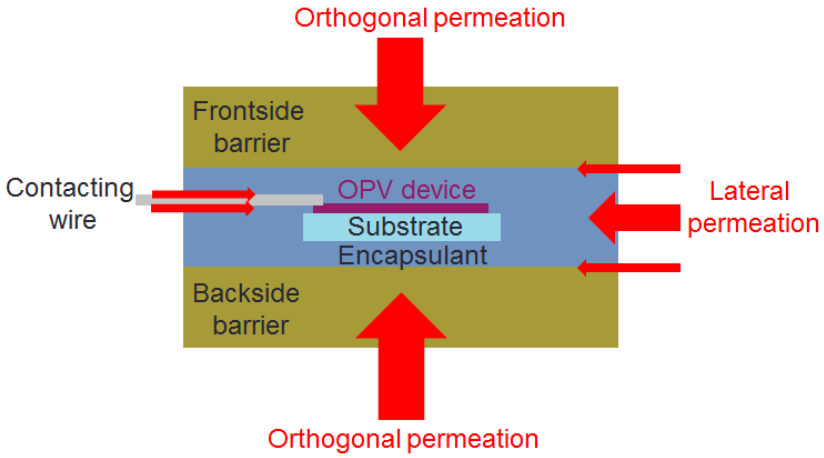

Figure 1.15: *Encapsulation architecture and permeation pathways of nocive species within an OPV device according to [123].*

Instead of rigid glass, a flexible encapsulation with polymer barrier layers is preferred for flexible devices. However, organic polymers feature a limited oxygen and moisture permeation hindrance. Nonetheless, their barrier properties can be improved by creating an alternated stack of polymer and dense inorganic layers. As a consequence of the addition of several sub layers within the barrier, the encapsulation materials can reach a significant cost, up to 60% of the complete prototype modules production cost [124–126]. Therefore, in order to limit the cost of such complex barrier layers, it is necessary to know the minimum barrier properties required to protect the devices for a given lifetime [127].

In addition, the barrier layers need to be held on the flexible devices with the help of encapsulant layers. As permeation can occur orthogonally to the devices, i.e. through the barrier layers, it can also occur laterally, through the bulk encapsulant layers, at the interfaces between the barrier layers or along the contacting wires required for reaching electrical contact outside the cells [123]. Therefore such encapsulant materials also play a critical role against permeation in addition to holding the barriers.

The transmission rate difference between the barrier materials (from less than 10^{-6} g.m^{-2}.day^{-1}

for glass [23] to $\approx 10^{-3} - 10^{-4}$ g.m^{-2}.day^{-1} for most flexible barrier materials [128]) and the encapsulant materials ($\approx$ a few g.m^{-2}.day^{-1} for relatively good encapsulant materials in terms of barrier properties), suggests that permeation in most of encapsulated devices does not occur through the barrier materials but from the edges of the encapsulation systems.

In accordance to these results, edge sealing of the encapsulation systems was performed [129]. A HelioSeals PVS 101 tape (ADCO) was placed between the adhesive interlayers before encapsulation. The device geometry is shown on Fig. 1.16a and results are shown on Fig. 1.16b.

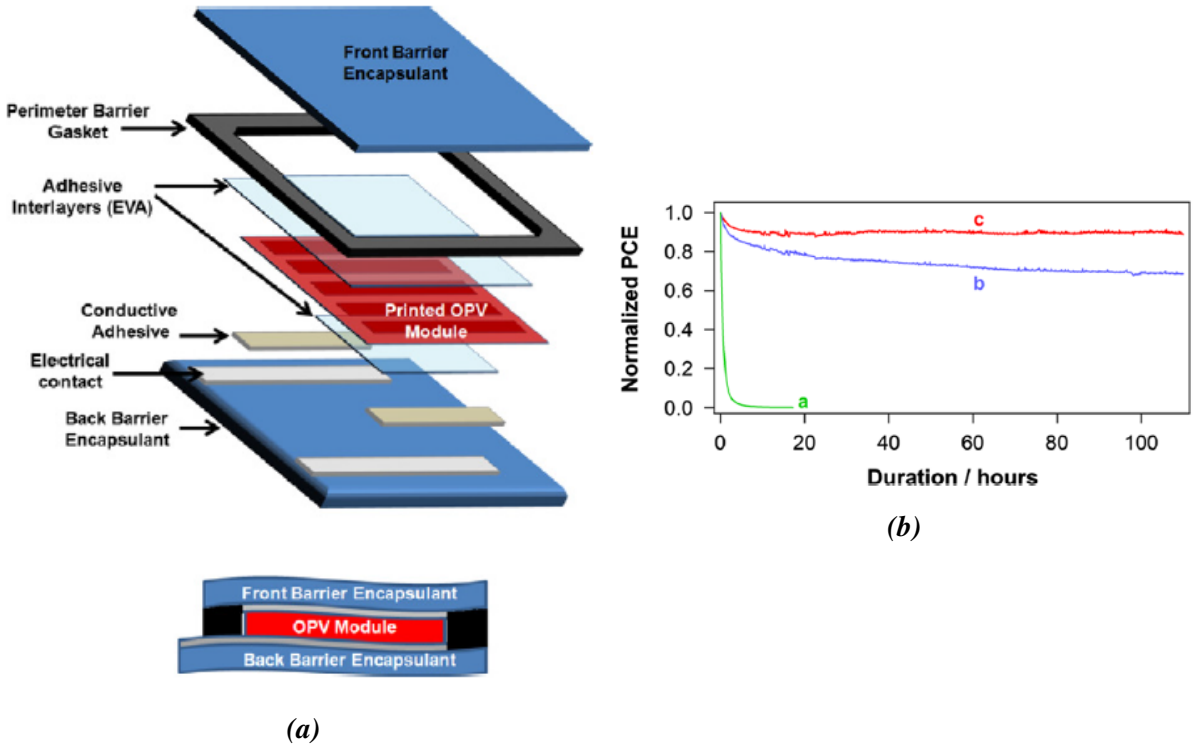

Figure 1.16: *(a) Flexible encapsulation geometry for edge sealed modules. (b) PCE over time under 1 sun in a 60 °C/50 % RH environment of modules : a-unencapsulated, b-encapsulated without edge sealing, c-with edge sealing. Reproduced from [129].*

The system with edge sealing completely prevents degradation once the burn in regime is over. In comparison with the system without edge sealing, a significant protection is brought and the lateral permeation is evidenced. Other studies support such observations [130]. In order to limit lateral permeation, moisture barrier encapsulants materials were developed [131].

Barrier requirements. In order to limit the cost of the barrier layers, the minimum barrier properties requirements, i.e. the minimal water vapor or oxygen transmission rate (WVTR and OTR respectively) needed for the barrier to bring a given lifetime before a certain amount of degradation, have to be determined.

A given barrier requirement value yields a cell lifetime assuming nocive species only permeate orthogonally to the cell, through the barrier materials. However, in real devices, permeation can occur laterally to the devices, possibly limiting the devices lifetime.

The quantity of diffusing water Q_t needed to degrade P3HT:PCBM cells, in conventional or inverted geometry, to 50% of their initial PCE at 38 °C/100%RH and under 1 sun illumination was experimentally determined as 2.1 10^{-2} g.m^{-2} and 1.14 g.m^{-2} [127].

Furthermore, the lag time introduced by the barrier materials, of a determined water vapor transmission rate (WVTR), in order to reach that quantity Q_t of water, has been calculated, as shown on Fig. 1.17a. As an example, a barrier material with a WVTR of 0.01 g.m^{-2}.day^{-1} would allow a T_{50}, the time needed for the cells to reach 50% of their initial performance, of ≈ 10 and 100 days for conventional and inverted geometries, respectively.

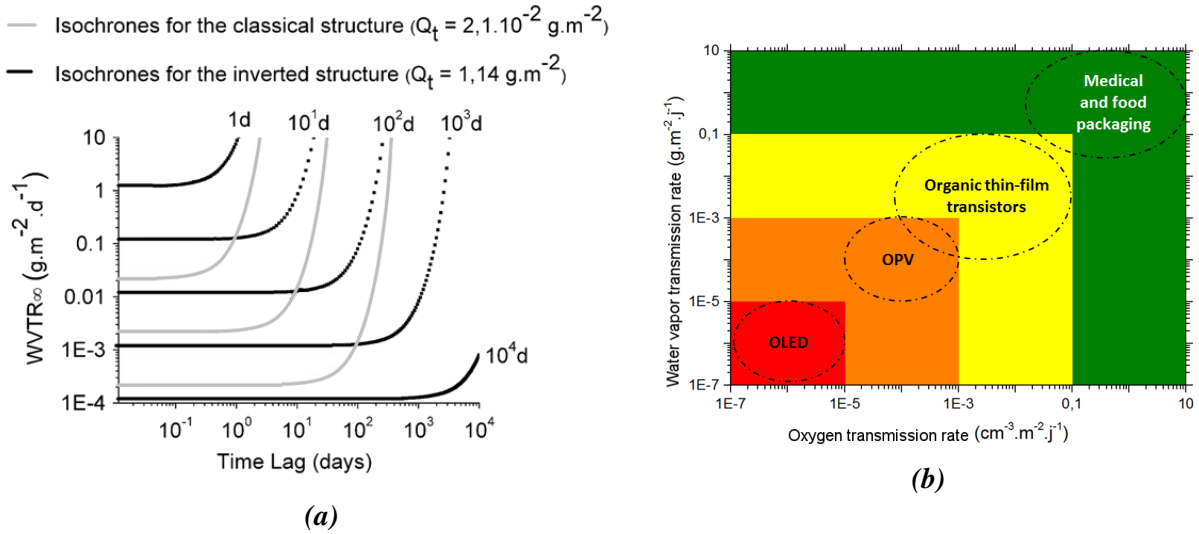

Figure 1.17: *(a) Estimated time lag brought by a perfect encapsulation to standard or inverted P3HT:PCBM cells in order to reach their T_{50} (time at which the samples reach 50% of their initial performances) as a function of the water vapor transmission rate (WVTR) of the barrier materials. Adapted from [127]. (b) Rule-of-thumb for barrier requirements toward oxygen and water transmission rates for several applications. Adapted from [132]*

From this study, it was estimated that the barrier layers must have a water vapor transmission rate lower than 10^{-3} g.m^{-2}.day^{-1} in order to allow inverted cells to reach a 1000 h T_{50} lifetime. Compared to other organic electronics technologies, this barrier requirement is less critical than the barrier requirements for OLEDs (10^{-5} g.m^{-2}.day^{-1}), as shown on Fig. 1.17b [127].

Encapsulation strategies. Despite their importance, the encapsulation materials (both the barrier and encapsulant ones) and processes are not extensively described in the literature [66]. Their influence on the device initial performances is even more scarcely described.

Three different encapsulation materials and processes were studied on a roll-to-roll line [133]: the lamination of a pressure sensitive acrylate adhesive (PSA) through rolls, the UV-curing of a solvent-free epoxy resin and a polyester hot-melt adhesive heated to 140 °C. Processes workflows are shown in Fig.1.18.

J(V) curves of PSA and UV-cured encapsulated modules immediately after encapsulation are shown in 1.19.

Immediately after encapsulation, air inclusions were reported within the PSA modules encapsulation. Devices encapsulated by PSA showed S-shaped J(V) curves, reversible under

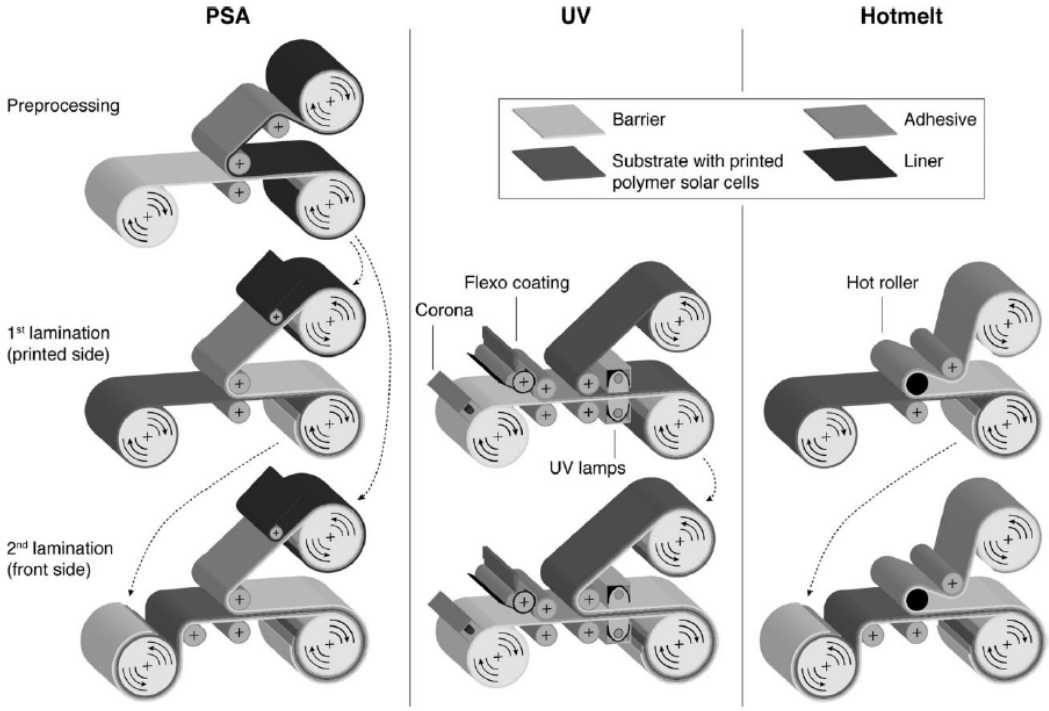

Figure 1.18: *Process workflow of roll to roll encapsulation of flexible OPV modules. Reproduced from [133].*

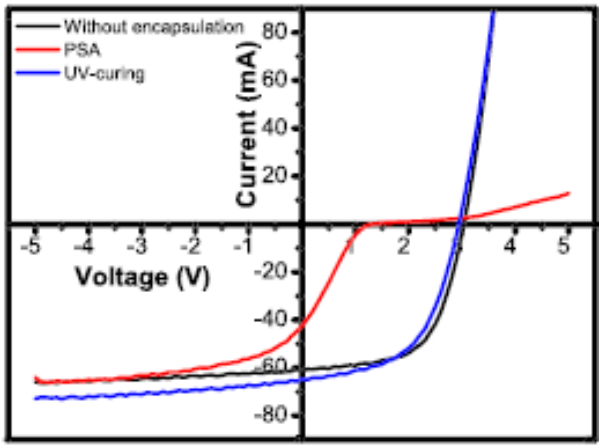

Figure 1.19: *Inverted OPV devices before encapsulation, after a PSA encapsulation or after a UV-cured encapsulation. The PSA curve evolve to a classical J-shape after prolonged illumination. Reproduced from [134].*

illumination and therefore attributed to oxygen presence [134], while UV-cured ones exhibited classical J-shaped curves.

PCE of UV-cured, hotmelt and PSA encapsulated devices are shown in Fig.1.20. In order to reduce costs, single side (on the printed side) and double side encapsulations were tested.

PSA devices were degraded significantly faster than hotmelt and UV-cured ones. V_{OC} was the PV parameter driving such performance degradation. After 900 h aging under illumination in ambient atmosphere, PSA devices showed significant photo-chemical bleaching of the active layer on the edges while the hot-melt and UV-cured ones suffered from little to no bleaching. Such effects were ascribed to the inferior density of the PSA compared to the two others

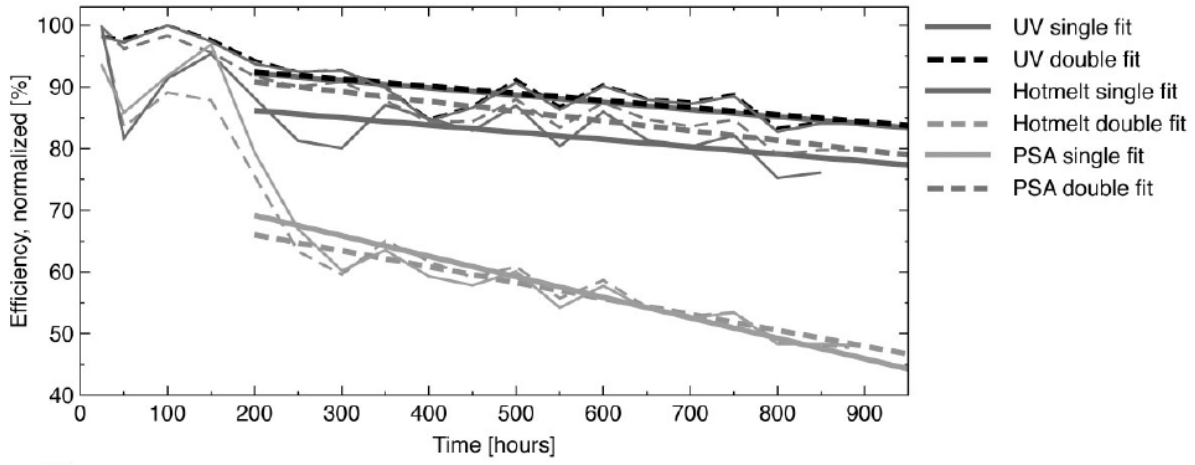

Figure 1.20: *PCE of encapsulated devices along aging time under standardized AM 1.5 G illumination in ambient atmosphere. Reproduced from [133].*

materials allowing for oxygen permeation. Gas bubbles observed in the PSA encapsulated devices immediately after processing may as well participate in degradation.

In a following study, UV-cured devices were aged according to standardized ISOS aging protocols. Detailed aging protocols can be found in ref.[87, 135]. Results of the aging studies are shown on Fig. 1.21.

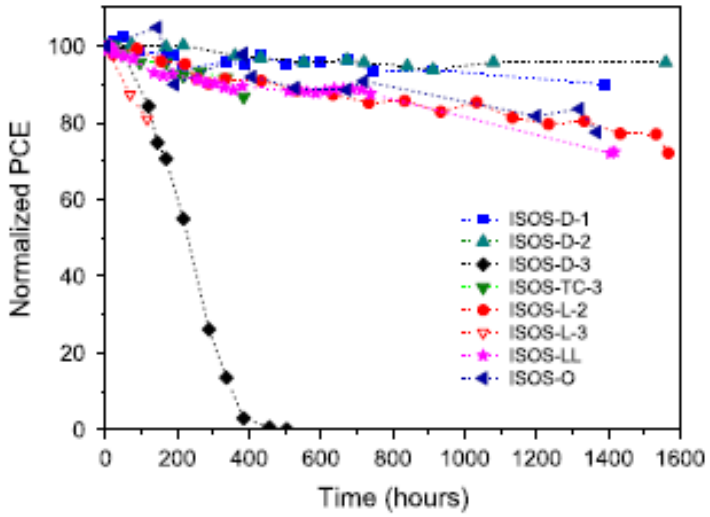

Figure 1.21: *PCE of UV-cured encapsulated devices along aging time under ISOS aging protocols. ISOS protocols can be found in ref.[87, 135]. Only modules exposed to relative humidities of 85 % at 65 or 85 °C (ISOS D-3 and ISOS L-3 protocols) did not reached a 1000 h T_{80}, time at which 80 % of the initial performances are reached. Reproduced from [134].*

Only cells exposed to relative humidity of 85 % at 65 or 85 °C (ISOS D-3 and ISOS L-3 protocols) did not reach a 1000 h T_{80}, time at which 80 % of the initial performances are reached. Devices in an oven at 65 °C (ISOS D-2) have proven a higher stability than the ones stored at room temperature (ISOS D-1). This can be explained by a low resistance of the encapsulation against moisture diffusion into the device.

Konarka Technologies, reported in late 2012 [21–23], flexible encapsulated modules which met the International Electrotechnical Commission (IEC) 61646 qualification [24]. Encapsulation system, undisclosed to our knowledge, included adhesive with fillers and an additional buffer layer in order to improve barrier properties.

Such modules suffered less than 10 and 18 % efficiency degradation after 1000 and 1800 hours of aging at 85 °C/85 % RH, respectively.

The passing modules were encapsulated with a high performance barrier (WVTR = $5.10^{-3} g.m^{-2}.day^{-1}$) while devices with less efficient barrier layers (WVTR = $5.10^{-2} g.m^{-2}.day^{-1}$) showed a $\approx 40\%$ efficiency degradation in less than 250 hours in the same aging conditions.

Encapsulation interest. Recent meta-analysis of the literature [20, 66] proves the interest of encapsulation. Fig.1.22a summarizes lifetimes of encapsulated or unencapsulated devices according to several aging protocols. Fig.1.22b shows performance versus lifetime scatter plot and histogram of the same studies categorized according to the encapsulation type, rigid or flexible.

As shown in Fig.1.22a, stability towards moisture, oxygen and illumination (in ambient atmosphere) is generally higher for encapsulated devices [136].

In addition, rigid and flexible encapsulated devices show similar lifetime timescales. This suggests that efficient barrier layers, with sufficient barrier properties, are commonly used in the literature. It also implies that failure factors are likely lateral permeation of nocive species or intrinsic (thermal, illumination-induced or mechanical) degradation.

Inverted configuration was initially developed because it allows the replacement of the aluminum electrode by a silver electrode of higher work function thus leading to significantly improved stability in damp conditions. However, the meta-analysis shows that efficiently encapsulated cells have the same stability in the dark regardless of their configuration. Additionally, lifetime of inverted devices was overally slightly lower when exposed to standardized AM1.5G illumination [20].

Partial conclusion

As shown in this section, OPV devices can be degraded by several factors, both intrinsic and extrinsic. Intrinsic degradation can be limited by engineering the devices architectures and materials directly. Extrinsic degradation can be mitigated by encapsulation techniques.

However, despite their importance, encapsulation processes and materials are scarcely described in the literature, even in aging studies. In addition, such encapsulation processes can have an impact on the devices initial performances. As a consequence, good encapsulation practices need to be defined in order to optimize the OPV devices performances, cost and lifetime.

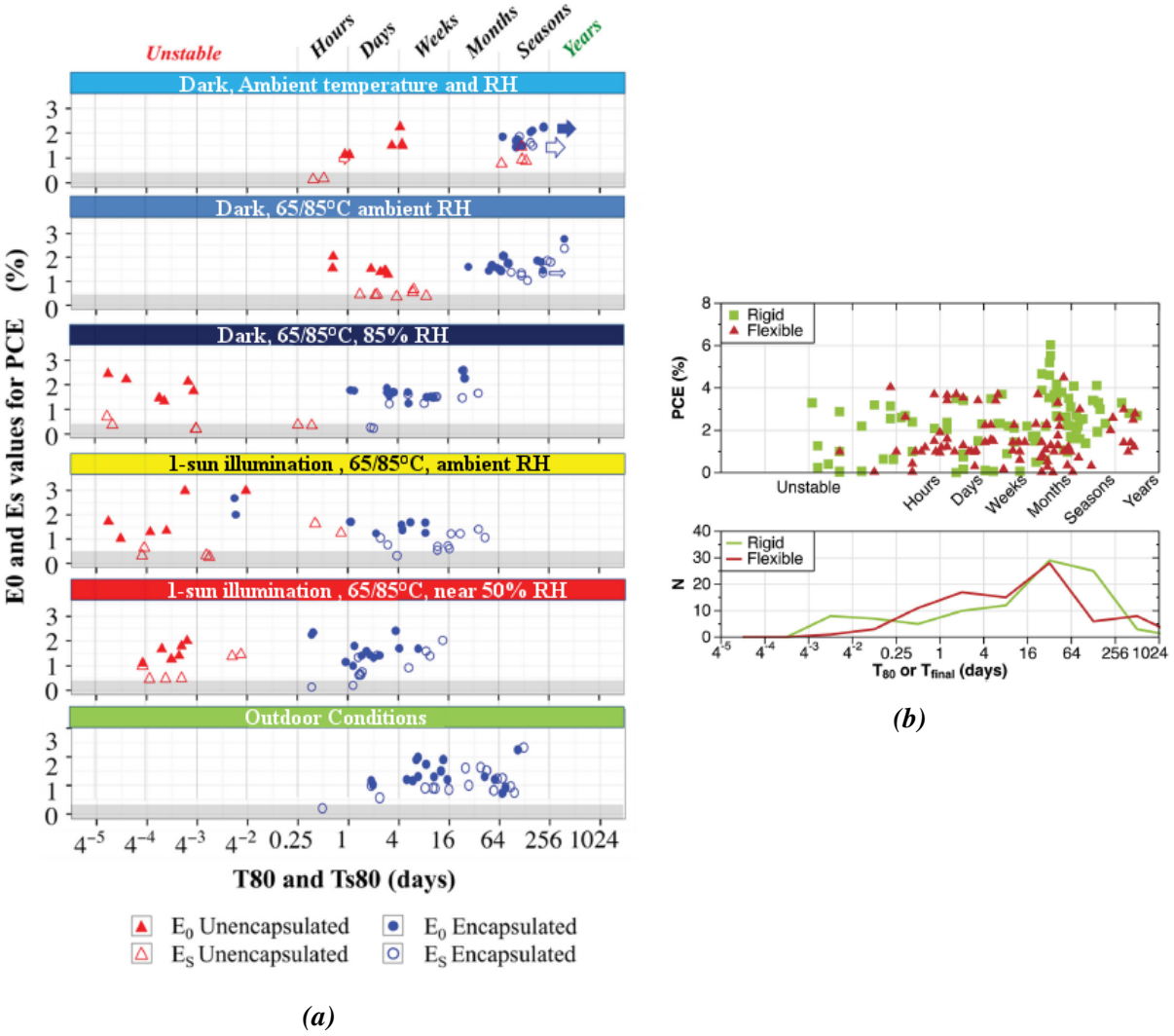

Figure 1.22: *(a) E_0 and E_S, the initial efficiencies of the devices before and after burn-in, respectively, as a function of their T_{80} and T_{80} times, which represent the time at which 80% of the initial performances (E_0 or E_S, respectively) remained. (b) PCE versus stability of devices according to the encapsulation type : rigid or flexible. All aging coditions were included in this analysis. Adapted from [66].*

1.3 Mechanical properties of OPV devices

Although they are generally being disregarded by most studies directed toward efficiency improvement, mechanical properties should be taken into account when speaking of high-speed manufacturing and viability under real-life conditions of devices sought to be flexible [126, 137–139]. Indeed, flexible OPV devices have to withstand the strains provoked by the fabrication, transport, installation, climate changes and manipulation during their lifetimes [25]. As shown in Sec.1.2.1, several aging studies in real-life conditions placed mechanical failure as a prime degradation factor before any photo-chemical stability issue [26, 27].

To study mechanical failure, we focused on critical mechanical degradation i.e macroscopic cohesive rupture in a single layer or adhesive rupture at the interface between two of them. This section will cover the basic adhesion mechanisms as well as characterization techniques able to study multi-layered thin films stacks. Finally, mechanical studies on OPV devices and strategies of improvement of the mechanically weak layers will be reviewed.

1.3.1 Theory of fundamental adhesion

Work of fracture. Macroscopic mechanical degradation occurs in two different ways depicted in Fig. 1.23 : the cohesive failure of a single layer and the adhesive failure between two of them [140].

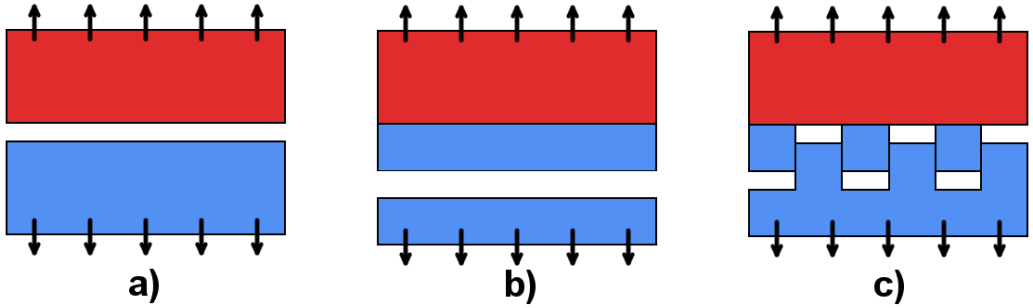

Figure 1.23: *Scheme depicting an object made of two materials under normal strain. This object is destroyed by a) adhesive rupture at the interface, b) cohesive rupture within a single material, c) mixed rupture.*

A mix of both modes is possible in case of inhomogeneous layers and/or internal stresses.

The work of adhesion, W_a, or the work of cohesion, W_c, is defined as the work needed to fracture the interface, or a single material, respectively. Fig. 1.24 describes the fracture of a two-solids material and the formation of new interfaces with the ambient gas.

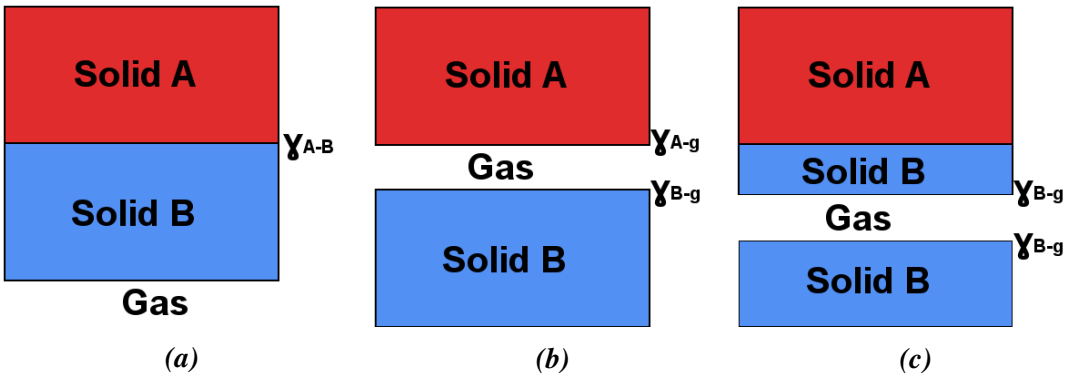

Figure 1.24: *Scheme representing two surfaces A and B : (a) bonded, (b) after adhesive fracture, (c) after cohesive fracture.*

The energy required to form an interface between solid A and B is known as the surface energy γ_{A-B}. The surface energy between the gas and solid A, or B are written γ_{A-g} and γ_{B-g}, respectively.

The work of adhesion W_a between two materials is therefore equal to the formation of two interfaces A/gas and B/gas, and the rupture of the A/B interface :

$$W_a = \gamma_{A-B} - \left[\gamma_{A-g} + \gamma_{B-g}\right] \tag{1.8}$$

In the case of a cohesive fracture, the work of cohesion W_c within a single material is therefore equal to the formation of two B/gas interfaces and the rupture of a B/B interface :

$$W_c = \gamma_{B-B} - 2\gamma_{B-g} \tag{1.9}$$

When the rupture mode is not perfectly known, we will use the term work of fracture which covers both failure types.

OPV devices are composed of many layers of different chemical natures and thicknesses (detailled in Fig. 2.4, page 75), which leads to complex adhesion mechanisms at their interfaces. We will thus describe the fundamental mechanisms ruling adhesion.

However, there is no unified theory of adhesion; there are several theories that can be relevant depending on the considered interfaces. In this section, various concepts used to describe adhesion between different layers will be presented. Please note that the boundaries between these theories are often blurred, as a result, some authors may treat these theories under different headings. For example, chemical theory is often treated as a part of the adsorption theory in some manuals [141] while others consider only secondary bondings (Van der Waals, etc...) in the latter.

Chemical theory. In this case, formation of strong covalent bonds between both surfaces is achieved. The bonded surfaces must be highly reactive and a curing step is sometimes necessary for this mechanism to occur.

Adhesion between two silicon surfaces has been extensively studied in the field of microelectronics for applications such as silicon on insulators [142]. At room temperature, the adhesion between hydrophilic silicon surfaces is achieved by hydrogen bonding through chemisorbed water. At temperatures above 150 °C, polycondensation reaction occurs; water is eliminated and covalent Si-O-Si replaces the previous bonding, thus increasing the adhesion. Before bonding, oxidative O_2 plasma treatments can be performed in order to break Si-O-R bounds (R being an alkyl contaminant) and further activate the surface by forming Si-O-H bonds in presence of water [143].

Adsorption theory. Adsorption theories such as the Owens-Wendt theory or the Van Oss & Good theory are often used to explain adhesion when there is no penetration between the two surfaces [144].

This theory implies that once both materials are in contact, attraction forces between them will be stronger than those between the materials and the ambient gas. These forces cover a number of molecular interactions such as dipole-dipole (Keesom) and induced dipole-dipole (Debye) interactions between polar or polarizable molecules, induced dipole-dipole interactions between neutral molecules (London) and hydrogen bonds between electronegative atoms and hydrogen [144]. Although weaker than covalent bonds, these forces are often more numerous and thus cannot be neglected before the former. Because the density of interaction is crucial for this mechanisms to be efficient, the good contact between the materials, i.e. a good wetting without contaminants, is of prime importance when considering this theory.

Highly polar polymers can be bonded on polar surfaces through hydrogen bonding mechanisms. Such mechanisms explain the adhesion of epoxy adhesives with metal-oxide surfaces [145].

Mechanical theory. Together with other adhesion mechanisms, mechanical interlocking can play a great role in the formation of strong bonds between two layers [145]. This phenomenon occurs when a low-viscosity liquid or melted polymer fills a rough or porous substrate surface. Once again a good wettability of the material over the substrate is a prerequisite.
When one considers mechanical interlocking, one must keep in mind that the greater specific surface between the layers also allows for more bonding interaction. Therefore the overall adhesion is increased as well. It is thus often difficult to dissociate the influence of mechanical interlocking itself from the influence of specific surface expansion [146].

This kind of mechanism can be relevant when considering an ink or a polymer above its glass transition on a rough substrate [147].

Electrostatic theory. Electrostatic adhesion is achieved when one can represent the interface as a capacitor [148].

As OPV devices are supposed to separate and conduct charges through numerous interfaces, this kind of mechanisms are expected to take place.

For example, a P3HT$^+$:PSS$^-$ strong interface layer can be expected at the BHJ / HTL in standard configuration devices due to vertical phase separation [149, 150].

Diffusion theory. Interface diffusion can occur when a polymer above its glass-transition temperature is in close contact with a compatible (i.e. non repulsive) surface [147]. This mechanism leads to a mixed interface of the two bonded layers where polymer chains entanglements play the role of chemical bridges.

For example, this mechanism is the principle of the polymer heat-sealing technique [151, 152].

1.3.2 Mechanical characterization methods

Adhesion measurement of nanometer-thick films. Each mechanical characterization is a measurement of an experimental (i.e apparent) adhesion. The experimental adhesion is in fact a function of the intrinsic adhesion (i.e. the forces binding the two surfaces together) and extrinsic factors dependent on the internal stresses [153] and measurement method parameters [141, 154]. The experimentally measured adhesion of a given system with a given intrinsic adhesion is thus not the same depending on the characterization technique employed.

Quantitative adhesion measurements of metallic thin films deposited onto glass, metal or oxides surfaces have been successfully achieved in a handful of ways such as pull-off, scotch tape, peel, shear, scratch and blister tests. Each method has its own advantages and drawbacks compared to the other ones.

Despite measurement of elastic-behaving metallic thin films has been successfully achieved, the viscoelastic characteristics of ductile materials, especially polymeric thin films, causes difficulties when applying the same characterization methods on those [155].

As schemed in figure 1.25, polymeric materials can dissipate energy through plastic deformation such as frictional sliding and stretching of polymer chains in the bulk of the layers neighboring the crack tip [156, 157].

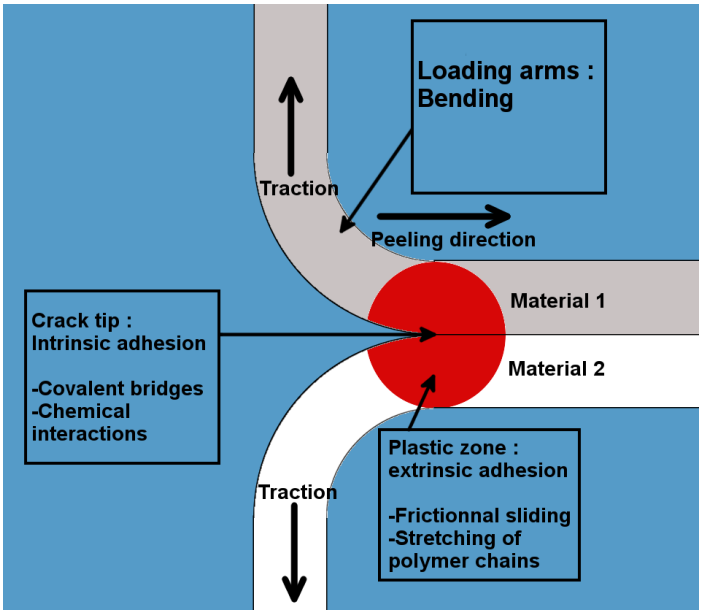

Figure 1.25: *Scheme representing a T-peel test of two polymer layers. The measured adhesion energy is a sum of contributions from the interfacial intrinsic adhesion, the energy dissipation in a plastic zone around the crack tip and the stiffness of the peel arms.*

Fig. 1.26b shows the load versus displacement curve of a viscoelastic Poly(methyl methacrylate) (PMMA) obtained from a double torsion experiment and Fig. 1.26a shows the simulation of the plastic strain during peeling of a ductile copper layer from an elastic substrate.

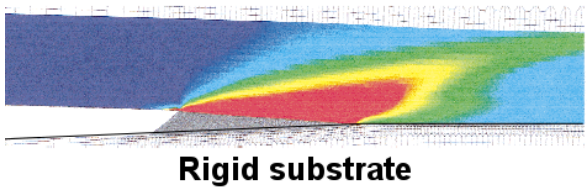

(a)

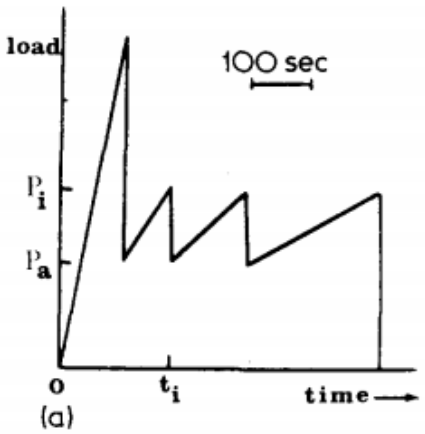

(b)

Figure 1.26: *(a) Simulation of the distribution of plastic strain in a 4.4 µm thick ductile copper layer during peel from a rigid substrate. The red zones are regions with a plastic deformation > 2%. Reproduced from [157] (b) Load-displacement curve of PMMA exhibiting plastic dissipation processes from a double-torsion experiment. Reproduced from [158].*

During load, the viscoelastic zone, as simulated in figure 1.26a, forms around the crack tip as the load increases. At a critical load, this zone ruptures and the crack propagates freely which causes a drop on the load-displacement curve. The crack eventually stops as the load drops and

the process can repeat itself. Such time-dependent processes lead to saw-tooth-like features on the load versus displacement curves obtained on such materials [158, 159].

This phenomenon is dependent on the dynamic viscoelastic properties of the materials, the bridging between the interfaces and the loading rate employed during the experiment. This mechanism has been studied on other polymer materials [160, 161] and was also confirmed with molecular-dynamics simulations (Figure 1.31) of cohesive failure in OPVs' active layer [162]. Thus, the measured apparent adhesion of such materials is significantly dependent on extrinsic factors linked to the measurement protocol and the samples design.

Furthermore, since viscoelastic films can dissipate energy to a range larger than their thickness, all the materials of multi-layered devices can potentially influence the measured adhesion despite the fact that rupture effectively occurs at a single place [156]. As a consequence, adhesion measurements of multi-layered thin-film systems, such as OPV devices, are particularly sensible to extrinsic factors.

Characterization of OPV devices. Various characterizations methods were applied to OPV devices in order to qualify the influence of processing or material changes over the mechanical stability.

Pr. R. H. Dauskardt and his team led extensive studies focused on the mechanical properties of standard and inverted OPV devices. They studied samples on rigid glass as well as flexible PET substrates in a number of collaborations [91, 94, 129, 149, 159, 162–172]. Double cantilever beam (DCB) and four points bend mechanical tests (figure 1.27) were performed after bonding an elastic (glass, Al, Silicon...) substrate on both sides of the devices with brittle epoxies.

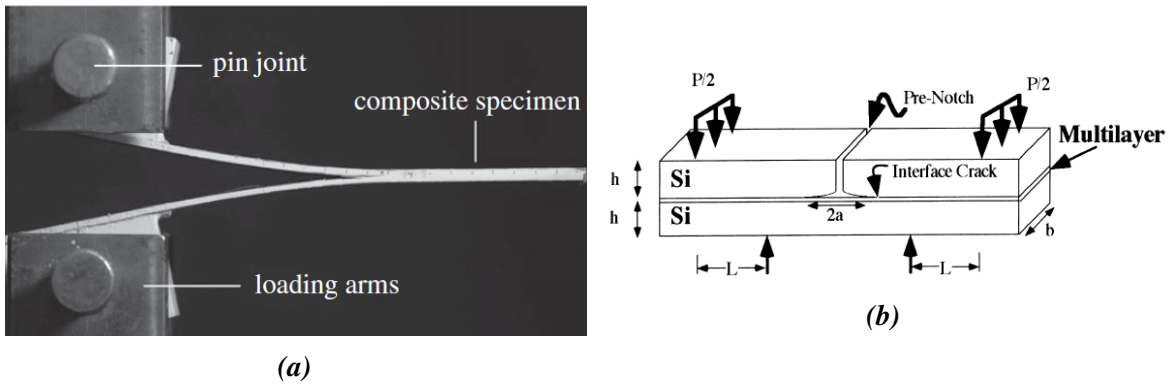

Figure 1.27: *(a) Double-cantilever-beam experiment from [173] (b) Four-point-bend sample from [156].*

From these experiments, they extracted a parameter : G_c, the fracture energy, defined as the energy applied for debonding the samples expressed in terms of the critical load P_c measured on the plateau of the load-displacement curves. Eq. 1.10 was used to determine G_c:

$$G_c = \frac{12P_c^2a^2}{b^2E'h^3}\left(1+0.64\frac{h}{a}\right)^2 \tag{1.10}$$

With P_c the critical load for debonding, a the debond length, measured from optical microscopy, E' the specimens plain strain elastic modulus, b and h the samples width and half-thickness, respectively.

After adhesion tests, in order to characterize the rupture path, the debonded surfaces were investigated with various characterizations techniques : X-ray photoelectron spectroscopy (XPS), contact angle measurements, atomic force microscopy (AFM), near edge X-ray absorption spectroscopy (NEXAFS) and UV-Vis reflection measurements.

Such techniques allow for a precise and quantitative measurement of the debond energy. However, the epoxy bonding and its curing applied during sample preparation are additional processing steps to the device fabrication which may cause additional extrinsic strains.

Other mechanical tests, although less quantitative, were succesfully carried out on OPV as well as on organic light-emitting diodes based on P3HT and 8-tris(hydroxyquinoline aluminum) active layers, respectively [174]. In this article, the interface of interest was the one between the active layer and the aluminum electrode present in most standard-architecture OPV devices.

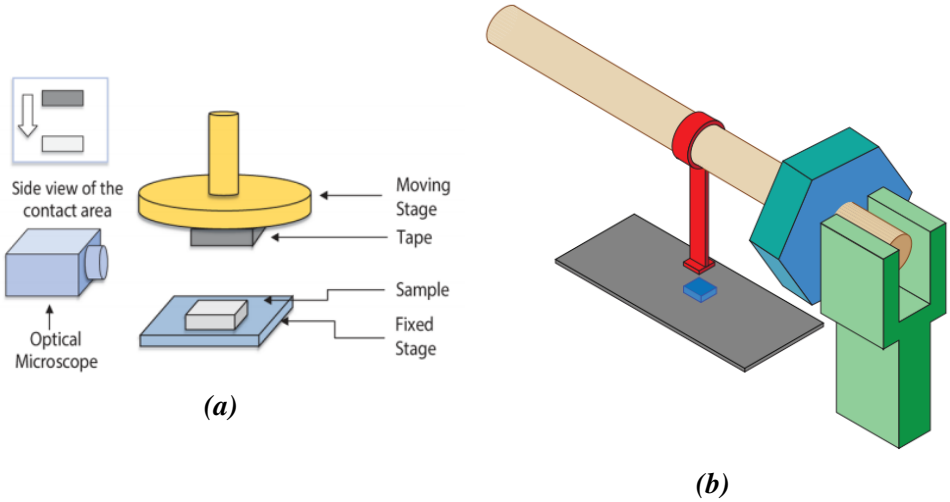

Figure 1.28: *(a) Semi-quantitative pull-off test experiment, (b) qualitative Scotch tape test.*

Pull-off characterizations (Fig. 1.28a) were performed on at least 30 samples allowing for statistical treatments of the measured pull-off force. Additionally, measurements of the delaminated area fraction were performed with Scotch tests (Fig. 1.28b). To confirm the rupture path, XPS, AFM and X-ray diffraction spectroscopy (XRD) were used. Such characterization method was also used by an other group [175, 176], who performed XPS characterizations to investigate the debond path.

The authors estimate sample-to-sample variations to be more significant [177] than measurement-related errors; therefore, using a statistically meaningful number of samples, the authors can compare apparent pull-off forces of different architectures. However, pull-off forces are dependent on extraneous factors such as the devices geometry, the pulled area or the interaction between the sample and the tape; thus the experimental conditions must be kept identical between all tested samples.

1.3.3 Studies of the mechanical properties of OPV devices

In this section, we will review the literature about the mechanical properties of OPV devices. Strengthening strategies of the weak spots identified in OPV devices will also be presented.

In a similar fashion than the previous section, this review will focus on inverted P3HT:PCBM devices.

BHJ/HTL adhesion and BHJ cohesion

In this section, we will review the work of Pr. Dauskardt's team which mainly focused on the BHJ / HTL adhesion and the BHJ layer cohesion.

Donor:Acceptor ratio. Fig.1.29 shows the fracture energy G_c of inverted devices (PET/-ZnO/P3HT:$PC_{60}BM$/PEDOT:PSS/Ag) as a function of the $PC_{60}BM$ weight fraction in the P3HT:$PC_{60}BM$ active layer [167].

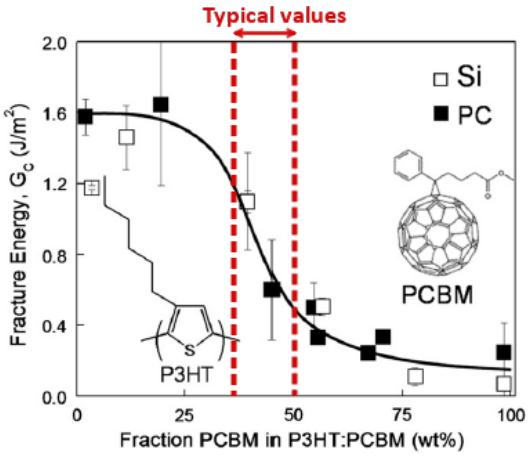

Figure 1.29: *Fracture energy of inverted devices as a function of the weight fraction of $PC_{60}BM$ in P3HT:$PC_{60}BM$ blend. The empty and plains squares represent different elastic substrates used for the DCB tests. Reproduced from [167]. Typical weight ratio values reported for most inverted devices are ranging between red dashed lines.*

All devices failed adhesively at the BHJ / HTL interface except for nearly pure PCBM devices that exhibited mixed adhesive / cohesive BHJ failure. The increased adhesion of high P3HT ratio devices is attributed to an increased number of Van Der Waals interactions between long chains of P3HT and PEDOT, that are not favored with PCBM. However, G_c values even for the stronger devices are still relatively weak compared to other systems, which will be reviewed later in this section, which attained values of several tens of $J.m^{-2}$.

Film thicknesses and P3HT molecular weight. No significant differences of adhesive fracture energy between the BHJ and the PEDOT:PSS layers are observed on the 10-40 nm range of PEDOT:PSS HTL thickness of inverted devices [149].

In a first time, the influence of the BHJ thickness was studied on standard architecture devices [171] which failed cohesively within the BHJ layer and no fracture energy differences are observed for values ranging from 50 nm to 250 nm.

In a second time, in other papers [159, 170], standard devices made of regio-regular P3HT with a molecular weight ranging from 28 $kg.mol^{-1}$ (or kDa) to 100 $kg.mol^{-1}$ were tested. Results are reported on Fig. 1.30a.

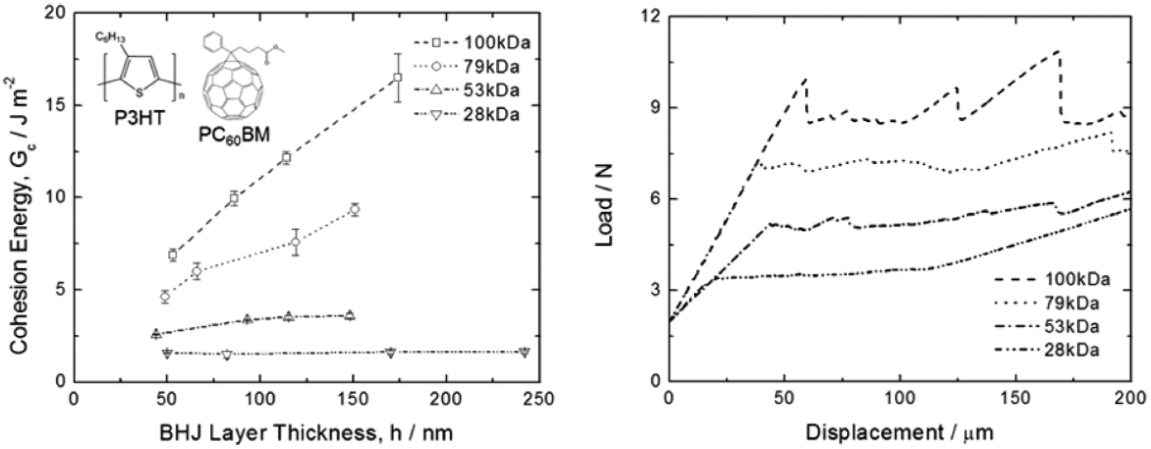

Figure 1.30: *(a) Cohesion energy of P3HT:PC_{60} layer in standard devices with varying molecular weight of P3HT and active layer thickness. (b) Corresponding representative load/displacement curves. Both reproduced from [159].*

In this study, all standard-architecture cells fractured cohesively within the BHJ layer. Increased molecular weight P3HT cells yield increased mechanical properties. Furthermore, as shown in Fig. 1.30b cells with P3HT of molecular weight >79 $kg.mol^{-1}$ show viscous yielding which further increases the mean resistance toward critical failure. Finally, cells exhibiting viscous behavior also show a fracture energy dependent upon the BHJ thickness; as the thickness increases, plastic zone of energy dissipation around the crack can expend and dissipate more energy.

Molecular dynamics simulations of P3HT:PCBM blends, with various ploymer molecular weights under strains were performed [162, 166, 169]. Fig. 1.31 shows a snapshot of a 200mer P3HT:PCBM blend under 300% strain.

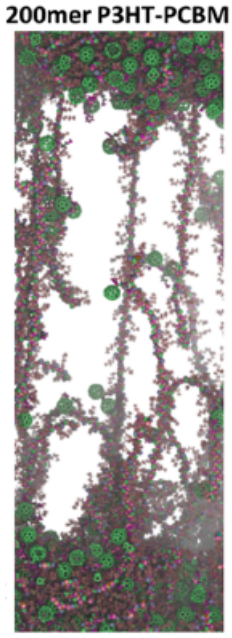

Figure 1.31: *Molecular dynamics simulation snapshot of 200mer P3HT (≈ 34kDa):PC_{60}BM blend under 300 % strain. Reproduced from [162].*

Such studies suggest that cohesive failure within the BHJ originates from rupture at the

polymer phase/fullerene clusters interface. For low molecular weight polymers, this leads to void formation that drive the fracture of the device. For high molecular weight polymers, such as the case represented in Fig. 1.31, polymer chain entanglement induces chain stretching at the crack tip which increases the overall cohesion energy.

Thermal annealing. 10 minutes thermal annealing was performed on inverted OPV cells after HTL deposition. The mechanical properties as well as the efficiency of corresponding cells were studied as a function of the annealing temperature (Fig. 1.32 [163]).

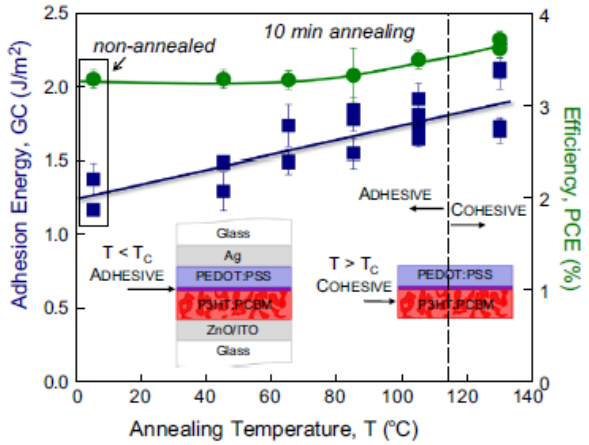

Figure 1.32: *Adhesion energy and PCE of inverted devices as a function of the annealing temperature for 10 minutes before electrode deposition. Reproduced from [163]. The cells have already been annealed at 130 °C for 10 min under inert atmosphere before deposition of the HTL layer.*

An improvement of devices efficiencies mostly from J_{SC} above 85 °C annealing is observed due to morphological change of the blend during the 10 minutes thermal annealing. The adhesion energy between the BHJ and HTL layers is found to increase with respect to the annealing temperature. In addition, an intermixed layer of BHJ and HTL is found at the interface for temperatures above 105 °C, the fracture then occurs at the BHJ / intermixed layer interface. Finally, for temperatures above 115 °C, rupture occurs cohesively inside the BHJ layer. As shown in the previous paragraph, low cohesion within the BHJ layer originates from rupture between the polymer phase and the $PC_{60}BM$ clusters. This can be explained by the formation of large $PC_{60}BM$ clusters when the annealing temperature exceeds the crystallization temperature of $PC_{60}BM$ at $\approx$ 120 °C. Such large clusters would create paths of low cohesion therefore decreasing the overall cohesion strength of the layer.

Adhesion energy of inverted devices as a function of the annealing time and temperature applied after electrode deposition [91] is shown in figure 1.33a.

For all the annealed devices, a growing intermixed layer of P3HT:PCBM / PEDOT:PSS increasing the adhesion at the interface is observed. In this case, fracture occurs for higher energies, at the interface between the BHJ layer and the intermixed layer.

Comparison between 130 °C thermal annealing before or after electrode deposition is made in Fig. 1.33b.

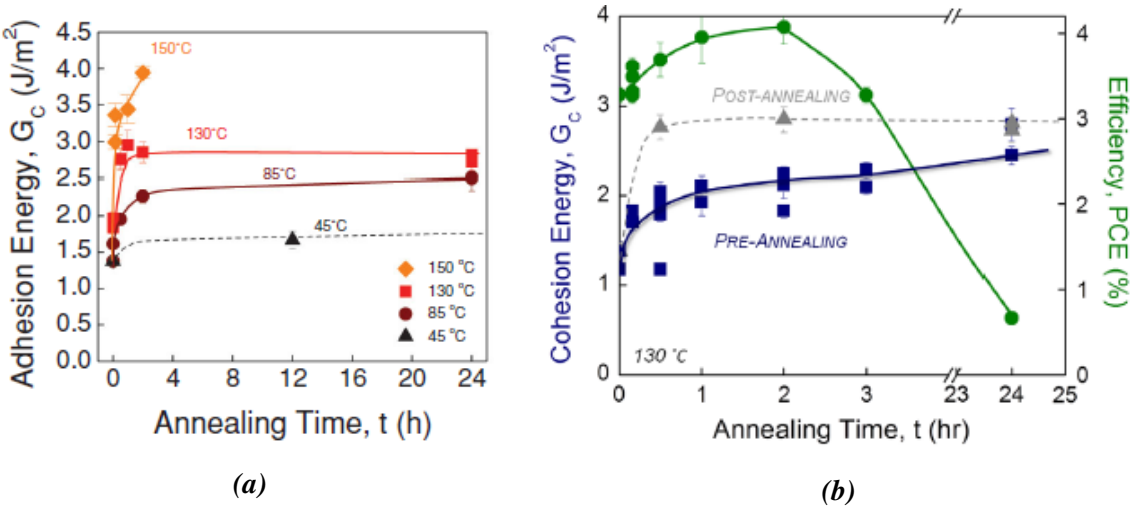

(a) *(b)*

Figure 1.33: *(a) Fracture energy of inverted devices as a function of annealing time for a range of annealing temperatures after electrode deposition. Reproduced from [91]. (b) Cohesion of the BHJ layer of inverted devices as a function of annealing time at 130 °C after electrode deposition (gray triangles) and before electrode deposition (blue squares). The cells have already been annealed at 130 °C for 10 min under inert atmosphere before deposition of the HTL layer. Reproduced from [163].*

For annealing times above two hours, the efficiency of the cells decreases. This is ascribed to a non-favorable morphological evolution.

Comparing the fracture energy of devices annealed before or after electrode deposition, one can see an increase in both cases. Interestingly, in the case of annealing prior to electrode deposition, the fracture path is located within the BHJ, whereas for annealing after electrode deposition, the rupture path is always located at the interface between the BHJ and the intermixed layer between the BHJ itself and the PEDOT:PSS layer. This effect is ascribed to spatial confinement of the $PC_{60}BM$ crystallites' growth by the relatively rigid electrodes thus limiting the cohesion loss in the BHJ layer.

Tuning the BHJ layer surface before HTL deposition. A 60 s O_2 plasma treatment prior to the PEDOT:PSS deposition step of inverted devices fabrication was performed on the BHJ layer in order to increase its roughness and lower its hydrophobicity [149]. This led to an increased wettability of the HTL layer on the BHJ. However, only a marginal increase of adhesion ($\approx$ 15%) is observed with power of the plasma treatment ranging from 100 kW to 180 kW. Furthermore, no detailed information about PCE values are reported and PCE losses could be expected due to exposition of the BHJ to an oxidizing environment [178].

More chemical treatments of the BHJ layer must have been explored but were not published to our knowledge: the introduction of CF_4 during plasma treatment in order to further enhance reactivity or the pre-deposition solvatation of the BHJ layer with the same solvent as the HTL's which might promote layers intermixing at the interface.

Depositing an interlayer on the BHJ layer before HTL deposition may also be an efficient strategy. Cross-linked poly(allylamine hydrochloride) - dextran (PAH-D) illustrated in figure 1.34 was developed [178].

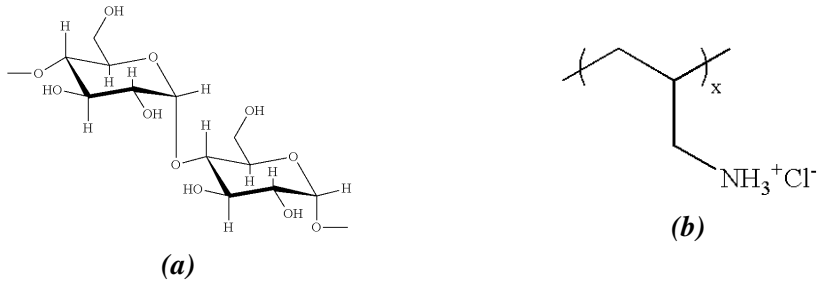

(a) *(b)*

Figure 1.34: *(a) Dextran and (b) poly(allylamine) (PAH) formulas. Reproduced from [179] and [180] respectively.*

Lower water contact angle of BHJ layer when covered by PAH-D reveals a more hydrophilic layer. This interlayer may therefore improve adhesion by promoting hydrophobic interaction between BHJ and the PAH-D backbone as well as polar interactions between the HTL and the ionic and hydroxyl parts of the PAH-D. Functional solar cells were fabricated using PAH-D but no comparisons with control cells nor adhesion measurements were provided.

Use of different PEDOT:PSS formulations. In order to improve the interface strength between the BHJ and the PEDOT:PSS layers, one must make sure that the area between both is as large as possible. Because of the hydrophobicity of the BHJ layer and the hydrophilic nature of the PEDOT:PSS, dispersed in alcohol or water-based solvents, it is difficult to make the PEDOT:PSS inks wet the BHJ. A common way to tackle this issue is to use additives in the PEDOT:PSS solutions in order to lower its surface tension.

Patents are pending on the use of non-polar additives such as fluoro-surfactant Zonyl ^{TM}[181] for example, deposited along with PEDOT:PSS in order to create an interlayer increasing both wettability and adhesion. However, as a drawback, these surfactants are known to decrease conductivity of the PEDOT:PSS [182].

Another strategy to promote adhesion between layers is to chemically bridge them together with a third compound. Difunctionnal organosilanes adhesion promoters are often used to improve adhesion between hydrophobic polymer surfaces and hydroxylated substrates such as ceramics or metals [145]. Such compounds can be found in commercial dispersions of PEDOT:PSS already in use in the field of organic electronics [183].

In other studies, a PEDOT:PSS solution in organic solvent was developed and tested with pull-off characterization [175, 176]. The use of organic solvent solution brought a 16% increase of the stress at break value (given in $N.m^{-2}$) compared to the reference water-based PEDOT:PSS solutions.

Fianlly, another group introduced polystyrene (PS) nanoparticles in its PEDOT:PSS dispersions [184].

These nanoparticles bear two purposes, sketched in Fig.1.35: First, they act as a binder for improving cohesion of the HTL layer itself by increasing the fracture path and distributing mechanical stress. Second, these hydrophobic PS particles are expected to have an increased interaction with the active layer than the hydrophilic PEDOT:PSS. Therefore, they also have an

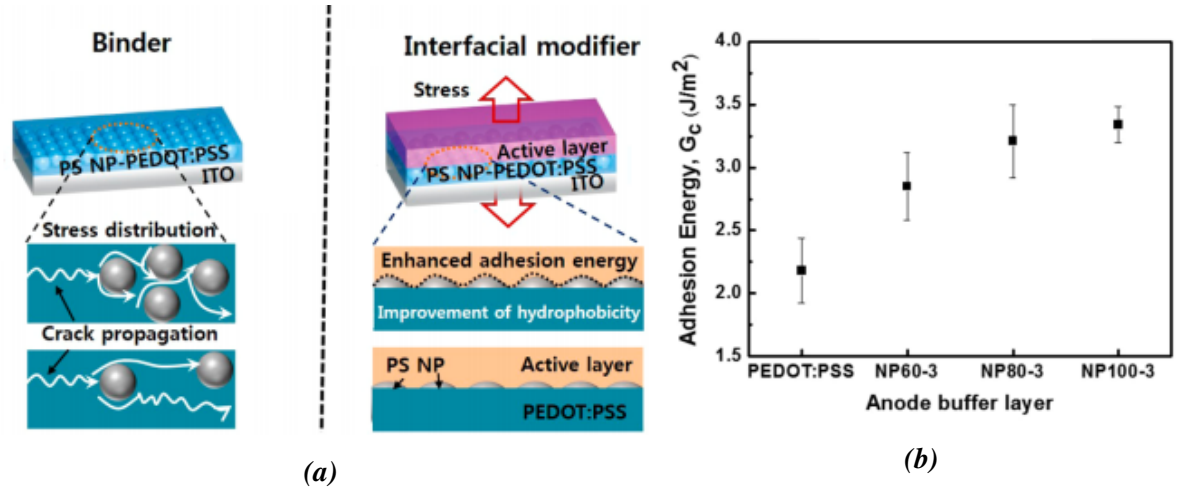

Figure 1.35: *(a) Scheme of the effect of polystyrene (PS) nanoparticles dispersed in PEDOT:PSS solutions on cohesion as well as on adhesion during mechanical stress (b) Adhesion energies measured by double cantilever beam (DCB) characterization of standard-architecture cells made with PEDOT:PSS containing 60% of PS nanoparticles of 60, 80 and 100 nm diameter from left to right. Reproduced from [184].*

adhesion promoter role as well. Contact angles of diodomethane droplets on the PEDOT:PSS + PS nanoparticles range from 17.3 °for pristine PEDOT:PSS to less than 5 °with 60% volume fraction of 100 nm large PS particles. Standard architecture devices with an active layer made of poly-[[4,8-bis[(2-ethylhexyl)oxy]benzo[1,2-b:4,5- b']dithiophene-2,6-diyl]-[3-fluoro-2-[(2-ethylhexyl)carbonyl]thieno[3,4-]thiophenediyl]] and phenyl C71-butyric acid methyl ester (PTB7:PC71BM) blend yielded adhesion energy values of 2.2 $\pm$ 0.3 to 3.4 $\pm$ 0.1 $J.m^{-2}$ for pristine PEDOT:PSS and with 60 % volume fraction of 100 nm PS particles (Fig. 1.35b). Power conversion efficiencies are unaffected by the nanoparticles even at highest volume fraction (60%) and diameter (100nm).

Use of metal oxides as HTL layers. Finally, in order to improve the BHJ / HTL interface in inverted devices, a straightforward strategy would be to replace the PEDOT:PSS layer by other materials. Due to the scarcity of good hole-conducting materials, the choice is limited. Metal-oxide layers identified as suitable materials have been studied in inverted devices [94, 149, 167].

30 nm of thermally-evaporated molybdenum oxide (MoO_3) as HTL layer (without further thermal annealing) lead to adhesion energies of 0.9 $\pm$ 0.2 J.m^{-2} [149]. This value is lower than the adhesion between the BHJ / PEDOT : PSS reference ($\approx$ 1.6 J.m^{-2}) cast by wet processes. In a more recent work [94], 10 nm thick molybdenum oxide (MoO_3) or tungsten oxide (WO_3) were deposited by electron beam in inverted devices. These devices yielded fracture energies between 1 and 2 J.m^{-2} and slightly over 3 J.m^{-2} after three weeks of aging at 85 °C.
In both experiments, rupture occurred adhesively between the BHJ and HTL layers. For devices aged under 85 °C, i.e. for annealed devices, cohesive failure within the BHJ was found to be limiting.

This is in contrast to slot-die coated vanadium oxide (V_2O_5) devices that achieved adhesion values from $\approx$ 75 to $\approx$ 150 J.m^{-2} for 130 and 190 nm thick V_2O_5 layers, respectively [167]. The V_2O_5 devices fracture within the BHJ, at the interface with a 10 nm thick BHJ/HTL

intermixed layer.

Two factors can explain this three order of magnitude increase from the reference systems:

First, the deposition process of V_2O_5 from a solvent based technique would allow intermixing of the HTL materials and the BHJ thus favoring the formation of a stronger interface.

Second, the thick V_2O_5 layer is expected to have an increased roughness compared to the other HTLs. Microscopic cracks within this layer have also been observed [185]. These topographic parameters could induce an increased interpenetration with the BHJ and could thus explain the high fracture energy values as well as the HTL thickness dependence.

TCO/ETL adhesion

The interface between the TCO / ZnO nanoparticles ETL was reported to have a poor adhesion [186, 187]. Pull-off measurements were performed on roll-to-roll processed inverted cells [186] without further characterization of the rupture path.

Depending on the synthesis route of the ZnO nanoparticules dispersions, various organic ligands (alkyl amines [188], alkyl thiols [189], carboxylic acids [190] for example) may be bonded as outer shell of the nanoparticles in order to avoid precipitation of the dispersions [187]. It is evidenced by XPS and ToF-SIMS measurements [102] as well as FTIR studies [186] that the ETL layer might still contain the aforementioned ligands after thermal annealing up to 150 °C. Two groups reported increased adhesion after removal of the ligands by photo-annealing (22h under AM 1.5G) [102] or oxidative plasma treatment. Furthermore, Krebs *et al.* observed decreased adhesion when organic salts are added to pure ZnO suspensions in methanol before deposition [187].

Fig. 1.36 shows PCE of roll-to-roll processed cells with or without improved adhesion by oxidative plasma treatment.

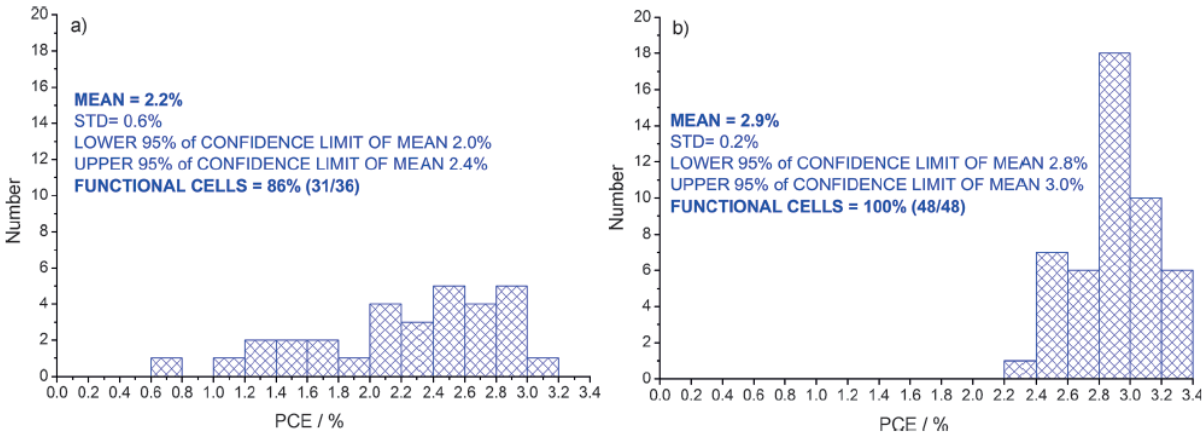

Figure 1.36: *PCE distribution of roll-to-roll processed inverted solar cells a) without and b) after plasma treatment. Reproduced from [186].*

This figure underlines the importance to achieve good adhesion between the TCO / ZnO layer which can greatly improve the reliability as well as the mean performance of industrially processed solar cells.

The mechanical stability of roll-to-roll (R2R) inverted modules using polyethylenimine-ethoxylate (PEIE) as ETL layer was investigated [129]. Fig. 1.37 shows the tested devices and the associated rupture paths.

Figure 1.37: *R2R inverted samples tested mechanically. Arrows represent the corresponding fracture path. Reproduced from [129].*

Complete modules fractured adhesively at the P3HT:PEDOT:PSS interface with a typical low energy $\approx 1.2\ J.m^{-2}$.
When samples were tested before HTL processing, $P3HT : PC_{60}BM$ ruptured cohesively within the BHJ layer with an energy $\approx 9\ J.m^{-2}$.
Finally samples tested before the BHJ processing fractured adhesively at the TCO/ETL interface with a significant energy of $\approx 28\ J.m^{-2}$.
In conclusion, the TCO/PEIE interface is not identified as a weak spot in this work. However, to our knowledge, samples with a ZnO ETL were only tested in complete devices and one can only tell that the TCO/ZnO interface in this case is stronger than the comparatively weaker BHJ/HTL interface.

1.3.4 Mechanical properties along aging

In this section, several articles focusing on the mechanical properties of OPV devices along different aging conditions will be reviewed.

Solar radiation. The mechanical properties of encapsulated inverted roll-to-roll modules exposed to standard AM 1.5G radiation were studied as shown in figure 1.38 [172].

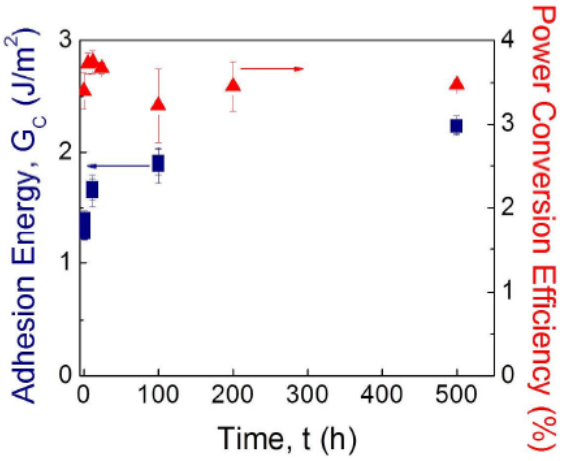

Figure 1.38: *Adhesion between the BHJ and HTL layers and PCE of encapsulated inverted solar cells as a function of time of exposure under standard AM 1.5G illumination. Reproduced from [172].*

Along aging, the fracture path was located at the BHJ/HTL interface. The adhesion energy increases logarithmically over a time of exposure of 500 hours. The potentially harmful UV radiation contained in AM 1.5G spectra did not decrease the mechanical properties. Although it is not indicated in the paper, encapsulation materials often contains UV cut-off filters [191] that could have protected the samples during this experiment. It is important to stress that an improved adhesion does not necessary mean improved PV performances of the devices. The cells have been heated up to ≈ 40-45 °C by IR radiation during aging. Long exposure times are thought to lead to a slow annealing process that would increase the adhesion at the interface .

However, in another article [168], inverted roll-to-roll modules did not see any significant improvement for the weak (≈ 0.1 - 0.3 $J.m^{-2}$) BHJ/HTL interface stressed under illumination for 24 hours, with or without UV component.

Relative humidity (RH). Moisture assisted tests plotting the crack growth-rate versus the applied driving-force for different relative humidity (RH) conditions are depicted in figure 1.39.

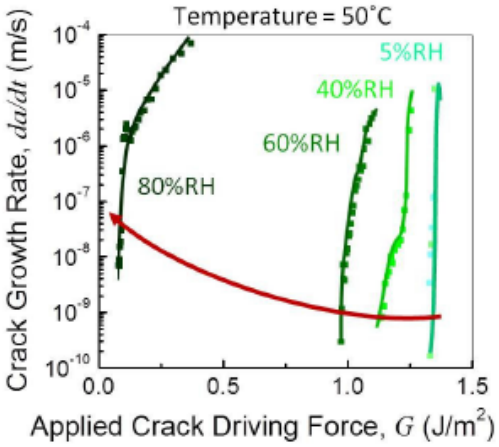

Figure 1.39: *Delamination rate as a function of the delamination driving force at different relative humidities at 50 °C. Reproduced from [172].*

Inverted OPV devices' mechanical properties are shown to be sensitive to relative humidity showing an initial rupture force (on the x-axis) of ≈ 1.3 J.m^{-2} at 5% RH and ≈ 0.1 J.m^{-2} for 80% RH. Steep curves such as the 5%RH curve correspond to adhesive debond between the BHJ and the HTL layers. Non-linear curves originates from an evolution from adhesive BHJ/HTL failure to cohesive failure within the PEDOT:PSS layer.

The phenomenon was further studied [165] and it is found that cohesive failure within the PEDOT:PSS layer is achieved through hydrolysis of PEDOT:PSS intermolecular hydrogen bonds under strain [161]. This result underlines the need for a good packaging of PEDOT:PSS OPV cells as their mechanical cohesion as well as their PV efficiency tend to decrease sharply under damp conditions.

Temperature influence. As previously shown in section 1.3.3, thermal annealing often has a beneficial effect on adhesion between the active layer and the HTL. This is explained by an increased interdiffusion of the materials forming an intermixed layer stronger than the pristine interface.

Surprisingly, for complete inverted roll-to-roll modules [168], such adhesion improvement between the BHJ and the PEDOT:PSS was only marginal : from $\approx 0.1\ J.m^{-2}$ for pristine devices to $\approx 0.4\ J.m^{-2}$ for samples aged 24 hours at 85 °C in inert atmosphere.

Finally, thermal interdiffusion was found to be a relevant mechanism for inverted cells with an electron-beam deposited MoO_3 or WO_3 HTL [94]. Corresponding results are shown on Fig. 1.40.

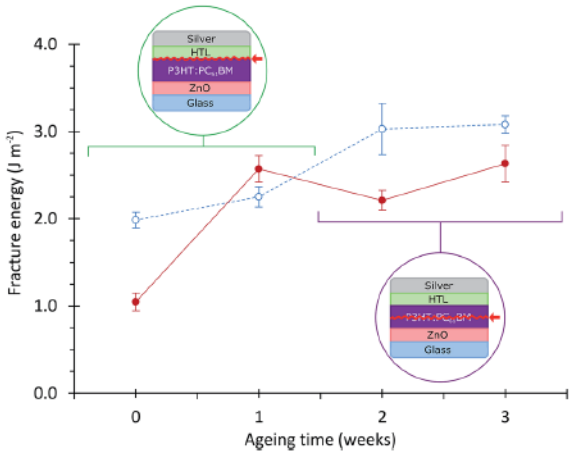

Figure 1.40: *Fracture energy of inverted cells with a (blue) MoO_3 or (red) WO_3 HTL as a function of aging time under at 85 °C. Reproduced from [94].*

Temperature (85 °C) was found to favor the formation of an intermixed layer in both cases, thus increasing the fracture energy. In a further stage of aging, the rupture occurred cohesively within the active layer with a slightly increased energy.

In another article, the effect of thermal cycling from -40 °C to +85 °C on the mechanical properties of inverted cells was also investigated [164]. The cycling was made at a 1.4 °C/min and the min and max temperatures were maintained for 15 minutes each. It is found that the fracture energy increases on the initial first 25 cycles from $\approx 2.6\ J.m^{-2}$ to $\approx 4.0\ J.m^{-2}$ before achieving stabilization of this value. Rupture path evolved from the BHJ/PEDOT:PSS interface to within the PEDOT:PSS and P3HT:PCBM layer themselves in a mixed fashion. This unusual behavior is explained by the 40% relative humidity which favors decohesion of the PEDOT:PSS layer.

Crossed factors. For roll-to-roll modules [168], in addition to the illumination and temperature effects discussed above, crossed effects of those parameters and relative humidity were investigated for 24 hours aging. For all tested conditions, the fracture occurred at the active layer / PEDOT:PSS interface with a relatively weak energy. Only the 85 °C and the 85 °C / 45 % relative humidity aged samples exhibited an increase of adhesion, from $\approx 0.1\ J.m^{-2}$ for pristine devices to $\approx 0.4\ J.m^{-2}$ for samples aged 24 hours. Additionally, the 85 °C / 45 % RH with UV illumination did not increase the adhesion of the samples. On one hand, the increased adhesion at the BHJ / PEDOT:PSS interface with temperature, assigned to interdiffusion, is effective even in damp conditions despite a strong PCE drop of corresponding devices from ≈ 1.2 % to ≈ 0.2 %. On the other hand, UV-light exposition limits this increase, probably by breaking polymer

chains of PEDOT:PSS [192]. This result highlights the fact that an increased adhesion does not necessarily corresponds to an increased PV performance.

In another publication [129], inverted devices, encapsulated or not, were aged for 100 hours in a 35 °C / 50 % RH and standard AM 1.5 spectrum. Despite the fact that the aging conditions are not discriminated rigorously, one can expect the encapsulation to offer a degree of protection against UV irradiation as well as relative humidity. Results are summarized in Fig. 1.41.

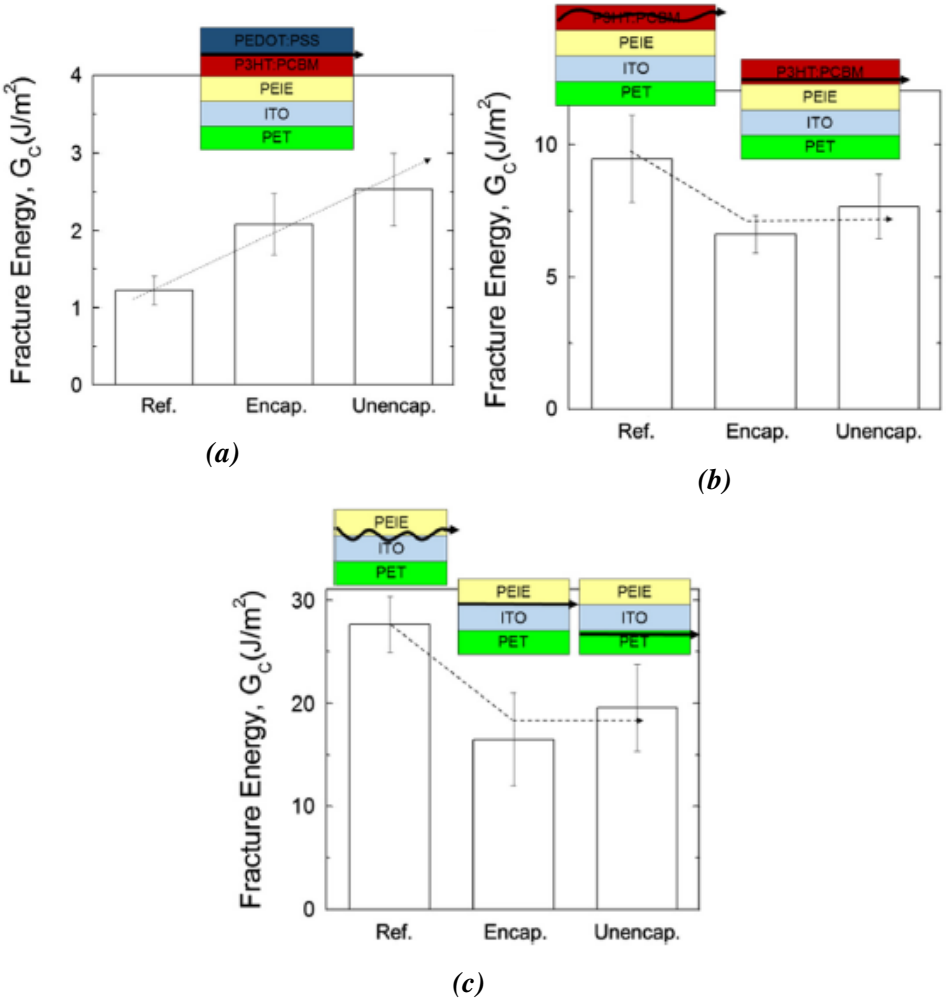

Figure 1.41: *R2R inverted samples tested mechanically. Arrows represent the corresponding fracture path. Samples were aged at 35 °C / 50% relative humidity and AM 1.5G illumination for 100 hours. Reproduced from [129].*

The weakest point in the complete OPV devices is the BHJ/PEDOT:PSS interface, however, the adhesion at this interface is increased by the temperature and is further increased by illumination and/or humidity (see Fig.1.41a). This was once again explained by an increased interdiffusion of the layers at the interface.

Samples without PEDOT:PSS fracture cohesively within the BHJ and only a slight decrease of fracture energy is shown along aging as shown on Fig. 1.41b.

The ITO/PEIE interface, showing relatively strong adhesion properties, is weakened by the aging conditions (Fig. 1.41c).

In both samples without PEDOT:PSS layer, the influence of atmospheric conditions on the mechanical properties, observable by comparing the encapsulated and unencapsulated results, is

not obvious.

Partial conclusion

As shown in this section, mechanical properties of OPV devices are critical parameters in order to guarantee the reliability of devices along their processing and use.

In this work, we focused on the adhesion between each layers constituting the devices. As reported in the literature, three weak points were identified: the interface between the transparent electrode (TCO) and the electron transport layer (ETL), the interface between the hole transport layer (HTL) and the active layer (AL) and finally the AL itself. For each weak spot, improvement strategies were proposed.

Improvement of the TCO/ETL interface was successfully reported in the literature. Such improvement was shown to increase the mean performances and lower the reject rate of devices manufactured in a roll-to-roll line. This result underlines the importance of the adhesion properties.

Several improvement strategies were proposed to improve the AL/HTL interface and the AL. However, to our knowledge, the few strategies that significantly improved such spots were at the cost of the devices performances. As a consequence, new mechanical properties improvement methods are yet to be found.

1.4 Local characterization of the optoelectronic properties of OPV devices

Degradation during processing and aging of the OPV cells is not necessarily homogeneous over their surface. Therefore, imaging techniques are required to link the performance loss determined on J(V) measurements and the micrometer-scale characterizations such as microscopy techniques. Furthermore, such techniques can also answer the need for fast, in-line, tools for quality control in production facilities. In addition, such characterization techniques can isolate specific steps that are part of the PV mechanism. Therefore, complementary imaging techniques can be used to decouple parts of the PV mechanisms, resolved on a local scale.

1.4.1 Laser-Beam Induced-Current (LBIC) mapping

The laser-beam-induced-current (LBIC) is a commonly used imaging technique to map the PV properties resolved on the cell active area.

Fig. 1.42a depicts a typical LBIC experimental setup.

A monochromatic laser, mounted on a moving rack, scans the surface of the cell. The output current of the cell under short-circuit conditions is recorded at the same time and an image of the photo-current produced by the cell is reconstructed. The LBIC technique probes locally the entire PV mechanism, from light absorption to charge extraction.

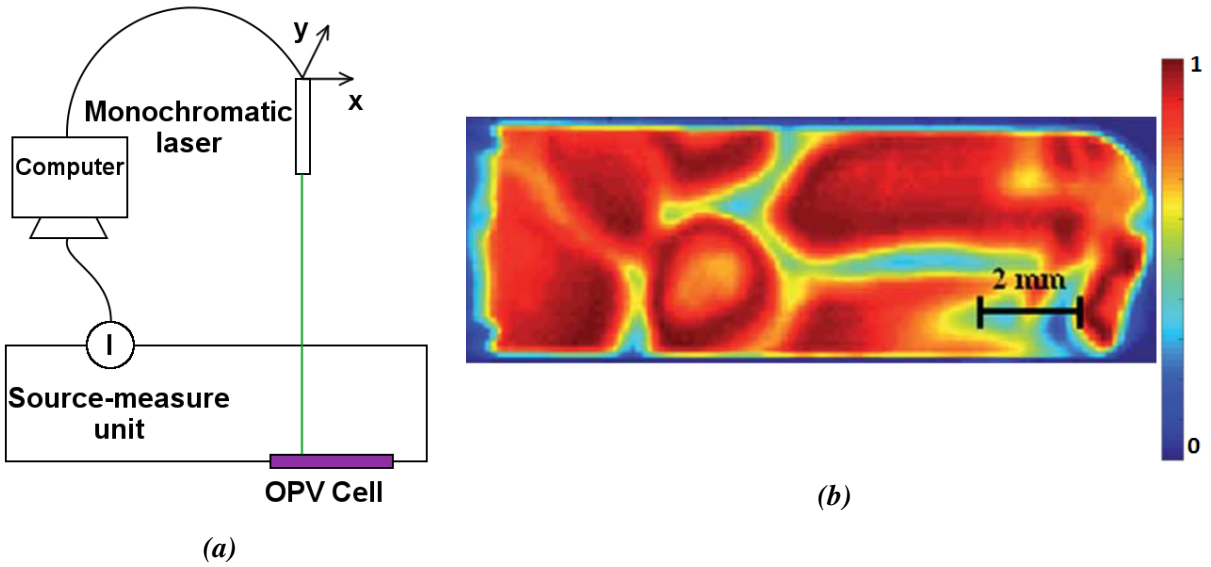

Figure 1.42: *(a) LBIC experimental setup. (b) LBIC image (relative J_{SC}) of an AnE-PV:PCBM OPV solar cell. Reproduced from [193].*

In the OPV research field, this technique was notably applied in order to study processing parameters [120, 194], electrode materials [77] or to measure the diffusion rate of moisture inside the devices [195] during aging experiments [196].

The LBIC lateral resolution is only limited to the size of the laser spot (assuming the cell output is still measurable by the source-measure unit). However, it is to be balanced with the measurement time, as a small laser spot requires more scans than a larger one to cover a given area. Such measurements can require up to a few hours to cover a 1 cm^2 area with a 125 µm resolution [197]. Therefore this technique is not adapted for the study of fast time-dependent processes or in-line measurements.

Improvements including light-emitting diode (LED) arrays to improve the measurement time [198], capacitive coupling allowing contactless characterization [199] or protocols designed for measuring modules of several cells [200] were developed.

An example LBIC image of a (poly(p-phenylene-ethynylene)-*alt*-poly(p-phenylene-vynilene)) (AnE-PV) : PCBM OPV cell [193] is given in Fig. 1.42b.

Large high-efficiency regions crossed by less-efficient channels can be seen. However, this technique alone cannot yield information on the origin of such patterns.

LBIC study of devices aged in outdoor conditions. Encapsulated inverted P3HT:PCBM modules were aged in outdoor conditions during one year in Denmark and were diagnosed by LBIC imaging at the end of aging [196]. J(V) characteristic of each module stripe as well as the LBIC image are shown on Fig. 1.43.

Several stripes are affected by a loss of current. The LBIC image is in good agreement with the I_{SC} measurements performed on each cell. Despite the fact that it is impossible to

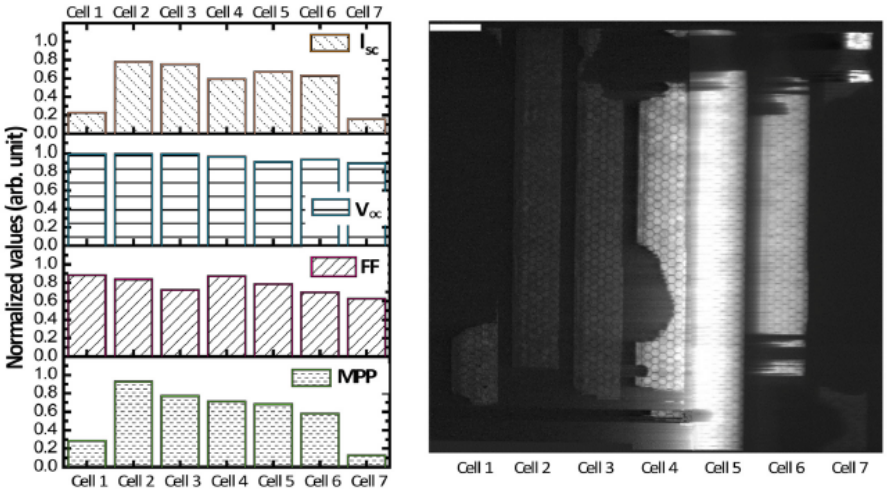

Figure 1.43: *(left) normalized I_{SC}, V_{OC}, FF and maximum power (MPP) for each module stripe. (right) corresponding LBIC image. Reproduced from [196].*

discriminate which degradation factors are responsible for the I_{SC} losses, three main hypothesis were advanced : the photo-oxidation of the active layer, the electrode delamination from the semi-conductor or the loss of conductivity of PEDOT:PSS.

The outer-cells, which suffered the most form I_{SC} losses, were imaged by optical microscopy, and only a few scattered, small spots seemed to be photo-oxidized. Therefore this degradation mechanism was thought to be only a minor factor of I_{SC} loss. The larger part of the outer stripes was thus thought to suffer from delamination of the silver electrode or loss of conductivity in the PEDOT:PSS layer.
Dark zones in the central area were also observed on other modules that were scratched; this is a possible explanation for those observations on this example.
Finally, the main degradation was though to originate from the unsealed edges of the module. Further investigations also showed that higher thicknesses of encapsulation adhesive (grooves) and the electrical contact tapes, used for connecting the cells after encapsulation, were responsible for faster permeation inside the devices.

1.4.2 Luminescence imaging

Among the recombination mechanisms discussed in Sec. 1.1.1, some of them can lead to emitting photons of wavelengths in the visible/near-infrared range, i.e. to produce luminescence. These wavelengths are characteristic of the recombination mechanism and they can be studied in order to better identify the losses during the PV operation and aging.

Introduction - Luminescence of semi-conductors. This paragraph will cover the basic theoretical concepts behind luminescence emission. Demonstrations of the concepts and formulas can be found in the cited literature.

Planck's law describes the intensity of electromagnetic radiation ϕ_{bb} normal to a black-body in thermal equilibrium [201] :

$$\Phi_{bb}(E_\gamma, T) = \frac{2\pi E_\gamma}{h^3 c^2} \frac{1}{exp\left(\frac{E_\gamma}{kT}\right) - 1} \tag{1.11}$$

Where h is Planck's constant, c the velocity of light, E_γ the energy of the radiation, T the temperature of the considered black-body and k the Boltzmann constant.

When such black-body in thermal equilibrium absorbs excess energy, for example in the form of photons, the excess energy will be re-emitted. The radiation Φ emitted from such body with an absorptance α is thus:

$$\Phi(E_\gamma, T) = \alpha(E_\gamma)\Phi_{bb}(E_\gamma, T) \tag{1.12}$$

Wurfel [202] observed that semi-conductors can expand energy equal to their band-gap E_g. The corresponding radiation formula of a semi-conductor material is [203]:

$$\Phi_{PL}(E_\gamma, T) \approx \alpha(E_\gamma)\Phi_{bb}(E_\gamma, T)\left[\exp\left(\frac{E_g}{kT}\right) - 1\right] \tag{1.13}$$

Where Φ_{PL} is the photon flux from the device. This formula is used to describe luminescence induced by optical excitation, i.e. photo-luminescence (PL). Interestingly, one can see that the more a body, or in our case an active polymer, absorbs photons, the more it emits photo-luminescence.

Conversely, such reasoning can be applied for electrical excitation, i.e. electro-luminescence. The absorptance is then replaced by the cell external quantum efficiency (EQE_{PV}), i.e. its efficiency to convert photons to electrical charges and the band-gap energy is replaced by the product of the electronic charge (q) and the voltage (V).

The corresponding electro-luminescence emission equation is thus [203]:

$$\Phi_{EL}(E_\gamma, V, T) \approx EQE_{PV}(E_\gamma)\Phi_{bb}(E_\gamma)\left[exp\left(\frac{qV}{kT}\right) - 1\right] \tag{1.14}$$

This formula implies that electro-luminescence will increase exponentially with respect to the excitation voltage. It also implies that devices with a high EQE will yield a correspondingly strong electroluminescence emission.

Luminescence mechanisms of organic solar cells. Luminescence of solar cells is commonly investigated by recording the emission spectra of the cells under monochromatic light, i.e. photo-luminescence (PL) [37, 39, 46, 47, 80, 204–210], or when injecting charges through their contacts, i.e. electro-luminescence (EL) [37, 46, 47, 72, 82, 204, 205, 209, 211].

The most common luminescence mechanism of semi-conductors is the band-to-band recombination depicted on Fig. 1.2 (a). It consists of the recombination of an electron in the conduction band and a hole in the valence band of the same material. The energy of the emitted photons μ_γ

will be equal to the band gap E_g of their respective material.

Additionally to band-to-band recombination, once an electron-donor and acceptor are blended, the charge-transfer (CT) state recombination (Fig. 1.2 (b)) can be observed as well on the PL spectra. The CT emission is red-shifted compared to the band-to-band emission due to the reduced energy of the CT state compared to the band gap energy of both materials.

Fig. 1.44a shows PL spectra of the pure donor poly[2,7-(9-di-octyl-fluorene)-alt-5,5-(4',7'-di-2-thienyl-2',1',3'-benzothidiazole)] APFO-3, the pure acceptor PCBM and their 1:4 weight ratio blend.

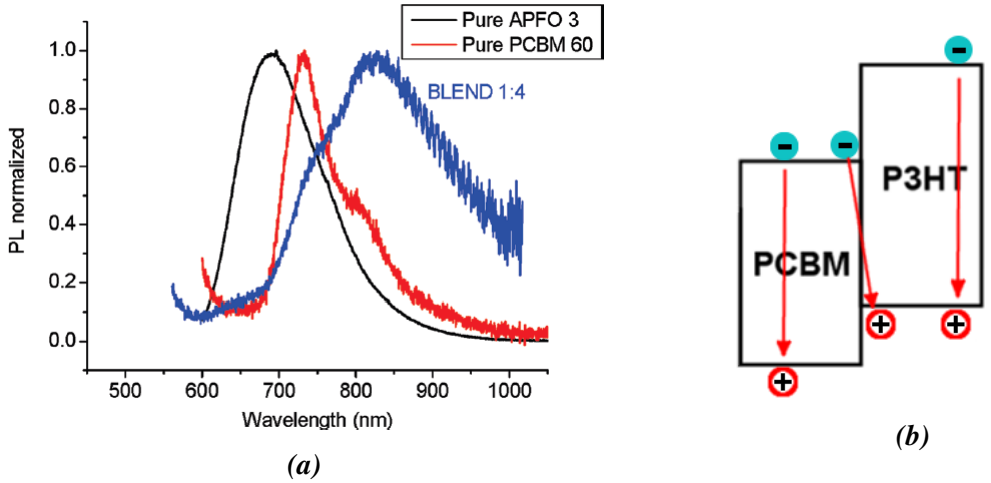

Figure 1.44: *(a) Normalized PL spectra from OPV cells made of pure donor APFO-3, pure acceptor PCBM and APFO-3:PCBM at a 1:4 weight ratio. Reproduced from [37]. (b) Scheme of the radiative transitions occuring in P3HT:PCBM devices.*

The pristine materials have a distinct spectra with a band energy characteristic of their respective band-gap. Once blended, the PL emission from both pure materials is decreased due to the dissociation of the photo-generated excitons. Moreover, the ratio of PL emission after compared to before blending can be harnessed as an indicator of the blend efficiency to dissociate excitons [37, 47, 204, 208–210]. In addition, a red-shifted band corresponding to the interfacial CT-state emission appears.

For reference, Fig. 1.44b summarizes the transitions one can observe for a P3HT:PCBM cell [47].

Electro-luminescence is also used to study the luminescence properties of the cells with excitation stemming from injected charges. The charges then follow the opposite mechanism of the PV mechanism.

Fig. 1.45 displays examples of EL spectra obtained from APFO3:PCBM devices.

As shown in Fig. 1.45a, the close energies of EL emission compared to PL CT emission suggest the same recombination mechanisms despite the different origins of the charges in each experiment. Some red shift of the EL band compared to the PL-CT band can be observed. It is due to the fact that injected carriers will preferentially access more ordered regions with less tightly-bound CT states than photo-generated carriers [37, 46].

During EL experiments, opposite charges are injected in the active layer through each material

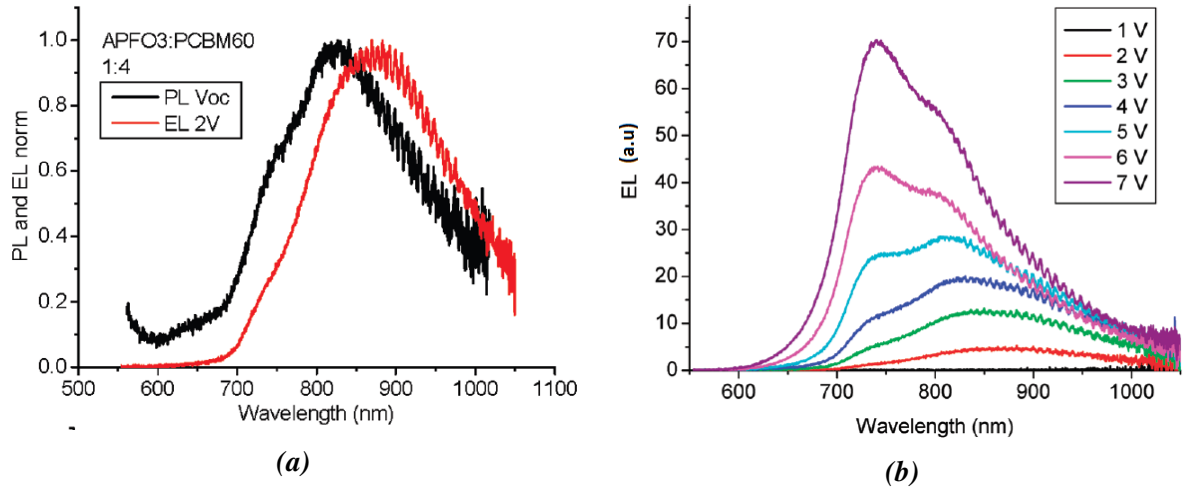

Figure 1.45: *(a) Normalized EL and PL spectra of an APFO-3:PCBM cell. Reproduced from [37]. (b) EL spectra of an APFO-3:PCBM cell at different voltage biases. Reproduced from [47].*

according to their affinities; they can thus meet and recombine only at the interfaces between them. As a consequence, the CT interfacial recombination is predominantly observed. However, as shown in Fig. 1.45b, at increased voltages, the CT states can be saturated and charges can populate both pure material phases (here PCBM) and eventually recombine through (relatively blue-shifted) band-to-band recombination [47].

Photo-luminescence under voltage bias. The quenching efficiency of excitons and charge-transfer states has been studied under the influence of a bias voltage [37, 82, 205].

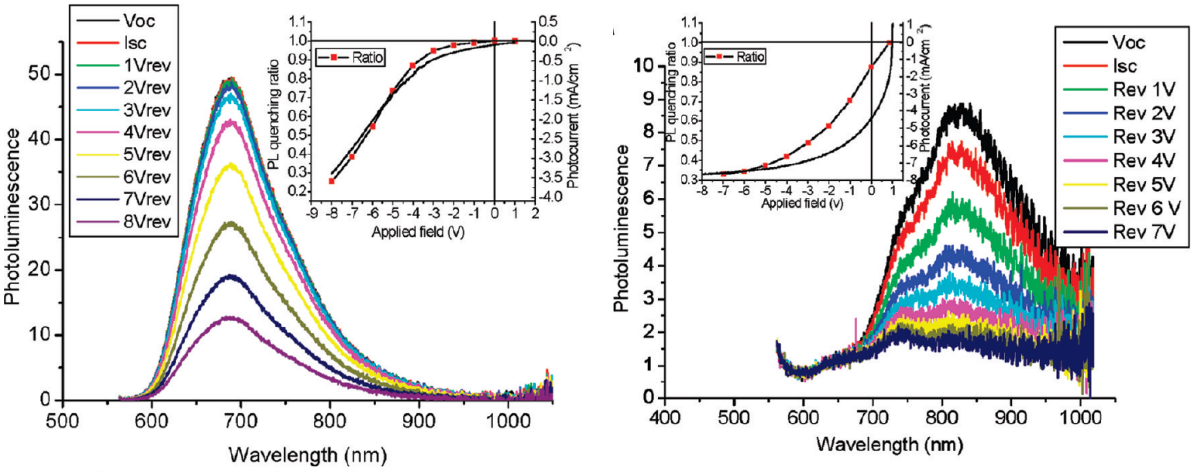

Figure 1.46: *PL spectra of (a) the band-to-band emission of an APFO-3 film and (b) the CT emission of an APFO-3:PCBM based cell at different voltage biases. Reproduced from [37].*

As shown in Fig. 1.46a, in the case of pure materials, a sufficiently strong electric field can dissociate excitons when their coulomb binding attraction is overcome. As a consequence, the band-to-band PL emission will be quenched under a relatively high applied voltage.

In the case of a bulk-heterojunction (Fig. 1.46b), the applied bias voltage favors the dissociation (quenches the emission) of the CT state at lower voltages than the excitons of the pure

materials because of the lower binding energy of excitons in the blend. However, the correlation between the CT PL quenching and the J(V) curve (shown in the insets) is less pronounced for the BHJ than for the pure materials; the dissociation of the CT state is therefore not the only mechanism limiting the photo-current extracted from this cell.

In contrast of the previous study, band-to-band photoluminescence of a P3HT:PCBM device has been observed to increase as a function of the reverse bias voltage [82].

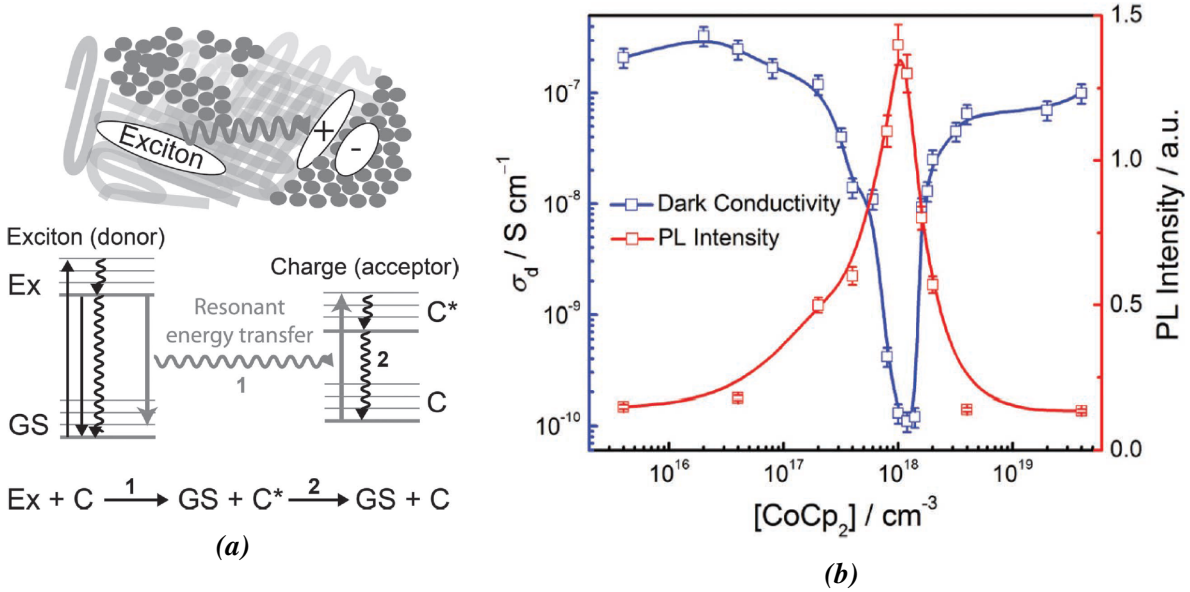

Figure 1.47: *(a) Resonant energy transfer mechanism. Reproduced from [212]. (b) Conductivity and PL emission of P3HT:PCBM films as a function of the n-doping material $CoCp_2$. Reproduced from [213].*

It is known from the organic light-emitting diodes (OLED) literature [210, 212] that excitons can be quenched by free charges. In the first step of Fig. 1.47a, the strongly emissive exciton (Ex) performs resonant energy transfer to a nearby free charge (C) and thus decays non-radiatively to its ground state. In a second step, the photo-excited free charge (C*) then decays through vibrational relaxation to its own ground state. As a consequence of these mechanisms, the emission of the material decreases. This mechanism is expected to be relevant for systems with high charge densities such as organic lasers, light-emitting transistors and OPV devices under strong illumination.

Such excitons-charges recombination have been shown to occur in P3HT:PCBM blends [212]. Moreover, in P3HT solid films, p-doping ions, although their origin and nature is not investigated in this study, have been shown to quench the band-to-band PL of such material [213]. Fig 1.47b plots the conductivity and photoluminescence emission of a P3HT film as a function of the density of $CoCp_2$, a compensating n-doping material. When the n-doping $CoCp_2$ concentration is lower than the p-doping species, the conductivity of the P3HT is high and its PL is quenched. At $\approx 10^{18}\ cm^3$ the $CoCp_2$ compensates the p-doping impurities; as a result, conductivity drops and PL increases. At higher $CoCp_2$ densities, the material is n-doped; conductivity is high and PL decreases again. An additional study made on MEH-PPV, another classical OPV polymer, shows similar quenching behavior related to p-doping by O_2 species, which can be reduced at reverse bias voltages [214].

Luminescence imaging for aging studies. Luminescence emission, whether it is induced by light or an electrical current, can be imaged with a camera. Our setup is described in Sec.3.1.2 and schemes representing both the photo-and electroluminescence apparatuses are shown in Fig.3.10. Such techniques allows lateral resolution of the luminescence emission which can be used to investigate the cells properties locally.

Standard-architecture Glass/ITO/PEDOT:PSS/P3HT:PCBM/Al devices were aged without encapsulation under 1-sun illumination or in dark storage [215]. Electro- and photo-luminescence images taken along aging time are displayed on Fig. 1.48.

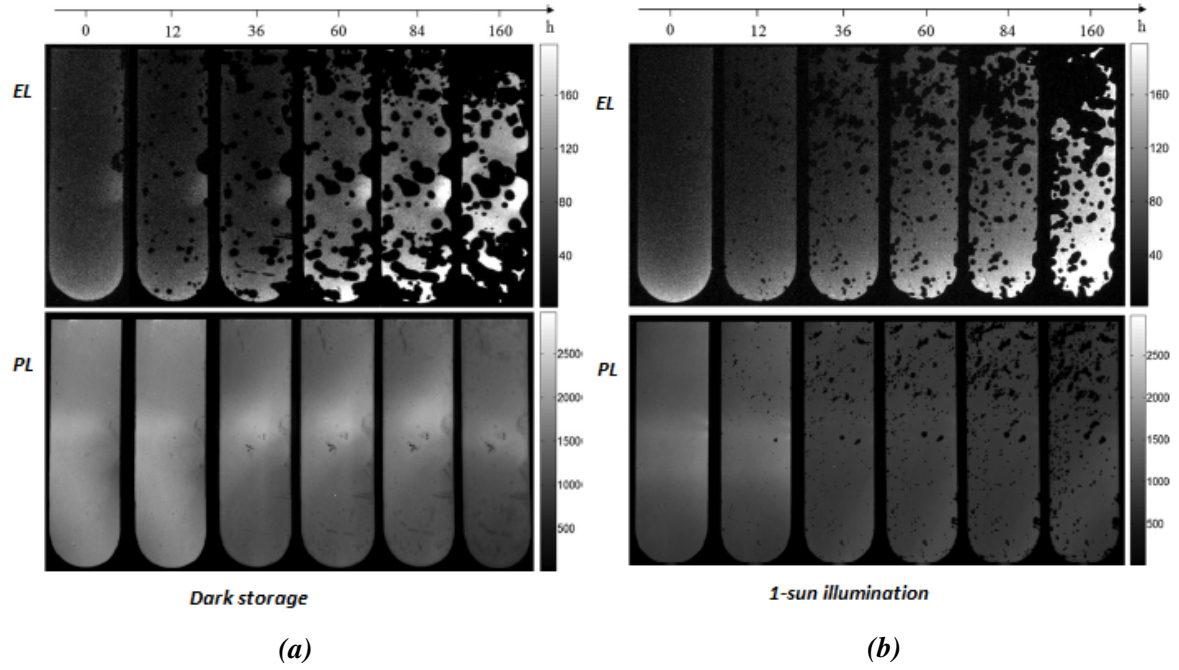

Figure 1.48: *Electroluminescence and photo-luminescence of un-encapsulated conventional-architecture devices after one week(a) in dark storage or (b) under 1-sun illumination . Reproduced from [215]).*

From Fig. 1.48a, which shows the dark storage condition, one can see a progression of the dark area on electroluminescence images and not on photoluminescence images. This is interpreted as the oxidation of the aluminum electrode which impedes current injection. The extincted area fraction on ELI images is perfectly correlated to the lost J_{SC} during aging; therefore such electrode oxidation is thought to be the main degradation mechanism occuring in the device.

On the images taken from cells aged under 1-sun illumination, both electro- and photo-luminescence images exhibit dark spots formation. The degradation of the PL active area is assigned of photo-oxidation of the active layer by oxygen diffusing through the electrode pinholes.

In another study, glass-encapsulated inverted P3HT:PCBM 6-cells modules were monitored by EL and PL imaging along aging at 65 °C and 85% RH in the dark [216]. The J(V) curves as well as EL images are shown on Fig. 1.49a and 1.49b, respectively.

The module J(V) curve gradually gains series resistance and shifts to an S-shaped curve. On the EL images, one can see a degradation pattern progressing from the edges of the device until

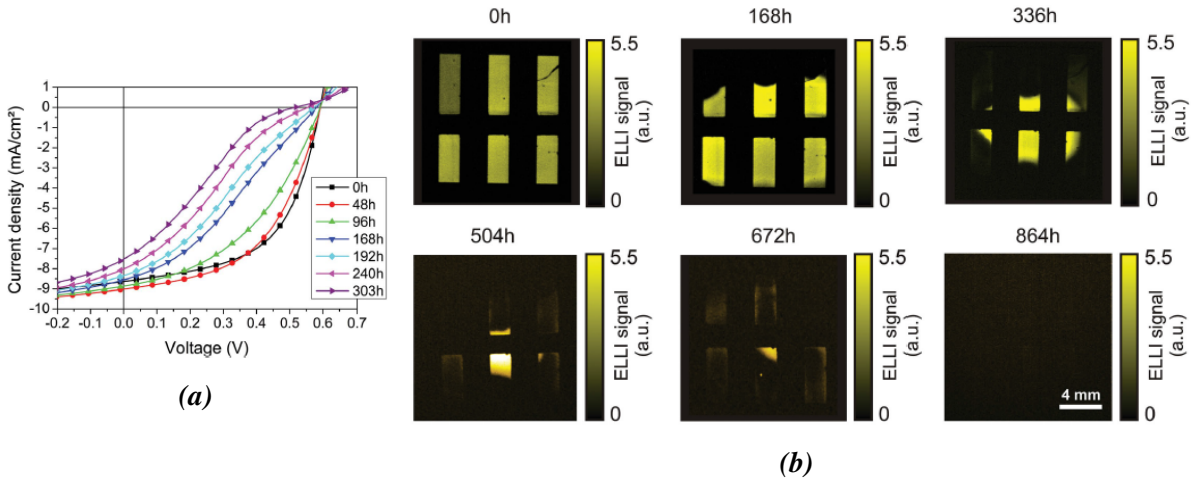

Figure 1.49: *(a) J(V) curves of a glass-encapsulated inverted P3HT:PCBM 6-cells module along aging at 65 °C and 85% RH in the dark and (b) associated EL images of the same device. Reproduced from [216]).*

complete extinction of signal. As the PL images were unaffected by the aging conditions, the degradation is thought to be a loss of contact between the active layer and the electrodes which is in accordance with the J(V) curves. Due to the absence of pinhole-type defects, the water permeation was thought to occur through the adhesive or along the adhesive/glass interfaces (permeation through glass is assumed to be negligible) and transferred to the PEDOT:PSS layer.

Assuming water to be the only degradation factor, the activation energy and the rate of diffusion and reaction of water during degradation could be calculated using the Arrhenius diffusion model.

According to these calculations, the degradation rate was found to be ten times faster at 65 °C than at 20 °C. The authors emphasize that these parameters could be used to compare different encapsulation materials and processes with the same geometry.

Voltage-biased photo-luminescence imaging. In a similar fashion, the voltage dependence of the PL emission has been exploited to map the cells optoelectronic properties. Several methods, each requiring several PL images under different voltages or illumination intensities, have been successfully developed for silicon solar cells [217–220]. However, these models require several assumptions which in turn require a good knowledge of the underlying physics of the systems. As a result, the technique was only applied qualitatively. To our knowledge, it was never applied to OPV systems. The example below shows its application on perovskite solar cells [221].

Fig. 1.50 shows an EL image and a PL image taken under short-circuit conditions of a $CH_3NH_3PbI_3$ perovskite solar cell.

In the EL experiment, the injected charges recombine, thus the white area of the EL image is connected to the cell terminals. Conversely, photo-generated charges which are extracted under short-circuit conditions are less likely to recombine than the stagnant ones; as a consequence, the electrically connected area appears dark on the PL-SC image.

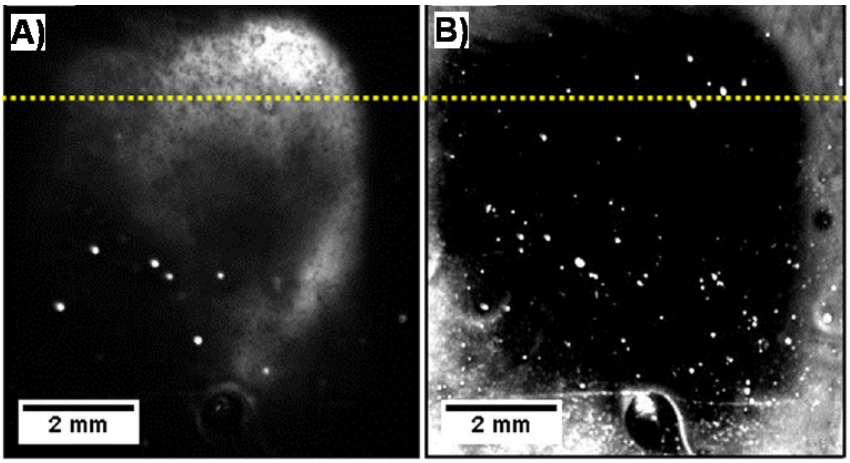

Figure 1.50: *a) EL image b) PL image under short-circuit conditions of a $CH_3NH_3PbI_3$. Reproduced from [221].*

1.4.3 Correlation of complementary imaging characterizations for aging studies

Non-destructive imaging characterizations are powerful tools in order to investigate degradation of the cells under different aging conditions. Using complementary techniques, one can unravel the location and origin of the degradation observed by performance monitoring of the cells during their aging.

The LBIC image is relevant as a probe of the whole PV mechanism resolved on the cell surface. EL images are constructed from free-charges injection; as a consequence, this imaging technique is more sensible for probing charge transport issues. PL images are notably dependent on the absorption and exciton-dissociation properties of the active layer, they are therefore convenient to detect degradation of the latter, such as deconjugation of the polymer or morphological changes. By comparing images obtained by these techniques together, a picture of the degradation mechanisms, resolved on the whole cell surface can be drawn.

These techniques were applied on several devices along aging at 85 °C and 1 sun illumination in the frame of a multi-laboratory study [222].

Fig.1.51 summarizes the characterizations of an un-encapsulated inverted ITO / ZnO / P3HT:PC_{60}BM / PEDOT:PSS / Ag cell after 25 hours of aging at 85 °C under 1-sun illumination.

From the LBIC image a), one can see an inhomogeneous PV activity on the device surface; this efficiency distribution is well-correlated to the EL image b). Darker areas on the EL and LBIC images are characteristic of a charge transport failure (extraction with LBIC and injection with EL [197]) typically induced by interfacial degradation such as delamination or formation of an electron-blocking metal-oxide interface. PL image c) reveals complementary information: the dark regions show degradation of the active layer itself exposed to the ambient conditions through pinholes in the electrodes. Dark lock-in thermography images, in forward d) and reverse e) operation, track the generation of heat in the device; it is a sensitive technique to track both shunting and series resistances within the cells.

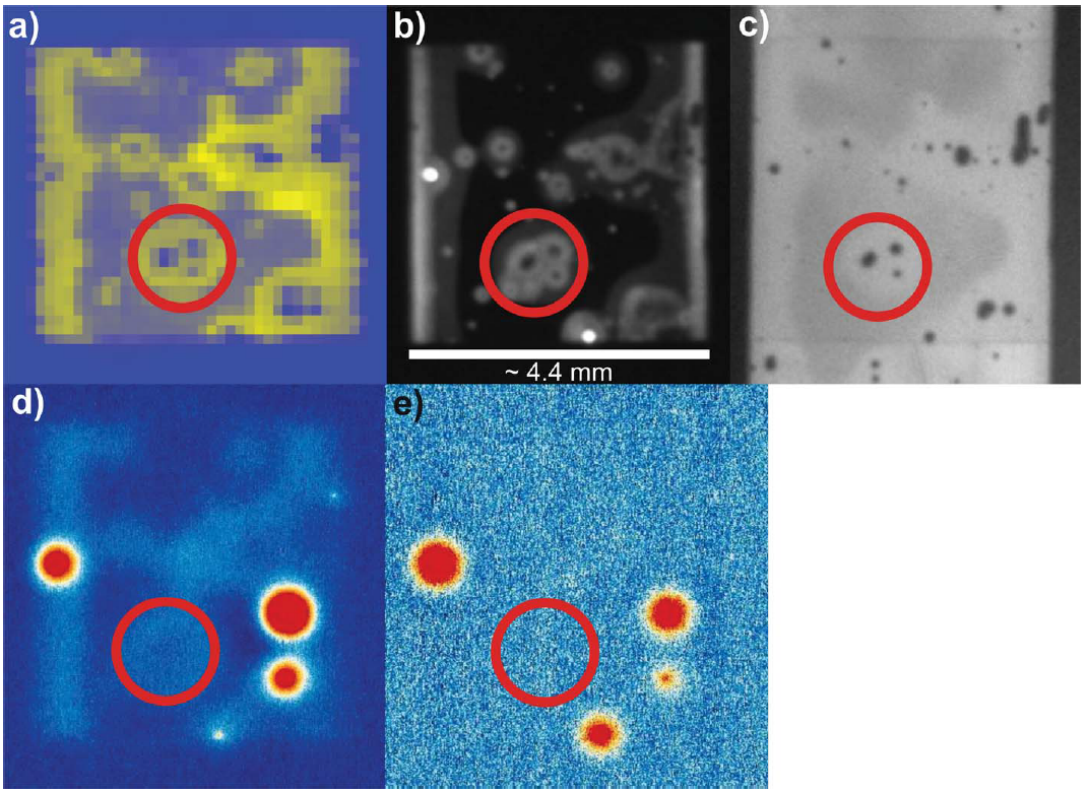

Figure 1.51: *a) LBIC image, b) EL image, c) PL image, d) & e) Dark lock-in thermography (DLIT) images in forward and reverse bias, respectively of an inverted OPV cell after 25 hours of exposition under 1 sun illumination and 85 °C . Reproduced from [222].*

Partial conclusion

As shown in this section, several non-destructive imaging techniques can be employed in order to study degradation of OPV devices. Such techniques can resolve laterally the opto-electronic properties of the devices and can separate several degradation factors. This allows one to study both the location and the mechanism of degradation impeding the cells performances.

The laser-beam induced-current (LBIC) mapping technique can yield maps of the complete PV mechanism resolved on a hundred of µm scale. Electro-luminescence images can map the charge transport properties whereas photo-luminescence maps the absorption properties of the devices with a few µm resolution. Using such complementary techniques, one can draw a complete picture of the degradation occurring during aging of the cells.

Conclusion

This state-of-the-art review allowed us to highlight a number of points:

– In a first section, we introduced the organic photovoltaic devices working principle and their architecture. The J(V) measurement curves and the parameters extracted from such to assess the cells performances were described as well.

– In a second time, aging of the OPV devices was studied. Both intrinsic and extrinsic degradation factors were described. Encapsulation methods, employed to mitigate permeation of nocive species within the devices were described. Such techniques are scarcely described

in the literature despite their importance in terms of cost as well as device performance and lifetime.

– In a third section, a focus was made on the mechanical properties of OPV devices. Such properties are suspected to be an important degradation factor in several literature reviews. Two interfaces were identified as mechanically weak: the transparent conductive oxide (TCO) / electron transport layer (ETL) interface and the active layer (AL) / hole transport layer (HTL) interface. The cohesion of the active layer itself was shown to be an issue as well. Several improvement methods were proposed for each weak spot.
– In the fourth section, imaging characterizations, used to map the opto-electronic properties of the devices were presented. Such complementary techniques are powerful tools allowing one to investigate both the degradation mechanisms and their location on the devices. Several studies successfully employed these techniques in order to unravel degradation mechanisms, whether optical or electrical, of cells aged in different aging conditions.

Chapter 2

Experimentals

2.1 OPV cells architecture

The cells studied in this work were made in the so-called inverted configuration with a substrate / electron transport layer / active layer / hole transport layer / metal back electrode stack.

The devices complete stack and its geometry is shown in Fig.2.1.

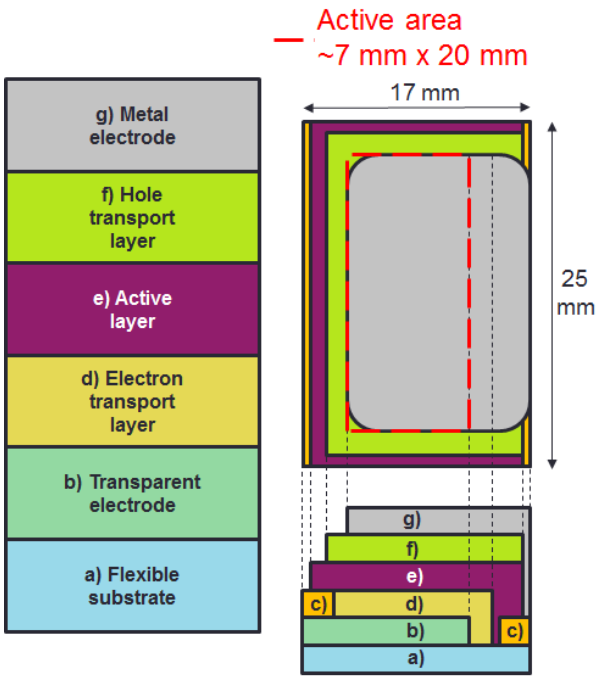

Figure 2.1: *(left) complete OPV stack in the active area of the cells. (top right) top-view of the solar cells fabricated in this work. The active area, where the OPV stack is complete is represented with red dashed lines. (bottom right) cross-section scheme of the devices. Layer c) corresponds to the cell contact points deposited on a) and b).*

The cell is deposited on a 17 x 25 mm^2 flexible PET substrate a). In order for the cell to generate an electrical current in a circuit connected to its terminals c), each charge type photo-generated in the active layer e) must be driven to the electrodes b) & g) by their respective transport layer d) and f).

Shunting, i.e. direct contact between both electrodes, must be avoided to prevent current losses. In order to make sure it is not the case, each layer of the stack is patterned during its deposition step.

The active area of the cells is defined as the overlapping area of all the layers composing them. This area is approximately of 7 x 20 mm^2. Due to slight geometry variations of the handmade layer patterns, the exact area is measured with a ruler for each sample. Due to the relatively high conductivity of the PEDOT:PSS HTL layer, areas without metal electrodes can participate to the current production of the cells, as shown in Sec.3.1.1. In this work, this contribution is assumed to be negligible.

2.2 Materials

2.2.1 Standard cells materials

PET substrate and transparent electrode 175 µm thick flexible "Flexshield 15" PET substrates were provided by Visiontek systems (Chester, United-Kingdom) with a transparent conductive layer used as the transparent front electrode of OPV devices. The transparent conductive oxide (TCO) layer was guaranteed by the supplier to have a conductivity of 15 Ω/sq, an optical transmission between 70% and 90% over the 450 - 650 nm range and a thickness of 150 nm.

Energy-dispersive X-ray spectra (EDX) were acquired with a scanning electron microscope (SEM) on the conductive substrates and the chemically etched PET substrate alone in order to study the composition of the electrode layer. From this study, the TCO layer is composed of oxygen, nitrogen, zinc and indium. This result suggests that the TCO layer is an indium-zinc oxide layer in agreement with some transparent conductive materials developed in the literature [223, 224]. The nitrogen peak may be representative of the use of indium-zinc oxynitrides, more recently used as transparent conductive layers [225, 226].

Electron transport layer (ETL) A zinc oxide nanoparticles dispersion in ethanol (40% in weight (wt.)) was purchased from Sigma-Aldrich (Saint-Louis, Missouri, USA). It will be later referred to as "ZnO A" in this document. The supplier guaranteed particle sizes below 130 nm. Traces of alkylammonium salts are indicated on the safety data sheet of the product.

Active layer Active layers deposited in this work follow the bulk hetero-junction (BHJ) concept. According to this design, electron donor polymers and electron acceptor molecules are blended in the active layer.

Regioregular poly(3-hexylthiophene) (P3HT) was used as donor polymer and phenyl-C61-butyric acid methyl ester fullerene derivative as acceptor molecule, commonly referred to as $PC_{61}BM$ or PCBM.

Solid P3HT Lisicon SP001 was purchased from Merck (Darmstadt, Germany). Supplier data indicate a regioregularity of 97.3%, a weight average molar mass of 74 kDa and a polydispersity

index of 2.1. Solid PCBM fullerene PV-A600 (purity > 99.5%) was purchased from Merck (Darmstadt, Germany).

Hole transporting layer (HTL) The HTL reference layer was cast from a conductive PEDOT:PSS dispersion in aqueous solvent, Clevios^{TM} P Form- CPP105D from Heraeus (Hanau, Germany).

This formulation contains several additives [227] : n-methyl-2-pyrrolidinone, which tweaks the morphology of the solid film after drying in order to achieve a higher conductivity [228], gamma-glycidoxypropyltrimethoxysilane as adhesion promoter with the underlying active layer as well as crosslinking agent for PEDOT and PSS and an acetylenic glycol-based nonpolar surfactant (Dynol 604 by Air Products)[64].

Silver electrodes 99.999% pure silver pellets purchased from Sigma-Aldrich (Saint-Louis, Missouri, USA) were used for the thermal evaporation process.

2.2.2 Alternative cells materials

Glass substrates Bare glass was often used in order to study single layers separately. Esco glass slides from Thermo Fisher Scientific (Waltham, Massachusetts, USA) were used.

Electron transport layer (ETL) Another ZnO nanoparticles dispersion, referred to as "ZnO B", was used. Dispersion solvent is the 1-butanol. The nanoparticles geometry was not investigated but is possibly different from the ZnO A batch.

Hole transport layer (HTL) Two alternative HTL materials were tested: a PEDOT:- complex dispersed in butyl benzoate, Clevios^{TM} HIL 8 from Heraeus (Hanau, Germany) and a triclinic WO_3 nanoparticles dispersion in isopropanol, WO_3 5014 from Nanograde (now Avantama AG, Stafa, Switzerland).

Inkjet printed silver electrodes For inkjet printing, a silver nanoparticles dispersion (70% wt.) in ethylene glycol, Ag-2103-EG from Nanogap (Milladoiro, Spain), was used. According to supplier data, particles size was distributed form 25 nm to 75 nm (95% confidence) with a 54 $\pm$ 15 nm diameter in average. Polyvinylpyrrolidone used as capping agent during particle growth might still be present as traces.

2.2.3 Encapsulation materials

In this work, encapsulation is composed of a barrier film attached to the devices by a pressure-sensitive adhesive (PSA) or a thermoplastic (TP).

The PSA is a 467MP adhesive transfer tape from 3M (Maplewood, Minnesota, USA). The adhesive is purchased as a roll of a 0.05 mm thick acrylic adhesive with a 0.10 mm thick kraft paper on top of it.

The thermoplastic is a 150 µm thick polyethylene film bought from Sekisui chemical (Osaka, Japan).

Barrier layer is an Oïke (Kyoto, Japan) VX-25T-2PO PET-based barrier film. According to the supplier data, its water-vapor transmission rate is $3.10^{-4} g.m^{-2}.day^{-1}$ at 45 °C and 85 %RH. According to the literature, such barrier material is passing the $1.10^{-3} g.m^{-2}.day^{-1}$ barrier requirement defined in order to obtain cells lifetimes of 1000 hours in the same aging conditions [127] (see Sec.1.2.2).

58 µm thick charge-collection solar tape 3007 from 3M (Maplewood, Minnesota, USA) was used to electrically connect the encapsulated cells.

2.3 Samples preparation

Cleaning procedure A common cleaning procedure was applied to all substrates, plastic or glass, used in this work. They were placed in a solvent bath for a 5 minutes long 45 kHz ultrasonic treatment in a Fisher Scientific (Waltham, Massachusetts, USA) equipment. Two isopropanol and three deionized water baths were performed successively. The substrates were then kept in a 100 °C oven for one hour in order to dry the solvents.

2.3.1 OPV cells fabrication

The fabrication process of the organic solar cells studied in this work will be detailed in this section.

Standard cells fabrication procedure. The deposition and patterning procedure of each layer as deposited in the standard devices will be detailed here.

a), b) & c) PET substrate preparation, transparent conductive electrode patterning and terminals deposition. The PET substrates were purchased already coated with a transparent electrode (TCO) layer.

The transparent electrodes were chemically etched by a diluted hydrochloric acid (HCl 6%) bath for five minutes while the area desired to be protected was covered with adhesive tape. Once the tape removed, the substrates were then cleaned according to the standard procedure described above.

Afterwards, conductive terminals were deposited on the edges of the cells by evaporation of 10 nm + 40 nm thick chromium + gold layers through a hard mask patterning the contacts.

d) Electron transport layer (ETL) deposition Before deposition of the ETL layer, a 10 minutes ultraviolet-ozone (UVO_3) treatment with a Jelight (Irvine, California, USA) equipment was performed on the substrates in order to remove organic contaminants on the TCO surface and to achieve better wettability of the alcohol-based ETL solutions.

The ZnO A stock solution was first diluted 20 times in ethanol in order to reach a 2% volume concentration of the zinc oxide nanoparticles inks. The diluted ZnO inks were then deposited on

a Suss Microtec (Munchen, Germany) Delta 10+ spin coater in open air on the cleaned substrates at 1000 rotations per minute (rpms) for 60 seconds. An additional spinning step at 2000 rpms during 30 seconds was then performed in order to pre-dry the layers.

The layers were then patterned with an isopropanol soaked foam swab. The devices were then annealed at 140°C in ambient air for 5 minutes in order to dry the layer.

Layer thickness of ZnO A layers as measured by mechanical profilometry was 94 $\pm$ 2 nm.

e) Bulk heterojunction active layer (BHJ Layer) The active layer was made from blends of electron donor polymers and electron acceptor molecules. Inks were made from a 1:0.88 mass ratio, previously determined as the optimal ratio yielding highest performances, of solid P3HT:PCBM weighted with a XP105 precision scale from Mettler Toledo (Columbus, Ohio, USA). The materials were then diluted in a nitrogen glove box (<1 ppm H_20, <50 ppm O_2) in 93/7 volume ratio of ortho-dichlorobenzene (o-DCB) and methylnaphtalene which enables good solubilization of the solid materials. Inks were then kept overnight at 60 °C under nitrogen atmosphere. They were brought to ambient temperature at least one hour previous to deposition.

The inks were then deposited with an SCS (Putten, The Netherlands) P6700 spin coater under nitrogen atmosphere on the previously deposited ETL layer. The samples were then patterned by an o-DCB soaked swab and then annealed for 10 minutes at 120 °C under nitrogen atmosphere to dry the solvents and optimize morphology of the active layer.

Thickness measured with a mechanical profilometer was 376 $\pm$ 16 nm.

f) Hole transport layer (HTL) Before the HTL ink deposition, in order to improve wettability of the aqueous PEDOT:PSS CPP105D on the hydrophobic active layer, the samples surfaces were gently rubbed with an isopropanol soaked foam swab. The HTL solution was spin-coated on the Suss Microtec Delta 10+ spin coater in air at 1500 rpms for 23 seconds and at 3000 rpms for 25 seconds. The layers were then patterned with an isopropanol soaked foam swab. The samples were then annealed for 10 minutes at 120°C in order to dry the layer. Such annealing was performed under nitrogen atmosphere in order to prevent water adsorption on the PEDOT:PSS layer.

Thickness measured by mechanical profilometry was 119 $\pm$ 11 nm.

g) Silver electrodes deposition Reference silver electrodes were deposited by thermal evaporation. The cells are first placed on a solid mask in order to pattern the electrodes. Evaporation was carried out in a MBraun (Garching, Germany) evaporator under high-vacuum below 5.10^{-6} mbar at a rate of 0.8 to 1.0 nm per second. Target thickness was 100 nm.

Alternative layer deposition procedures.

d') ZnO B electron transport layer ZnO B layers were deposited with the exact same procedure as the ZnO A layers without further optimization.

f') Alternative hole transport layers. Clevios^{TM} HIL 8 layers were deposited with the exact same procedure as the Clevios^{TM} P form CPP105D layers without further optimization.

WO_3 layers were deposited with the same spin-coating equipment as our reference HTL layer. Processing parameters optimization was performed and will be detailed in section 4.5.1.

g') Silver electrode inkjet printing Inkjet printing consists of jetting a silver ink through a piezo-electric nozzle. This technique allows precise custom patterning and relatively fast deposition speeds.

From the silver nanoparticles stock solution NP Ag-2103-EG, a 30:35:35 weight fraction ink of silver nanoparticles, IPA and ethylene glycol was prepared for jetting. This ink was then filtered through a 5 µm Polytetrafluoroethylene (PTFE) filter to prevent nozzle clogging and then jetted with a Fujifilm Dimatix DMP-2800 (Santa Clara, USA) printer according to parameters previously optimized in the laboratory.

2.3.2 Encapsulation processes

Two encapsulation materials/processes were studied in this work: the roll-to-roll compatible lamination of a pressure sensitive adhesive called PSA/R2R and the sheet-to-sheet melting and lamination of a thermoplastic called TP/S2S.

Prior to any lamination process, silver conductive tapes, reaching out of the encapsulation system, were placed on each electrodes in order to collect charges towards the outside of the devices once encapsulated.

PSA/R2R encapsulation. Fig.2.2 represents the process work flow of the PSA/R2R encapsulation strategy.

Laminations were performed by passing the samples between two silicone rolls turning in opposite directions of a Dynachem (Caronno Varesino, Italy) ML-3024 manual laminator. Samples for lamination were placed on a 3.35 mm thickpolytetrafluoroethylene (PTFE) coated glass carrier, a roller air pressure of 0.83 bar and a carrier speed of 0.5 m/min. It should be noted that the air pressure applied to the rolls is different from the actual pressure applied to the samples which is unknown.

The process work flow is the following:

a) Protective liners are removed from both sides of the barrier layer. The barrier is then placed on the glass carrier. One side of the protective liner of the PSA is removed (by unrolling). The PSA is then glued to the barrier extremity and kept tight during the roll lamination. At least a 48 h adhesive maturation delay was respected before further processing. Large areas of PSA/barrier were fabricated and kept for several months in a closet before use.

b) The PSA/barrier stacks were cut with a razor blade to the desired size depending on the OPV samples to be encapsulated. The encapsulation systems were roughly 2 cm larger and wider than the OPV samples dimensions. The liner on the PSA layer is then removed.

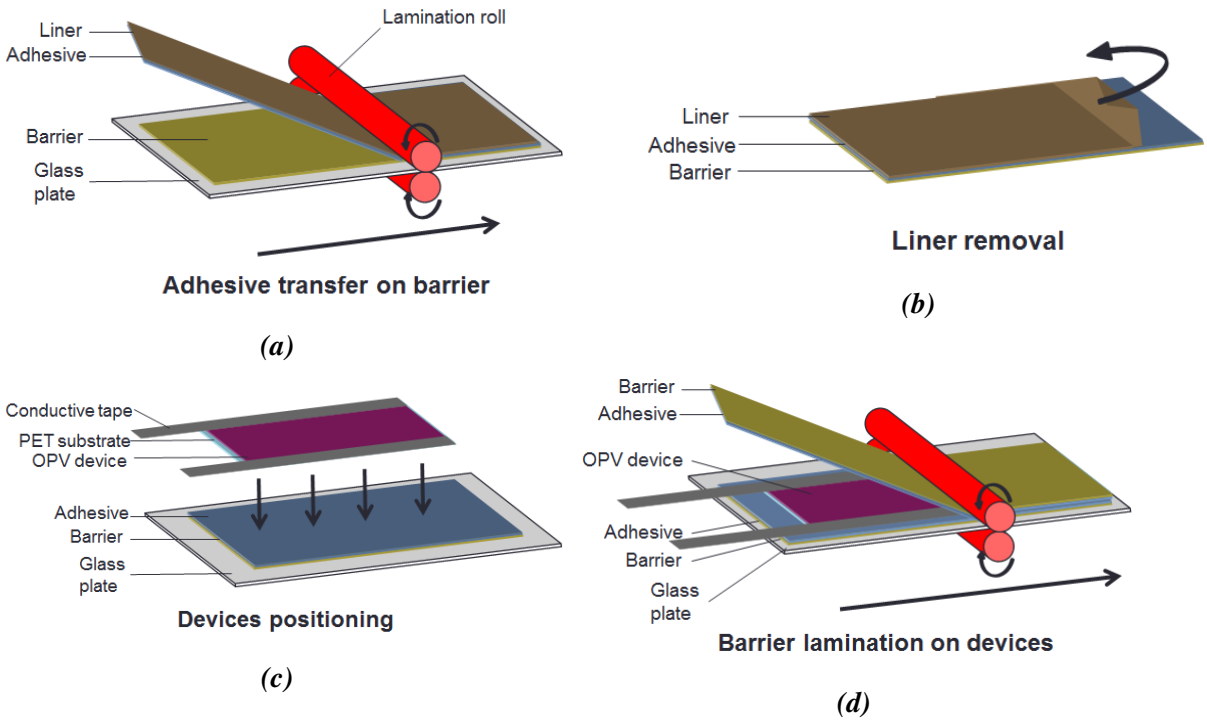

Figure 2.2: *Process work flow of the pressure sensitive adhesive (PSA) material / roll-to-roll (R2R) encapsulation process performed in this work. (a) A pressure sensitive adhesive (PSA), purchased with its protective liner, is transferred on a flexible barrier layer by laminating both between rolls. (b) The liner is removed after transfer. (c) The OPV device, on its flexible PET substrate, is placed on the free adhesive surface. The adhesive + barrier is 5 mm larger on both sides of the devices in order to prevent permeation from the edges. (d) Another barrier + adhesive stack is finally laminated on the device between the rolls.*

c) The OPV device is then placed in the middle of the encapsulation system, on the PSA surface. A rough 1 cm encapsulation rim is respected on each side of the device.

d) An additional PSA/Barrier stack, symmetrical to the first one, is then glued to the edge of the opposite encapsulation layers. Roll lamination was then performed while the PSA/barrier upper stack was kept tight. The symmetrical encapsulation was then carefully cut to a 5 mm rim with a razor blade. Samples were kept at least 48 hours in a nitrogen glove box to ensure the adhesive maturation.

TP/S2S encapsulation. Sheet-to-sheet lamination was performed with a Swiss Solar Systems (Lyss, Switzerland) laminator. Fig.2.3 shows a schematic cross section of the laminator during encapsulation of an OPV device.

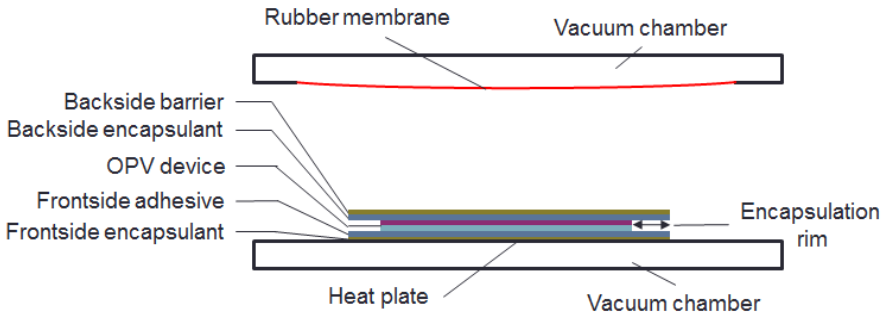

Figure 2.3: *Scheme of the heat-vacuum encapsulation process.*

The barrier and thermoplastic (TP) encapsulant layers were first cut 2 cm larger and wider than the samples to be encapsulated. Protective liners from the barrier layers were then removed. The following stack was then assembled on a glass carrier covered with a PTFE sheet: barrier / TP / OPV device / TP / barrier. The TP and barrier layers were aligned together and the OPV device was placed in the center area of the encapsulation sheets. An additional PTFE sheet was placed on top of the stack.

The samples were then loaded into the laminator pre-heated at 130 °C. A 1 bar pressure, created by applying vacuum on the bottom plate, was then progressively applied on the samples (total cycle time: 13 minutes) at the same temperature. After unloading, the samples encapsulation was carefully cut to a 5 mm rim with a sharp blade.

Fig.2.4 shows a cross section of our reference encapsulated OPV devices and summarizes the thickness of each layer.

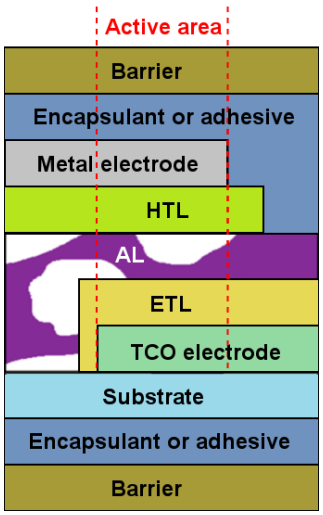

(a)

Layer	Material	Thickness
Backside barrier	PET-based multilayer	75 µm
Encapsulant	Acrylic adhesive hotmelt polyoletylene	50 µm 150 µm
Opaque electrode	Silver	100 nm
Hole transport layer	PEDOT:PSS	120 nm
Active layer	P3HT:PCBM	375 nm
Electron transport layer	Zinc oxide	90 nm
Hole transport layer	PEDOT:PSS	120 nm
Transparent electrode	Indium-Zinc oxide	150 nm
Substrate	PET	175 µm
Encapsulant	Acrylic adhesive hotmelt polyoletylene	50 µm 150 µm
Frontside barrier	PET-based multilayer	75 µm

(b)

Figure 2.4: *Cross section of our reference inverted OPV device. The table lists the different materials and their thicknesses used as standards in this work.*

2.3.3 Aging experiments

Aging experiments were performed under three conditions: storage in a nitrogen glove box, aging at 85 °C under vacuum and aging at 85 °C and 85 % relative humidity. Cells were characterized out of the climate chambers one at a time in order to make sure they spent no more than two hours out of their aging environment.

Aging under 85 °C in vacuum was performed in a 45071 oven from Fisher Scientific (Waltham, Massachusetts, USA). Vacuum was maintained under 0.02 bar.

Damp heat aging was performed in a C40-100 CTS (Hatfield, UK) climate chamber.

2.4 Characterization methods

2.4.1 Characterizations applied to complete devices

J(V) curves.

J(V) curves acquisition J(V) measurements consist of applying a voltage sweep on the cells terminals and measuring the corresponding output current in the dark or under illumination. Experimental parameters are set by a custom-developed LabVIEW (National Instruments (Austin, Texas, USA)) software controlling a source-measure unit.

Voltage sweeps were performed from -1.5 V to 1.5 V with a 0.05 V step between each measurement. For each measured samples, their active area was recalculated with a ruler and inputted in order to obtain current densities from the measured currents.

Several J(V) curve measurements were performed on the cells until they achieved stabilization of their performances, defined arbitrarily as when the measured PCE difference between at least four consecutive measurements was less than 0.02 points.

In this work, data reported on cells under standard illumination are given after their stabilization. The reported dark J(V) curves reported were acquired after their stabilization under illumination.

Two J(V) measurements setups were used in this work: one inside a nitrogen glove box and one in open air used only for measuring encapsulated cells.

The former is an Oriel® SP94043A solar simulator from Newport (Irvine, California, USA) using a 450 W xenon lamp from USHIO (Tokyo, Japan). Voltage sweep and current measurements were performed with a 2400 source-measure unit (SMU) from Keithley Instruments (Cleveland, Ohio, USA) and recorded by a 34970A data acquisition unit from Agilent Technologies (Santa-Clara, California, USA).

The latter is an Oriel® 92190 solar simulator from Newport (Irvine, California, USA) using a 1600 W xenon lamp from Newport. Voltage sweep and current measurements were performed with a 2602A source-measure unit (SMU) from Keithley Instruments (Cleveland, Ohio, USA).

The spectral match with the simulated AM 1.5G solar irradiation is regularly checked with an AESCUSOFT (Fribourg, Germany) spectrophotometer to be A class according to the ASTM standard [229]. This standard requires a 75% to 125 % matching of the simulated spectrum with the AM 1.5G standard. Therefore, even if both simulators fulfill the A class requirements, significant discrepancies can be observed between measurements performed on each. As a consequence, in this work, comparisons between samples or between aging times will only be made for measurements performed on the same equipment.

In addition, a daily verification of the simulators illumination power of 1000 W/m^2 is

performed by measuring the PV characteristics of a reference crystalline silicon solar cell calibrated at the Fraunhofer Institute for Solar Energy Systems [17].

J(V) data analysis Data is then processed by a custom-developed LabVIEW (National Instruments (Austin, Texas, USA)) software.

Open-circuit voltage V_{OC} and short-circuit current J_{SC} are calculated from linear regressions made on seven experimental data points sets centered around the closest J=0 and V=0 points, respectively.

Fill factor (FF) is the quotient of the highest V x J product divided by the V_{OC} x J_{SC} product. The highest J x V product is calculated from a polynomial fit made on a seven data points set centered on the highest experimental J x V point.

Power conversion efficiency (PCE) is then calculated as the product of V_{OC}, J_{SC} and FF divided by the lamp illumination power of 1000 W/m^2.

The series resistance (R_S) and shunt resistance R_{SH} are calculated as the inverse of the slope of linear regressions made on five data points sets centered at +0.8 V and -1 V, respectively.

Laser-beam induced current (LBIC) imaging. The local current extracted from the cell was investigated by a homemade laser-beam induced current (LBIC) imaging apparatus built by N. Charvin from the LEPMI laboratory. Excitation was performed using a monochromatic 532.5 nm laser diode from Thorlabs (Newton, New Jersey, USA) with a 5 mW output power. Current measurements were performed with a Keithley Instruments (Cleveland, Ohio, USA) 2602 source-measure unit. Sample area was scanned by the laser diode mounted on a X-Y stage controlled by a Matlab homemade software. Data was first processed with a custom Python script then colorized, thresholded and cropped using ImageJ.

Detailed information on the experiment development, its operation and the output data treatment is given in Sec.3.1.1.

Luminescence imaging. Photoluminescence and electroluminescence emission of the OPV cells were imaged. The luminescence imaging setup used in this work is based on a customized solution from Greateyes (Berlin, Germany). Additional optical filters from Edmund optics (York, UK) were added in order to allow spectral resolution on the setup. Photo-induced excitation was performed with monochromatic 520 nm LED arrays. Electro-induced excitation was performed with a TDK-Lambda power source (Tokyo, Japan) during electroluminescence imaging experiments and with a Keithley Instruments (Cleveland, Ohio, USA) 2602A source measure unit for voltage-biased photoluminescence imaging ones.
Any additional image treatment (cropping, colorization or thresholding) was performed with the ImageJ freeware [230].

Detailed information on the experimental protocol is given in Sec.3.1.2.

Image treatments. All image treatments in this work were performed with the imageJ freeware [230].

During their treatment, all images were saved in a lossless 16-bits depth (65536 gray scale) TIFF format allowing precise and quantitative measurements of signal intensity.

Image parameters, such as the mean signal intensity and its standard deviation for example, were calculated on several images of a single sample after a careful manual alignment of the sample edges on all images. A subsequent cropping of the studied area was then performed. Although the manual character of the operation induces some error in the calculations, the cropped areas are sufficiently wide (around 100x300 pixels for the active area) to reasonably neglect such cropping shifts.

Thresholding operations were performed after calculations. The resulting images were saved in the lighter PNG format prior to their inclusion in this work.

Peeling tests. 180 °peeling tests (also known as T-peel tests) were performed on OPV devices in order to assess their mechanical properties. Each sample arms were loaded in a Shimadzu AGS-X traction bench and peeled at a constant displacement-rate of 100 mm per minute in traction mode. During the test, the strength applied to the traction arms of the sample was recorded as a function of their displacement.
The debonding path was then investigated using other physico-chemical characterization methods on the debonded surfaces.

Detailed information on the samples geometry and the data analysis is given in Sec.3.2.

2.4.2 Materials characterizations

Morphological characterizations

Optical microscopy. Optical micrographs were acquired on a Leica (Wetzlar, Germany) DM LM equipment in reflection mode and bright field. Brightness and contrast were adjusted for each acquisition. Three magnification objectives were employed:

- A 1.25x magnification objective leading to a 4.00 µm per pixel resolution.
- A 10x magnification objective leading to a 0.51 µm per pixel resolution.
- A 50x magnification objective leading to a 0.10 µm per pixel resolution.

Resolutions were calculated according to images made on a micro-ruler.

Mechanical profilometry. Thicknesses and roughnesses were probed by an Alpha step IQ mechanical profilometer from KLA-Tencor (San Jose, California, USA).

Thickness measurements have been performed by measuring the height difference between the layer and an area without it. To create such steps, two techniques were used: in the event where the studied layer is deposited on a harder substrate, for example on a glass plate, a trench was dug with metal pliers. In the case where the substrate is of similar hardness to the measured layer, a low-adhesive tape was placed on the substrate prior to layer deposition and was subsequently removed.

Eight consecutive scans were performed with a 4 mg stylus force at a 20 µm/s scanning speed leading to a 0.4 µm lateral resolution.

Dynamic light scattering. Dynamic light scattering experiments were performed with a Zeta Nano S equipment from Malvern Instruments (Malvern, UK).

Incident light angle was 173°. 12 to 17 accumulations were performed until software validation of the results consistency. Each measurement was performed 3 times on different samples from the stock solution.

WO_3 dispersions were studied with this technique. Their solvent, isopropanol, was inputted in the calculations with 2.04 Pa.s viscosity [231] and a 1.38 refractive index [232].

WO_3 refractive index was inputted to be 2.2. This value was found for sol-gel [233] or [234] evaporated WO_3 different from our samples. Therefore the size ratios calculated from the measurements are assumed to be biased and will not be presented. However, the presence in the dispersion of a size population can still be assessed.

Physico-chemical characterizations

Fourier transform infra-red (FTIR) Spectroscopy. FTIR spectra were acquired in attenuated total reflection (ATR) or transmission mode on two different equipments.

ATR spectra were made on a Perkin-Elmer (Waltham, Massachusetts, USA) Paragon 1000 PC IR spectrophotometer. Spectra were made on a diamond crystal, allowing for a ≈ 1.7 µm penetration depth of the beam in the sample. The diamond crystal was cleaned with an ethanol soaked cloth before every acquisition.

Transmission spectra were performed on glass substrates on a Perkin-Elmer (Waltham, Massachusetts, USA) Spectrum One IR spectrophotometer. Glass absorption below 2000 cm^{-1} does not allow to exploit spectra of the samples in this spectral range.

Eight scans were performed from 600 to 4000 cm^{-1} with a 4 cm^{-1} wide spectral resolution and 1 cm^{-1} interval. The resulting averaged spectra were baseline corrected by the setup corresponding software. Blank scans acquired in similar conditions were performed every three measurements or after a 20 minutes delay and were subtracted to the raw spectra of the samples.

SEM-EDX. Back scattered electrons images, yielding composition contrasts, were acquired with a Nova NanoSEM 630 from FEI (Hillsboro, Oregon, USA) now part of Thermo Fisher Scientific (Waltham, Massachusetts, USA). Measurements were performed in a 0.8 mbar water atmosphere in order to study electrically insulating layers without damaging them. A gaseous analytical back scattered electrons detector was used. Primary electron beam was accelerated with a 12 kV voltage. Work distance was kept at 6.5 ± 0.5 mm.

Contact angle measurements. Contact angle measurements of solvents on solid layers were performed with a Krüss equipment. Fig.2.5 summarizes the relevant physical constants at 20 °C of the solvents used.

The water contact angle with the sample will be an indicator of polarity of the layer while the diiodomethane will probe the opposite disperse property. Height droplets of constant volume were used for all measurements performed with a given solvent.

Solvents	Surface tension (mN/m)		
	Total	Polar	Disperse
Water	78.8	50.2	22.6
Diiodomethane	50.8	1.8	49.0

Figure 2.5: *Surface tensions at 20 °C of contact angle solvents with their polar and disperse components. Values were found in [235].*

Thermogravimetric analysis. Thermogravimetric measurements were performed with a TGA 2050 CE equipment from TA Instruments (New Castle, Deleware, USA). Samples, solids or liquids, were loaded in a platinum basket tied to the instrument scale. Measurements were performed under a 105 psig air gauge pressure.

Opto-electronic characterizations

UV-Visible absorption. UV-Visible absorption spectra were acquired with a UV-2600 instrument from Shimadzu (Kyoto, Japan) with an ISR-2600Plus integration sphere attachment in order to detect the diffused, reflected and transmitted light. 3 averaged measurements were performed from 200 nm to 1000 nm with a 0.5 nm sampling. A deuterium light source was used for the 200-323 nm range and a halogen lamp was used for the 323-1000 nm wavelength range.

Luminescence spectroscopy. Two luminescence spectrometers were employed:

We used a first type of tool within the frame of a short-term scientific mission welcomed by Pr. F. Zhang [236] at the Department of physics, chemistry and biology [237] of Linköping University, Sweden and funded by the COST (European cooperation for science & technology) program [238] in the action MP1307 "Stable Next-generation photovoltaics" [239].

PL excitation was carried out by a 5 mW, 532 nm monochromatic laser diode which was cropped with a diaphragm to a 1000 µm diameter disc giving an excitation area of 0.785 mm^2. EL excitation was carried out with a Keithley (Cleveland, Ohio, USA) source-measure unit.

The spectrometer consists in a Newton EM-CCD Si array detector cooled to -60 °C connected to a Shamrock SR-303I-A Spectrograph from Andor Tech (Belfort, UK). An Oriel® liquid light guide from Newport (Irvine, California, USA) was connected to the detector array and the other end was put as close as possible to the samples.The system was wavelength calibrated by an argon lamp to a resolution better than 0.5 nm. Back illumination of the Si-CCD detector increases the sensitivity but also the noise observed on the resulting spectra. Acquisition was performed from 550 to 1000 nm. PL and EL integration times were 2 and 60 seconds, respectively.

The second one was an instrument from the Nanocharacterization platform (PFNC) [240] at Grenoble, France. The equipment is a Raman microscope which was modified to perform PL experiments.

PL excitation was carried out by a 514 nm argon laser diode. EL excitation was performed

with a 2602A source-measure unit from Keithley Instruments (Cleveland, Ohio, USA).

Luminescence spectra were acquired by a Si-CCD detector through a 100x magnification objective and a 600 lines per mm diffraction grating. Spectra were acquired from 550 to 1000 nm for a 10 seconds integration time.

Kelvin probe. The kelvin probe is a capacitor based device used to measure the potential difference between Fermi energy levels of an electrode and the surface of the investigated material [241, 242].

Measurements were performed with a SKP Kelvin probe from KP Technologies (Beavercreek, Ohio, USA).

Fig.2.6 describes the energy diagram of a silver layer, an unknown sample and the apparatus electrode.

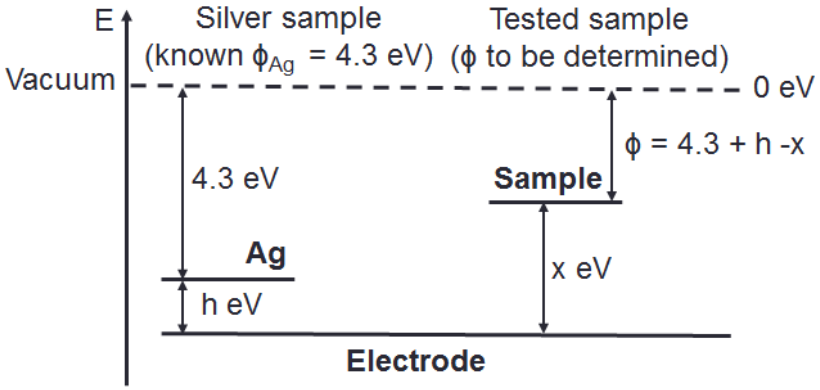

Figure 2.6: *Energy diagram used to deduced a sample Fermi level. The Kelvin probe apparatus yields potential differences relative to its electrode level. The absolute Fermi level can be deduced with a reference layer of a known work function.*

The Kelvin probe experiment applied on an unknown sample yields the potential difference, called x, between the sample and the apparatus electrode. By measuring the potential difference, called h, between the electrode and a reference layer (here freshly evaporated silver) with a known work function Wf, the Fermi level position compared to vacuum of the sample, called ϕ can be calculated with the formula : $\phi = Wf + h - x$.

In our case, a 100 nm thick silver reference on a glass substrate was used with a tabulated work function value of -4.3 eV [90]. To prevent from any significant time deviation, a freshly prepared reference silver sample was measured every two hours.

The potential gradient measured between the upper position and the lower position of the vibrating gold tip is a parameter which is only dependent on the reference gold electrode distance to the sample surface. In this work, a potential gradient of 400 mV was chosen, allowing us to work with a similar electrode distance for all samples.

Chapter 3

Development of characterizations adapted to study flexible encapsulated OPV devices

In order to study the behavior of encapsulated organic solar cells during their processing and aging, several characterization methods were developed in this work.

As shown in Sec.1.4, a range of non-destructive imaging characterizations, such as luminescence imaging [211, 243, 244], laser-beam induced current (LBIC) mapping [77, 120, 193–200] and thermography [245–247] for example, allows for tracking the devices state at any moment of their lifetime [215, 216, 248]. The use of such complementary characterization techniques can yield valuable information on how and where degradation takes place in encapsulated devices. Therefore, the first section of this chapter will cover the development of imaging characterizations.

First, laser-beam induced current (LBIC) imaging was developed in order to laterally resolve the whole PV mechanism of the cells. Such characterizations will require to be fast and adapted to samples of relatively large areas in order to draw significant statistics from their results.

Secondly, photo-induced and electro-induced luminescence imaging (PLI and ELI, respectively) were developed in order to investigate the localized ability to respectively photo-generate and then collect electrical charges.

Finally, a voltage-biased photo-luminescence imaging (vbPLI) technique was set up in order to replace the destructive electro-luminescence imaging technique yielding similar results.

In addition, as shown in Sec.1.3 and 1.3.4, several mechanically weak points are identified in the OPV devices and can be at the origin of delaminations suspected to be an important degradation factor during processing and aging of the OPV devices. Such weak points can be the interface between two layers, for example the active layer/PEDOT:PSS HTL interface [91, 163, 165, 167, 175] or the TCO/ETL one [129, 186, 187], ultimately leading to adhesive rupture between both layers. In addition some layers such as the active layer [159, 162, 163, 166, 169–171] or the PEDOT:PSS one [161, 165, 172] themselves are suspected to rupture cohesively. Thus, in order to quantify the peeling strength of each interface of our devices, a widely used mechanical characterization technique, the 180° peeling test (also known as T-peel test), was

adapted in order to be performed on encapsulated flexible OPV devices.

3.1 Imaging opto-electronic properties of OPV devices

Characterization of photovoltaic devices can be made on various scales. Macroscopic efficiency of the devices is commonly probed by plotting the J(V) curves of the cells or modules. Microscopic characterizations yield detailed and comprehensive information on the devices characteristics but they are not suitable to evaluate the entirety of a device in a convenient time. Imaging characterizations are part of the mesoscopic set of characterizations available in order to test the entirety of the devices resolved on a millimeter to micrometer scale. Such techniques find a particular interest in the field of quality control in production lines, where large device areas must be tested in a limited time.

In the frame of this work, a homemade laser-beam induced current (LBIC) equipment was developed and characterized, allowing us to laterally resolve the PV efficiency of our devices in a limited time.

Subsequently, in order to further investigate the impact of several degradation factors on the cells overall performance, complementary luminescence imaging techniques were developed, allowing us to separately track the efficiency of charge-carriers photo-generation and collection mechanisms.

3.1.1 Laser-beam induced current (LBIC) mapping

In order to probe the PV efficiency of the cells resolved on a local scale, laser-beam induced current mapping is the most straightforward method. It consists in mapping the short-circuit current induced by a laser spot scanning the sample surface.

This characterization probes the entire PV mechanism, from light absorption to free-charges extraction through the terminals of the device. It is therefore a convenient end-line control tool for complete OPV devices [199, 249]. We wanted to study with this method broad batches of cells in order to have a statistical comprehension of some fabrication processes or aging conditions on the cells performance. This require a reduced characterization time and the ability for the equipment to cover relatively large areas, up to the module scale (a few centimeters wide and long). Although LBIC systems are commercially available [250], we decided to develop our own system, more flexible, to meet our speed and area requirements. This development included the setup development as well as the data and image analysis routines.

Experiment description. A scheme and a photograph in Fig.3.1 describe the LBIC setup developed during this work in partnership with N. Charvin from the LEPMI laboratory [251].

It consists in a laser diode attached to a computer-controlled X-Y stage which scans the sample surface. The output current in short-circuit conditions (i.e at a 0 V bias voltage) is recorded by a Keithley 2602 (Cleveland, Ohio, USA) source-measure unit in order to construct

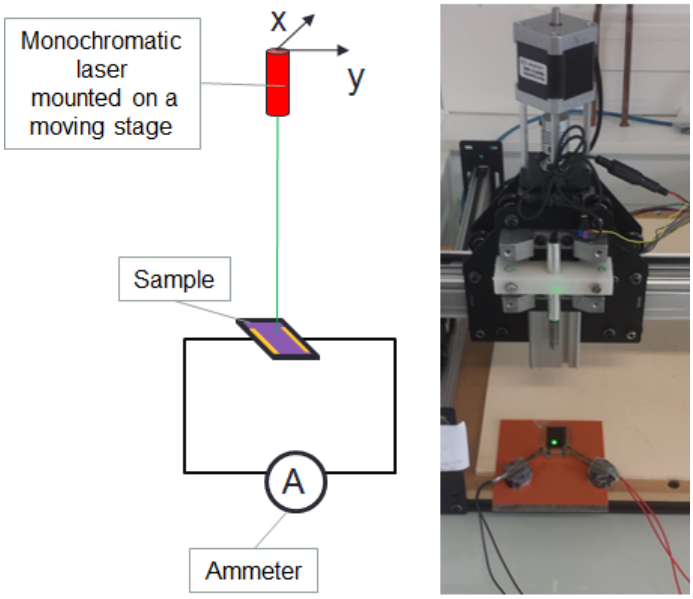

Figure 3.1: *Scheme and picture of our laser-beam induced current (LBIC) setup.*

a J_{SC} map of the cell area. The source measure unit have a $\pm$ 0.025% + 400 pA precision for current measurements in the µAmps range.

A monochromatic 532.5 nm "CPS532" diode laser from Thorlabs (Newton, New Jersey, USA) with a 5 mW output power and a 3.5 mm diameter ($\approx$ 520 W/m^2) was used. As shown in Fig. 3.2, the laser emission wavelength was chosen according to the maximum absorption of our samples, in order to maximize the measurable output current. The whole setup is protected from external light sources in order to reduce background noise.

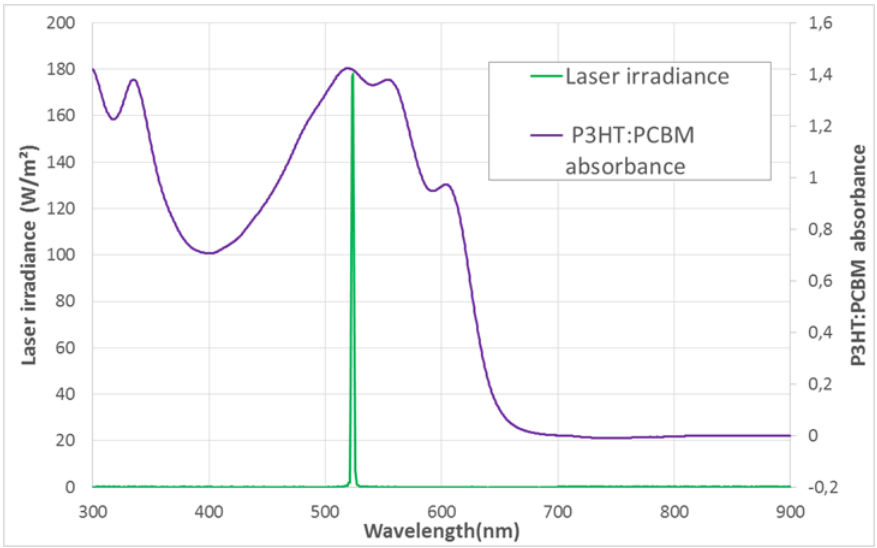

Figure 3.2: *Absorbance of a P3HT:PCBM thin film and the laser irradiance spectrum of the LBIC apparatus.*

Scanning grid pattern. The cell is expected to produce current only on its active area of $\approx$ 20x7 mm^2 (plus a smaller surrounding area due to collection by the relatively high conductive PEDOT:PSS layer), therefore there is no need to scan a significantly larger area. Fig. 3.3 schemes the scanning pattern used on our samples in this work.

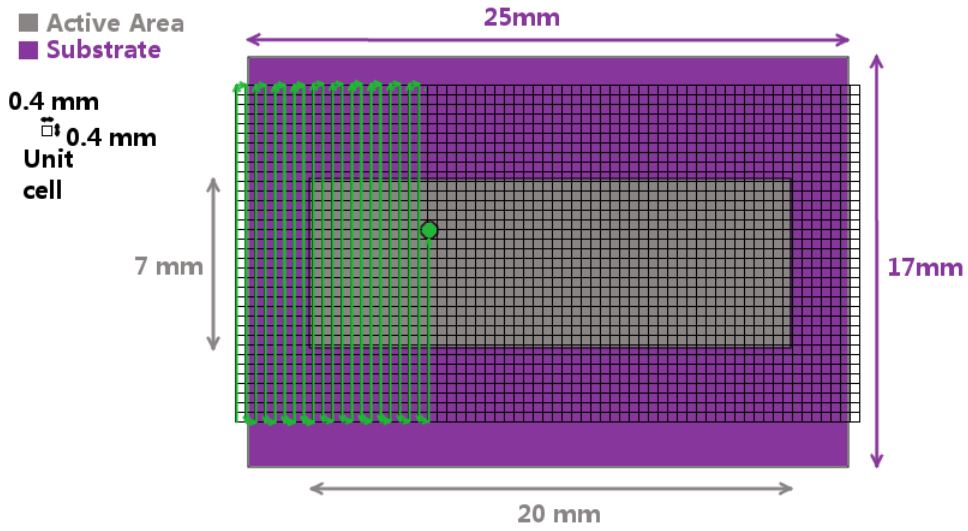

Figure 3.3: *Scheme of a LBIC-experiment scanning pattern. A green laser spot scans the active area following the green S-pattern over a 26x14 mm^2. Each grid intersection corresponds to a measure point.*

The X-Y stage scans a 26x14 mm^2 area following a S-pattern with each raw separated by 0.4 mm and 35 measurements taken on each raw. The average resolution of the scanning grid is therefore 0.4 mm. The resulting output data is a 66x35 short-circuit-currents matrix.

2310 data points must be collected for each image. In order to decrease the total measurement time down to 20 minutes, the current measurements are performed on the fly while the laser scans the sample. As a consequence, the acquisition positions on each raw are not strictly the same for each scan.

Using a homemade Python [252] script, the raw data is interpolated on a 260x140 pixel^2 grid. A background current of a few microamps, mostly originating from the presence of external light, defined as the average current output measured when the laser is located on the image border, is subtracted and an image is constructed on 256 grey-levels scaled from 0 to the measured maximum short-circuit current. The scale is finally divided by the laser spot area in order to obtain current-density maps.

Spatial resolution. During early experiments with the setup, a laser diode with a 3.5 mm diameter spot was employed. Due to the large area covered by the laser compared to the much smaller scanning grid (illustrated on the left part of Fig. 3.4), resulting images, such as the one depicted on the left of Fig. 3.5, appear blurry.

A better solution consists of using a smaller laser spot, in our case with a 0.7 mm diameter through a hard mask. As illustrated on the right side of Fig. 3.4, the spot diameter is still larger than the scanning grid, the resolution of the images is therefore limited by the latter (400 µm).

Fig. 3.5 represents two LBIC images of the same cell with a 5 mm wide opaque rod blocking light on top of it. These images allow comparison of images taken with different laser sizes and after image processing for the blurry image.

The raw image taken with the 3.5 mm wide spot gives a crude information of the short circuit current distribution on the device surface. One can see that the image taken with the smallest spot size gives a much richer information of the short circuit current extracted from the cell.

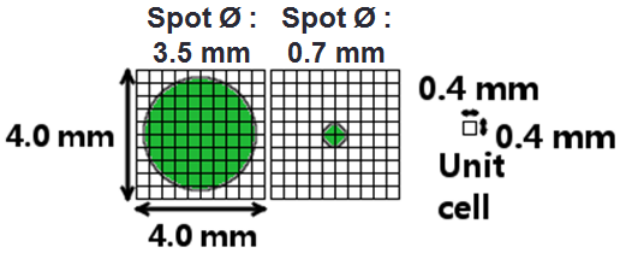

Figure 3.4: *Laser spot sizes as compared to a 10 x 10 pixels^2 scanning grid of 4 x 4 mm^2.*

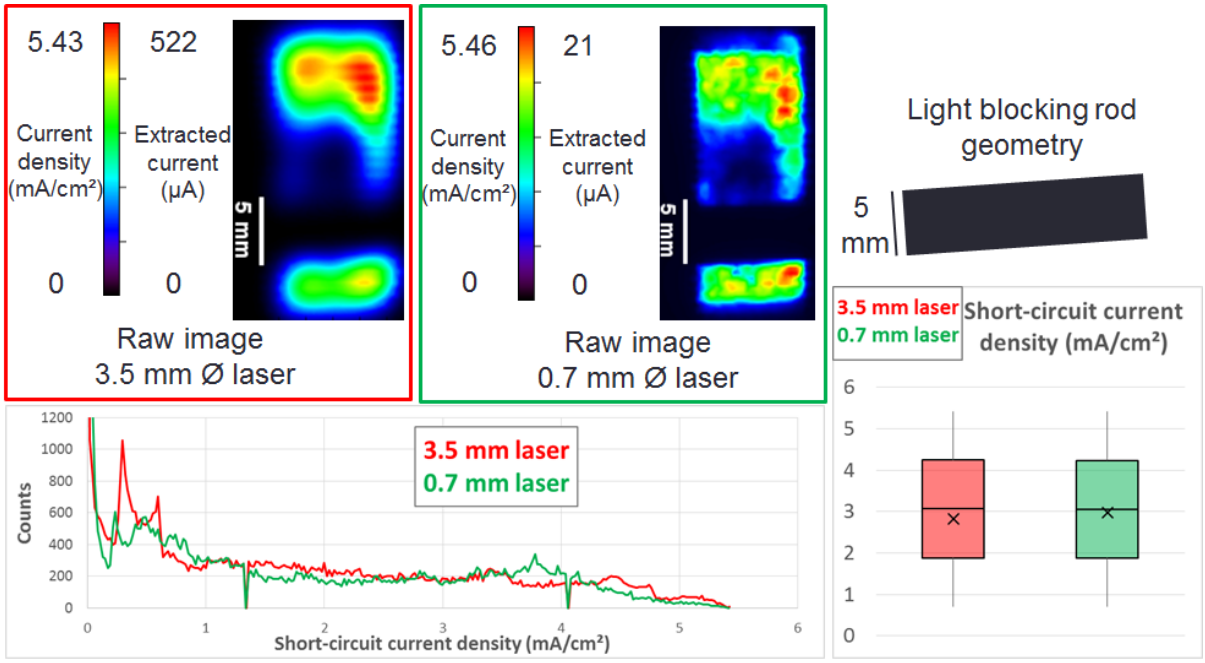

Figure 3.5: *LBIC images of the same cell with a 5 mm wide rectangular opaque rod blocking light on top of it. Left image was taken using the wide 3.5 mm diameter laser spot, right image was taken with the 0.7 mm diameter laser spot. Histograms from each images are shown below. Distributions of short circuit current density extracted from the histograms are shown in box-plot representation on the right. For this box-plot graph, pixels below 0.7 mA/cm^2 were ignored in order to limit noise influence on this box plot.*

Furthermore, the measured current densities between both images are in good agreement.

However, with the smaller laser spot, the absolute current extracted from the cell is significantly lower, in the µA range, in correlation with the laser spot area. As a consequence, hiding the cell from external light sources and using a well-adapted laser wavelength become mandatory in order to detect areas with a low current output.

This LBIC technique will be used in several contexts in this work. It represents a first step toward optimization and degradation study of OPV cells.

Samples conditioning. LBIC images intensities were empirically observed to be strongly dependent on the time elapsed between the J(V) measurements and the LBIC imaging experiment. This is at least partially related to the conductivity of the zinc oxide (ZnO) layer which reversibly increases during J(V) measurement due to the UV component of the xenon lamp removing oxygen adsorbed on the nanoparticles [77, 104, 253]. Such oxygen adsorption/desorption mechanisms are reversible.

In this work, when measuring the cells performances, as well for J(V) curves or LBIC experiments, samples were exposed to a simulated 1-sun irradiation until their J(V) performances were stable (see Sec.2.4.1). Empirically, such performances were observed to be stable for less than an hour. However, LBIC experiments take 20 minutes to be performed plus ten minutes to be prepared. As a consequence, quantitative LBIC images had to be obtained immediately after their J(V) measurement.

A practical case is presented in Fig.4.5 in Sec.4.2.2 where one LBIC image is in contradiction with the J(V) data. This is correlated with a long acquisition time of the LBIC image. A cell conditioning issue is thus thought to be responsible for the inconsistent LBIC data.

3.1.2 Electro-photoluminescence imaging (ELI & PLI)

In order to dissociate several degradation causes responsible for the loss of performance of the cells, photo- and electro-luminescence can be performed in order to study the active layer or the transport and electrode layers degradation, respectively.

Photoluminescence and electroluminescence spectra. Before imaging the luminescence emission, luminescence spectra of the separate layers and complete cells should be recorded in order to understand the luminescence mechanisms and to efficiently design the imaging experiments.

Typical photoluminescence spectra Photoluminescence (PL) is achieved when a semiconductor emits light after it absorbed photons. Photoluminescence primarily occurs when an electron located in excited energy states of a material radiatively recombines with a hole located in the valence band. This process is known as band-to-band recombination.

Normalized PL spectra of pure P3HT, PCBM and the 50/50 % weight blend of both are reported in Fig. 3.6. Excitation wavelength was 514 nm.

Separate active layers materials, P3HT and PCBM gives PL signals peaking at 708 and 735 nanometers, respectively. The 50/50 % weight blend PL peaks at 698 nm. P3HT is the main contributor shaping the blend PL spectrum due to its high absorption of the 514 nm diode excitation compared to the weak absorption of PCBM at this wavelength. The slight blue shift between the blend and the P3HT spectra is representative of lower energy losses by inter-chain relaxations and therefore increased packing of the P3HT chains [35]. The absolute blend emission intensity was much weaker compared to the pure materials'. This phenomenon is known as PL quenching and it is an indicator of a good mixing between the electron donor and acceptor phases of the blend. This quenching, calculated from the absolute peak area ratio of the pure polymer compared to the blend's, is more than 90 % efficient for our devices. This is in agreement with the literature, where optimized blends often reach 99 % quenching efficiency.

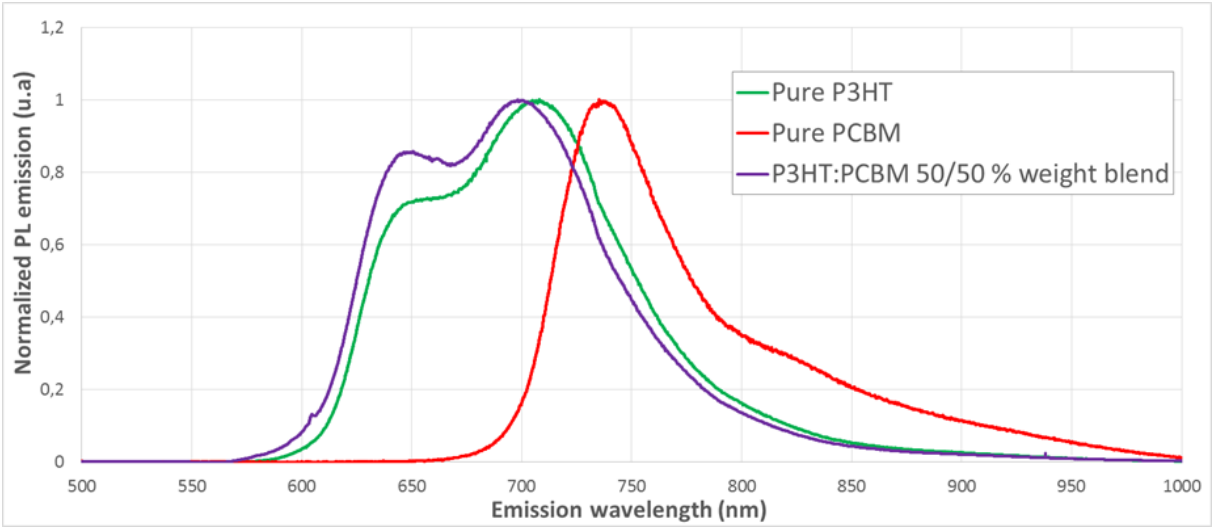

Figure 3.6: *Photoluminescence spectra of pure P3HT, pure PCBM and their 50/50 weight % blend layers on glass substrates normalized to their maximum. Excitation was carried out with a 514 nm monochromatic laser diode.*

Photoluminescence spectra of the active layer Fig. 3.7 plots a typical experimental PL spectrum of a 50:50 wt P3HT:PCBM layer deposited on a glass substrate and annealed for 10 minutes at 120 °C. Excitation was carried out with a 514 nm monochromatic laser diode.

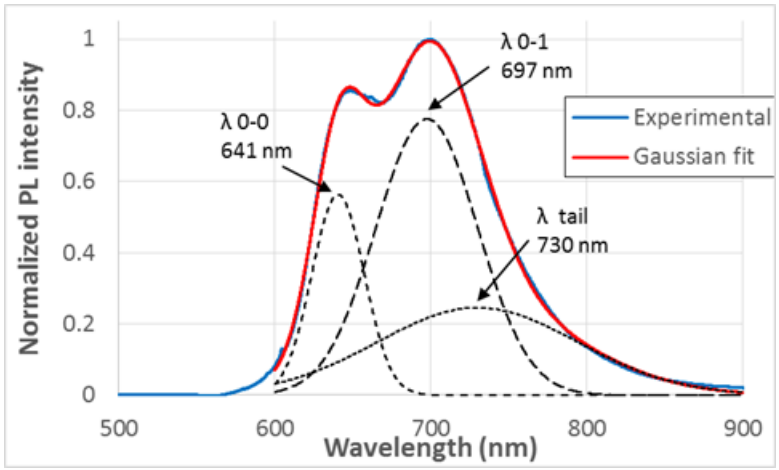

Figure 3.7: *Typical photoluminescence spectrum of a 50:50 wt P3HT:PCBM layer normalized to its maximum and deconvoluted over the 600 - 900 nm range. Excitation was carried out with a 514 nm monochromatic laser diode.*

Such PL spectra can be deconvoluted in the 600 to 900 nm range by Gaussian functions centered at at 641 nm, 697 nm and 730 nm (1.93, 1.78 and 1.70 eV, respectively). According to the literature [35, 254, 255], the 641 nm peak is attributed the 0-0 monomer (i.e. from the conduction band to the valence band) emission of P3HT. The $\approx$ 0.15 eV shift between the first two peak centers corresponds to the stretching energy of double C=C bonds, suggesting emission occurs after intra-chain vibrational relaxation in polymer H-type aggregates. The 697 nm peak is thus thought to be representing the 0-1 transition, one vibrational level narrower than 0-0. The large tail is thought to be originating from less ordered (i.e. amorphous) regions in the film. The overall broadness of the peaks is explained by torsional disorder of the polymer chains and possibly a small contribution from pure PCBM domains.

Electroluminescence spectra of the active layer Electroluminescence (EL) is achieved when charge carriers injected via the device terminals recombine yielding a photon emission; it is the working principle of light-emitting diodes.

Fig.3.8a compares two EL spectra, taken at two bias voltages and a PL spectrum obtained with a 532 nm laser diode obtained on a complete P3HT:PCBM cell.

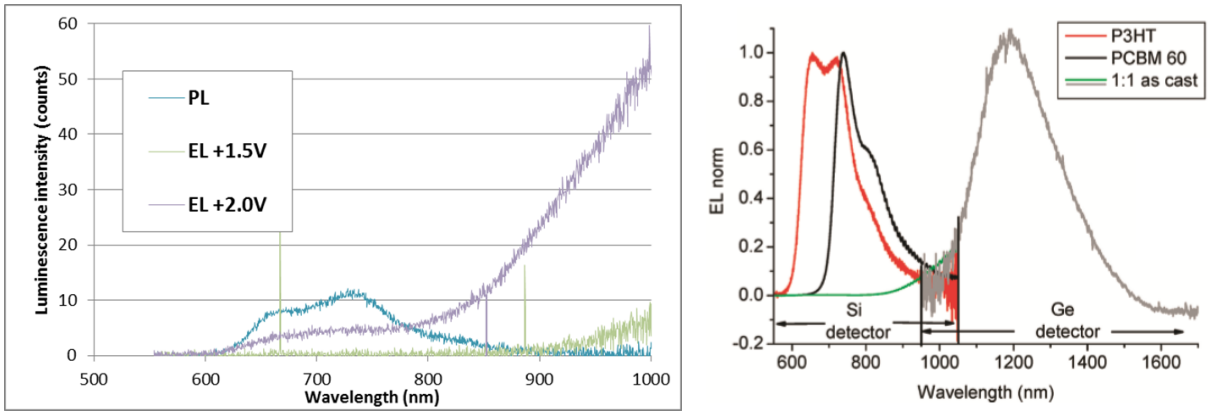

(a) *(b)*

Figure 3.8: *(a)Photoluminescence (PL) spectrum and electroluminescence (EL) spectra taken at a 1.5 V and 2.0 V forward bias voltage of a complete P3HT:PCBM cell. PL excitation is achieved by a 532 nm monochromatic laser diode. (b) EL spectra, normalized to their maximums, of the pure P3HT, PCBM and their blend. Reproduced from [47].*

As seen in Fig.3.8a, in EL experiments, a higher wavelength (i.e. lower energy) is emitted from the active layer than when performing PL. This is the CT-state emission which corresponds to the recombination between an electron in the acceptor conduction band and a hole in the donor valence band. Thus, the CT states energy is the difference between the PCBM LUMO and the P3HT HOMO. As shown in Fig.3.8b, for P3HT:PCBM, this energy is reported to be $\approx$ 1.0 to 1.2 eV leading to emission peak-wavelengths in the IR range (1180 nm in the literature [47]).

The apparition of lower wavelength band-to-band recombination emitting in the visible (around 700 nm) region can be observed at 2 V while it is absent at 1.5 V. This is due to the fact that the injected charges populate the lowest energetic CT states first and then populate the donor phases at higher injection voltages if the CT energy states are already saturated.

Finally, although it has been reported in the literature on highly efficient OPV blends [47], we never observed any CT states emission during PL experiments.

Fig.3.9 shows the different energetic transitions leading to luminescence of OPV devices and summarizes the emission mechanisms that we observed to occur for each excitation condition.

Luminescence imaging setup presentation and characterization. Luminescence can be observed by imaging techniques in order to study the devices properties resolved on a mesoscopic scale.

The luminescence imaging setup used in this work is based on a customized solution from Greateyes (Berlin, Germany). Additional optical filters from Edmund optics (York, UK)

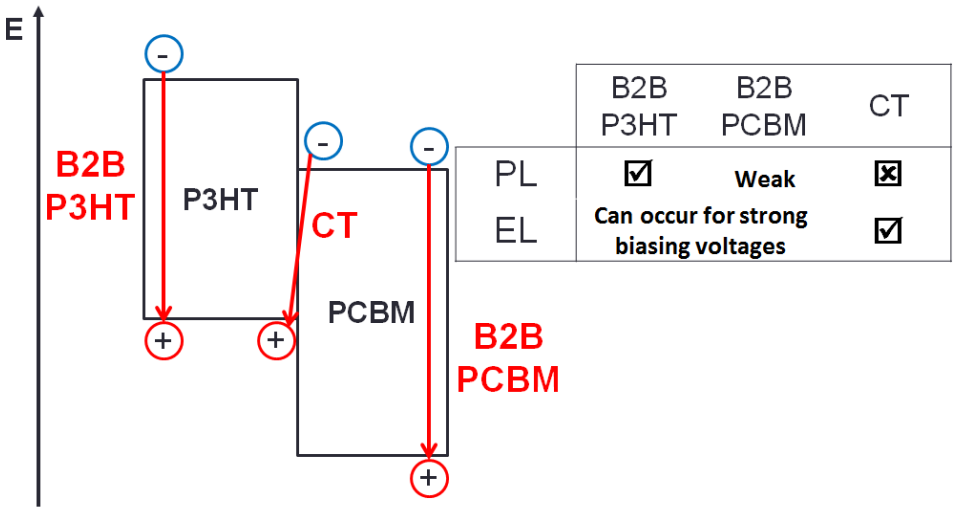

Figure 3.9: *Energy diagram representing the possible radiative transitions to be observed during luminescence experiments. The possible recombination mechanisms according to each experiment is summarized in the table.*

were added in order to allow spectral resolution on the setup. In-depth characterizations were performed in order to extract the most relevant and quantitative data possible from the output images.

Luminescence imaging working principle Electroluminescence imaging is performed following three steps:

1. Charges carriers are injected through the device terminals.
2. The injected charge carriers may recombine radiatively in the active layer, leading to electroluminescence emission.
3. The light then goes through the camera optics and reaches the Si-CCD detector of the camera. An optional optical filter can be used in order to select the emission site (band-to-band in the bulk donor phase or CT states at the D:A interfaces) to be observed.

The corresponding experimental setup used in this work and the relevant spectral data are depicted in Fig. 3.10a and 3.14, respectively. The data corresponding to each step described above are labeled in red circles.

Photoluminescence imaging uses the same working principle as electroluminescence except the fact that the excitation is optical instead of electrical. As a consequence, the use of optical filters is mandatory in order to prevent the excitation light from reaching the camera detector.

Photoluminescence imaging is performed following three steps:

1. The cell is excited by an homogeneous illumination from 520 nm monochromatic LED arrays.
2. Light is absorbed by the active layer and photoluminescence is emitted at a higher wavelength.

3. The excitation light is blocked by an optical filter. The filtered luminescence light then goes through the camera optics and reaches the Si-CCD detector.

The experimental setup used in this work and the corresponding spectral data are depicted in Fig. 3.10b and 3.15, respectively. The data corresponding to each step described above are labeled in red circles.

Setup description A basic description of the setup will be given in this paragraph. Additional characterizations of the LED arrays, optical filters and camera can be found in the paragraphs below. Fig.3.10 represents schemes of the setup during EL or PL imaging measurements.

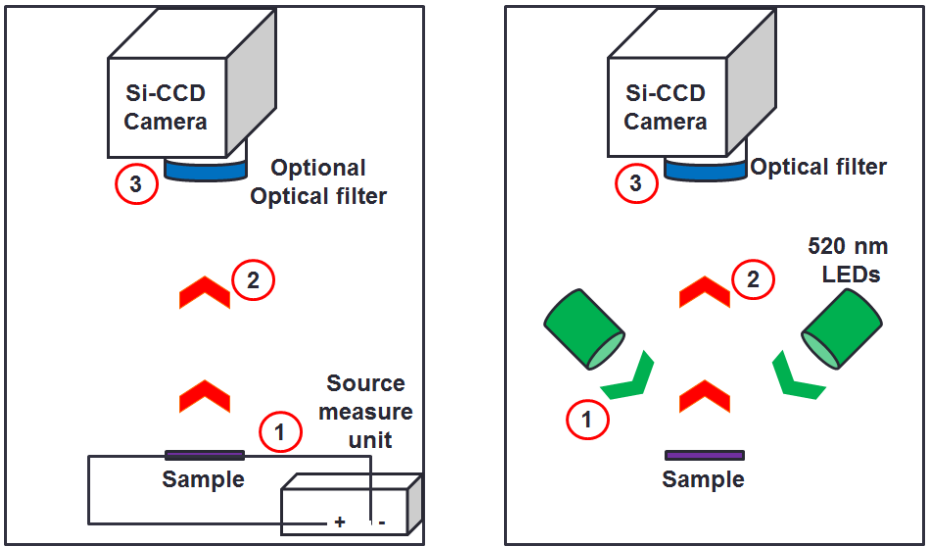

Figure 3.10: *Experimental setups of (a) electroluminescence and (b) photoluminescence experiments. The labels in red circles correspond to the experimental steps described above.*

The experimental setup used in both types of experiments is the same. It is composed of an opaque casing with a Peltier-cooled Si-CCD camera placed 28 cm above the sample plate. Using a PL image of a silicon solar cell shadowed by a ruler, a pixel size of 67.1 µm was determined. A drawer located between the camera's objective and detector is designed to place an optical filter.

During PL imaging experiments, optical excitation is carried out by two symmetrical monochromatic LED arrays placed 25 cm above the sample plate and controlled by a TDK-Lambda power source (Tokyo, Japan). The power source operates the LEDs at constant voltage and current.

During EL imaging experiments, electrical excitation is carried out by the same power source connected to the samples terminals. The voltages or currents are chosen by the operator.

In order to accurately record the applied voltages and currents flowing through the samples during EL or PL experiments, an external Keithley 2602A source measure unit is connected to the cells.

Both the excitation devices, whether optical or electrical, and the Si-CCD camera are synchronized to a computer using Greateyes' "Lumisolar" proprietary software.

LED arrays characterization The excitation illumination from the LED arrays was characterized with a spectrometer yielding the spectral distribution of the illumination and a pyranometer displaying the total illumination power. The merged data obtained from both experiments are presented in Fig.3.11.

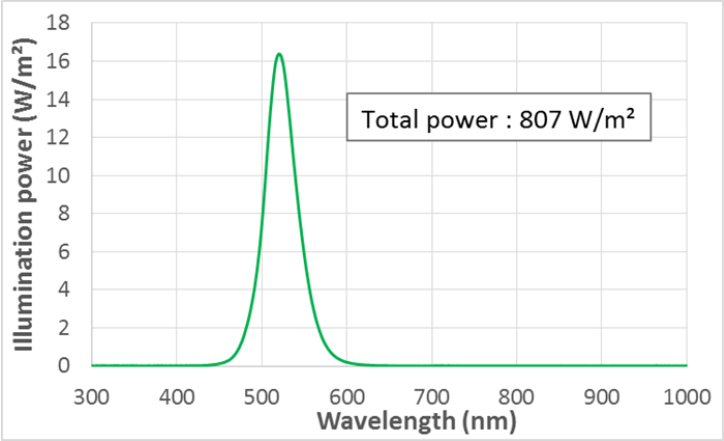

Figure 3.11: *Illumination power, at the samples position, of the LED arrays used in PL imaging experiments.*

A total illumination power, integrated over the 300 to 1000 nm range, of 807 $\pm$ 2 W/m^2 was found with a peak intensity of 16.4 W.m^{-2}.nm^{-1}, centered at 520 nm and a full width at half maximum of 43 nm. This allows a strong excitation of the P3HT:PCBM blend, leading to an intense response signal, and a sufficiently thin wavelength span to be cut by optical filters. Furthermore, according to pyranometer measurements, this illumination was found to be homogeneous on a 8x8 cm^2 area on the sample plate, giving a comfortable margin for positioning the samples for characterization.

Camera efficiency In order to image the luminescence emission, a 1024x1024 pixels^2 Si-CCD array was used. To allow focusing and exposition control, an objective with a high IR transmission and a diaphragm ring was used. The camera quantum efficiency (its photon to signal yield) multiplied by the objective transmission, which represents the total camera system efficiency, is plotted in Fig.3.12 from supplier data.

As one can see, Si-CCD arrays are better suited to detect radiation in the visible range than in the NIR/IR range.

Optical filters use and characterization Luminescence emission of OPV cells can be emitted from two sites: in the bulk material, as band-to-band (i.e. from the conduction band to the valence band of the donor) recombination, and at the interface between the donor and acceptor phases, as charge-transfer (CT) states recombination.
Both recombination types yield photons with different energies: the former is in the visible range between 600 and 850 nm (Fig.3.6) and the latter is located in the IR range with a band tail in the NIR range between 900 and 1000 nm (Fig.3.8a).

Using optical filters with relevant transmission wavelengths, one can spectrally select one emission source over another. Additionally, such filters are mandatory in order to suppress the

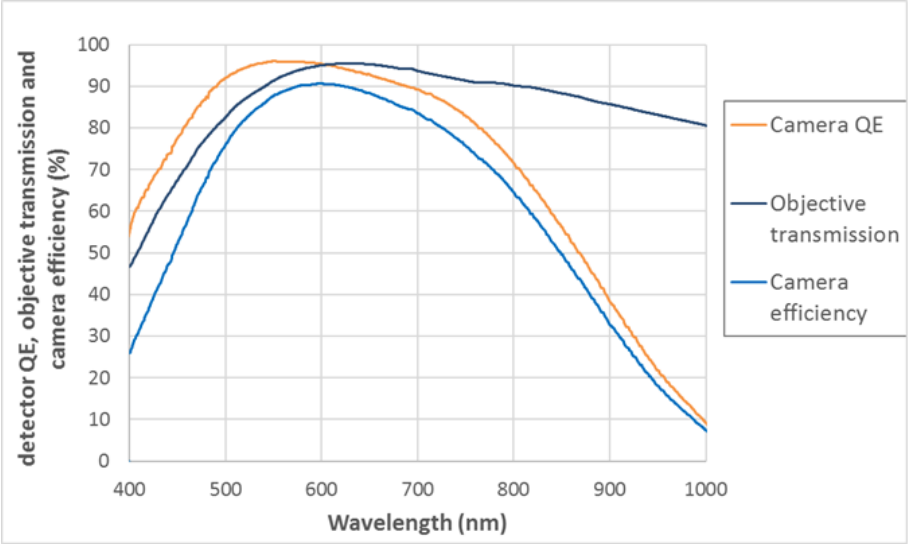

Figure 3.12: *Quantum efficiency of the Si-CCD array, objective transmission and camera total efficiency, defined as the product of both.*

excitation light detected by the camera during PL experiments.

In this work, two optical filters were used in order to separate each emission sites: a band-pass filter featuring a transmission wavelength centered at 700 nm and a 50 nm wide band, and a high-pass filter with a cut-off wavelength at 875 nm. Their absorption spectra, as well as the different emission they are expected to block or transmit are shown in Fig.3.13.

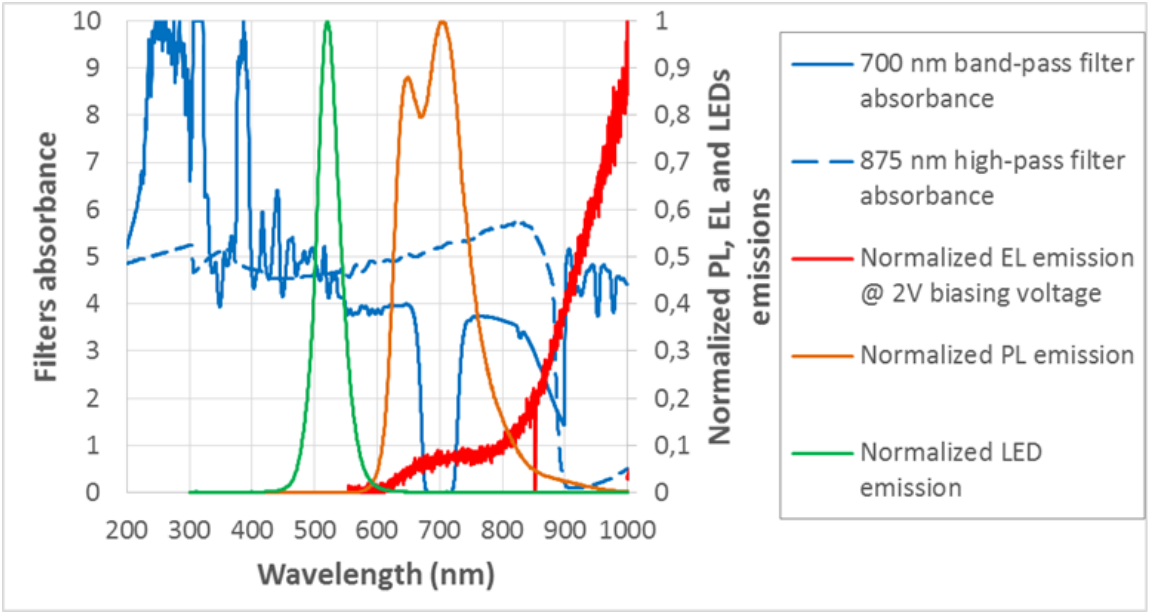

Figure 3.13: *Absorbance of the optical filters used in this work. Emission types they are expected to block or transmit are plotted as well.*

Both filters have a strong absorbance (at least 4) in the LED arrays emission wavelength range. It means that less than $1/10000^{th}$ of photons emitted from the excitation source in the blocking region of the filters are able to reach the detector. The band-pass filter features a high transmission at the 700 ± 22 nm wavelength and at least two orders of magnitude lowered transmission for wavelengths above 800 nm. It is therefore efficient to select the band-to-band radiation. The high-pass filter features a high absorption (at least 4) for wavelengths below 880

nm and a high transmission in the NIR range. It is thus used to isolate the CT emission.

From the product of the camera efficiency curve with the filters transmission spectra, overall detection efficiencies of the system, according to the chosen filters, can be calculated.

Figures 3.14 and 3.15 give a comprehensive overview of spectral data relevant to both electro- and photo-luminescence imaging experiments, respectively.

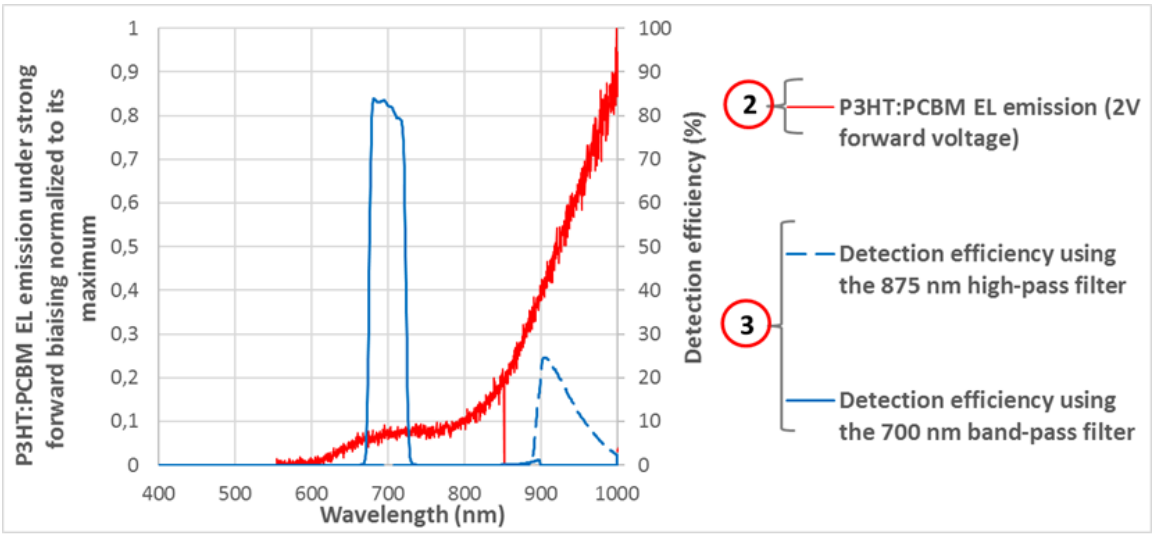

Figure 3.14: *Comprehensive spectral data relevant for electroluminescence experiments. EL emission of a P3HT:PCBM cell normalized to its maximum and detection efficiencies according to the chosen optical filter. The labels in red circles correspond to the experimental steps described above and in Fig.3.10.*

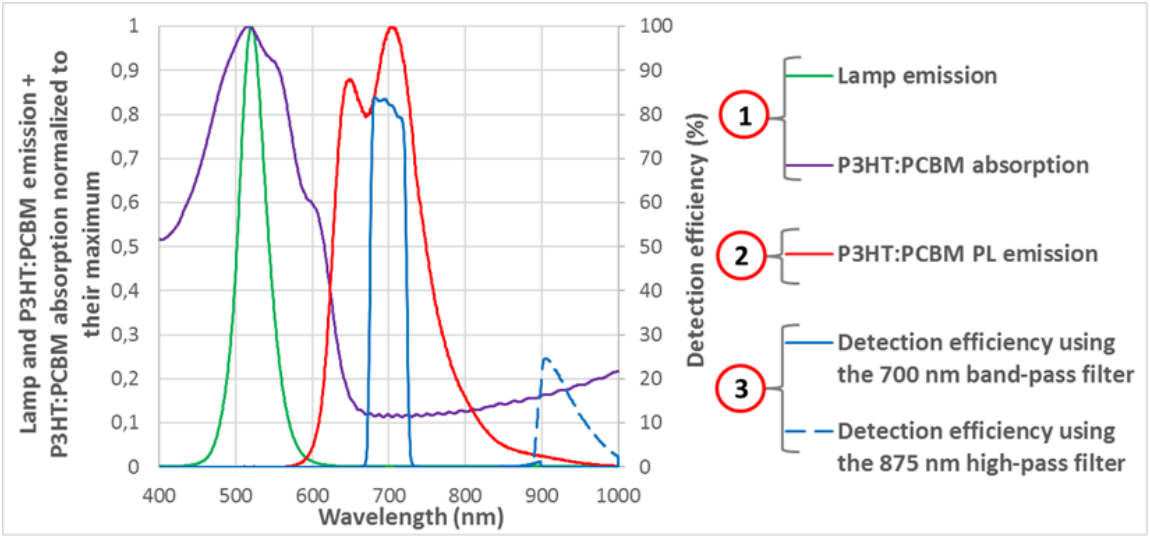

Figure 3.15: *Comprehensive spectral data relevant for photoluminescence experiments. Emission spectra of the LED arrays and a P3HT:PCBM cell and P3HT:PCBM absorption spectra, normalized to their maximum. Detection efficiencies curves of the imaging system according to the chosen optical filter. The labels in red circles correspond to the experimental steps described above and in Fig.3.10.*

From Fig.3.14, primary CT-state emission, occurring in the NIR range, is poorly detected by our system even when using the 875 nm high-pass filter. Practically, this constrains us to use long integration times when performing EL imaging experiments.

Secondary band-to-band emission, occurring at strong biasing voltages once all CT-states emission sites are saturated, can be observed with the 700 nm band-pass filter.

For PL imaging experiments, depicted in Fig.3.15, the good match between the excitation wavelength and the polymer absorption maximum leads to strong band-to-band luminescence emission which is also well matched to the system detection efficiency. CT-states emission, which has not been observed in any of our spectrally resolved experiments, is thought to be weaker than the band-to-band recombination spectral tail. We therefore think that PL images acquired with the 875 nm high-pass filter are primary band-to-band PL images.

Luminescence imaging protocol. We will detail here the protocol developed for photo-and electroluminescence imaging experiments.

In order to decrease the parasitic signal observed on images taken with Si-CCD devices, the sensor is set to 20 °C by the Peltier cooling system. For each image acquired, a background image, without excitation light or current, taken in the same experimental conditions is recorded. Excitation is then switched on and an image is acquired. The background image is then systematically subtracted to the latter.

1. The sample is placed flat on the sample plate and connected electrically to the source measure units. Keeping the sample immobile along different experiments allows for efficient and convenient comparisons of the output images.
2. PL images are taken (without caring about filters or acquisition parameters) in order to adjust focus of the camera by the objective's focusing ring.
3. An optical filter is chosen according to the type of radiation one would like to observe.
4. The experimental parameters, namely, the aperture of the objective, the acquisition time and the biasing voltage for EL experiments are roughly chosen according to our experience with the same kind of device.
5. Background and luminescence acquisitions are successively performed. According to the resulting output image, steps 4. and 5. can be repeated in order to correct under- or over-exposition.
6. Finally, 1024x1024 pixels^2 output images are saved under a loss-less 16-bits TIFF file format.

As a rule of thumb, PL images are usually taken in approximately one second with a minimal objective aperture and EL images are integrated over 60 seconds with a maximized aperture.

Calibration of the setup. As shown previously, depending on the radiation one would like to observe as well as the excitation method, the luminescence intensity can vary greatly between experiments. Therefore, in order to obtain quality images (i.e. without under- or over-exposition), the experimental protocol must be adapted for each experiment or, in the worst case, for each

sample.

Three experimental parameters are accessible to adapt the signal strength: the acquisition integration time, the objective aperture described by its f-number and the injection voltage or current in the case of EL experiments.

The influence of each experimental parameter on the perceived signal intensity was investigated. The aim of such studies is to be able to convert the raw images, dependent of the experimental measurement conditions, to comparable normalized images.

Integration time Fig.3.16 plots the mean PL emission from the active area of an OPV cell, calculated from images acquired with both filters, as a function of the experiment integration time.

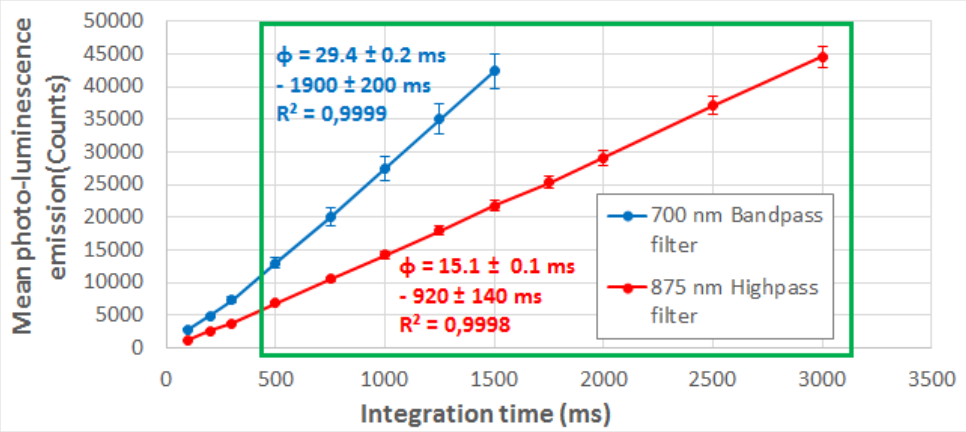

Figure 3.16: *Mean PL emission, integrated over 82 x 116 pixels^2 images taken with each optical filter, from an OPV cell as a function of the experimental integration time. Linear regressions were performed on the green square region above 500 ms integration times.*

The detected PL signal shows a linear dependence with respect to the integration time above 500 ms for both filters. The non-linear behavior below 500 ms integration times is related to the fact that the LED arrays take a short time to reach and leave their plateau intensity value. This offset time can be neglected for longer integration times.
Consequently, in this work, typical integration times used were between 750 and 2000 ms in the linear area.

Objective f-number The f-number of an objective is defined as the ratio between its focal distance to its entrance pupil diameter set by a diaphragm. As a consequence the number of photons received by the detector, proportional to the opened surface of the diaphragm, is inversely proportional to the square of the f-number.

Fig.3.17 plots the mean PL emission of the active area of an OPV cell, calculated from images acquired with both filters, as a function of the f-number.

Looking at the 875 nm high-pass filter data, one can see that the detected PL emission indeed follows an inverted quadratic rule to the f-number for f-numbers above 4. For lower f-numbers

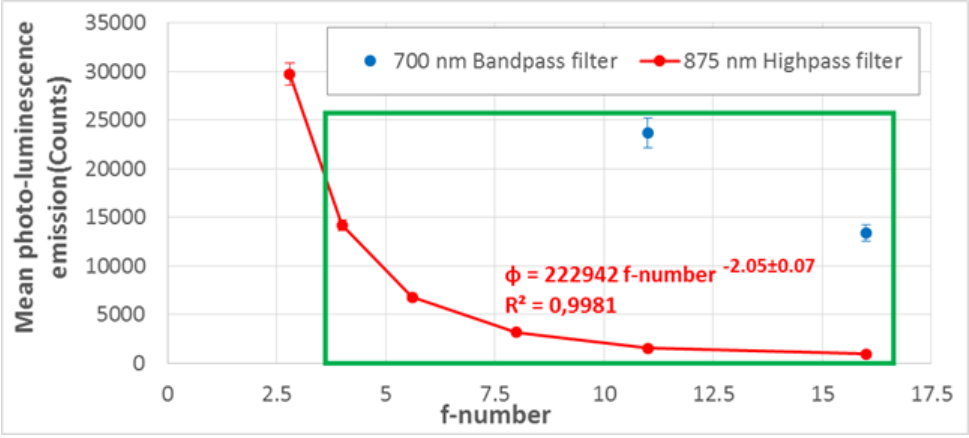

Figure 3.17: *Mean PL emission, integrated over 82 x 116 pixels^2 images taken with each optical filter, from an OPV cell as a function of the objective f-number. The square regressions was performed on the green square region above f numbers of 4.*

below 4, diffraction of the light tends to cause defocus, therefore such values are avoided if possible in this work.

Because images taken with the 700 nm band-pass filter, even with a minimal 500 ms integration time, were over-saturated with f-numbers below 11, we could not fit its behavior with this method. However, we can reasonably assume an inverted quadratic behavior as observed with the high-pass filter.

Biasing voltage For electroluminescence, as shown in Sec.1.4.2, in addition to the previous parameters, the biasing voltage directly plays a role on the detected luminescence intensity.
For ideal systems, the EL intensity is expected to increase exponentially in respect with the forward biasing voltage according to Eq. 1.14 [201, 203]. A voltage correction could thus be applied on EL images acquired from such systems.
However, for systems with non-radiative recombination channels, such as those made of P3HT:PCBM, deviations from this exponential law are observed [72]. The electro-luminescence emission intensity then follows Eq.3.1.

$$\Phi_{EL} \, \alpha \exp\left(\frac{V}{n.V_{th}}\right) \tag{3.1}$$

With Φ_{EL} the luminescence intensity, V the biasing voltage, n the cell ideality factor and V_{th} the thermal voltage, constant for a given temperature.

Deviation from the exponential law is related to the cell ideality factor [70]. This factor is possibly changing as a function of the aging of the cells. Therefore, because voltage alone cannot be sufficient to correct EL images along aging, quantitative comparison of the electro-luminescence images for different aging times is impossible.

In order to compare luminescence images acquired in different experimental conditions, a correction must be applied on the raw images. A corrected luminescence counts per second,

expressed in kilo-counts per second (kcts/s) assuming a unity f-number, can be calculated following Eq.3.2:

$$Counts_{corrrected} = Counts_{raw} * \frac{f^2}{t_{int}} \tag{3.2}$$

With $Counts_{corrected}$ the corrected luminescence counts number, $Counts_{raw}$ the raw grey level obtained directly after the experiments, f the actual f-number of the objective and t_{int} the integration time of the experiment in seconds. Such corrected grey level is proportional to the luminescence intensity by a constant detection factor. It is comparable for all images taken with the same optical filter and whatever the excitation conditions.
In this work, all presented luminescence images are implicitly corrected according to this calculation.

Conclusion: Photo- and electro-luminescence images. Electro- and photo-luminescence images bring several informations about the device state, resolved on the device surface.

Fig.3.18 shows four images taken with each excitation mode and each filter.

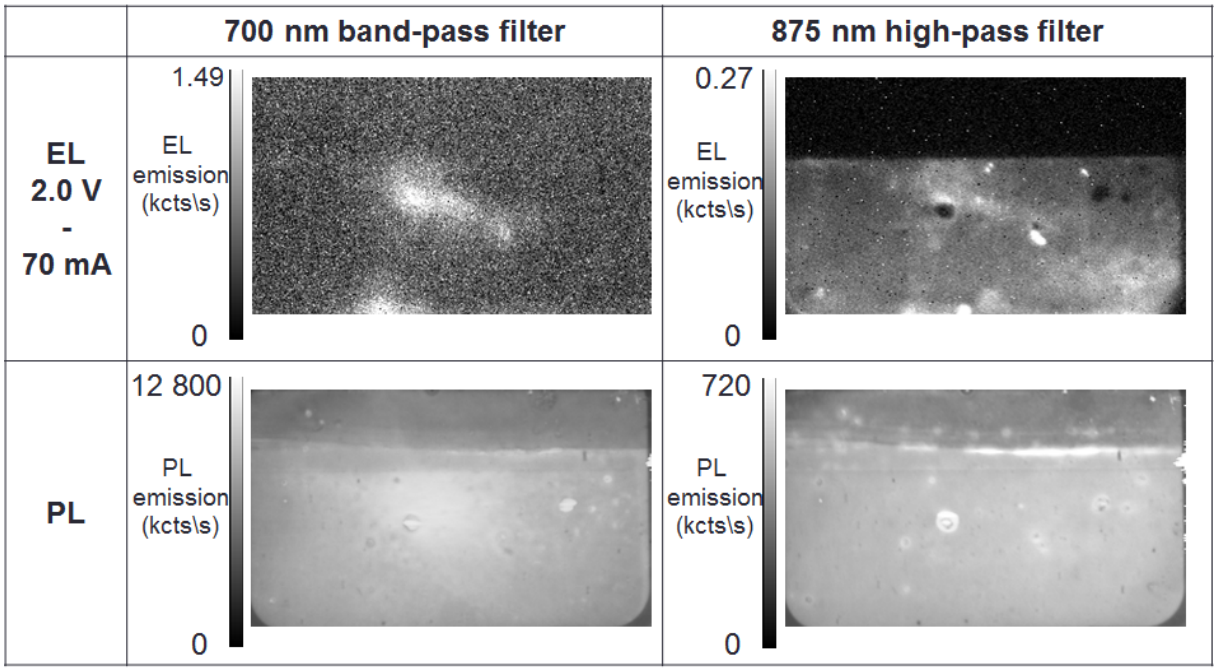

Figure 3.18: *PL and EL images taken with different filters.*

Electroluminescence, no matter which kind of recombination is observed, originates from the encounter in the active layer of two opposite charge carriers injected from the cell terminals. Thus, a dark spot on an EL image means that no carriers were injected on this place during the EL experiment. In contrast, a particularly bright spot means a strong recombination rate made possible by shunting. In conclusion, this technique is used in order to track transport issues on the active area of the cells.

On the EL image taken with the 875 nm high-pass filter, the detected luminescence signal is

relatively weak. Therefore, in order to obtain a usable output image, long integration times and strong excitation voltages must be applied.

In the visible region around 700 nm, electroluminescence is not significantly discerned from the noise. This suggests that, for this sample, low-energy interfacial CT states of this sample are not all filled at a 2 V bias voltage.

As seen on Fig. 3.8a, band-to-band (B2B) recombination mechanisms can take place at high biasing voltages. In order to isolate the primary CT emission alone, the 875 nm high-pass filter has been used on all EL imaging experiments presented in this work. In addition, biasing voltages were kept as low as possible. To this end, EL images were acquired iteratively with a gradually increasing voltage until an exploitable image was obtained.

Photoluminescence in contrast originates from the recombination of charge carriers within the active layer after their generation in the same layer from absorbed photons. Consequently, luminescence is emitted as long as the active layer absorbs light.

From the study of the PL spectra in Fig.3.6 we assume that only the bulk band to band recombination within the P3HT of the active layer is observed with both filters. Brighter localized spots on images taken with the 875 nm high-pass filters likely correspond to undissolved PCBM aggregates which emit at higher wavelengths than P3HT, as shown in Fig.3.6.

The images taken with the 700 nm band-pass filter yield significantly more signal than those taken with the 875 nm high-pass filter. This is explained by the stronger overlap between the 700 nm band-pass filter passing region and the emitted B2B luminescence. The 875 nm high-pass filter only allows passing of the band-tail of the B2B recombination. CT has never been observed in spectrally resolved experiments and is therefore expected to be negligible.

The excitation light, as well as the luminescence itself, can be reflected on the back metal electrode, yielding a higher signal than in regions without.

Furthermore, despite the high absorbance of the optical filters used in PL imaging experiments, a fraction of the excitation light can be reflected on some reflective surfaces and observed by the camera. This is particularly true when the 700 nm band-pass filter, which passing region is closer to the peak wavelength of the excitation light, is used. In order to limit the influence of excitation light reflection on the resulting PL images, we will only present images acquired with the 875 nm high-pass filter. However, images were systematically taken with both filters in order to confirm the observed results.

3.1.3 Voltage-biased photoluminescence imaging (vbPLI)

For practical use, electroluminescence suffers from several drawbacks strongly limiting its usefulness. In response, we developed a method yielding similar results based on voltage-biased photoluminescence (vbPL) imaging. In a first place, the main limitations we encountered when we experimented with EL imaging are presented. To our knowledge, such issues are scarcely discussed in the literature. Secondly, the influence of the biasing voltage on the cells PL is investigated with spectrally resolved data. Finally, the vbPL imaging protocol is detailed and images obtained from several techniques are compared and discussed.

Electroluminescence imaging limitations. As discussed previously, due to the weak detection efficiency of the Si-CCD camera towards electroluminescnence emission, as shown in Fig.3.14 and Fig.3.18, EL imaging experimental parameters must be adjusted in order to obtain usable images.

After maximizing the objective aperture, two means are left to increase the intensity of the images: the integration time and the injection voltage.
Relatively long integration times of 60 seconds were chosen for all EL experiments.
In order to limit the possibility to observe B2B recombinations, biasing voltages were kept as low as possible. However, even at low biasing voltages, long EL imaging experiments can significantly damage the samples.

Fig.3.19 shows two LBIC images of the same cell taken shortly before and after a routine EL imaging experiment. EL acquisition was made for 60 seconds at 1.2 V injecting a mean 60 mA current. The resulting EL image is shown on the right.

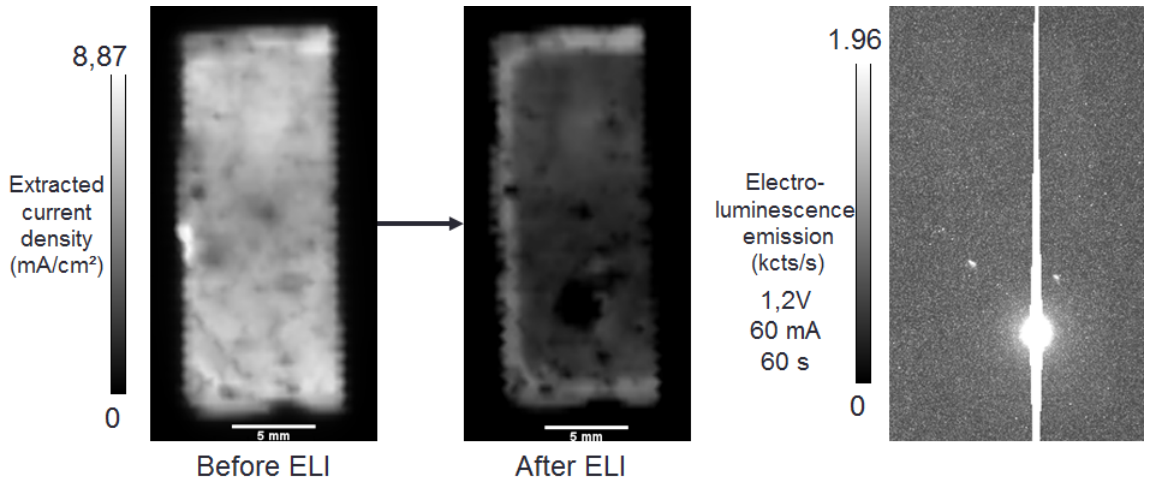

Figure 3.19: *(left) LBIC images of an OPV cell before and after electro-luminescence imaging. ELI was carried out at a 1.2 V forward voltage yielding a 60 mA current injection for one minute of integration. (right) Corresponding resulting EL image.*

From the LBIC images, one can see that the cell has been severely damaged by the EL imaging experiment. Furthermore, EL imaging also yielded very poor information on the device, except a very bright spot in its center. Injected charges flow through the less resistive path of the cell. If such less-resistive path happens to be a localized shunt, a significant part of the total current will be injected through this small region. According to calculations made with the method developed by Seeland *et al.* [211], this injection can be up to several amps/cm^2 for 60s; this heats up the cell to such temperatures that even the PET substrate melts, which was effectively observed.

To limit such damage, several solutions can be found in the literature : the use of lock-in techniques [216], allowing for a better signal to noise ratio for similar excitation conditions, or the use of a more infrared sensitive Indium-Gallium-Arsenide camera would allow for images to be acquired at lower biasing voltages and acquisition times, expected to be less harmful.

In addition to damaging the samples during the experiments, the injection regime can be troublesome for obtaining images of the whole cell area. Charge carriers injected in the device follow the less-resistive path to the active layer. Therefore, depending on the electrical resistance distribution within the devices, there are some cases where it is impossible to obtain a complete EL image of the cells active area. Two distinct electrical series resistances are to be considered : the first one, called "$R_{S\ Stack}$", through the cell thickness, composed of the contact and bulk resistance of the OPV stack and the second one, crossing the cell laterally originating from the transparent electrode layer called "$R_{S\ TCO}$". The dominant series resistance will define where the charge carriers are injected and drastically influences the output EL image. Fig.3.20a represents both series resistance types on the cross section of a device. Fig 3.20b shows EL images and J(V) curves of a $R_{S\ Stack}$ dominated cell in blue and a $R_{S\ TCO}$ dominated sample in red.

On the TCO series resistance dominated red cell, the EL image only shows the border between the TCO and silver electrodes. On the stack series resistance dominated blue cell, the whole active surface is probed and a high throughput image is obtained. In both cells, the TCO series resistance is expected to be the same. In the red cell, the stack series resistance (through the thickness of ETL, AL and HTL) is lower than the TCO lateral resistance, therefore all the injected charges follow this path instead of scattering on the device active area. In contrast, in the blue cell, the stack resistance is higher than the TCO resistance, the charges then scatter in the transparent electrode across the whole active area before recombining in the active layer. Due to the high overall series resistance of the blue cell, a higher voltage is needed in order to inject the same current as in the red cell. Such issues do not allow us to characterize low stack series resistance devices. In addition, a localized injection is expected to damage the cells more than a distributed one.

The case of shunted cells also causes a similar issue as the injected charges will preferentially flow through the localized shunt instead of scattering on the device surface.

Potential degradation of the samples added to the inability of imaging all the devices make the electroluminescence imaging technique an inconvenient technique for investigating the devices properties at several times of their processing or aging. As a response to these issues, we developed a voltage-biased photoluminescence (vbPL) imaging technique allowing us to gain insight into the cells charge transport abilities without degrading them.

Working principle of the voltage-biased photoluminescence imaging technique. Compared to EL images, PL images are much faster to acquire and do not induce degradation of the samples. We thus looked for a way to make it yield information on the charge extraction process by connecting the cells terminals to collect the photo-generated charges.

Fig.3.21 shows PL spectra of a single cell taken under various biasing voltages.

One can see that the main emission process originates from band-to-band recombination from 650 to 800 nm. Such PL emission decreases as a function of the forward bias voltage. This cannot be confounded with EL-type CT recombination : for biasing voltages below V_{OC} ($\approx$ 550

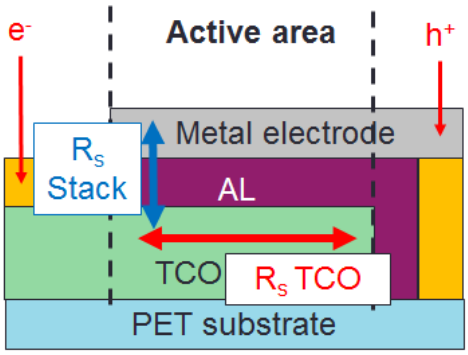

(a)

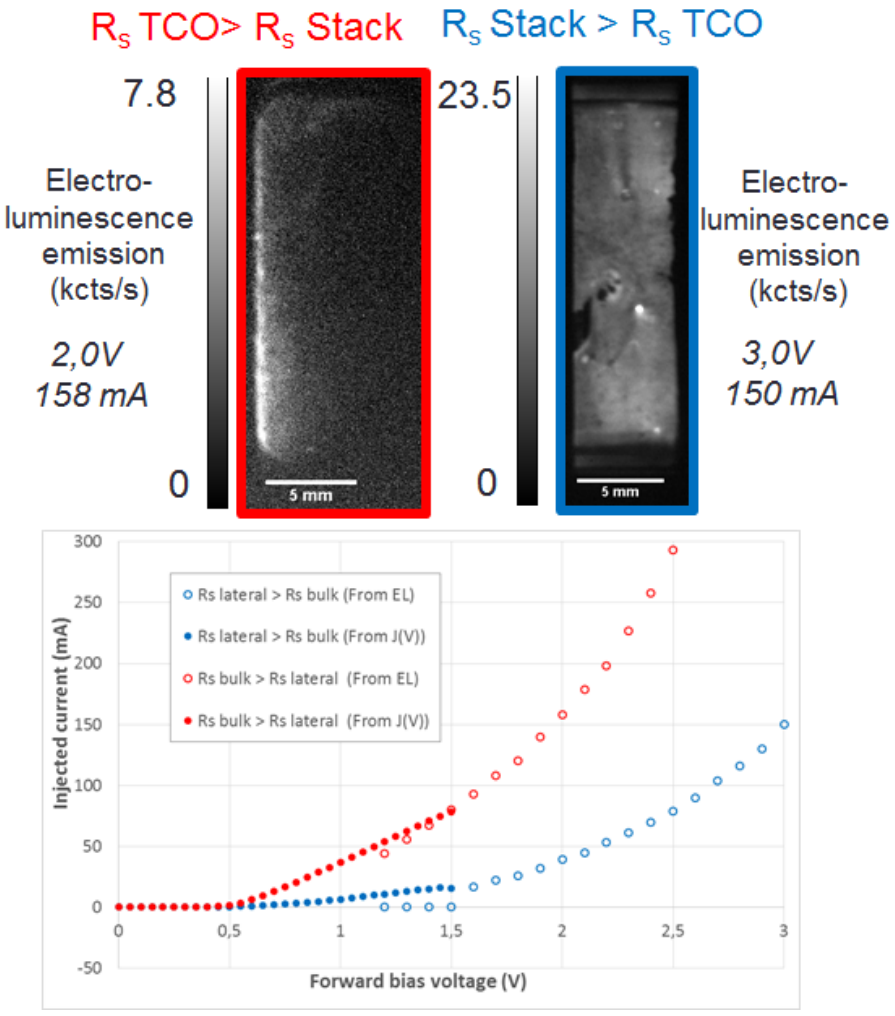

(b)

Figure 3.20: *(a) Scheme of an OPV solar cell during EL experiment. Electrons are injected in the transparent conductive electrode and holes are injected to the metal electrode. The injected charges then follow the path with the lowest resistance : either the series resistance from the stack ($R_{S\ Stack}$) or the lateral series resistance induced by the transparent electrode ($R_{S\ TCO}$). (b) Electroluminescence images filtered with the 875 nm high-pass filter of two different cells and their associated J(V) curves in the injection regime. J(V) data were obtained either from classical J(V) measurements in the dark or from current measurements performed during the EL imaging experiments. From linear regressions between 0.8 V to 1.3 V, the blue cell calculated total Rs is ($\approx 25\ \Omega.cm^{-2}$) cell and the red cell total Rs is ($\approx 126\ \Omega.cm^{-2}$)*

mV), injected charges do not have sufficient energy to populate the CT states. This is confirmed by the spectral data as only the spectrum taken at 2.5 V forward bias voltage exhibits significant

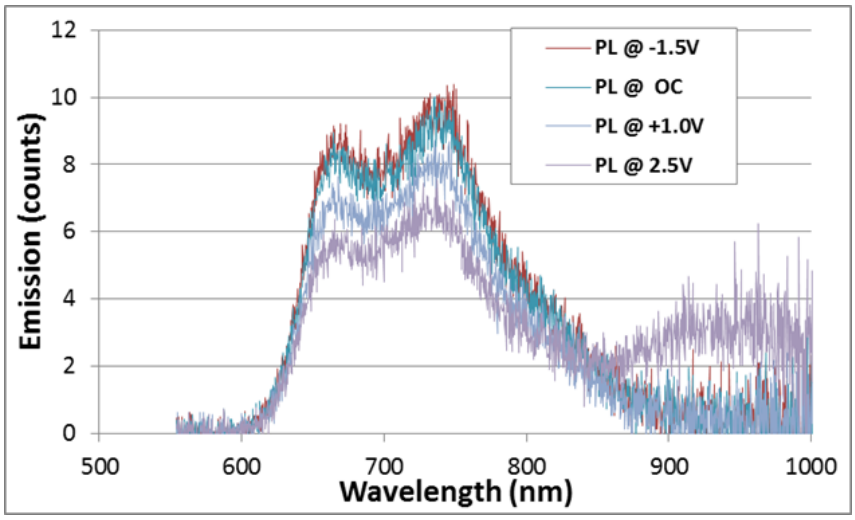

Figure 3.21: *Luminescence spectra of a P3HT:PCBM cell under excitation of a 532 nm monochromatic green laser at different biasing voltages.*

luminescence increase above 900 nm.

Regarding imaging, comparing two images taken at different bias voltages should allow us to spot where luminescence emission changed and therefore where a bias voltage has been applied. Similarly to EL imaging, this allows us to investigate which areas of the cells are connected to its terminals.

In the literature, band-to-band PL emission is generally described as decreasing when a bias voltage is applied, whether in forward or reverse polarity [37, 205]. This is commonly interpreted as the influence of the applied electric field which participates in the exciton dissociation process and therefore lowers the recombination (i.e. PL emission) rate.

π-conjugated polymers, and in particular P3HT, are generally accepted to have a significant charge defect density ($\approx 10^{16} - 10^{17}\ cm^{-3}$) doping their conductivity [213, 256]. Among doping species, charge carriers have been shown to be able to quench excitons [212] thus decreasing the PL emission intensity. Upon application of a reverse voltage bias, the photo-generated charge carriers are swept out of the cell. This may explain the increase of PL when charge carriers are extracted by a reverse bias voltage.

vbPL imaging experimental protocol. The experimental setup is the same for a biased PL imaging experiment as for classic OC photoluminescence imaging.
Biased photoluminescence images are obtained according the following protocol:

1. The sample is placed on the sample holder and its terminal are wired to the external Keithley source measure unit. The focus and exposition of the sample are set according to the protocol presented in Sec. 3.1.2.
2. A reference image first is taken.
   The sample is kept in open-circuit conditions, i.e. without current injection or extraction,

and a classic OC PL image is acquired. It is obtained from a background image taken without illumination subtracted to the illuminated image taken in the same conditions.

3. A voltage biased image is then acquired.
   The sample is biased under a reverse bias voltage. A background image is taken with this voltage bias on. This background thus consists of a typical reverse bias EL image. Unless the cells are strongly shunted, few charges are injected into the cell and the background image appears completely dark. Such background image is then subtracted to the illuminated image, still under voltage bias.

4. Finally, the voltage-biased PL image is compared to the reference open-circuit PL image. This is achieved with the imageJ freeware by dividing the biased image by the OC PL one. The resulting image, called in this work the vbPL image, is then thresholded between 1.00 (i.e. no difference between the two images) and a superior to one value representing the maximum relative intensity difference observed between the biased and OC images.

In this work, comparisons between OC and reverse bias images were interpreted in terms of charge extraction. Bright areas correspond to areas where photo-generated charges were extracted from the cell by the contacts.

Images made from comparison between a reverse and a forward bias are better defined due to the increased difference in excitation conditions, but the interpretation can only be made in terms of applied potential, with both injection and extraction modes superimposing. In that case, the conclusion on charge extraction is not straightforward.

Study of degradation by several complementary imaging characterization. Fig.3.22 shows the LBIC, classic PL (i.e. in open-circuit conditions), EL and voltage-biased PL images of the same cell. The 875 nm high-pass filter was used for all luminescence imaging experiments.

The presented cell corresponds to the cell degraded by ELI in Fig.3.19. This first EL imaging experiment made the PET substrate melt in the red circled area and decreased the short circuit current output of the cell in its active area covered by silver.

The LBIC image shows a large non-working area in the center of its active area, circled in red, corresponding to the melted PET and a relatively well-functioning area on its borders, corresponding to the PEDOT:PSS area without silver on it.

From the OC PL image, we can see that the active layer itself seems not to be damaged. The dark areas on the LBIC image are barely visible on the PL image. We ascribe such slight contrast to a small loss of reflexion due to the PET melting rather than an active layer degradation.

The -1V vbPL image shows that current extraction is impeded in the melted PET area. Other dark areas, in agreement with the LBIC image, are shown to suffer similar issues. The dark spots observed on the biased PL image appear smaller than on the LBIC image.

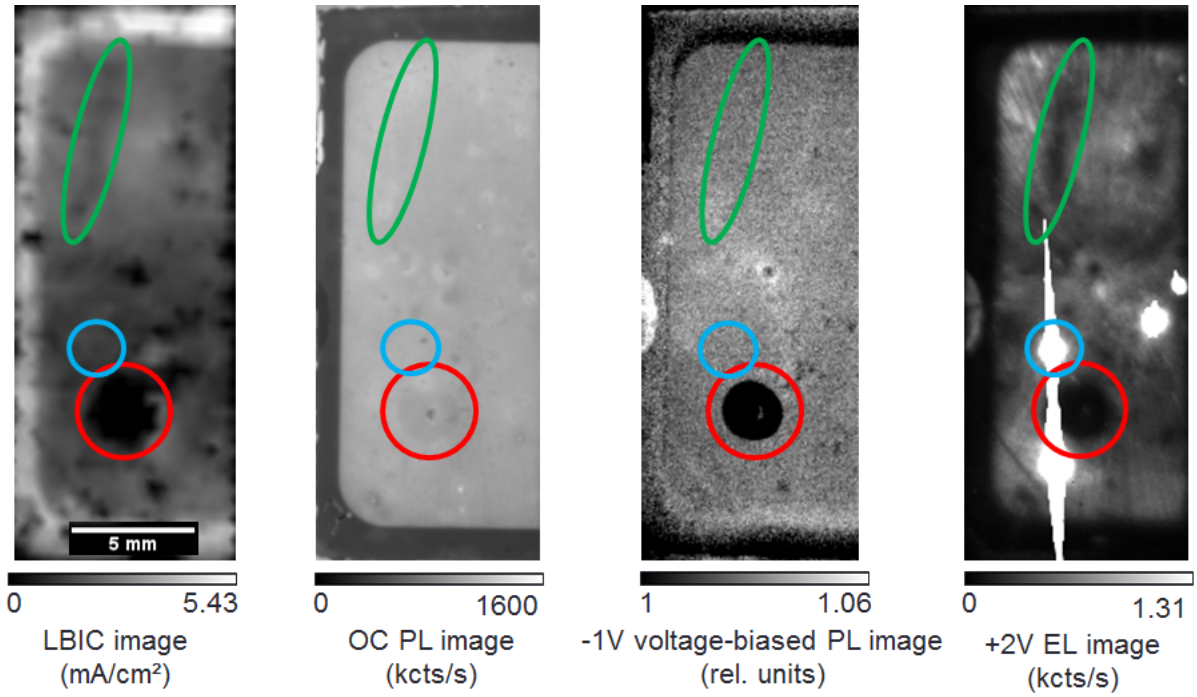

Figure 3.22: *From left to right: LBIC, OC PL, voltage biased PL and EL images of the same cell. Experiments have been performed from left to right in chronological order. The 875 nm high-pass filter was used for all luminescence imaging experiments.*

The EL image, taken after the other characterizations, yields more contrasted images. It shows that charge carriers injection is prevented as well in the red circled region. However, compared to the biased PL image, it is less resolved due to the maximized aperture of the objective. A rod-shaped area, circled in green, displays decreased injected current. It is in agreement with the LBIC image where this pattern is barely visible. However, this pattern is unseen on the biased PL image. This suggests that a local energetic barrier is effective at +2 V bias voltage and in short-circuit condition and completely overcame at -1 V bias voltage. Several strongly bright spots can be observed. These are interpreted as increased recombination spots originating from local shunting. Although some can be correlated to the other images, the bright spot circled in blue is visible only on the EL image. We thus think that this shunt has been formed during the last EL experiment. Finally, the HTL border, shown to extract current on the LBIC and voltage biased PL images, is not apparent on the EL image. This is due to the limited conductivity of PEDOT:PSS compared to the neighboring silver electrode.

Fig.3.23 summarizes the advantages and drawbacks of each imaging methods we developed and used in this work.

With LBIC characterizations, we are able to localize defects limiting the global output of our cells. These defects can be further investigated by luminescence imaging.

Photoluminescence imaging (PLI), in its classic use in open-circuit conditions, is a method allowing us to selectively probe the status of the active layer. Its evolution over time or processing gives us an indication on its morphology and a complete extinction of the PL signal results from its complete degradation.

Electroluminescence imaging (ELI) can yield insight into the carrier injection to the active layer. However, we have shown that this characterization can be destructive toward the probed

Imaging technique	Quantified signal	Local property probed	Acquisition time	Assets & Liabilities
LBIC	Extracted short-circuit current density	Whole PV mechanism	≈ 20 minutes	+ Low interpretation required +Non-destructive - Long acquisition times - No discrimination of degradation mechanisms
Classical OC PLI	B2B recombination intensity	Active layer absorption and morphology	≈ 1 second	+ Fast +Non-destructive - Optical defects (Scratches, electrode reflexion…) can pollute the data
Voltage-biased PLI	B2B recombination intensity difference once under biasing	Charge extraction ability	≈ 2 seconds	+Fast +Non-destructive - Precise working principle yet to be understood
ELI	CT recombination intensity	Charge injection ability	60 seconds	- Potential samples degradation - Can not be used on all samples - Probes injection mechanisms (not directly relevant for PV operation)

Figure 3.23: *Recapitulative table of the imaging characterizations used in this work.*

sample. As a replacement, we developed a voltage-biased photoluminescence imaging (bPLI) method. This technique, brings valuable information on the charge extraction from the active layer to the contacts without degrading the samples. This technique, although its exact working principle is yet to be understood, is expected to be usable for all active materials whose PL emission is influenced by a biasing voltage. In this work, it will be used routinely instead of ELI if possible. ELI will still be performed as a destructive characterization in order to confirm the patterns observed by vbPLI.

During this work, these imaging techniques were used routinely in various contexts, for the study of fabrication and encapsulation processes until the aging of complete organic solar cells.

3.2 Mechanical properties of OPV devices

One of the most critical assets expected from thin film PV technologies and in particular OPV is the flexibility of the devices. Such flexibility allows a wide range of new applications and enables the roll-to-roll production of the devices. To enable flexible OPV devices, a first step is to make sure that a good adhesion binds all the layers together.
Adhesion measurement techniques are widely spread in a number of engineering fields. However, such characterizations may be unsuitable when applied to thin-film, multi-layered devices. Most of them yield at best semi-quantitative results and the more precise techniques need to bind additional layers to the samples prior to characterization which may bias the measurement results. We developed a simple peeling test method suitable for testing flexible encapsulated OPVs,

leading to comparatively quantitative results, which does not need any additional preparation step prior to peeling. We tested the limitations and the reproducibility of the characterization and developed a method in order to attribute the measured peeling strength to each interface of the devices.

3.2.1 Mechanical characterization

In order to study the mechanical resilience of OPV devices, we chose to perform 180° peel tests (also known as T-peel tests) as a fast and simple method, only requiring a traction bench, to perform comparative characterizations of flexible OPV samples. To avoid any bias introduced by sample preparation methods (gluing and subsequent curing of rigid arms, notching of the samples...) such as those used in several other characterization techniques, we decided to use both sides of the devices' encapsulation systems themselves as peeling arms. As a consequence, this characterization reflects the mechanical properties of samples as close as possible to real-life modules, under a mix of shearing and normal stresses inherent to the peeling method.

Samples design. 50x50 mm^2 partial or complete OPV devices were fabricated on 100x50 mm^2 flexible PET substrates according to the same layers deposition protocols as described previously. Large substrates were laminated on rigid aluminum plates in order to avoid bending during spin coating. In order to simulate the metal electrodes' comb geometry seen on some large area devices [257–259], two stripes of 15x50 mm^2 electrodes were deposited, separated by a 10x50 mm^2 gap without electrode materials. This allows us to study the influence over statistically-relevant large areas of the relatively rigid metal electrodes on the mechanical properties. Geometry of the samples at this step of fabrication is shown on Fig.3.24.

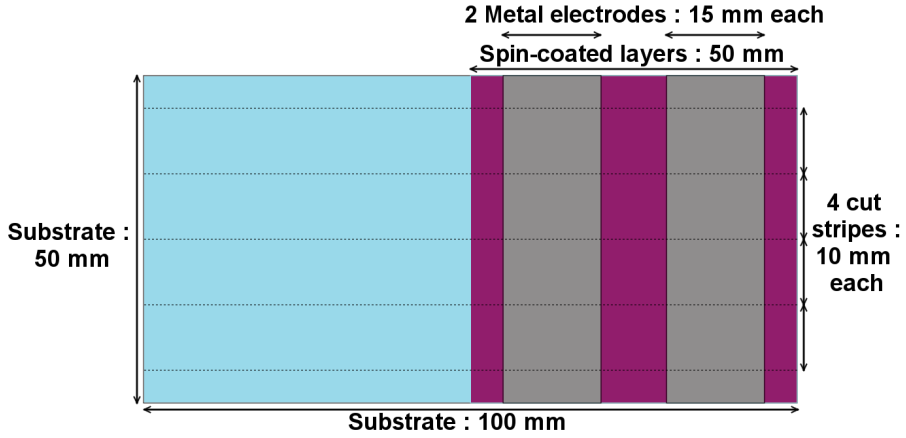

Figure 3.24: *Top-view of a module from which are cut peeling samples.*

The outer lateral 5 mm of the modules were then excluded in order to prevent any edge effects occurring during spin coating of large areas. Four 10x100 mm^2 stripes were then cut from each substrate with a razor blade. The four stripes were finally encapsulated separately according to the same processes as described in Sec.2.3.2 with a 5 mm rim around them. Cutting of the samples had to be performed prior to encapsulation in order to prevent any mechanical degradation. Each side of the encapsulation system constitutes the two peeling arms required

for testing. In order to easily separate the peeling arms, a non-adhesive foil (baking paper) was placed between each arm prior to encapsulation. A cross-section of the samples ready for testing is displayed in Fig. 3.25a. A photograph of such sample once loaded in the traction apparatus is shown in Fig.3.25b.

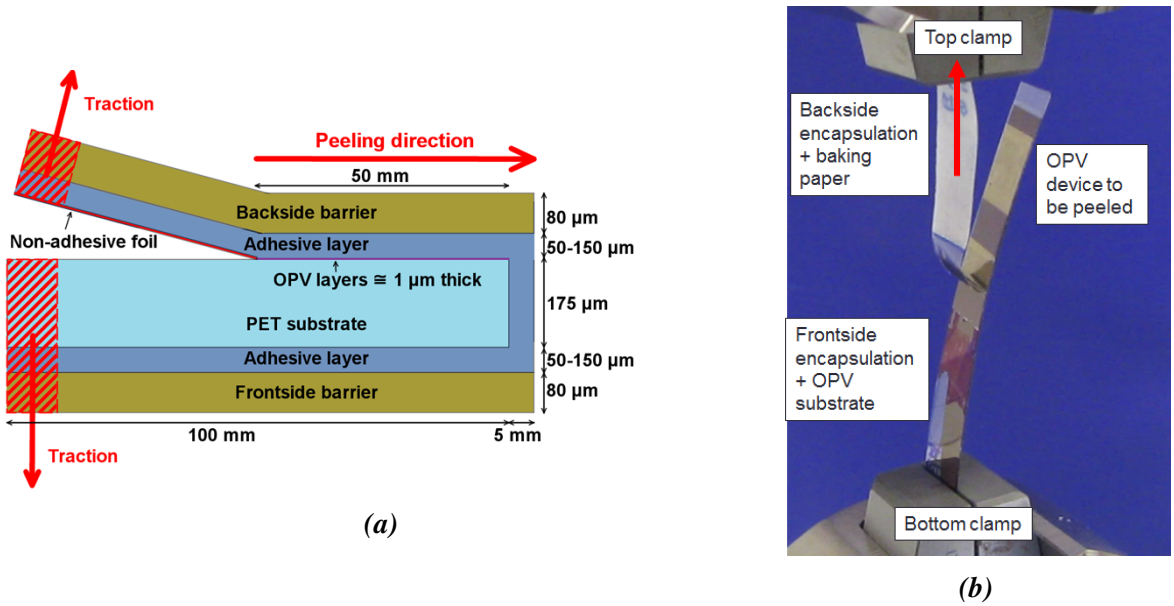

Figure 3.25: *(a) Cross-section of an encapsulated peeling stripe ready for testing. Scale of the thicknesses is respected. (b) Photography of a peeling sample loaded into the equipment prior to testing. Each arm of the OPV sample is loaded into each clamp. During the peeling tests, the top clamp moves away inducing the traction force required to peel off the sample.*

At this point, samples could be characterized immediately or aged in conditions representative of those applied to standard cells.

Peeling test. Prior to mechanical testing, the encapsulation rim around the samples was carefully removed with a razor blade. The 10x10 mm^2 extremities of each peeling arms were loaded into a Shimadzu AGS-X traction bench according to Fig. 3.25a. 180° peeling was achieved at a constant displacement-rate of 100 mm per minute. During the test, the strength applied to the traction arms of the sample was recorded as a function of their displacement.

Fig.3.26 displays typical peeling curves represented above their corresponding device's cross-section.

This is our complete reference device; its complete characterization is given as an example to illustrate the whole characterization methodology which was developed and then applied routinely on all samples tested in this work.

On such peeling strength versus displacement curve, a focus is made on three main areas: the two areas including metal electrodes, between 5-20 mm and 30-45 mm of peeling displacement respectively and the 20-30 mm gap area between them. To avoid any edge effects which may occur during spin-coating or encapsulation, the 0-5 mm and the 45-50 mm outer areas of the samples will not be studied.

The measured peeling force is systematically normalized by the samples width yielding peeling strengths in N/cm. In each of the three areas, data acquired in the two outer mm is

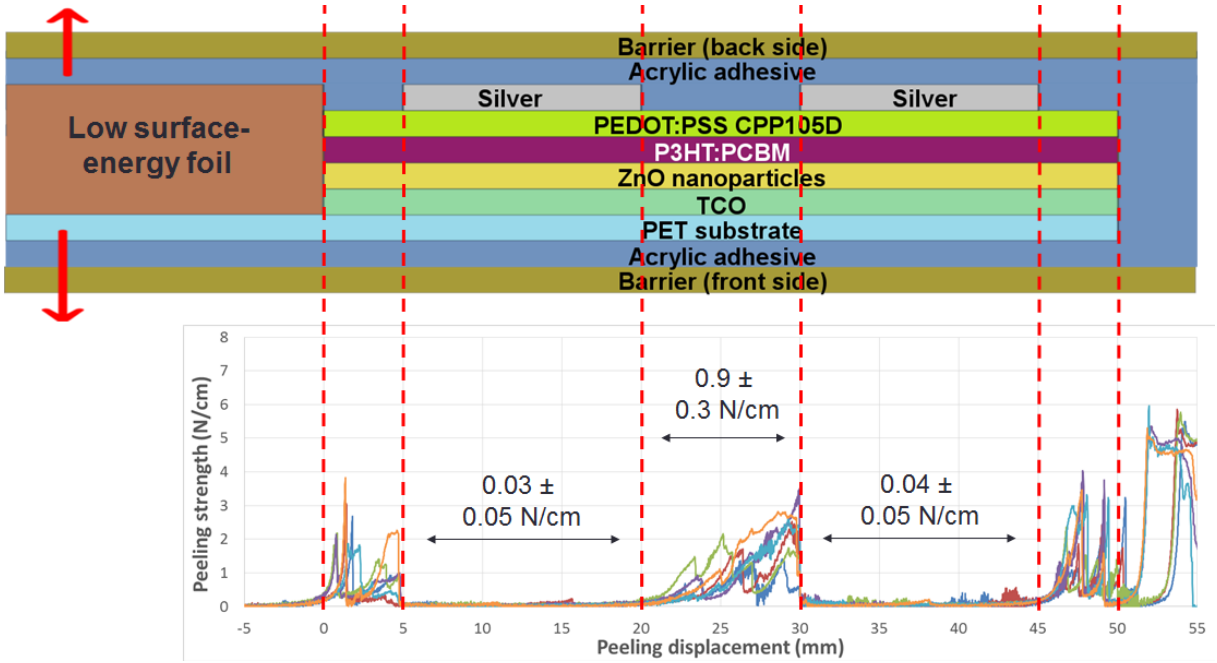

Figure 3.26: *Cross section of our reference OPV sample encapsulated according to the standard acrylic adhesive process and six corresponding peeling curves. Peeling strength are normalized by the samples width.*

rejected in order to avoid edge effects. The mean peeling strength and the standard error are then extracted. To give an overview of the data dispersion, the minimum, the first three quartiles and maximum recorded values are shown in box plots if necessary.

The setup absolute error was investigated with calibrated weights and estimated to be less than 0.05 N. Uncertainties are thus given as the highest value between the setup absolute error or the statistical error over at least four stripes with a 95% confidence assuming a Student's-t distribution [260] of the measured data. Peeling-strengths averaged over the relatively large areas tested on each stripe yield relatively low relative errors between similar samples, allowing us to make a relatively small number of samples, at least four per tested architecture, as compared to other studies [174].

In Fig.3.26, the peeling strength of the stack in the three areas from left to right, averaged over 7-18, 22-28 and 32-43 mm, respectively, is 0.03 ± 0.05, 0.9 ± 0.3 and 0.04 ± 0.05 N/cm, respectively.

3.2.2 Rupture path characterization

During the peeling test, rupture occurs either adhesively at the weakest interface or cohesively within the weakest layer of the whole stack, therefore, the measured peeling strength is only representative for a single rupture in the studied sample while the other unpeeled interfaces are necessarily stronger than the peeled one. It is therefore necessary to know where the rupture occurred in the studied stack in order to attribute the measured peeling strength to the corresponding weakest region.

After peeling, the samples are divided in two stripes: the "front arm" including at least the front barrier, the front adhesive and the PET substrate and the "back arm" including at least the

back barrier.

In this work, we did not perform time-consuming or complex surface (less than 10 nanometer deep) characterizations. Using only characterizations which probe micrometer-deep in the samples, we can confirm the presence of each layer on each side of the debonded surfaces and then deduce the rupture path. In the following, and in each case, analyses are performed on the internal side of the arms (i.e. the side which was previously bonded).

In this section, all the provided figures are actual characterizations made on the reference sample presented in Fig. 3.26.

- As a first step, visual observation and pictures inform us on the location of the metal opaque electrodes. This can guide us in our choice of further characterizations.
- In some cases, the metal electrodes are still on the front arm after debonding. It means that rupture occurred within the encapsulation system or at its interface with the OPV device. Fourier-transform infrared spectroscopy in ATR mode (analyzing thicknesses in the micrometer range [261]) is then performed in order to investigate the nature, cohesive or adhesive, of the rupture.

  Fig.3.27 shows an example of FTIR investigation performed on a sample with a simplified stack which visibly ruptured outside the OPV stack. The aim of this study is to determine if the rupture occurred cohesively within the pressure sensitive adhesive (PSA) layer or adhesively at the Ag / PSA or PSA / barrier interface.
  This sample is not a standard sample. Its simplified stack was studied in order to assess the HTL / Ag interface peeling strength.

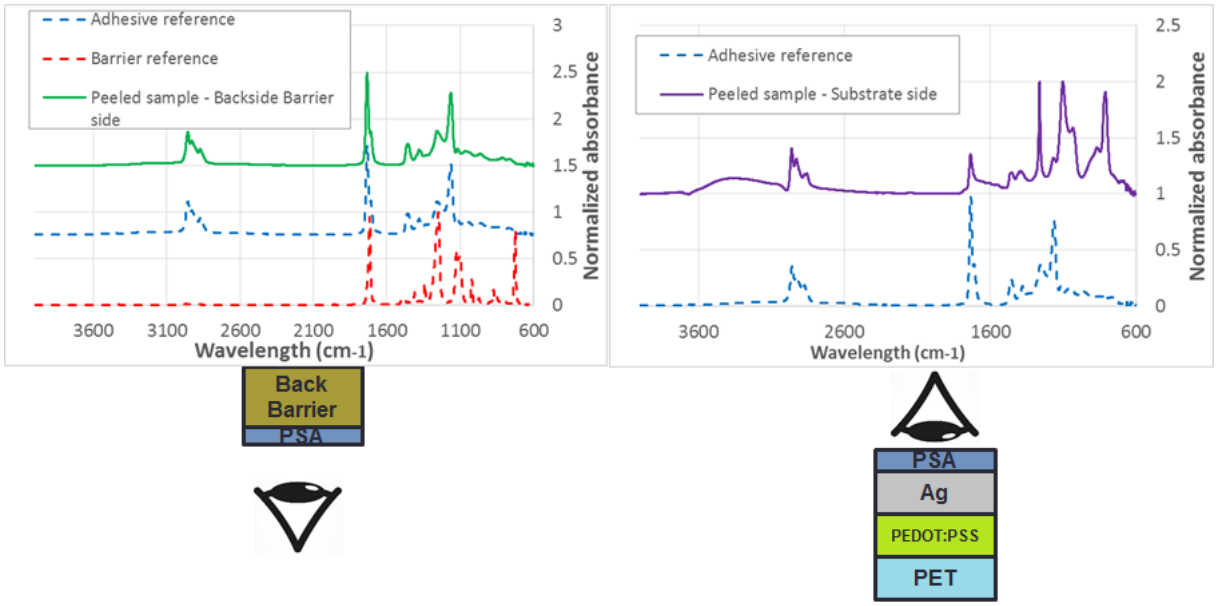

Figure 3.27: *Fourier-transform infrared spectra performed on both sides of a peeled sample. Left spectrum is acquired on the peeled backside barrier side and the right one on the peeled substrate side.*

The FTIR spectrum acquired on the peeled barrier side is perfectly matched with a reference PSA spectrum acquired alone. No characteristic barrier bands are observed suggesting rupture occurred a few µm away from the PSA / barrier interface.
On the spectrum acquired on the peeled substrate side, characteristic bands of the PSA

reference can be recognized, suggesting rupture occurred cohesively within the PSA layer.

– Photoluminescence imaging, initially developed for other purposes in this work, can unambiguously detect a twenty nanometer thick active layer on the whole debonded sample in a few seconds. Therefore, PL imaging can detect cohesive rupture within the active layer if it occurred at least 20 nm far from the interfaces with other materials.
Fig.3.28 shows a PL image of both peeled surfaces of our reference device.

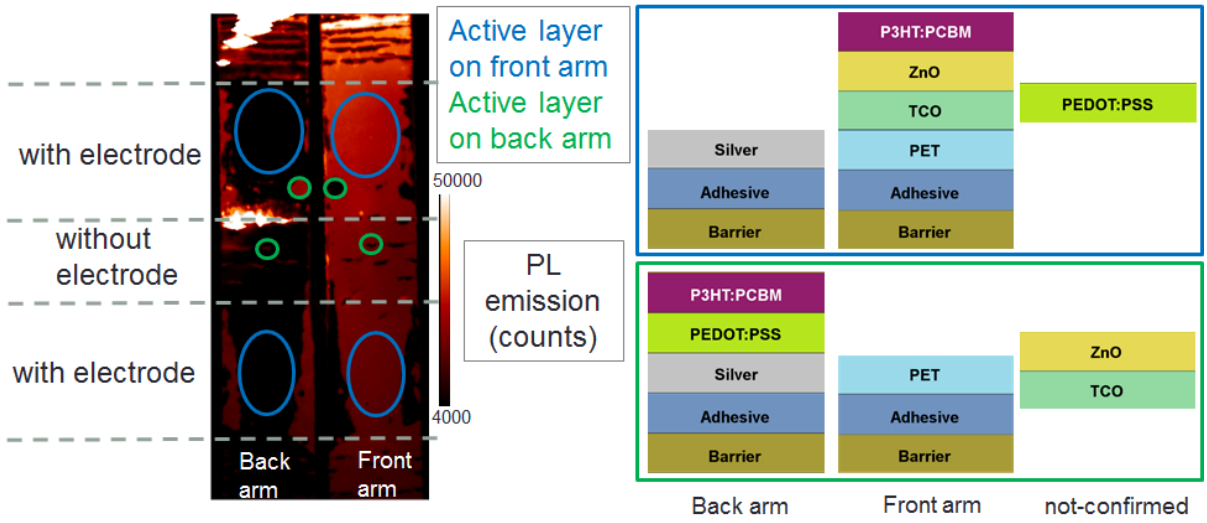

Figure 3.28: *PL image of the reference device described in Fig. 3.26. Two different behaviors are observed and circled in blue and green. According to the PL image, the deduced layers position on the peeled arms for each behavior have been indicated.*

Most of the PL signal is emitted on the front arm of the peeled sample while some smaller patches emit on the back arm.
To allow PL emission from the front arm of the peeled device (blue circles), it is necessary that the active layer must have remained on it. Additionally, the opaque metal electrodes have to be transferred on the back arm of the encapsulation. Therefore, rupture occurred within the HTL layer or at its interfaces with the active layer or the silver electrodes. The PEDOT:PSS layer must thus be spotted by an other technique.
In contrast, for PL to be emitted from active layer materials located on the back arm (green circles), rupture must have occurred in the TCO/ZnO stack or at its interface with the active layer or the PET substrate. The TCO and ZnO layers positions are thus left to be found.

– Scanning electron microscopy with energy dispersive X-ray spectrometry allows us to know the chemical composition of a few micrometer thick surface. It is particularly sensitive to high atomic-number elements such as inorganic atoms.
Given the micrometer depth of the EDX analysis, contribution of several layers is expected on the spectra of the peeled samples. Identification of the peeled stack composition is thus deduced from the presence or absence of specific elements identified separately on single reference layers.
Table 3.1 references the characteristic atomic peaks observed on such reference layers

probed separately .

	PET substrate	TCO	ZnO	P3HT:PCBM	PEDOT:PSS CPP105D	Silver electrode
Sulfur (S)				✓	✓	
Zinc (Zn)		✓	✓			
Indium(In)		✓				
Silicon (Si)					✓	
Silver (Ag)						✓

Table 3.1: *Elements appearing when each reference layer has been probed by EDX.*

By comparing the detected signals on peeled samples with this reference table, one can deduce the presence of each layer.
Results obtained on the peeled surfaces in the electrodes zones of our reference sample presented in Fig.3.26 are detailed in Fig.3.29.

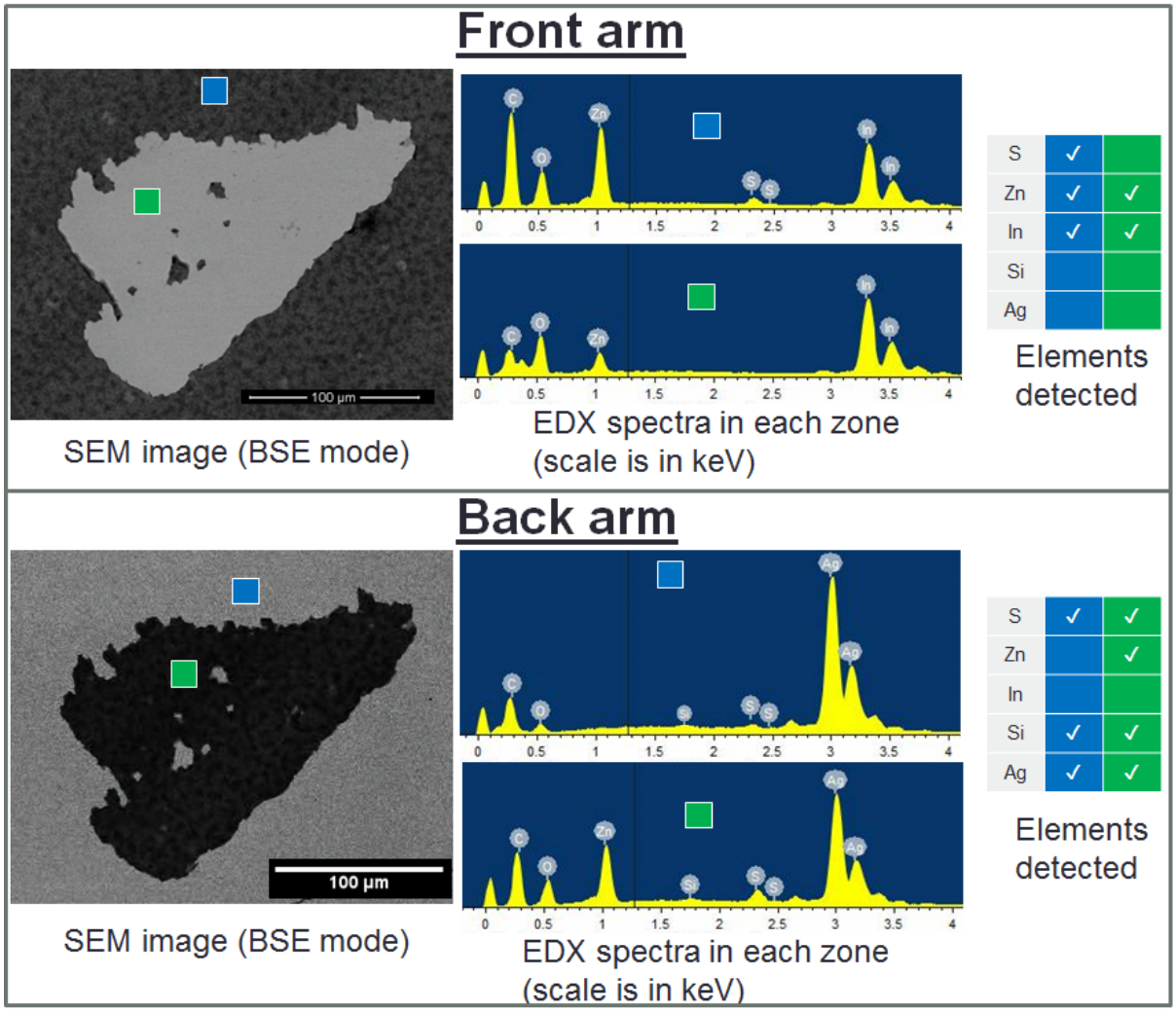

Figure 3.29: *SEM images in back-scattered electron (BSE) mode and associated EDX spectra of the same samples displayed in Fig.3.26 and 3.28 in a region with silver electrodes. Two different behaviors, as seen on PL images in Fig. 3.28, were observed and labeled with the same color code.*

The different behaviors observed previously with PL imaging in Fig. 3.28 were observed as well with the SEM-EDX technique.

Focusing on the front arm of the peeled device, one can see that both patterns contain zinc and indium. As a consequence, the TCO layer is present on the front arm in each case.

On the back arm of the peeled samples, silver and silicon are detected. Therefore, in both cases, PEDOT:PSS is present on this side.

In the blue region, according to the PL image and the SEM spectra, the active layer remained on the front arm and no silicon was detected. Therefore, the rupture is identified to occur between the P3HT:PCBM and the PEDOT:PSS layers.

In the green regions, zinc is detected, without indium, on the back arm of the peeled devices. Thus, rupture occurred either adhesively between the TCO and the ZnO layers or cohesively within the ZnO layer.

Fig.3.30 summarizes the conclusions drawn on the rupture path on this reference device.

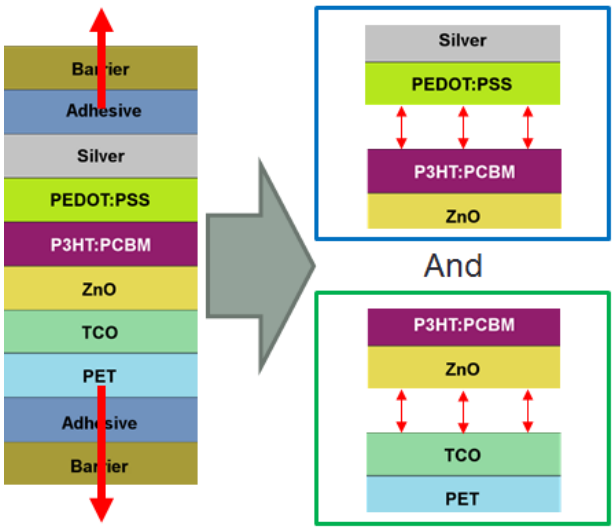

Figure 3.30: *Rupture pattern of the samples studied in Fig.3.26, 3.28 and 3.29. Color code is consistent between each figures.*

In our reference sample, delamination occurs mainly between the P3HT:PCBM and the PEDOT:PSS layers (blue areas) with smaller patches of delamination between the TCO and ZnO layers (green areas). In such case of mixed rupture, peeling strength of each interface cannot be accurately measured. Thus, each peeling strength will have to be measured separately on simplified devices, containing only one of those weak interfaces at a time.

Table 3.2 summarizes the characterizations performed in order to locate the position of each layer on the peeled samples.

Peeling curves cannot discriminate the peeling strength of each interface of a complex stack separately. Therefore, partial devices, only including one interface at a time, have been tested in Sec.4.3 in order to accurately measure each peeling strength separately.

In addition, despite the fact that the rupture locations are roughly similar between areas including electrodes and those not, the average measured peeling strength is higher in the latter case (0.05 ± 0.05 N/cm versus 0.9 ± 0.3, respectively). This is indicative of extraneous factors contributing to the measured peeling strength. Such factors are discussed in the next section.

Characterization method	Visual inspection	FTIR	PL imaging	SEM-EDX
Barrier	✓			
Pressure sensitive adhesive		✓		
Thermoplastic encapsulant	✓	✓		
Metal electrode	✓			✓
Hole transport layer				✓
Active layer	✓		✓	
Electron transport layer				✓
Transparent electrode				✓

Table 3.2: *Layers composing an OPV sample and the respective characterization techniques used to locate them on peeled devices.*

3.2.3 Factors influencing the measured peeling strength of flexible OPV devices

The measured peeling strength is the addition of the lowest intrinsic cohesion/adhesion strength within the sample plus extraneous energy dissipating processes depending on the sample nature, geometry and the experimental parameters. In order to correctly interpret the peeling data, one has to know which factors can bring an extraneous contribution to the measured peeling strength. The major factors expected to influence the peeling strength, according to the literature and our experience, are discussed here.

Sample bending. Sample bending during the course of the peeling tests is expected to bias the measured peeling strengths due to the elastic bent samples applying force on the traction clamps.

Fig.3.31 represents four peeling curves obtained on identical samples.

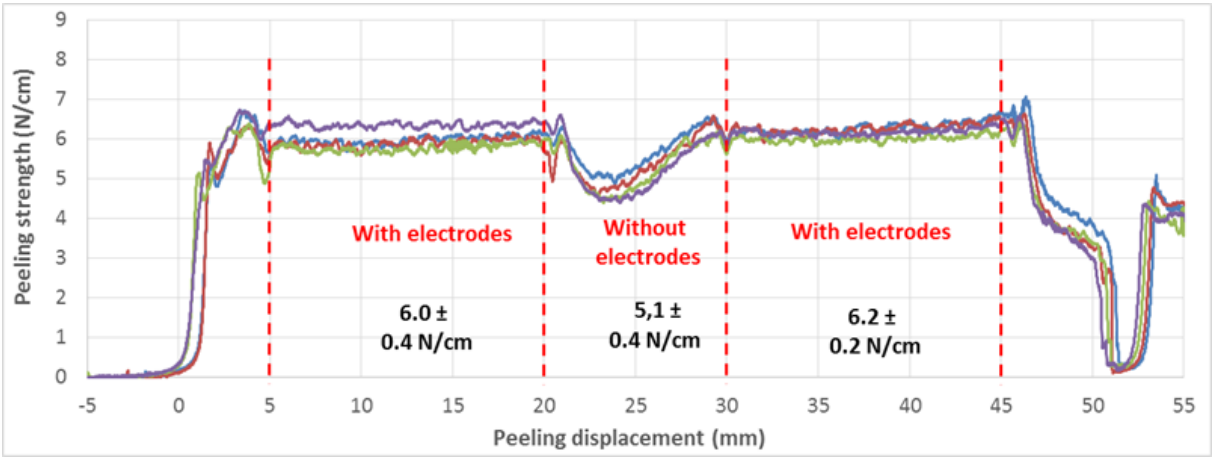

Figure 3.31: *Four peeling curves obtained from samples with an identical architecture.*

In agreement with all samples tested in this work, there is no significant difference of peeling strength between the similar first and second electrode areas. Therefore, evolution of the bending angle of the sample during the tests, often suspected to influence the measured strengths in peeling experiments [141], is assumed to be negligible in this work. Thus, for greater statistical precision, the peeling strengths of both areas with electrodes are merged together when reported.

Viscoelasticity of the encapsulation materials. Fig.3.32 displays the peeling curves of the same OPV sample encapsulated by the 130 °C vacuum process either by a viscous acrylic adhesive or an elastic polyethylene layer.

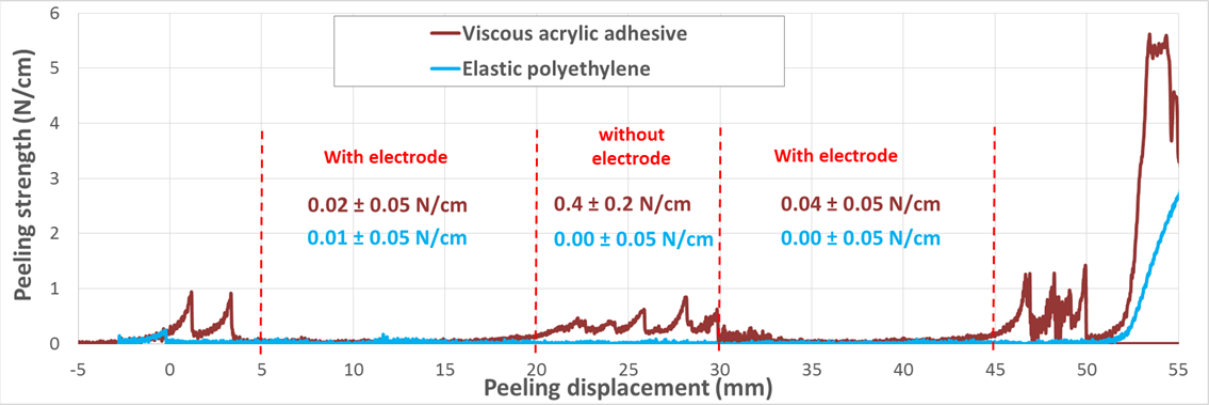

Figure 3.32: *Peeling strength versus displacement curves for two reference OPV samples encapsulated with the same 130 °C vacuum lamination process with a viscous acrylic adhesive and an elastic polyethylene material.*

Focusing on the area without electrodes, from 20 to 30 mm of peeling displacement, one can see saw-tooth like features on the peeling curve with the acrylic adhesive with an average 0.4 ± 0.2 N/cm peeling strength against the flat 0.00 ± 0.05 N/cm curve with the thermoplastic (with failure occuring at the same interface). The sawtooth-like features are characteristic of time-dependent viscous energy dissipation processes occurring around the crack tip [156, 159]. Such processes have at least a micrometer-scale because they can expand energy from the crack progressing within the OPV device to the bulk of the encapsulation materials. As a result, as shown on Fig.3.33, a macroscopic wrinkling of the acrylic adhesive can be observed on peeled PSA samples. In contrast, no such effect is observed for the elastic thermoplastic.

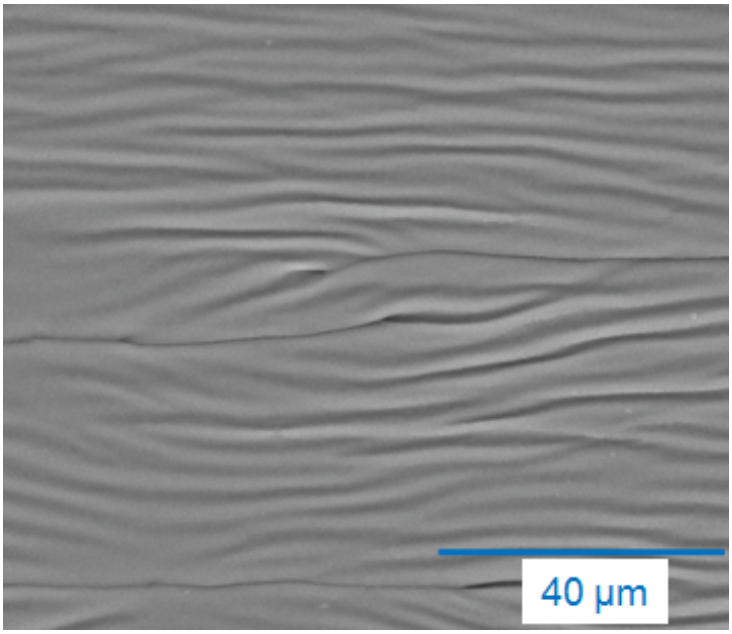

Figure 3.33: *SEM image (BSE mode) of a peeled PSA surface.*

Such processes are also expected to take place within the OPV layers [166]. However, the

relatively thin OPV layers, compared to the thick encapsulation systems (hundred of nanometers compared to tens of microns, respectively, as illustrated in Fig.3.25a), seem not to dissipate sufficient energy for such effects to be observed with our peeling apparatus.

Rigidity and thickness of the metal electrode. On the peeling curves of samples encapsulated by viscous adhesive, such as in Fig. 3.26 or 3.32, one can see a flat, weak peeling strength in regions with a metal electrode, in contrast with areas without electrodes where sawtooth-like features, increasing the overall peeling strength, are observed.

According to the literature [159], the rigid metal electrode confines viscous energy transmission and dissipation mechanisms such as those seen above. Fig.3.34 compares peeling curves of the same sample with different evaporated metal electrode thicknesses. Rupture was located at the same interface, whatever the electrode thickness.

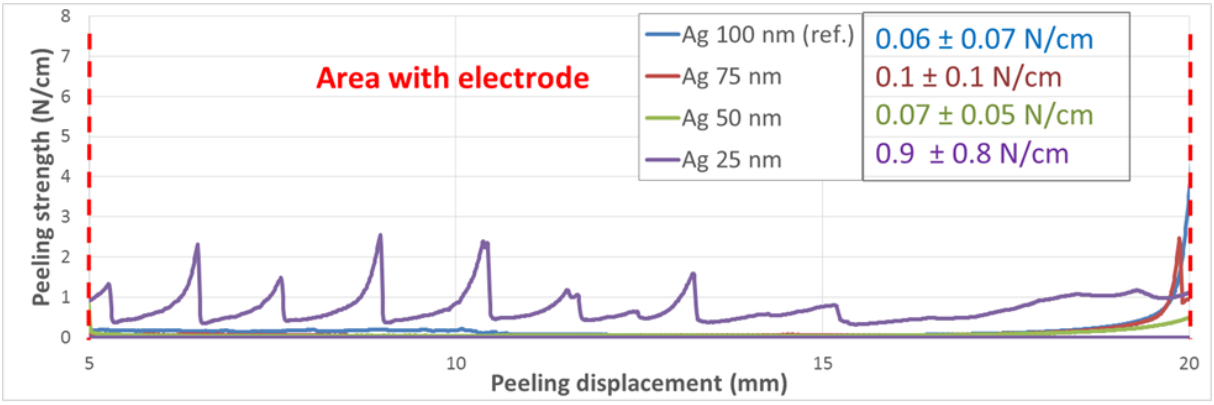

Figure 3.34: *Peeling strength versus displacement curves of reference devices, encapsulated with roll-to-roll acrylic adhesive process, with different thicknesses of evaporated silver electrodes.*

For evaporated silver thicknesses of 50 nm and higher, weak (below 0.1 N/cm) peeling strength are measured. In contrast, for a thinner 25 nm electrode, a higher peeling strength of 0.9 $\pm$ 0.8 N/cm is recorded with the characteristic saw-tooth features related to viscous dissipation. This result suggests that the rigidity of the 25 nm electrode is sufficiently low to allow energy transmission to the thick acrylic adhesive layer.

For practical use, it is more convenient to compare peeling strengths measured in the electrodes areas because they are less sensitive to the extraneous contributions brought by the encapsulation systems.

These results give an indication that encapsulation materials with a significant viscoelastic character are expected to better protect the cells from delamination issues than materials with only an elastic behavior. This is particularly true for devices who bear a comb metal geometry.

This characterization methodology has been successfully applied to investigate all the interfaces of our reference devices. It has also been applied to characterize the improvements we performed on the weakest interfaces.

Conclusion

In this chapter, we developed several non-destructive mesoscopic imaging techniques allowing us to assess the devices properties during their processing and aging.

First, the laser-beam-induced-current (LBIC) technique allows us to quantitatively measure the efficiency of 400 μm spots over the cell area. The limited acquisition time ($\approx$ 20 minutes for standard cells) allows for characterization of a dozen cells a day.

Second, photo-luminescence (PL) imaging, in its common mode under open-circuit conditions, allows us to track the degradation of the active layer separately. This technique is also sensitive to the donor:acceptor (D:A) morphology and can therefore yield insight on the latter.

Third, electro-luminescence (EL) imaging can be used to look for injection issues between the cell contacts and the active layer. However, it has been shown that this technique is potentially destructive; thus it cannot be used to follow a device properties along an aging campaign, for example. Furthermore, this technique cannot be applied on every device and the output images can therefore be misleading.

In replacement, we developed a voltage-biased photoluminescence (vbPL) imaging method which offers several assets compared to the electroluminescence imaging technique: it is non-destructive, faster, better resolved and it offers insight on the extraction mechanisms, better suited for studying PV efficiency than injection mechanisms. All these techniques allow us to develop a good understanding of the weak spots of our cells during processing and aging.

Mechanical characterizations suitable for flexible, multi-layered, thin film devices were also developed. The peeling method helps us to study the adhesion properties of the structures in conditions close to real-life devices. The technique leads to quantitative peeling strength values which can be compared between different stacks in order to identify the weak interfaces and to assess the improvement we tried to bring to them. Subsequent characterization of the rupture path, led with relatively widespread instruments, allows us to attribute such peeling strength to precise interfaces rather than on the complete stack.

Chapter 4

Encapsulation impact on initial performances of OPV devices: influence of mechanical stability

Introduction

Encapsulation of the organic solar cells is mandatory in order to achieve acceptable lifetimes of the cells in their environment. However, despite their importance and their potential cost (up to 60 % [124]), encapsulation processes and materials are scarcely described in the literature if even mentioned [66]. To our knowledge, the impact of the encapsulation processes on the devices initial performances is even more rarely investigated [133].

In this work two materials/encapsulation processes pairs will be studied: the roll-to-roll compatible lamination of a pressure sensitive adhesive called PSA/R2R and the sheet-to-sheet melting and lamination of a thermoplastic called TP/S2S.

In this chapter, the impact of such encapsulation materials/processes pairs on the cells initial performances will be studied. To further investigate the observed performance losses, imaging characterizations will be performed before and after the encapsulation step. Then, the mechanical properties of the devices, suspected to be the main limiting factors explaining the imaged degradation, will be investigated. Improvements of such properties will be developed according to the results obtained on the reference devices. Finally, the effect of such improvements on the cells performances (initial and after encapsulation) will be assessed and discussed.

4.1 Impact of the encapsulation on the cells' initial performances

In order to assess the impact of the encapsulation materials and processes pairs on the cells' initial performances, their J(V) curves were recorded before and 48 hours after encapsulation. The 48 hours delay was chosen according to the PSA maturation time as recommended by the

supplier.

Both the PSA/R2R and the TP/S2S processes were studied in this section. In addition, in order to differentiate the effect of the encapsulation materials and the processes, a third pair using the pressure sensitive adhesive (PSA) laminated with the sheet-to-sheet (S2S) process was studied in parallel with the standard material/process pairs described in Sec.2.3.2.

Fig.4.1 shows the J(V) curves of three representative cells each encapsulated with each material/process pair.

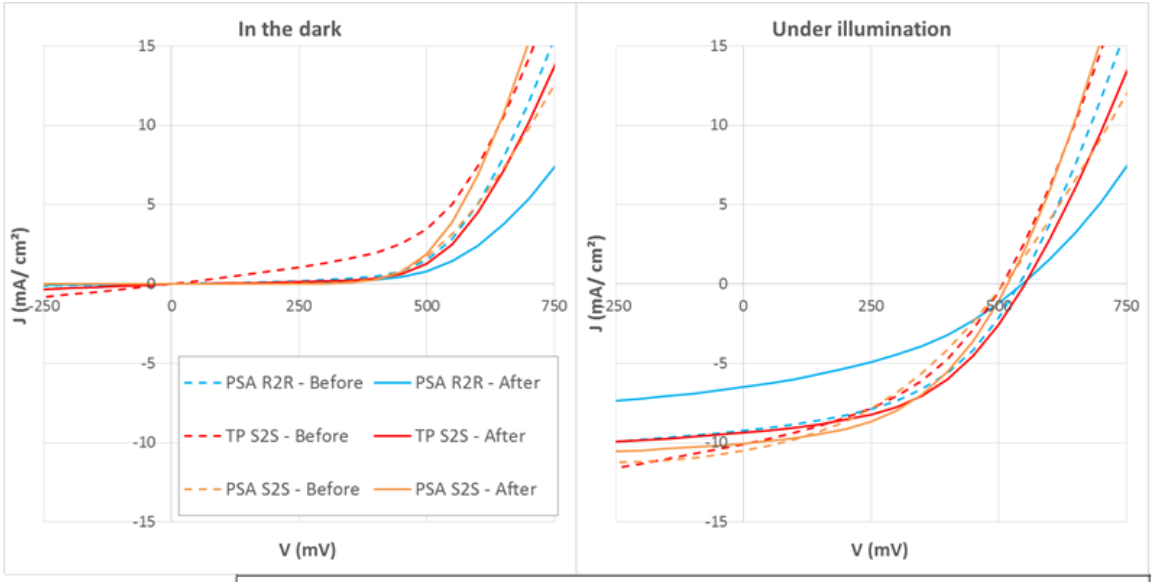

		PCE (%)	Voc (mV)	Jsc (mA/cm²)	FF(%)	Rs (ohm.cm²)	Rsh (ohm.cm²)
PSA-R2R	Before	**2,32**	541	**9,2**	**47**	**17**	1580
	After	**1,37**	548	**6,5**	**39**	**35**	1450
TP - S2S	Before	**2,15**	**505**	10,0	**42**	16	**1100**
	After	**2,47**	**549**	9,3	**48**	21	**1780**
PSA-S2S	Before	**2,05**	509	10,4	**39**	**64**	2900
	After	**2,34**	512	9,5	**48**	**21**	2480

Figure 4.1: *J(V) curves and corresponding absolute PV parameters values of representative cells before and after encapsulation according to each process/material pairs studied in this work.*

The PSA/R2R cell suffers a significant J_{SC} and FF decrease correlated to a strong R_S increase. Its V_{OC} and R_{SH} are unaffected evidencing that no shunting occurred during the encapsulation. The presented TP/S2S cell shows a typical improvement behavior observed on such samples. From a sample with a poor R_{SH} and V_{OC} value, the curve straightens to a more satisfactory J-shape after encapsulation, increasing both parameters. However, it features a slight J_{SC} loss. Finally, the PSA/S2S curve is typical of a S2S encapsulated cell with good initial PV performance. The series resistance decrease improves the FF but the J_{SC} still decreases slightly.

From such J(V) curves plotted after encapsulation compared to those recorded before, statistics of the relative PV parameters were plotted in Fig.4.2. Because absolute PV parameters values

are dispersed for the as-prepared cells as well as for the encapsulated samples, only relative values are discussed in order to emphasize the encapsulation effect. 18 cells were tested for the PSA/R2R encapsulation and 11 for the TP/S2S and the hybrid PSA/S2S processes. The relative PV parameters values of each cell whose J(V) are reported in Fig.4.1 are labeled on the box-plot statistics with white circles.

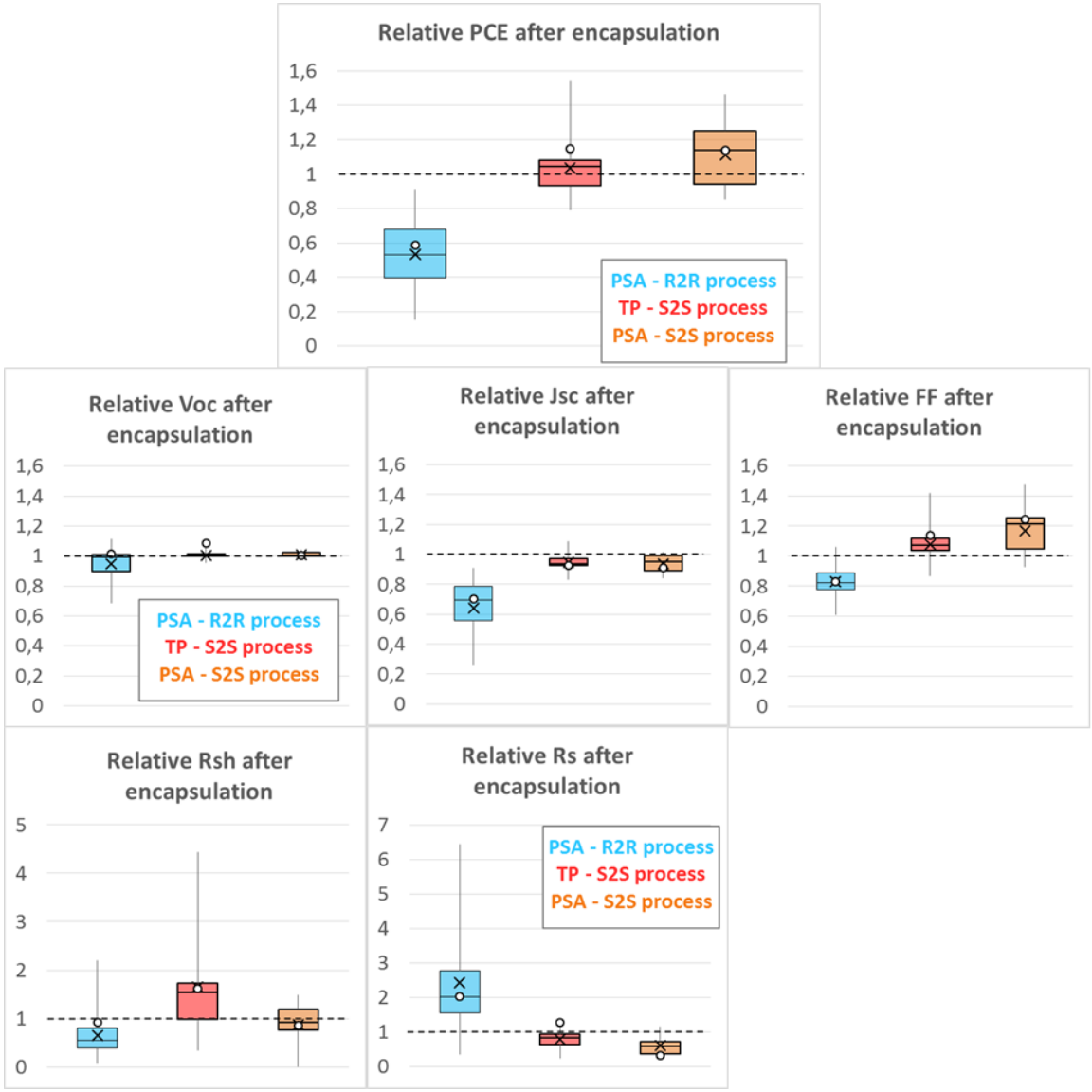

Figure 4.2: *Box plot representation of the relative PV parameters values after PSA/R2R, TP/S2S and PSA/S2S encapsulation of 18, 11 and 11 cells, respectively, compared to their values before encapsulation.*

For cells encapsulated with the roll-to-roll (R2R) process and the pressure sensitive adhesive (PSA) material, the relative power conversion efficiency (PCE) after encapsulation compared to before is on average 53 % of their initial performance. Relative PCE values are broadly distributed between 15 to 91 % with half of the cells ranging from 40 to 68 %. This performance loss is shown to be mostly driven by J_{SC} and FF decreases, with a relative a 64 % average J_{SC} along with a 83 % average normalized FF after encapsulation. Such J_{SC} and FF losses are correlated with a more than doubled R_S average value. V_{OC} losses were occasionally observed on half the samples along with decreased R_{SH} values.

In contrast, all cells encapsulated by the sheet-to-sheet (S2S) process, whether the encapsulant material was the thermoplastic (TP) or the pressure-sensitive adhesive (PSA), follow a somewhat similar behavior. The overall normalized PCE of the TP/S2S and PSA/S2S increased slightly to 104 and 111%, respectively, compared to their performances measured before encapsulation. A slight J_{SC} decrease, less than 10 % in average, was observed with a stronger 8 and 16 % FF increase for the TP and PSA cells, respectively. FF increase was correlated with a slight R_S decrease. Occasionally, a large R_{SH} increase, up to a factor 4, was observed on some cells which gained significant performances, up to 155 %, during the encapsulation step.

From such data, a few conclusions can be drawn:

– First, cells encapsulated with the S2S process, no matter the materials employed, lead to significantly better results than those with the R2R process. Therefore, the R2R process is thought to be responsible for the observed degradation. It is nevertheless not excluded that a synergistic effect between the PSA and the R2R process yields the observed performance loss.
– Furthermore, the PSA/R2R pair encapsulation strategy yields strongly dispersed PCE and J_{SC} values after encapsulation. This suggests that an uncontrolled parameter is responsible for the degradation of such parameters. Only a limited samples suffered shunting, it is therefore excluded as a primary factor for the overall degradation observed.
– Finally, the S2S encapsulated cells on average gain performance thanks to the improved R_{SH} and V_{OC} values observed for some initially shunted cells. This suggests that the heating temperature of 130 °C applied during the S2S encapsulation process, above the P3HT glass transition temperature of 56 °C [89], allows P3HT to flow and fill the shunting path responsible for the relatively low initial performances. The slight decrease of J_{SC} without R_S increase can be, at least partially, inferred to the insertion of moderately absorbing (or reflecting) encapsulation materials (encapsulant + barrier layers) on the incoming light path.

The study of the J(V) curves only yields scarce information on the degradation induced by the encapsulation processes on the devices. Advanced characterizations are required to be performed on the encapsulated devices in order to deepen our understanding of the degradation mechanisms.

4.2 Study of encapsulation processes impact by imaging techniques

To further investigate the degradation suffered by the cells during the encapsulation processes, imaging characterizations, such as those developed in Chapter 3, can be used to monitor the cells performances during processing. Such characterizations offer the advantages to be non-destructive and applicable to encapsulated devices.

To further investigate the S2S and R2R encapsulation processes, LBIC and luminescence imaging techniques were applied, before and after the encapsulation step, on the cells whose PV performances are shown in Sec.4.1.

4.2.1 TP/S2S encapsulation

Cells encapsulated with the thermoplastic (TP)/sheet-to-sheet (S2S) encapsulation strategy were shown to have a decreased R_S leading to a better FF after encapsulation. A R_S decrease is usually correlated to an increased J_{SC} due to reduced thermal losses. However, J_{SC} was shown to be slightly decreased by the encapsulation. As thermoplastic and barrier layers were added on the incoming light path, a fraction of the J_{SC} loss can be inferred to absorption or reflection of those layers.

Photoluminescence properties of 5 cells (divided over two encapsulation campaigns) were studied with our imaging system before and after TP/S2S encapsulation. Representative images of a cell before/after PL, filtered with the 875 nm high-pass filter in order to limit excitation-light reflection, are shown in Fig.4.3.

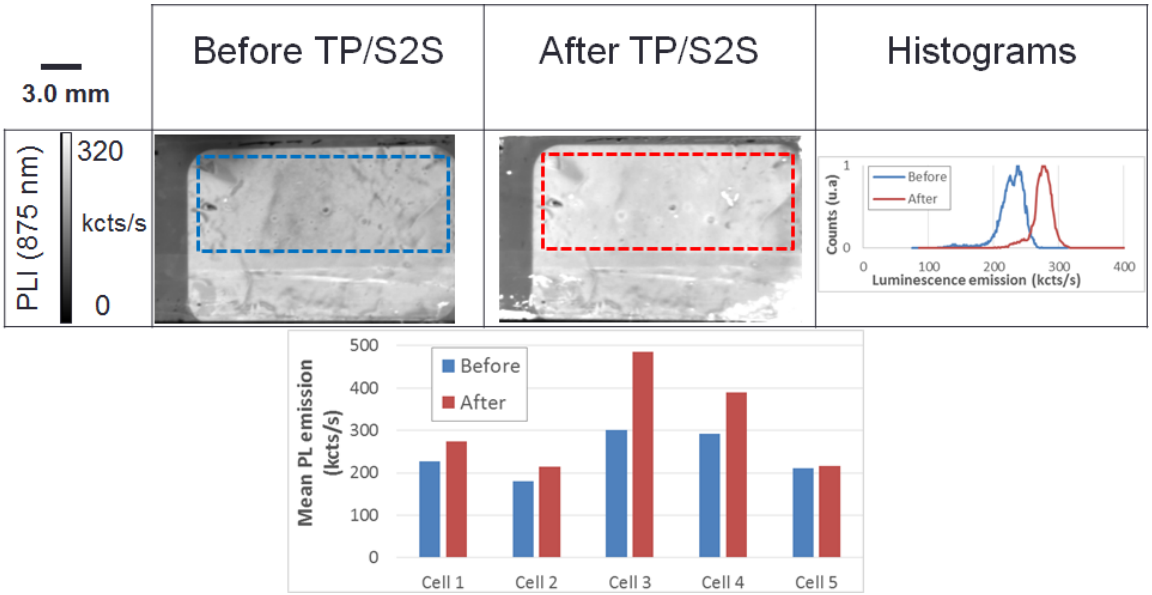

Figure 4.3: *(top) Photoluminescence images of a cell before and after encapsulation with the TP/S2S process. The dashed rectangles represent the area from which histograms have been drawn. This area roughly corresponds to the active area of the devices. (bottom) Mean PL emission, calculated according to the same method, of five cells before/after the TP-S2S encapsulation process.*

As shown clearly on the histograms, an increased photoluminescence intensity is observed for the cell after encapsulation. This observation is reproducible as the five tested cells showed such a behavior with an average 28 % $\pm$ 19 % increased PL emission intensity after encapsulation. From spectrally resolved luminescence experiments, no significant spectral shifts were observed on the cells. This suggests that the recombination mechanisms did not change fundamentally and that the images intensities can be compared quantitatively.

Band-to-band photoluminescence emission is ruled by two factors: the number of absorbed photons and the ratio of excitons recombination versus dissociation events. An increased photoluminescence intensity after encapsulation means that at least one of those two increased. Absorption of photons is expected to be decreased after encapsulation due to the insertion of absorbing/reflecting layers in the optical path of the excitation light. Therefore, the increased PL intensity can only be explained by the increased radiative recombination of excitons compared to their dissociation.

This result suggests that the morphology of the active layer was changed by the 130 °C temperature applied for 13 minutes by the S2S encapsulation process. P3HT domains larger than the excitons average diffusion length ($\approx$ 10 nm) are likely to have formed during encapsulation. The exciton recombination rate thus increased at the expense of their dissociation rate. As a consequence, the short-circuit current of the cells decreased due to the encapsulation process.

To mitigate such J_{SC} loss, lower processing temperatures could be applied during encapsulation. In our case, for a pure polyethylene encapsulant material, a temperature slightly higher than its melting temperature, 96 °C according to differential scanning calorimetry measurements, should be applied.

4.2.2 PSA/R2R encapsulation

From the J(V) data shown in Sec. 4.1, such a process induces a strong series resistance (R_S) increase, leading to a short circuit current density (J_{SC}) and fill factor (FF) deterioration which in average halved the cells performance after encapsulation.

We chose three cells, labeled A, B and C, which are representative of the range of degradation undergone by the samples during their PSA/R2R encapsulation, to be characterized by non-destructive imaging techniques before and after encapsulation. Fig.4.4a shows the position of those three cells compared to the global statistics presented before. Their J(V) curves, plotted before and after encapsulation are also reported in Fig.4.4b. Photographs of both sides of cell C after encapsulation are shown in Fig.4.4c.

Cell A is an above average cell which performed better than 75 % of the samples. It only features a moderate increase of R_S and decrease of J_{SC} and FF. Cell B is representative of most of the tested samples with a doubled R_S yielding lower performance than cell A. Visual inspection of both cells does not allow to perceive any degradation. Cell C yielded the worst after-encapsulation performances reported in this work. In addition to the larger trends of R_S, J_{SC} and FF observed on the other PSA/R2R cells, it also features a significant V_{OC} and R_{SH} decrease. During the R2R lamination, the PSA wrinkled and the cell has been visibly damaged, as shown by the pictures in Fig.4.4c. The damage, inducing the metal electrode cracking on the back side and a change of refractive index on the front side of the cell, is suspected to be delaminations within the OPV stack.

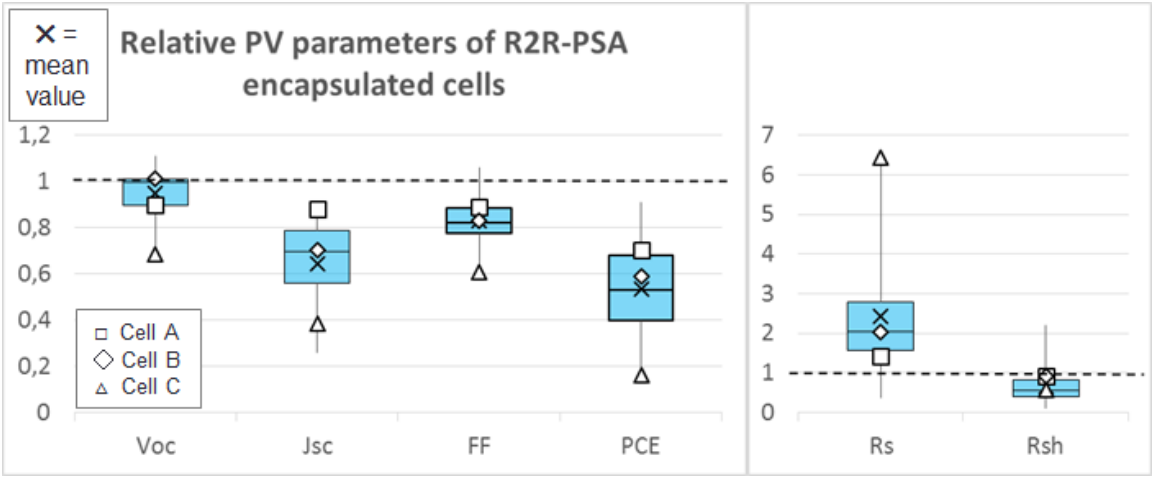

(a)

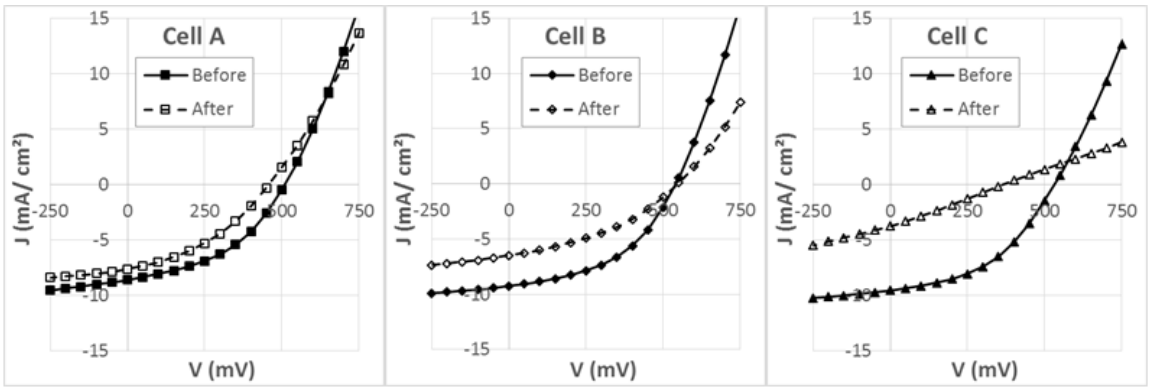

		PCE (%)	Voc (mV)	Jsc (mA/cm²)	FF(%)	Rs (ohm.cm²)	Rsh (ohm.cm²)
Cell A □	Before	1,91	507	8,5	44	19	3430
	After	1,35	457	7,5	39	27	3100
Cell B ◇	Before	2,32	541	9,2	47	17	1580
	After	1,37	548	6,5	39	35	1450
Cell C △	Before	2,28	531	9,5	45	23	1390
	After	0,37	365	3,7	27	149	800

(b)

(c)

Figure 4.4: *(a) Relative PV parameters statistics of the PSA/R2R encapsulated cells compared to their as prepared performances. 3 cells, labeled A,B and C were chosen for imaging characterizations.(b) J(V) curves and absolute PV parameters of the three cells chosen for the imaging characterizations.(c) Photography of cell C. Wrinkling of the adhesive during the R2R lamination caused damage in the cell center.*

LBIC images. As outlined in Sec.3.1, laser-beam induced current (LBIC) mapping is an efficient technique to use in order to probe the whole PV efficiency of the cells resolved on a

few hundreds of square micrometers. LBIC images of the three A,B and C cells before and after encapsulation are shown in Fig.4.5a. The time elapsed between the conditioning of the cells and the end of their LBIC imaging is shown in Fig.4.5b.

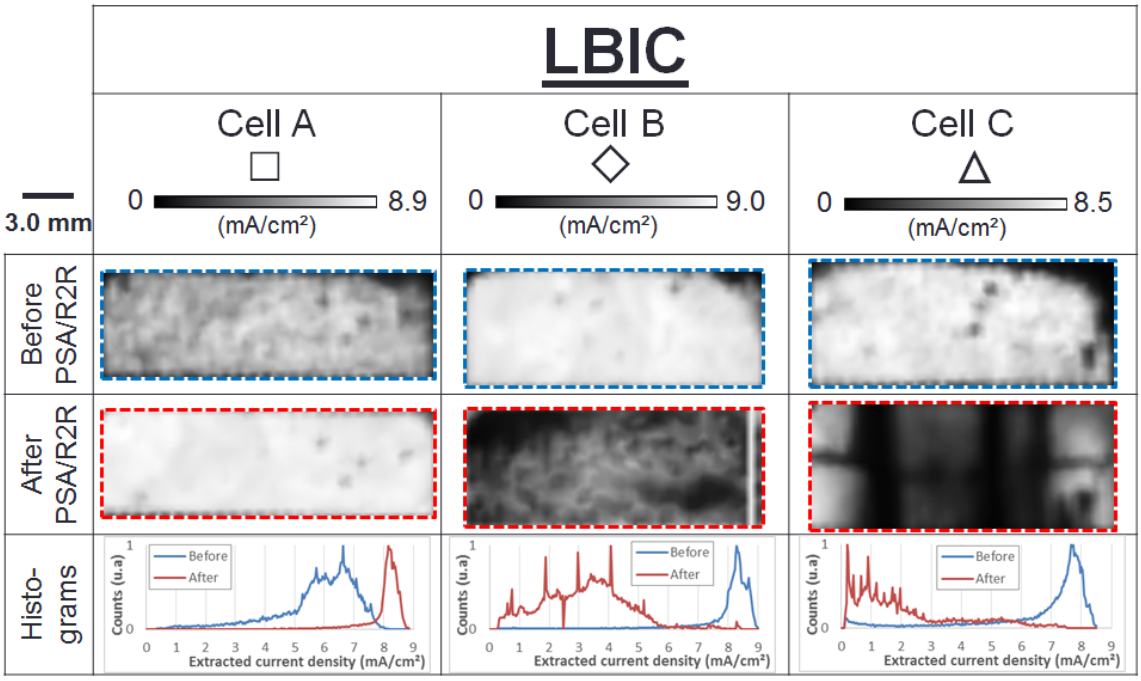

(a)

	Cell A	Cell B	Cell C
Before encapsulation	103 mins	33 mins	32 mins
After encapsulation	26 mins	33 mins	27 mins

(b)

Figure 4.5: *(a) LBIC images of the three cells before and after encapsulation with the PSA/R2R process. The dashed rectangles represent the area from which histograms have been drawn. This area roughly corresponds to the active area of the devices. (b) Time elapsed between the J(V) measurements and the end of LBIC imaging of the cells before and after encapsulation.*

Comparing the LBIC data before encapsulation of the three cells, cell A features a lower overall extracted photo-current and a slightly broader spatial distribution than the other two. This is in opposition to the J(V) curves data where the short circuit current density difference between the cells is significantly less pronounced. As detailed in Sec.3.1.1, this is likely related to the longer acquisition time of this image which provoked the loss of the sample's conditioning effect and thus biased the corresponding output LBIC image.

Focusing on the histograms of the cells after encapsulation in Fig.4.5a, one can see the overall extracted photo-current decreasing from cell A to C in good agreement with the measured short-circuit current-densities shown in Fig.4.4b. The broadening of the histograms of cells B and C indicates discrepancies in the spatial distribution of the extracted photo-current. Indeed,

the corresponding images feature large areas which do not participate to the cell extracted photo-current. The macroscopic degradation of cell C visible to the bare eye in Fig.4.4c is also observable on the LBIC image. However, the other dark spots of cell C and those of cell B could not be related to any defects visible with the bare eye.

The LBIC characterization shows the same cells hierarchy as the J(V) curves. In addition, it provides the information that the degradation seems localized, rather than homogeneous on the samples surface. However, it does not allows us to understand the nature of the observed degradation; to this end, luminescence imaging have been performed on the same samples.

Open-circuit photo-luminescence images. These LBIC images were compared to the raw PL images taken in open-circuit conditions presented in Fig.4.6.

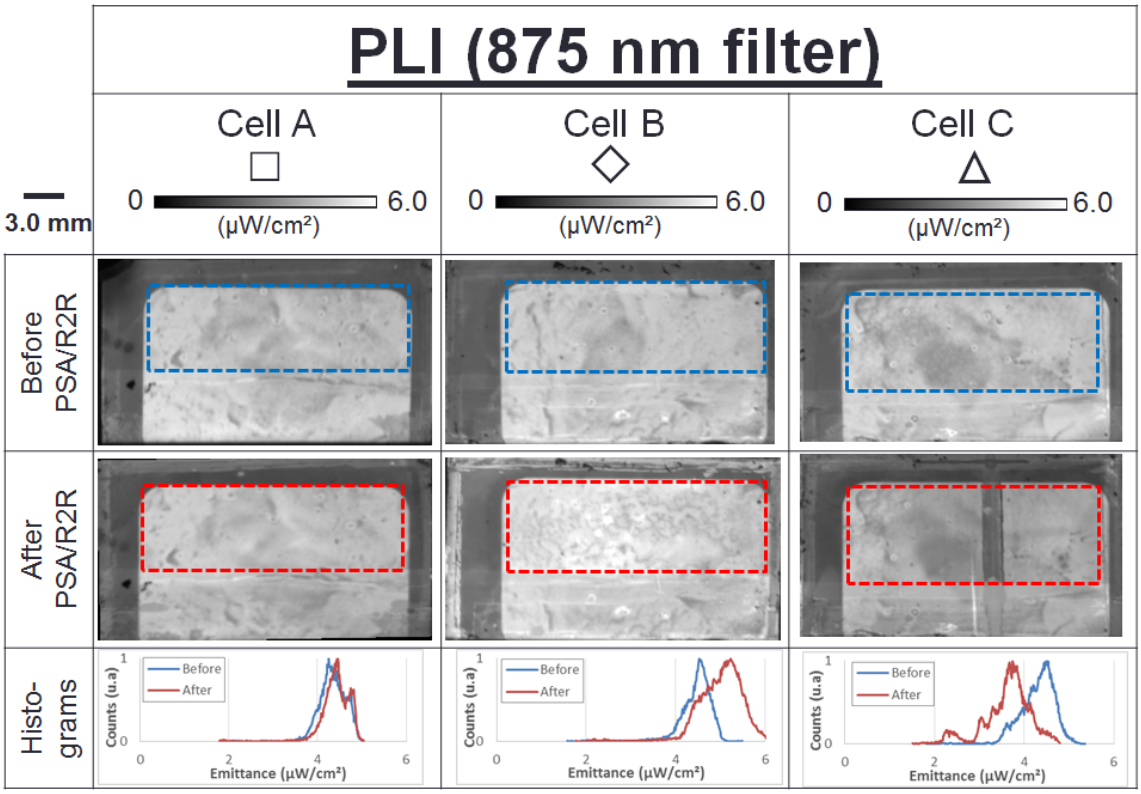

Figure 4.6: *PL images (875 nm high-pass filter) of the three cells before / after encapsulation with the PSA-R2R process. The dashed rectangles represent the area from which histograms have been drawn. This area roughly corresponds to the active area of the devices.*

After encapsulation, only the macroscopic degradation visible to the naked eye is observed on cell C. A check board-like pattern is also barely visible on cell B. The overall intensity of the histograms of cells B and C are slightly shifted when compared to those obtained before encapsulation.

PL intensity is related to three inter-related events: the absorption of a photon by the active layer, the band-to-band recombination of the exciton formed from the photon absorption and the non-radiative recombination or dissociation of the exciton.

Because of the lack of thermal stress and the mild atmospheric conditions applied for a short time to the cells during the encapsulation process, we can reasonably rule out an active layer morphology evolution, as seen on the S2S processed cells, to cause such PL variations. In addition the PSA/S2S cells was shown in Fig.4.2 to yield significantly better performances than cells encapsulated with the roll-to-roll process; thus a chemical degradation of the cell by the acrylic PSA material on a 48-72 hours time scale is unlikely. Therefore, the ratio of dissociated versus recombined excitons is not expected to have changed due to the PSA/R2R encapsulation process and the active layer is thought to be unaffected by the encapsulation.

Observed PL variations are more likely to be related to optical changes i.e. changes of the absorption and reflection properties of the cells. Global variations of the intensity between after and before encapsulation images can be caused by both the absorption of the inserted PSA + barrier layers and the slight sample tilting during the imaging experiments. Localized contrast changes can be originating from the reflective electrode creasing or air gaps on the front side of the cell.

Biased photo-luminescence images. In order to probe charge transport from the active layer to the cell contacts, -1 Volt biased photoluminescence images were compared to open-circuit photoluminescence images following the protocol detailed in Sec.3.1.3. Results of such characterizations, performed before and after encapsulation of the three cells described above are shown in Fig.4.7.

Such images are closely correlated to the patterns observed with LBIC characterizations. Few changes are observed between images of cell A before/after encapsulation. Images taken after encapsulation of cell B and C feature a strong broadening of their intensity coupled to several completely dark spots. Location of such dark spots are perfectly correlated to those observed in the previously described LBIC images.

As shown in Sec.3.1.3, dark areas on voltage-biased photoluminescence images are indicative of a poor collection of photo-generated charges.

Conclusions. In this section, the performances losses of the samples encapsulated by the PSA/R2R process were investigated with imaging characterizations.

From the LBIC data, one can see that the strong degradation of the cells performances are related to localized, complete degradation patterns rather than global efficiency losses.

Classical open-circuit photo-luminescence images do not show strong contrast after encapsulation compared to before. Therefore, we can conclude that the strong performance loss is not related to an active layer degradation and we will assume that the amount of photo-generated charges is not drastically affected by the PSA/R2R material and process.

The strong correlation between -1 V biased PL and LBIC images suggests that the collection failure of the photo-generated charges from the active layer to the contacts is the dominant factor

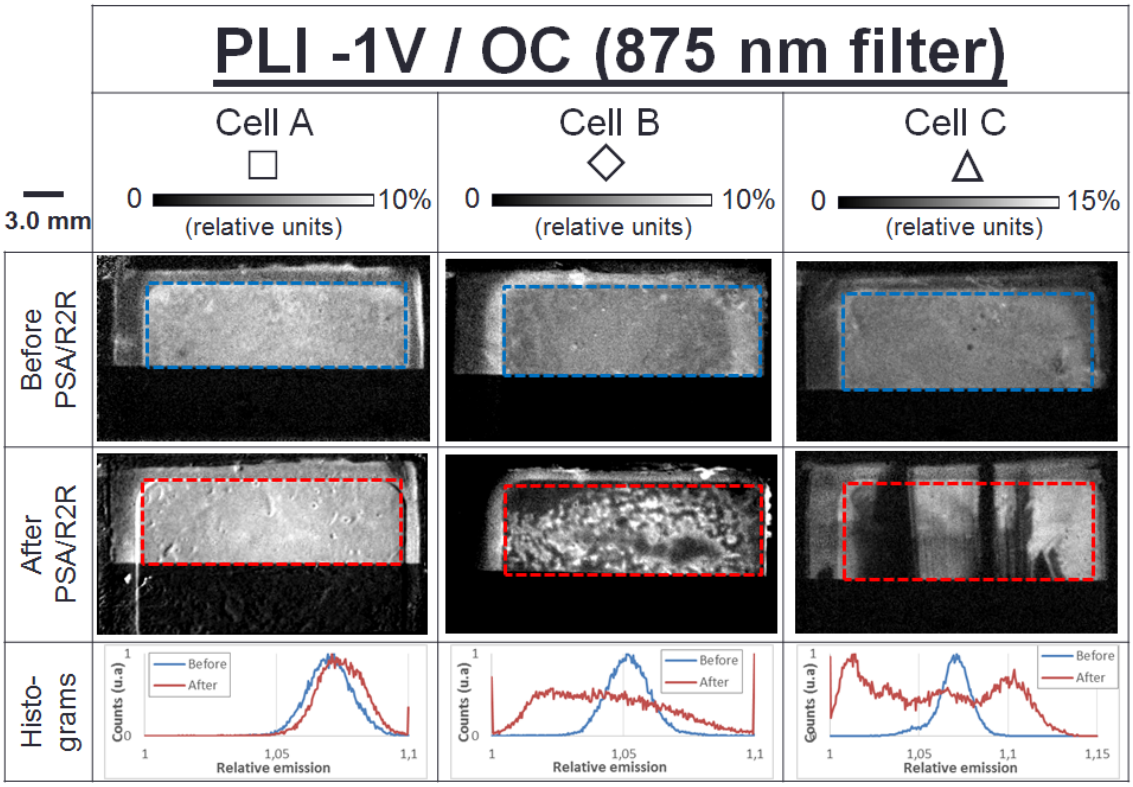

Figure 4.7: *bPL images (875 nm high-pass filter) of the three cells before / after encapsulation with the PSA/R2R process. The dashed rectangles represent the area from which histograms have been drawn. This area roughly corresponds to the active area of the devices.*

inducing the performance decrease observed during PSA/R2R encapsulation. Its precise origin, whether chemical degradation of the electrode/transport layers or delamination occurring at their interfaces is yet to be determined.

In the literature, strong R_S increases have been observed for delaminating inorganic thin-film modules [262]. A degradation incoming from mechanical stress was therefore hypothesized for our devices. Indeed, while the sheet-to-sheet encapsulation process only applies normal pressure to the samples, the roll-to-roll process involves a mix of normal and shear stresses which may damage mechanically weak interfaces within the devices and therefore provoke the losses of contact observed with imaging techniques.

4.3 Mechanical properties of reference OPV devices

In order to confirm the hypothesis of a mechanical degradation occurring during the roll-to-roll encapsulation process, we have to estimate the adhesion strength between all the interfaces of our devices. This adhesion can be of particular importance if one wants to produce devices for applications requiring them to be flexible and therefore mechanically resilient in order to reach a viable operational lifetime.

In this section, the mechanical characterization methodology described in Sec.3.2 was employed in order to identify the mechanically weak interfaces of our reference devices. Only devices encapsulated according to the PSA/R2R protocol will be shown here.

4.3.1 Description of the samples configuration

In a first place, complete devices comprising every reference layers were tested. Detailed results were presented in Sec.3.2 as an example for presenting the mechanical characterization methodology. From this study, the reference devices were shown to be likely damaged by mechanical stress at two weak interfaces: the first one between the transparent conductive oxide (TCO) electrode and the "ZnO A" electron transport layer (ETL) and the second one between the P3HT:PCBM active layer (AL) and the PEDOT:PSS hole transport layer (HTL). The global peeling strength of the complete devices was therefore limited by these two weak spots and was estimated below 0.05 N/cm, our experimental setup lower detection limit.

However, because such weak interfaces limit the whole devices mechanical properties, the peeling strengths of stronger interfaces could not be assessed by testing complete devices. In order to study the other interfaces, we applied the characterization method to samples made of a reduced number of OPV layers, encapsulated by the PSA/R2R encapsulation system.

Fig. 4.8 summarizes all the sample configurations which were tested in order to investigate the peeling strength of all the interfaces in our reference devices. The rupture path, as characterized after debonding, is illustrated by dashed red lines. The sample on the far left is the complete encapsulated device; its complete characterization is detailled in Sec.3.2. The sample on the far right of the figure was tested by using the top barrier on one arm (instead of the PSA + barrier as for all other configurations) and all the other layers on the other arm. This allowed us to test the PSA/Barrier interface.

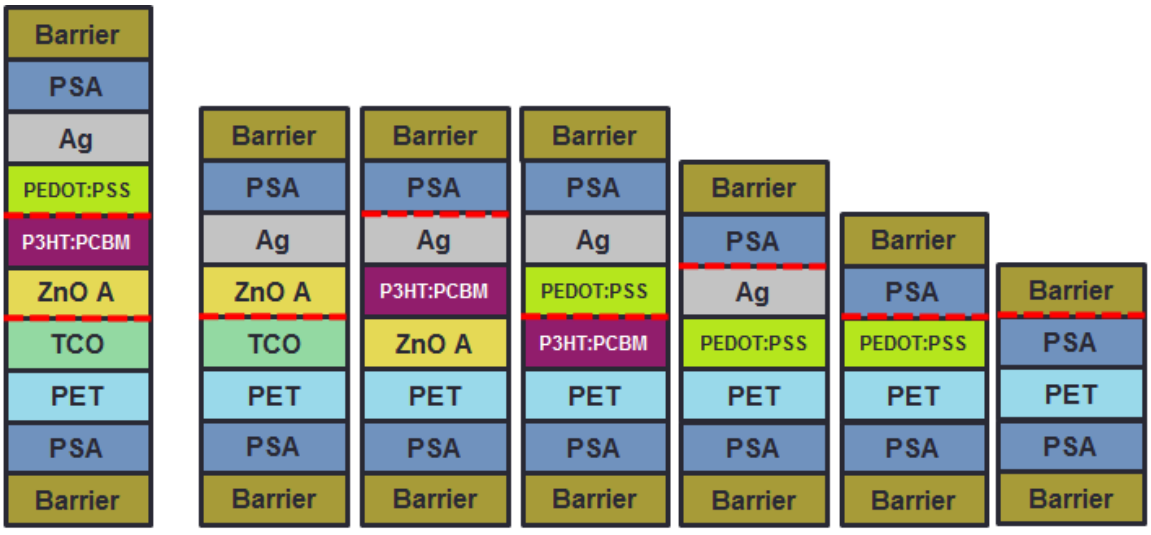

Figure 4.8: *Tested configurations in order to assess peeling strength for all the interfaces within the reference devices. Rupture locations during mechanical testing are represented with dashed red lines.*

For example, the interface between the ZnO A and the active layer was studied in a sample made of a PET substrate/ZnO A/P3HT:PCBM/Ag stack encapsulated by the symmetrical PSA/Barrier layers, the third stack from the left in Fig.4.8.

For particularly strong interfaces, rupture occurred between the encapsulation system and the

OPV stack instead of between two OPV layers. Therefore, the peeling strength of the interface between the OPV layers was estimated to be stronger than the peeling strength measured between the sample and the encapsulation.

4.3.2 Results

Fig.4.9 summarizes the measurements or estimations of the peeling strength of all interfaces within our reference OPV devices. At least four samples, each containing two 15 mm long areas of interest, were tested for each reported value.

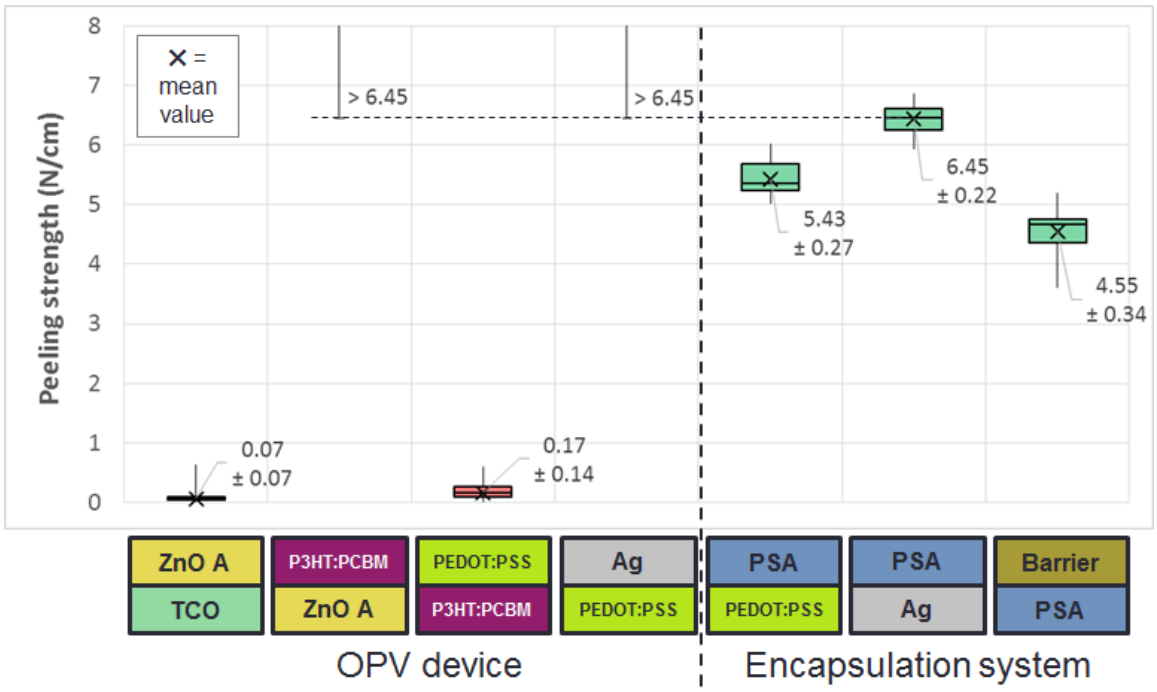

Figure 4.9: *Measured and estimated peeling strengths of interfaces present in our reference devices.*

From this study, several conclusions can be drawn:

- First, the PSA encapsulation system withstands relatively strong peeling strengths. Its weakest interface, between the PSA and the barrier layers, corresponds to 4.55 ± 0.34 N/cm. The PSA adhesion with the cells, whether we consider an area covered by silver or by the PEDOT:PSS HTL, is at least 5.43 N/cm.
- Second, the OPV device itself, comprises two strong interfaces, ZnO A / P3HT:PCBM and PEDOT:PSS / Ag. In all tested configurations, mechanical failure occurred at the device / PSA interface rather than at the two former. Thus, these two interfaces are necessarily stronger than the Ag/PSA interface, which was measured to be 6.45 N/cm.
- Finally, two particularly weak interfaces were observed, in agreement with our study of the complete device : the TCO / ZnO A interface and the P3HT:PCBM / PEDOT:PSS featuring barely measurable peeling strengths of 0.07 ± 0.07 and 0.17 ± 0.14 N/cm, respectively.

Such weak interfaces are likely to be damaged under mechanical stress applied to the flexible devices. Such mechanical stresses would be ordinary in a wide range of applications for the

OPV technology and in the roll-to-roll (R2R) manufacturing and encapsulation of the devices. The strong degradation suffered by the devices during the PSA/R2R encapsulation process, as investigated in Sec.4.1 and 4.2, is indeed likely to be related to delaminations at such weak interfaces.

In order to hamper the performance losses induced by the PSA/R2R encapsulation process and to improve the devices mechanical resilience for flexible applications, we will develop strategies in order to improve adhesion at those weak interfaces.

The set goal is to improve the two weak interfaces to the range of peeling strengths attained by the other relatively strong ones; at least one order of magnitude increase of the peeling strength of both weak interfaces is desired, without degrading other interfaces.

4.4 Mechanical improvement of the TCO/ETL interface

4.4.1 TCO/ZnO adhesion improvement

The TCO / ZnO A interface was shown to be a weak interface with a 0.07 ± 0.07 N/cm peeling strength. However, the chemical composition of the layers, indium-zinc oxide (In_2O_3/ZnO) for the TCO and zinc oxide nanoparticles (ZnO NPs) for the ETL, should allow a strong interaction at the interface. As the TCO layer is UVO_3 treated prior to the ZnO deposition, we expect this surface to be clean and to have its surface energy largely increased, which should be favorable for a strong interaction with ZnO NPs. Therefore, the lack of interaction at the TCO/ZnO A interface would rather be related to the ZnO nanoparticles.

The safety data sheet of the ETL materials reveals a small amount ($\approx$ 5-10 % mass) of alkylammonium salts in the nanoparticles dispersion. Such alkyl compounds are often used as ligands shells to the nanoparticles in order to increase the stability of the ZnO nanoparticles dispersions [187].

We investigated the chemical composition of ZnO films in order to confirm if alkylamine compounds were still present in the ZnO layers after deposition and thermal annealing.

Fig.4.10 shows Fourier-transform infrared (FTIR) spectra, normalized at 2100 cm^{-1}, taken in attenuated total reflection (ATR) mode of a µm thick ZnO A layer annealed for 5 minutes at 140 °C like our reference layers. The probed layer had to be thicker than the 30 nm thick reference in order to yield good signal-to-noise ratio of the spectra.

According to the literature [263, 264], Zn-O stretching vibrations are expected out of our scanning range at $\approx$ 430 cm^{-1}. This should be the only band visible if a pure ZnO layer was probed. Characteristic C-H, and C-N bands suggest that alkylamine compounds are still present in the ZnO layers after spin-coating and thermal annealing. Furthermore, the FTIR spectra were unchanged even after a one hour long 140 °C annealing. Such species are therefore not eliminated by this thermal treatment.

Such alkyl species are often used as shells of the nanoparticles in order to stabilize their

Bond	Vibration type	Frequency (cm^{-1})
C-H	Stretching	2859 - 2950
	Bending	1374 - 1459
Aromatic C-H	Bending	933 - 869
Aromatic C=C	Stretching	1580
C-O	Stretching	1101
C-N	Stretching	1293
O-H	Stretching	3451

Figure 4.10: *FTIR ATR Spectra of a µm thick ZnO A layer annealed for 5 minutes at 140 °C. Characteristic bands are tabulated below the graph according to [231]*

.

dispersions in solvents [187]. Such alkyl shells are however required to have poor interaction with oxide surfaces, such as other nanoparticles and the TCO layer, thus leading to weak adhesion if still present in dry layers.

From the hypothesis of alkyl shells around the ZnO nanoparticles preventing adhesion with the TCO layer, we chose to either remove such shells after deposition of the reference ZnO A layer or to use a different ZnO nanoparticles dispersion, called "ZnO B", which does not have the same chemical composition.

In order to remove alkyl contaminant compounds from electronic devices, oxidative O_2-plasma and UV-ozone (UVO_3) treatments are often performed [265, 266]. We applied such UVO_3 treatments on the zinc oxide nanoparticles layers after their deposition and thermal annealing. In Fig.4.11, the amount of alkyl compounds was controlled by FTIR spectroscopy recorded on a µm thick ZnO layer as a function of the UVO_3 treatment time. For the recording of the FTIR spectra, the ZnO films had to be micrometer thick. Spectra were normalized at 2100 cm^{-1}.

Compared to the pristine layer spectrum, the alkyl content, monitored for example with the

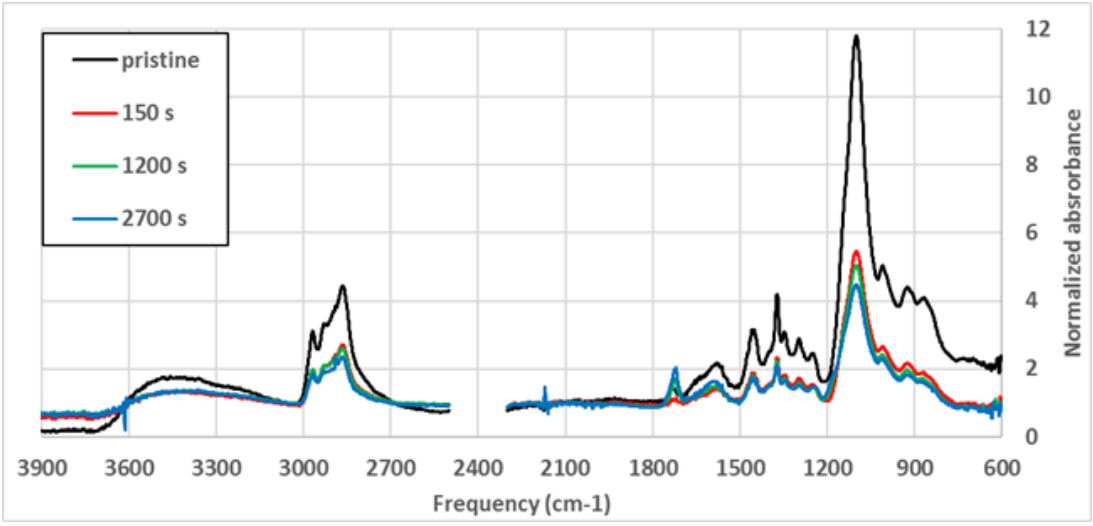

Figure 4.11: *FTIR (ATR mode) spectra normalized at 2100 cm^{-1} of a µm thick ZnO A layer annealed for 5 minutes at 140 °C after several UVO_3 treatment times.*

bands intensities between 2850 and 2950 cm^{-1}, of the dry films decreased sharply in a relatively short time of 150 seconds. For longer treatment times, up to 2700 seconds (45 minutes), the alkyl content only decreased slightly as compared to the initial loss. It is likely that alkyl species remaining after the longest treatments are located deep in the thick ZnO layer, where UV light and activated oxygen cannot reach [266]. In addition, the carbonyl band intensity, visible at 1736 cm^{-1}, increases as a function of the UVO_3 time following an opposite trend to the alkyl bands. Such oxidized carbons may likely be degradation products from oxidized alkyl contaminants still bound to the ZnO layer.

In order to investigate the surface properties of the ZnO layers after UVO_3 treatments, contact angle measurements of polar (water) or dispersive (diiodomethane) solvents on ZnO A layers processed in a similar fashion to real solar cells were conducted. The effect of a 2'30 minutes UVO_3 treatment on the contact angles was studied in Fig.4.12. Reported angles were calculated according to an elliptical fit based on a snake-based procedure developed by Stalder *et al.* [267] with the imageJ [230] software.

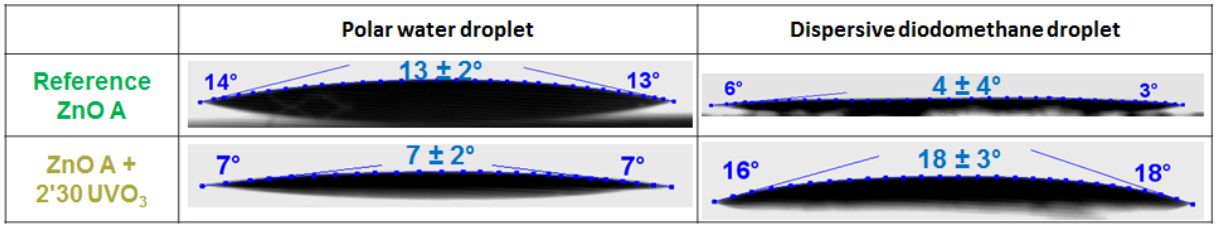

Figure 4.12: *Contact angle measurements of water and diiodomethane droplets on a ZnO A layer with or without a 2'30 miutes UVO_3 treatment.*

Contact angle of the polar water droplets with the ZnO A layer decreased for UVO_3 treated ZnO layers. In contrast, contact angle of the non-polar diiodomethane droplets increased with the UVO_3 treatment. This is indicative that the ZnO layer surface is less hydrophobic after UVO_3

treatment. This is in good agreement with the alkyl-species oxidation and removal mechanism suggested by the FTIR spectra shown above.

Another ZnO nanoparticles dispersion, called "ZnO B" was studied by FTIR spectroscopy on thick thermally annealed layers as well. Deposition parameters were kept identical between ZnO A and B. Results are shown in Fig.4.13.

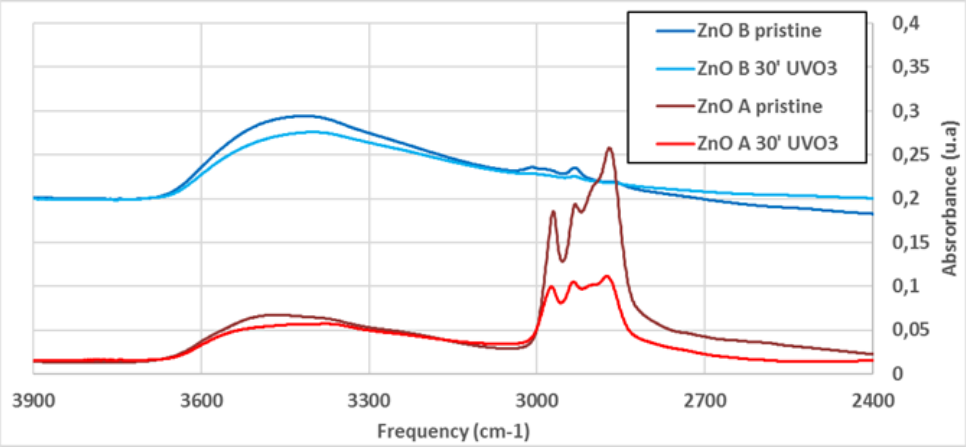

Figure 4.13: *FTIR (transmission mode on glass substrates) spectra of* µm *thick ZnO A and ZnO B layers annealed for 5 minutes at 140 °C and after subsequent 30 minutes UVO_3 treatment. For the sake of clarity, ZnO B spectra were shifted by a +0.2 absorbance units.*

Both ZnO layers comprise alkyl species after their spin coating and 5' thermal annealing at 140 °C. However, the alkyl bands between 2800 and 3050 cm^{-1} of ZnO B are different from those of the ZnO A suggesting different alkyl compounds nature. The peak intensities between each dispersions should not be interpreted because the layers' thicknesses can vary greatly between both samples. A 30' UVO_3 treatment removes a significant part of the alkyl compounds from both samples.

In order to quantify the alkyl content in each dispersions, the loss of mass as a function of the temperature was investigated by thermogravimetric analysis in air. Both pristine solutions, ZnO A and B were tested by directly pouring them into the scale basket. An additional micrometer thick ZnO A layer, similar to those investigated previously by FTIR, was thermally annealed for 5 minutes at 140 °C and treated for one hour by UVO_3. The film was then scratched and the resulting crust was placed in the scale basket.

From room temperature, the samples were heated at a 10 °C per minute rate up to 140 °C. Then, they were kept at this temperature for one hour in order to evaporate the solvents, either ethanol for ZnO A or 1-butanol for ZnO B, whose boiling points are 78 and 118 °C, respectively [231]. Finally, the temperature was increased by a 10 °C per minute rate up to 550 °C. The mass of the samples, normalized to their mass measured at 140 °C, and its temperature derivative are shown in Fig. 4.14.

The pristine ZnO A looses 16 % of its mass between 140 and 550 °C. According to the

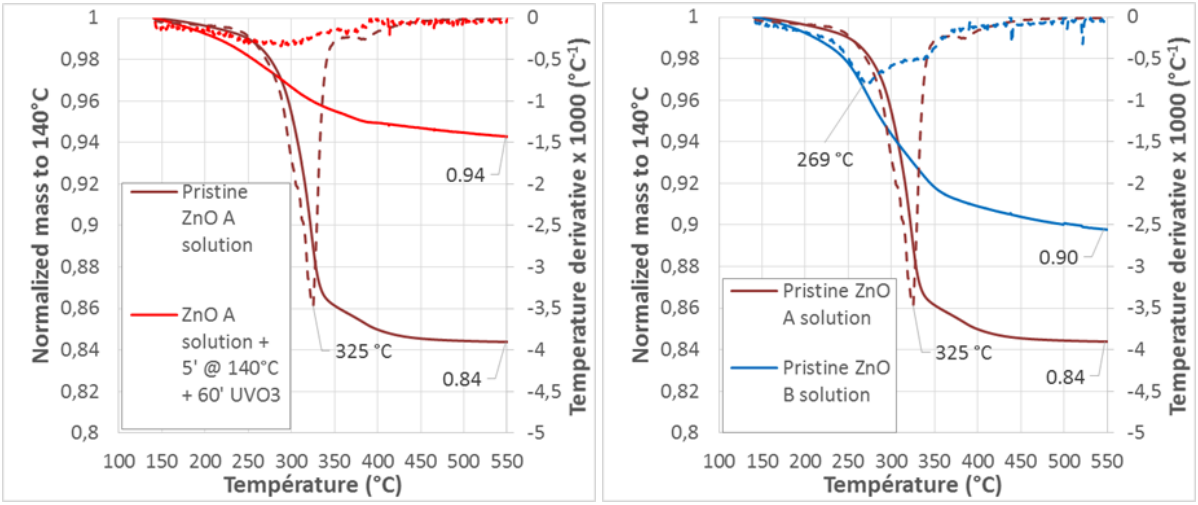

(a) *(b)*

Figure 4.14: *Normalized mass to 140 °C as a function of the temperature is shown with plain lines. Dashed lines represent the temperature derivative of this mass. All samples were kept at 140 °C for one hour in order to remove the solvent content. Temperature from 140 °C to 550 °C was then increased by 10 °C per minute. (a) represents a pristine ZnO A solution and a dry film treated for 60 minutes by UVO_3. (b) represents both ZnO A and B pristine solutions.*

derivative of this curve, the mass-loss rate peaks at 325 °C. This is in the range of reported decomposition temperatures of alkyl compounds in air [268].

For the ZnO A thick-film treated one hour by UVO_3, the measured mass-loss between 140 and 550 °C is less than 6 % suggesting that a significant amount of alkyl species were removed by the UVO_3 treatment. This result supports the conclusions drawn from the FTIR spectra that the UVO_3 treatment removes partially the alkyl compounds present in micrometer thick ZnO A films after drying.

The ZnO B curve features decomposition temperatures different from ZnO A suggesting different alkyl ligands nature in agreement with the FTIR spectra shown in Fig. 4.13. The alkyl weight fraction of pristine ZnO B after drying is 10 % which is lower than the pristine ZnO A dispersions.

In order to assess the effect of alkyl removal from the ZnO layers on the TCO/ZnO interface peeling strength, peeling tests were performed on TCO/ZnO/P3HT:PCBM/Ag stacks encapsulated by the PSA/R2R system. This stack is equivalent to a complete device whose PEDOT:PSS layer was removed. Such configuration allows us to measure the effect of the ZnO modifications by testing both the TCO / ZnO interface and the ZnO / P3HT without interference from the weak P3HT:PCBM / PEDOT:PSS interface. The left part of Fig.4.15 reminds the peeling strength of the three interfaces of interest measured separately on the reference stack. The right part of the figure shows the measured peeling strengths of PSA encapsulation/PET/TCO/ZnO/P3HT:PCBM/Ag/PSA encapsulation stacks with or without UVO_3 treatment or replacement of the ZnO A layer. At least 4 peeling samples were tested for each configuration.

From the study of the reference devices, the TCO / ZnO A (ref.) interface was identified as

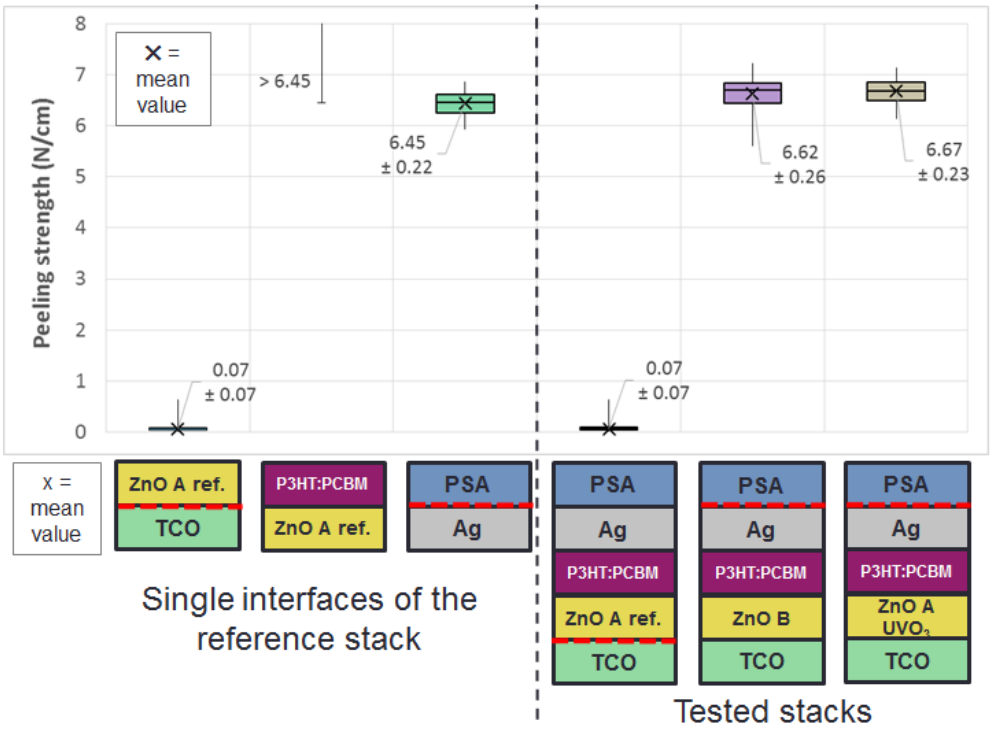

Figure 4.15: *(left) Reference peeling strengths of the relevant interfaces considered in this study. (right) Measured peeling strengths for tested configurations. Dashed red lines represent the rupture path during mechanical tests as characterized after debonding. For the sake of clarity, the symmetrical PSA encapsulation system and the PET substrates are not represented on the devices' schemes. At least four samples were tested for each configuration.*

the weakest interface of the devices with a 0.07 ± 0.07 N/cm measured peeling strength. The ZnO A (ref.) / P3HT:PCBM interface (and the P3HT:PCBM / Ag interface) was stronger than the Ag / PSA interface (6.45 ± 0.22 N/cm) between the devices' layers and the encapsulation. Therefore, its peeling strength was estimated to be above 6.45 N/cm.

On the quasi-complete reference devices the global peeling strength is limited to 0.07 ± 0.07 N/cm by the weak TCO / ZnO A (ref.) interface. The quasi-devices whose ZnO A layer was UVO_3 treated for 2'30 minutes or replaced by the ZnO B material yield strong peeling strengths above 6.6 N/cm and rupture at the Ag / PSA interface. As a consequence, for both improvement methods tested, the peeling strengths of both the TCO / ZnO and the ZnO / P3HT:PCBM are estimated to be stronger than the Ag / PSA interface > 6.45 N/cm. In addition, handmade scratch tests performed on all the improved samples and a ZnO A sample annealed at 400 °C for 10 minutes gave comparable scratch resistance while reference pristine ZnO A samples were scratched without effort.

Physico-chemical characterizations coupled to peeling tests strongly suggest that alkyl ligands present in the ZnO A films are responsible for the weak adhesion with the TCO layer. Such ligands can be removed by UVO_3 treatments performed after deposition and thermal annealing of the ZnO films. Finally, an other ZnO nanoparticles dispersion, featuring different alkyl ligands, also yields better adhesion with the TCO layer even without UVO_3 treatment. Complete alkyl compounds removal is therefore not mandatory in all cases to achieve good adhesion with the

TCO layer.

4.4.2 UVO_3 treatment of the ZnO A layer - Influence on the devices as-prepared and encapsulated performances

In the previous section, the TCO/ETL interface was mechanically improved by applying a UVO_3 treatment or replacing the ZnO materials. However, in addition to changing the mechanical properties, such processing variations are expected to bring change to the opto-electronic properties and the PV performances of the devices.

Furthermore, we demonstrated in Sec.4.1 and 4.2 that the broadly distributed, low performances of the devices after encapsulation by the PSA/R2R process were related to localized failure of the photo-generated charges transport. From mechanical characterizations performed on the reference devices in Sec.4.3, we proposed delamination between layers as the main mechanism causing such performance losses.
After strengthening by approximately two orders of magnitude the weak TCO/ZnO interface, we investigated the post PSA/R2R encapsulation PV statistics of the mechanically improved devices.

In this section, the impact of a 2'30 UVO_3 treatment performed after ZnO A deposition on the PV performances of as prepared and encapsulated devices will be assessed.
The impact on the PV performances induced by the replacement of ZnO A by ZnO B was not investigated as the observed differences may originate from several factors which are impossible to isolate (particles size and shape, chemical composition, layer morphology, energy level alignements...).

Fig.4.16a shows the J(V) curves of representative cells fabricated with or without a post-ZnO A deposition 2'30 UVO_3 treatment. Their curves were recorded just after fabrication and after their PSA/R2R encapsulation. Fig.4.16b shows the PV parameters extracted from 6 and seven cells with or without 2'30 minutes UVO_3 treatment on the ZnO layer, respectively. Parameters were acquired before and after PSA/R2R encapsulation on two separate studies.

From the data of as-prepared cells, shown in Fig.4.16 in pale colors, one can see that, on average, the UVO_3 treated cells yield a relative 12 % increased power conversion efficiency (PCE) compared to the reference cells. Such PCE increase is mainly driven by a 13% fill-factor (FF) increase, caused by a 20% series resistance (R_S) drop. Such R_S decrease is likely caused by the removal from the ZnO films of the relatively insulating alkyl species.

After their PSA/R2R encapsulation, shown in Fig.4.16 in dark colors, the reference devices show a typical behavior, in agreement with the previous results shown in Fig.4.2, with dispersed performance values with an average 70% ranging from 57 to 91% of their initial PCE. As shown in the previous section, such PCE losses are driven by J_{SC} and FF drops reaching 78% and 90%

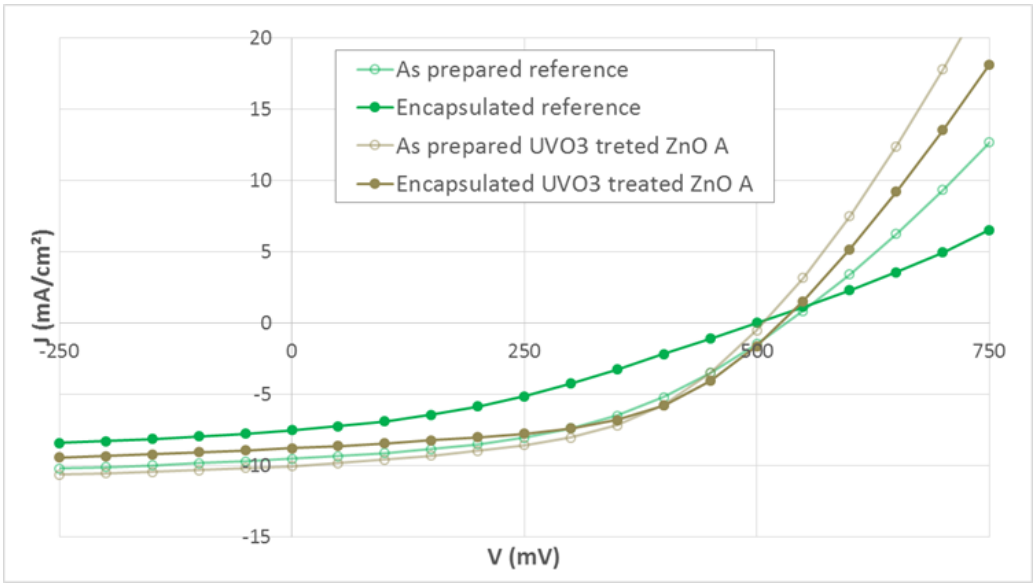

(a)

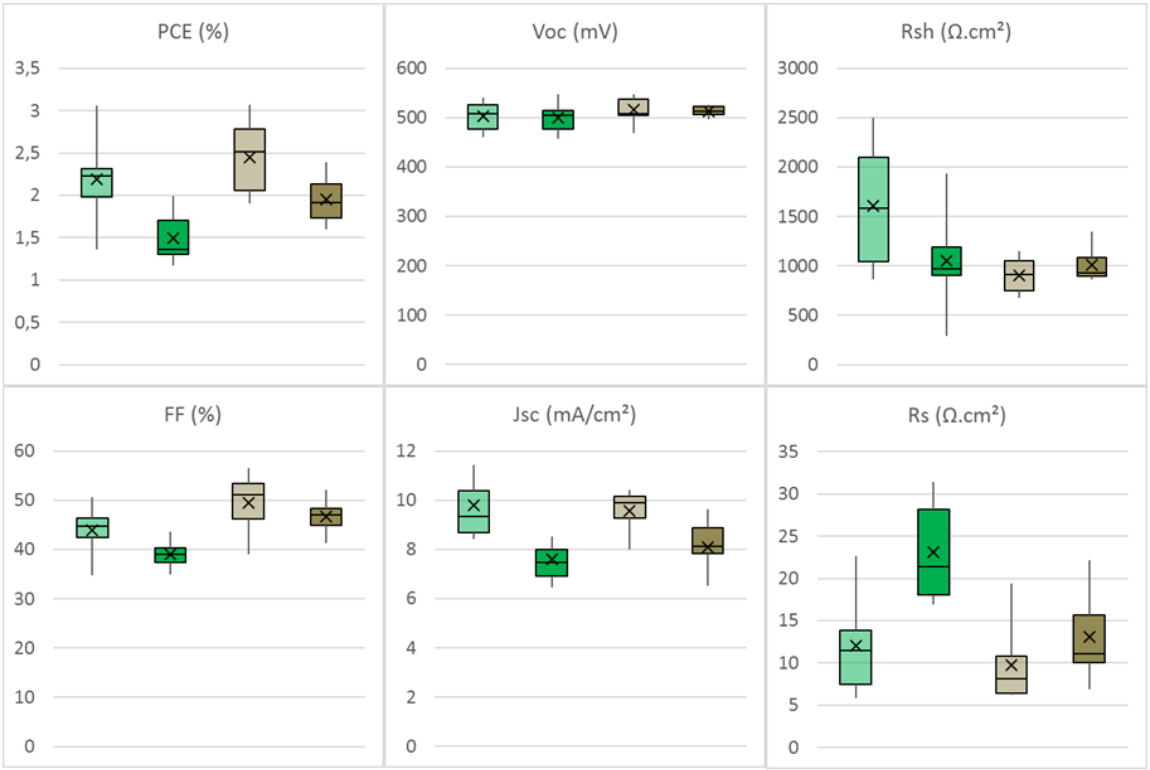

	PCE (%)	Voc (mV)	Jsc (mA/cm²)	FF (%)	Rs (ohm.cm2)	Rsh (kohm.cm2)
As prepared reference ZnO A	2.19 ± 0.56	502 ± 34	9.8 ± 1.5	44 ± 6	12 ±7	16.1 ± 6.8
Encapsulated reference ZnO A	1.50 ± 0.33	500 ± 34	7.6 ± 1.0	39.± 4	23 ± 7	10.5 ± 5.4
As prepared UVO_3 treated ZnO A	2.45 ± 0.48	515 ± 28	9.6 ± 0.9	50 ± 7	10 ± 5	9.1 ± 10.2
EncapsulatedUVO_3 treated ZnO A	1.95 ± 0.31	513 ± 12	8.1 ± 0.9	47± 4	13 ± 5	10.1 ± 1.9

(b)

Figure 4.16: *(a) J(V) curves of the hero cells after fabrication made with or without a 2'30 UVO_3 treatment of the reference ZnO A layer. (b) PV parameters of six cells each before and after a PSA/R2R encapsulation with or without a 2'30 UVO_3 treatment of the reference ZnO A layer.*

of their initial values, respectively. They are themselves driven by a strong 2.2 fold R_S increase. **Devices with the improved TCO/ZnO interface show on average 81 % of their original PCE ranging from 54 to 95%. They show 85% and 95% of their as-prepared J_{SC} and FF values and a limited 1.4 fold R_S increase.**
Such data strongly suggest that performance degradation of the reference devices induced by the PSA/R2R encapsulation, reflected by the J_{SC} and FF decrease and the R_S increase, is indeed at least partially related to mechanical degradation at the TCO / ZnO A interface and can be overcome at least partially by adhesion improvement.

The 2'30 UVO_3 treatment applied to the ZnO A, allows improved as-prepared performances and also mitigates the losses observed during the PSA/R2R encapsulation of the cells. As a consequence, the performances of the encapsulated improved cells (1.95 $\pm$ 0.31 % PCE) are 30% better than those of encapsulated cells without an improved TCO/ZnO interface (1.50 $\pm$ 0.33 % PCE).
Such results are achieved by the combined effect of the alkyl removal, decreasing R_S and increasing FF, and the smaller degradation observed during the PSA/R2R encapsulation process, limiting the J_{SC} and FF losses and R_S increases during encapsulation.

Improvement of the adhesion between the TCO and ZnO A layers was shown to have the side effect to increase performance of the cells at the end of their fabrication. Furthermore, although the UVO_3 treated devices still comprise a mechanically weak P3HT:PCBM / PEDOT:PSS interface, the observed performance decrease induced by the PSA/R2R encapsulation process is mitigated by the TCO / ZnO A adhesion improvement. This is an encouraging result suggesting that mechanical improvement of the P3HT:PCBM / PEDOT:PSS interface could further limit degradation during the PSA/R2R encapsulation process.

4.5 Mechanical improvement of the AL/HTL and HTL/metal electrode interfaces

4.5.1 P3HT:PCBM/HTL adhesion improvement strategies

The P3HT:PCBM / PEDOT:PSS was also identified to be a mechanically weak interface with a measured peeling strength of 0.17 $\pm$ 0.14 N/cm. Such weak adhesion is reported in the literature as a consequence of the lack of interpenetration between both layers [91, 149, 163].

In order to focus on the improvement of the AL/HTL interface improvement, all cells and peeling samples tested in this section were made with the 2'30 UVO_3 treatment of the ZnO A layer, improving the TCO/ZnO A originally weak interface.

Here we present the different possible strategies to improve the AL/HTL interface.

Thermal annealing after PEDOT:PSS deposition. In the literature, a 10 minutes 130 °C thermal annealing was found to promote an interpenetrated interface between the active and hole-transport layers which increases adhesion up to a factor 3 [163].

In our case, a 10 minutes 120 °C thermal annealing is routinely applied in our reference process immediately after deposition of the PEDOT:PSS HTL layer. Samples annealed for up to 30 minutes after the HTL deposition were mechanically tested but have shown no measurable improvement of the peeling strength. Longer annealing times or higher temperatures were not tested because of the PET substrate limited tolerance against heat and the possible thermal degradation of the active layer morphology [89].

PEDOT dispersion formulation. The limited interpenetration of both layers can be explained by the orthogonal hydrophilic solvents used in most PEDOT:PSS solutions as compared to the hydrophobic active layer.

Our reference HTL formulation (Clevios CPP105D from Heraeus) is an aqueous dispersion of PEDOT:PSS. A surfactant and an adhesion promoter are already present in the commercial CPP105D solution [227]. As a consequence of the mismatch between the hydrophobic P3HT:PCBM layer and the aqueous HTL dispersion and despite the surfactants in the dispersion, a poor wettability of the CPP105D solution on the dry active layer is observed during HTL deposition. Such poor wettability, thus such poor phase mixing, subsequently limits interpenetration and can create voids at the interface both which ultimately lead to weak adhesion between both dried layers.

A PEDOT-complex dispersion in butylbenzoate, Clevios HIL 8 from Heraeus, was chosen for testing. Experimentally, this solution as well exhibited poor wettability on the P3HT:PCBM active layer.
It however showed a good miscibility with ortho-xylene, a solvent able to dissolve our active layer. So, in order to dissolve the surface of the active layer and to promote the creation of a mixed interface upon drying of the HTL, o-xylene was mixed, from a 0.5 % to a 10 % volume ratio, to the HIL 8 pristine solutions. Spin coating of the reformulations were then performed with our reference HTL deposition parameters and the cells were annealed for 10 minutes at 120 °C on a hot plate immediately after coating.
As a result, all cells prepared with such reformulated HTL solution were short-circuited, suggesting that o-xylene, even in the lowest concentration, was able to dissolve (at least locally) the whole active layer thickness of $\approx$ 400 nm and not only its surface. No obvious improvement of the adhesion was observed with handmade adhesive tape tests or scratch tests with pliers.

Such reformulation of a PEDOT HTL with an active layer solvent indicated that there should be a delicate balance of the o-xylene concentration in order to dissolve only the top surface of the active layer. Furthermore, no guarantee of adhesion improvement was obviously drawn from the first experiments performed; we therefore abandoned such experiments in order to focus on other ideas.

Metal-oxide HTLs. Another strategy explored in the literature is the employment of metal oxide HTLs instead of PEDOT based ones.

Dupont *et al.* observed a two order of magnitude increased fracture energy for R2R processed P3HT:PCBM inverted OPV cells with a 130 to 185 nm thick V_2O_5 HTL layer compared to a 200 nm thick PEDOT:PSS reference [167].

In stark contrast, 30 nm thick thermally evaporated MoO_3 layers were shown to yield even lower adhesion to the active layer than their reference PEDOT:PSS [149]. 10 nm thick MoO_3 and WO_3 HTL layers processed by electron-beam deposition also showed limited adhesion compared to the thick V_2O_5 layers [94].

From these studies, no general rule stating that metal oxide HTLs yield better adhesion with P3HT:PCBM than polymeric HTLs can be drawn. This suggests that stronger interactions between oxides and the active layer are not sufficient to explain alone the strong adhesion observed with V_2O_5.

However, specifications for a metal oxide HTL layer yielding a good adhesion to the active layer can be defined:

1. **Layer morphology** The V_2O_5 layers were significantly thicker (130-185 nm) compared to the MoO_3 and WO_3 ones ($\leqslant$ 30 nm). In addition, a more than two-time increased adhesion was observed for 185 nm thick V_2O_5 layers compared to 130 nm thick ones. Such relatively thick layers were shown to develop a particular roughness and microscopic cracks [185]. Such HTL roughness favors interpenetration of both layers and cracks can create anchor points for P3HT chains to fill, further increasing the overall adhesion.
   In the literature [94, 118, 189, 269], metal oxide layers thicknesses are of a few tens of nanometers in order to limit the series resistance brought by the relatively insulator nanoparticles.

2. **Deposition processes** The V_2O_5 HTL layer was deposited by a solution-process slot-die coating technique while MoO_3 and WO_3 were deposited by thermal evaporation or electron-beam techniques. The former deposition method tends to favor intermixing between both layers at their interface which is often required in order to achieve good bonding between two surfaces. Indeed, a 10 nm thick interpenetrated interface between the active layer and the solution-processed V_2O_5 layer was evidenced by XPS depth-profiling. Such results strongly suggest that solution-based deposition methods favor adhesion between the active and hole-transport layers.

3. **Electronic properties** Finally, to be a relevant HTL material, the metal oxide layer must have electronic levels suitable to the transport of holes while preventing the transport of electrons. This energy level, called the electronic work function, is at -4.7 eV for our reference PEDOT:PSS HTL [64]. This value represents a target for enabling good functionality of our HTL layer.

From such specifications, we tested the solution-processed deposition by spin-coating of WO_3 nanoparticles dispersed in isopropanol. According to the product data sheet, the particles should have a 7 nm diameter. Dynamic light scattering experiments performed prior to use showed a diameter range from 20 to 190 nanometers. According to the data sheet and the literature [189, 270], its work function is located between -5.5 and -5.3 eV; such energy levels are deep enough to allow a suitable use as HTL material. The HTL layers were subsequently annealed for 10 minutes at 120 °C in a nitrogen atmosphere in order to dry solvents in a similar fashion than our reference PEDOT:PSS layer.

Stoichiometry of metal oxides depends heavily on the synthesis conditions as well as the environment they are exposed to [189, 270, 271]. A more correct name would be WO_x, however, as commonly accepted in the literature, we denote the tungsten oxides as labeled by the supplier: WO_3 even though the deposited films are likely to be non-stoichiometric.

4.5.2 P3HT:PCBM/WO_3 adhesion improvement

Peeling tests were performed on PSA encapsulation / PET / TCO / UVO_3 treated ZnO A / P3HT:PCBM / WO_3 / PSA encapsulation samples.

Fig.4.17 summarizes the measured peeling strengths and rupture locations observed on such samples. Several spin-coating speeds, expressed in rotations per minute (rpm), leading to different film thicknesses, were tested for WO_3 layers annealed for 10 minutes at 120 °C. An additional 1000 rpms coated WO_3 layer without annealing was tested as well. In this campaign, only two samples per architecture were tested (against four in other campaigns). Therefore the statistical information is less relevant than for other data presented in this work.

Unlike the reference samples which ruptured at the P3HT:PCBM/PEDOT:PSS interface with an almost negligible 0.17 ± 0.14 N/cm peeling strength, all the annealed WO_3 samples debonded at the WO_3/PSA interface with an average 10.2 ± 0.7 N/cm peeling strength. The P3HT:PCBM/annealed WO_3 interface is thus necessarily stronger than the WO_3/PSA interface for all the tested WO_3 spin coating speeds. **Its peeling strength is therefore at least 60 times higher than the reference interface.**

In addition, the measured peeling strength of the 1000 rpms WO_3 stack annealed for 10 minutes at 120 °C in a nitrogen atmosphere is 10.9 ± 0.1 N/cm in stark contrast with the same stack without WO_3 annealing, which features a 0.9 ± 0.4 N/cm peeling strength. This shows that thermal annealing is required to obtain the high peeling strength desired.

The P3HT:PCBM/WO_3 relatively strong adhesion, most likely related to their intermixing at the interface, is expected to be influenced by two factors: the use of a solution-based deposition process and the morphology of the interface. However, only the annealed WO_3 layers were shown to yield good adhesion values; the influence of the deposition process alone is therefore thought to be limited.

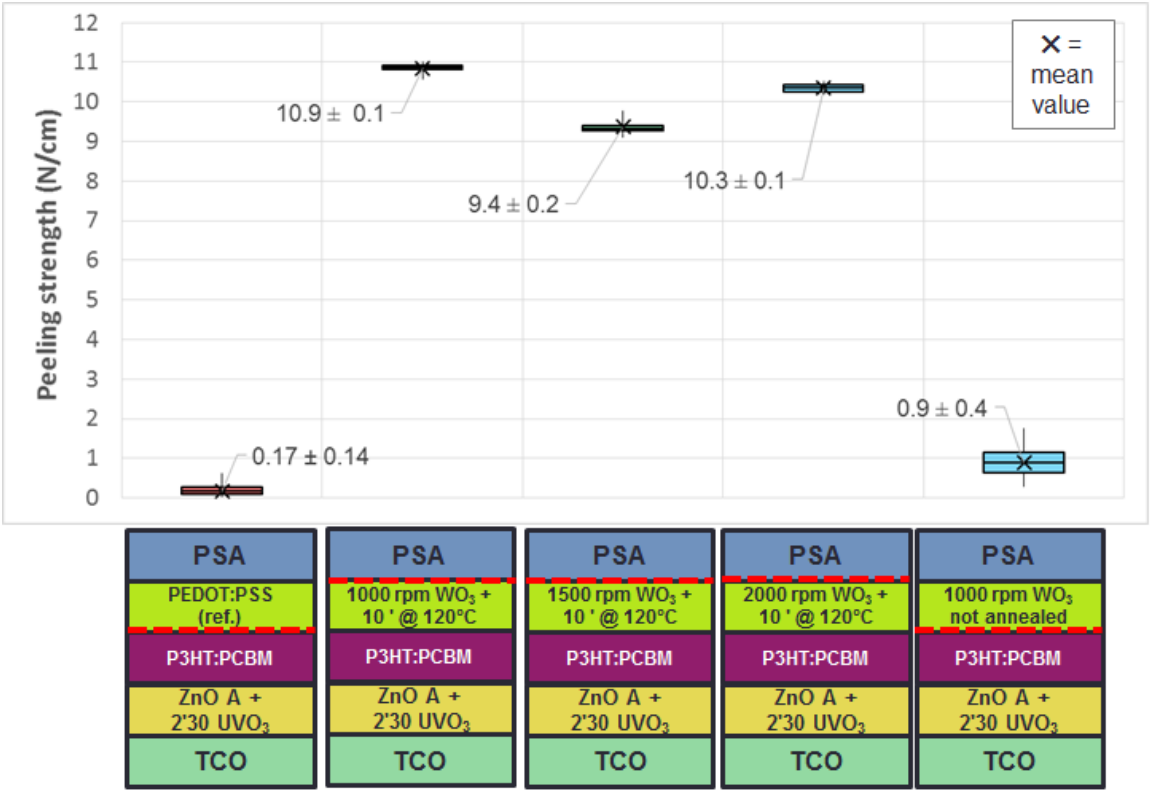

Figure 4.17: *Measured peeling strengths during the HTL replacement study. Reference PEDOT:PSS was replaced by WO_3 deposited with several spin-coating speeds and annealed for 10 minutes at 120 °C. Samples coated at 1000 rpms without subsequent annealing was tested on the far right. Dashed red lines represent the rupture path during mechanical tests as characterized after debonding. For the sake of clarity, the symmetrical PSA encapsulation system and the PET substrates are not represented on the devices schemes.*

In order to investigate the morphology of the WO_3 layers, mechanical profilometry and optical microscopy were performed on the WO_3 layers.

WO_3 layers were spin-coated at different speeds on a reference P3HT:PCBM layer previously deposited on a cleaned glass substrate. They were subsequently annealed for 10 minutes at 120 °C in a nitrogen atmosphere. Fig.4.18 shows the roughness profile of two such layers recorded over a 1 cm length with a mechanical profilometer. Mean thicknesses and their associated standard deviations were calculated on the 20 000 sampling points composing both profiles. Adhesive tape was placed on half the active layer area before WO_3 deposition in order to create a clear step allowing us to easily set the zero height of the WO_3 layers profiles.

WO_3 layers were shown to be 45 and 71 nm thick for the 2000 rpm and 1000 rpm deposition speeds, respectively.

Such layers, and especially the 1000 rpm layer, feature two different kinds of roughnesses: a macroscopic roughness of ≈ a hundred nm thick over several hundreds of micrometers large and a microscopic roughness a few nm deep distributed on the whole layer surface.

Our HTL layers are thicker than those optimized in most publications using metal oxides as HTLs. This is expected to cause high series resistance to our devices due to the thickness of such relatively insulating layer. However, thick WO_3 layers allows us to limit the probability to have

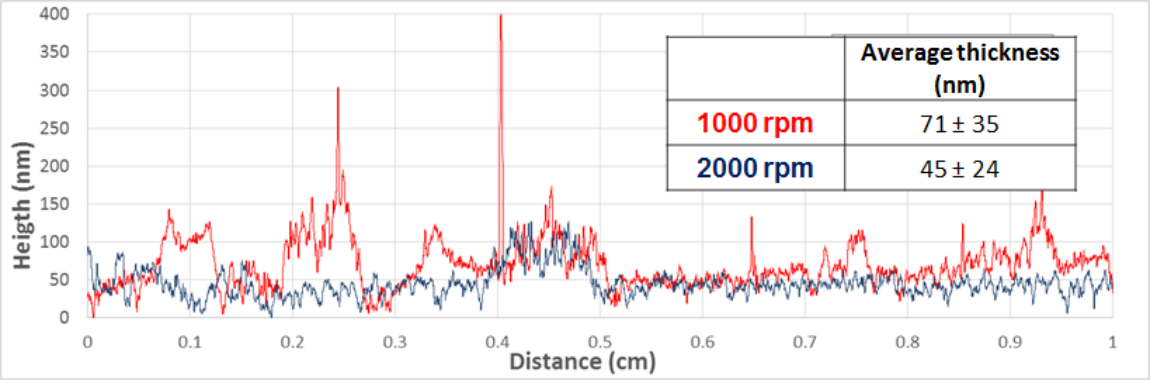

Figure 4.18: *Surface profile of two WO_3 layers deposited on a P3HT:PCBM layer as a function of the spin-coating speed. A thermal annealing of 10 minutes at 120 °C in a nitrogen atmosphere was then performed. Zero height was determined from the step measured between an area without WO_3 next to the layer.*

holes in the films due to their strong roughnesses compared to their thicknesses. We therefore chosed the 1000 rpm rotation speed as our reference layer deposition speed.

In order to further investigate the macroscopic roughnesses, deposition and thermal annealing of the WO_3 layer were followed by optical microscopy during each fabrication step of an actual OPV cell deposited by spin-coating on a flexible PET substrate. Fig.4.19 shows optical micrographs of the active layer prior to HTL deposition, a WO_3 layer spin-coated at 1000 rpms immediately after deposition, the same layer after a 10 minutes annealing at 120 °C in a nitrogen atmosphere and a micrograph from the literature of a V_2O_5 layer annealed for 2 minutes at 140 °C.

The WO_3 layer just after deposition is a relatively homogeneous film with several aggregates of a few micrometers of diameter. Behind such relatively large grains, a white trail indicating a thinner layer, typical of spin coated solutions with aggregates, can be observed. Such macroscopic grains are thought to be responsible for the large inhomogeneities seen on the roughness profiles described in Fig.4.18. This observation suggests that an ultrasonic treatment step should be performed on the dispersion in order to break such macro aggregates. An additional filtering should be performed as well prior to deposition of the layers.

After thermal annealing for 10 minutes at 120 °C in a nitrogen atmosphere, the layer shows numerous microscopic cracks, similar to those observed in the literature [185]. Such cracks are likely to be responsible for the microscopic roughness observed on the profiles. Due to the mechanical profilometer tip size, larger than the cracks width, it is possible that the cracks are significantly deeper than the heights measured on the roughness profiles.

A significant increase of the adhesion between the active and HTL layers was observed when the PEDOT:PSS HTL material was replaced by WO_3. Such adhesion increase was only observed when annealing WO_3 for 10 minutes at 120 °C. It is likely related to the increased intermixing at the P3HT:PCBM/WO_3 interface enabled by the temperature above P3HT T_g of 56 °C [88]. The coincidental appearing of macroscopic cracks in the WO_3 layer during thermal annealing

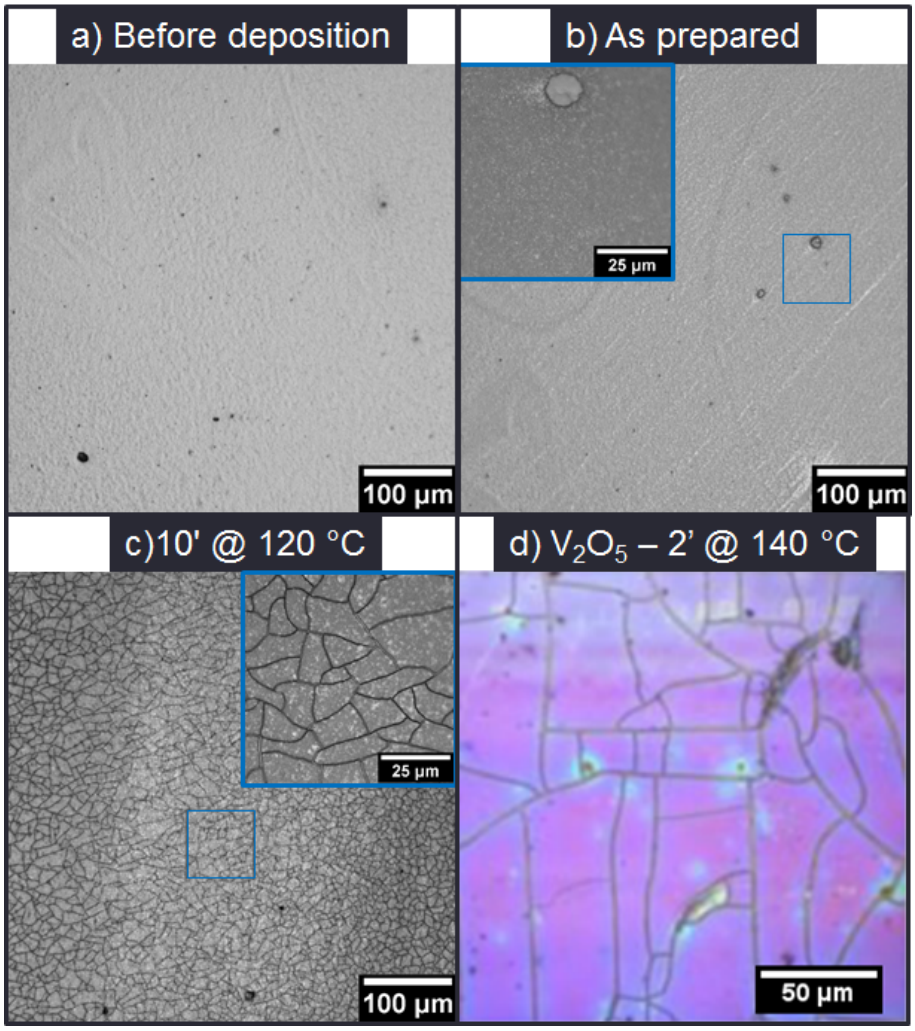

Figure 4.19: *10 times magnified optical micrographs of a) the active layer prior to HTL deposition, b) a WO_3 layer spin-coated at 1000 rpms on the P3HT:PCBM layer c) the same WO_3 layer after a 10 minutes thermal annealing at 120 °C. Insets are 50 times magnifications of the areas in the blue squares. d) Optical migrograph reproduced from [185] showing a V_2O_5 layer annealed for 2 minutes at 140 °C.*

may also increase the macroscopic adhesion as the cracks may play the role of anchor points for P3HT chains to fill during annealing.

4.5.3 WO3/metal electrode adhesion improvement

In the previous section, in order to isolate on the P3HT:PCBM/HTL interface, we focused our investigation on the mechanical properties of complete OPV stacks with the exception of the silver metal electrode. As developed in Sec.3.2, the peeling samples are divided in regions with or without evaporated silver in order to simulate the behavior of a device with a back electrode in a comb geometry. The complete peeling curves and the associated rupture path of a 1000 rpms annealed WO_3 sample are shown in Fig.4.20.

In the area without silver back electrodes, one can see a strong peeling strength of 10.9 ± 0.1 N/cm, in agreement with the previously presented results, showing an effective improvement of the P3HT:PCBM/WO_3 interface. However, compared to the reference PEDOT:PSS/Ag interface

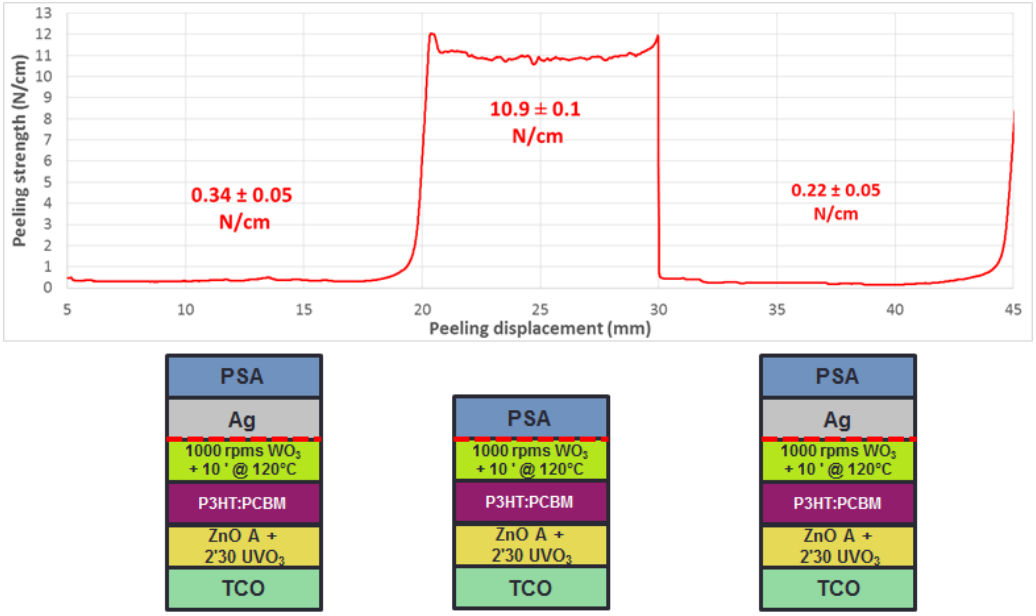

Figure 4.20: *Peeling curve of a 1000 rpms WO_3 sample annealed 10 minutes at 120 °C. Regions with a silver electrode show significantly weaker peeling strength than regions without. Dashed red lines represent the rupture path during mechanical tests as characterized after debonding. Mean peeling strength and standard errors measured between 7.5-17.5, 22-27 and 32.5-42.5 mm peeling displacement are displayed.*

which was estimated in Fig.4.9 to give peeling strengths above 6.45 N/cm, the WO_3/Ag interface is significantly weaker, with an average 0.3 ± 0.1 N/cm peeling strength.

The WO_3/metal electrode interface therefore requires improvement of its mechanical properties in order to be able to strengthen the device as a whole.

Once again, a relevant improvement strategy is to increase interpenetration of both layers at their interface. As suggested in section 4.5.1, a good method to improve interpenetration is to use solvent based deposition processes instead of evaporation processes in order to maximize the contact area between both layers and to promote anchor points-based adhesion mechanisms. This idea seemed promising as it could exploit the cracks observed in the WO_3 annealed layers by filling them with silver nanoparticles dispersed in a solvent.
However, peeling tests performed on samples whose ≈ 350 nm thick back electrodes were deposited either by inkjet-printing of a silver-nanoparticles paste or by thermal evaporation yielded similar results, with on average 0.2 ± 0.3 N/cm peeling strengths versus 0.2 ± 0.1 N/cm, respectively. No further investigations were performed after debonding to investigate the penetration of jetted silver nanoparticles in the WO_3 cracks.

Alternatively, a strategy exploiting both the strong P3HT:PCBM/WO_3 and PEDOT:PSS/Ag interfaces was to use a P3HT:PCBM/WO_3/PEDOT:PSS/Ag bilayer-HTL architecture. However, such architectures yielded no mechanical improvement as the measured peeling strength was 0.1 ± 0.1 N/cm. Rupture occurred at the AL/WO_3 interface. Because of the greater complexity of such architecture, we did not further investigate this potential improvement path.

Another strategy is to replace the silver electrode by other conductive materials. Adhesion between metal-oxides and metals is mostly investigated in the field of ceramics where annealing treatments with temperatures far above our limits are commonly performed. However, a general rule of thumb concerning the adhesion can be drawn from the literature [272–278]: the lower the free enthalpy of oxide formation of a metal electrode, the more adhesion with an oxide surface should be expected. A crude indicator of such oxide formation readiness can be found in the standard redox potentials of the corresponding metals. The lower the standard reduction potential is, the higher the adhesion can be expected. Such theory implicates a direct contact between the oxide nanoparticles and the metal electrode; we will therefore assume that there is no outer shell on the particles.

We therefore tried to replace the reference silver electrode by other metals more prone to oxidation. Fig.4.21 summarizes the different evaporated electrode materials tested in this study, their lowest standard reduction potentials, the associated redox couples and the measured peeling strengths of at least 4 samples for each material. Peeling tests were performed on complete samples with a UVO_3 treated ZnO A layer and a thermally annealed for 10 minutes at 120 $^{\circ}$C WO_3 layer. Standard reduction potential were found in ref. [231]. Electrode materials are sorted from left to right according to a decreasing standard reduction potential, i.e. an increasing expected adhesion.
The reference evaporation process was used for all electrode materials. Due to its very limited stability toward water [279], calcium was used as a thin 20 nm electrode layer protected by a thicker 200 nm aluminum layer on top of it. In addition, because chromium is often reported to be a good interlayer for promoting metal adhesion in general [280–282] and in the OPV literature [283] ,we tested a configuration with a 10 nm thick chromium interlayer between the HTL layer and the reference silver electrode.

All tested metal electrodes, at the exception of the nickel electrodes, yielded poor peeling strengths, less than 0.4 N/cm average, during mechanical testing of the samples. From a basic visual inspection, such poor peeling strengths were all associated with a WO_3/metal rupture, similar to the silver reference devices. In stark contrast, nickel electrodes failed adhesively at the metal/PSA interface with an average 9.0 ± 0.5 N/cm peeling strength. Such results, surprising at the first sight, were confirmed on three different testing campaigns made of four samples each.

The measured peeling strengths are not correlated to the standard reduction potentials of the metal electrodes. This strongly suggests that electro-chemical constants are not relevant to explain the high WO_3/Ni adhesion.

Tungsten trioxide is known to be able to form bronzes with some metal structures [284]. Among the metals we tested, only nickel, to our knowledge, is able to form such bronze structure shown in Fig.4.22.

Such bronze species are perovskite structures made of nickel atoms at the corners of the cubic lattice, with a tungsten atom at its center and oxygen atoms on the face centers. The

Evaporated metal electrode	Ag 100 nm (ref.)	Cu 100 nm	Ni 100 nm	Cr 10 nm + Ag 100 nm	Cr 64 nm	Al 200 nm	Ca 20 nm + Al 200 nm
Lowest standard reduction potential (V)	+0,80	+0,34	-0,26	-0,91	-0,91	-1,66	-3,80
Corresponding redox couple	Ag^{+}/Ag	Cu^{2+}/Cu	Ni^{2+}/Ni	Cr^{2+}/Cr	Cr^{2+}/Cr	Al^{3+}/Al	Ca^{+}/Ca

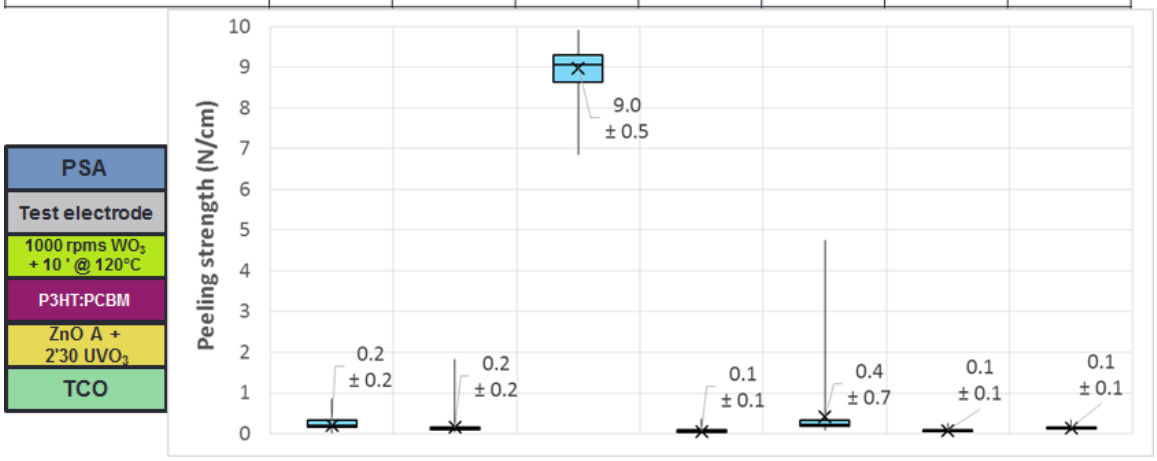

Figure 4.21: *Comprehensive list of the evaporated metal electrodes tested in this work. For each material, the lowest standard reduction potential of the metal, the corresponding redox couple, and the box plot representation of the peeling test measured on at least four samples made with such electrode are given. The materials are sorted from left to right according to a decreasing standard reduction potential i.e. an increasing expected adhesion according to the theory described in this section. Standard reduction potential values were found in [231].*

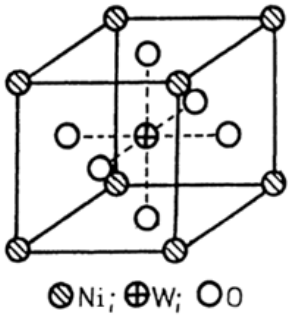

Figure 4.22: *Nickel/WO_3 bronze structure. Modified from [284].*

formation of such structures at the interface between the WO_3 and Ni layers may be a possible explanation for the higher adhesion observed with nickel electrodes. However, WO_3 bronzes are scarcely described in the literature for metals other than sodium. Therefore, the formation of such interfacial crystalline structures should be demonstrated before drawing any conclusions. A stronger interaction of a possible outer shell of the WO_3 nanoparticles with the Ni electrode may be another possible explanation.

Complete peeling samples fabricated with all our mechanical improvements rupture adhesively between the PSA encapsulation system and the top electrode of the OPV devices with an average 9.0 $\pm$ 0.5 N/cm peeling strength. It means that **all the interfaces within the device are stronger than this 9.0 N/cm peeling strength. This represents a more than two orders of magnitude increase compared to the 0.05 N/cm global peeling strength measured on the**

reference device comprising both the TCO/ZnO and the P3HT:PCBM/PEDOT:PSS weak interfaces.

Interestingly, we did not observe any cohesive rupture within the active layer as often reported in the literature when the P3HT:PCBM / PEDOT:PSS interface is strengthened. The interface between PCBM rich and P3HT rich domains is reported to be particularly weak due to the limited interpenetration between both phases [166]. Therefore, such interfaces are stronger in our devices than in those reported in the literature.

4.5.4 HTL and electrode materials replacements - Effect on the devices initial performances

Due to the numerous interrelated properties required from each OPV layer for the good operation of the complete devices, replacing two of the layers is expected to have a great impact on the devices performances. The PV performances of the devices with improved mechanical properties will be studied in this subsection.

PV performances of adhesion enhanced cells. Fig.4.23 shows PV performances after fabrication of four sets of three cells each. From left to right, the cells were mechanically improved sequentially, from the reference devices on left, with an improved TCO/ETL interface, adding an improved AL/HTL interface and finally the completely improved devices on the right column of the graphs.

Due to an evaporation equipment failure which occurred during fabrication of this set of cells, the Ni electrodes thickness was 67 nanometers instead of the desired 100 nm. Although such thickness variation is expected to have an impact on the devices electrical performances, we assume that adhesion with the WO_3 underlying layer is related to interfacial interactions and is thus not affected.

In agreement with the larger statistics presented in Sec.4.4.2, UVO_3 treatment of the zinc oxide layer brings a moderate improvement to the performances of the devices, from 2.47 ± 0.06 % to 2.60 ± 0.05 % PCE, by decreasing the series resistances and therefore slightly improving the fill factor values.

Devices whose PEDOT:PSS HTL layer was replaced by WO_3 yield significantly lower performances from 2.60 ± 0.05 % to 0.66 ± 0.18 % PCE. A R_S increase, decreasing J_{SC} and a large R_{SH} decrease, decreasing V_{OC} are observed. Both resistance parameters evolution negatively affect the fill factor value. Globally, the diode rectifying properties of the WO_3 cells were significantly worse than the PEDOT:PSS ones.

The R_S increase (and the related J_{SC} decrease) was expected to some extent. Indeed, the replacement of the conductive PEDOT:PSS layer (a few hundreds of $S.cm^{-1}$ [285]) by a relatively insulating metal oxide layer of comparable thickness (values ranging from 10^{-4} to 10^{1} $S.cm^{-1}$ for vacuum annealed films [286, 287]) is expected lead to a series resistance increase.

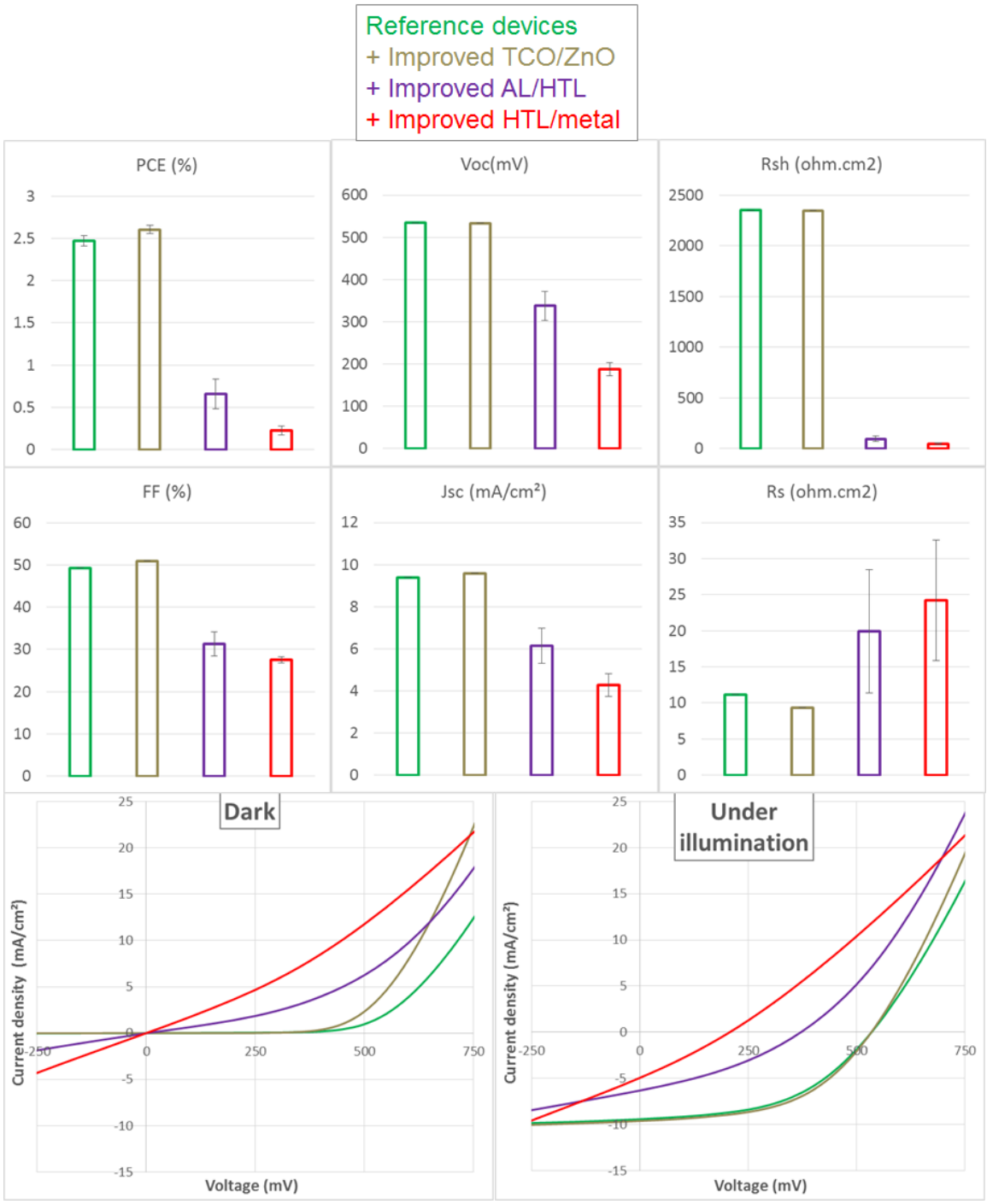

Figure 4.23: *PV parameters after fabrication of four sets of three cells each. From left to right, mechanical improvements of the TCO/ETL, AL/HTL and HTL/metal electrode interfaces were sequentially performed.*

Furthermore, the literature generally advises the use of metal oxide layers no thicker than 10 nm in order to limit such resistive losses [94, 118, 189, 269, 288]. However, for the early studies performed in this work, WO_3 film thicknesses of 71 nm were chosen in order to reduce the probability of holes in the films. Reducing the WO_3 layer thickness by increasing the spin-coating speed should reduce the R_S value. In Sec.4.5.1, we showed that peeling strengths were strongly increased at least for coating speeds slower than 2000 rpm (i.e. thicker layers).

The R_{SH} loss was further investigated and will be discussed in the next paragraph.

Replacement of the 100 nm silver electrode by a thinner 67 nm Ni electrode also caused an

additional performance loss from 0.66 ± 0.18 % to 0.22 ± 0.05 % power conversion efficiency. The WO_3/Ni cells suffer the same emphasized symptoms already observed on the WO_3/Ag cells. The rectifying properties of the cells were worsened compared to the already damaged WO_3/Ag ones.

The R_S increase and associated J_{SC} decrease can be explained by the electrical conductivity of the selected metals and their thicknesses. According to ref.[231], nickel conductivity ($\sigma_{Ni} = 1.44 \times 10^7\ S/m$) is roughly four times lower than silver ($\sigma_{Ag} = 6.30 \times 10^7\ S/m$). Therefore replacing the silver electrode by a nickel electrode is expected to increase the cells series resistances. The Ni electrode thickness is yet to be optimized to improve its conduction efficiency. Geometry of the cells should not need to be changed as the TCO is still the most resistive electrode ($\sigma_{IZO} \approx 10^4\ S/m$) of the cells, according to the literature [223, 224, 289].

WO_3 layers properties. As shown on the previous paragraph, the rectifying properties, i.e. the ability to drive electrons and holes to their respective terminal, quantified by the R_{SH} parameter, of the WO_3 HTL cells compared to the PEDOT:PSS HTL ones were significantly lower. A selective transport layer can fail either because it does not transport well-enough its affinity charges or because it does not form an energetic barrier towards the opposite charges.

According to Fig.4.23, no "S-shape", reverse diode effect is observed on the WO_3 J(V) curves. This suggests that WO_3 fails at preventing electrons to reach the metal anode, rather than at transporting holes.

In addition, comparing the WO_3/Ag curve to the WO_3/Ni one, one can see the rectifying behavior of the nickel sample is even worse than with silver. According to ref.[231], the work function of nickel (Wf_{Ni} = 5.04-5.35 eV) is higher than silver (Wf_{Ag} = 4.52-4.74 eV). It means that electrons will more easily transfer to nickel rather than silver. Such data suggest that the silver and nickel electrodes are exposed to electrons that were able to pierce through the WO_3 selective hole transport layer.

Furthermore, J(V) curves and PV parameters of representative cells with a WO_3, PEDOT:PSS or a bi-layer of standard WO_3/PEDOT:PSS HTL are shown in Fig.4.24. Such bi-layer HTL architecture was shown in the previous section to have unsatisfying mechanical properties.

The same observations made on Fig.4.23 can be drawn from comparing the PEDOT:PSS and WO_3 cells J(V) curves. Particularly, the J(V) curve of the WO_3 cell features low diode rectification properties compared to those of PEDOT:PSS. Interestingly, inserting a PEDOT:PSS layer between the WO_3 and electrode layers recovers the superior V_{OC} and R_{SH} observed with the lone PEDOT:PSS layer. J_{SC} and FF are still impacted by the R_S increase due to the presence of the relatively insulating thick WO_3 layer in the bi-layer cells.

If WO_3 induced a hole blocking behavior, the addition of a PEDOT:PSS would not drastically change the J(V) curves. Such data is another evidence that the WO_3 layers are not preventing electrons from reaching the metal anode.

Such electron leakages through the HTL layer can originate from two factors: voids

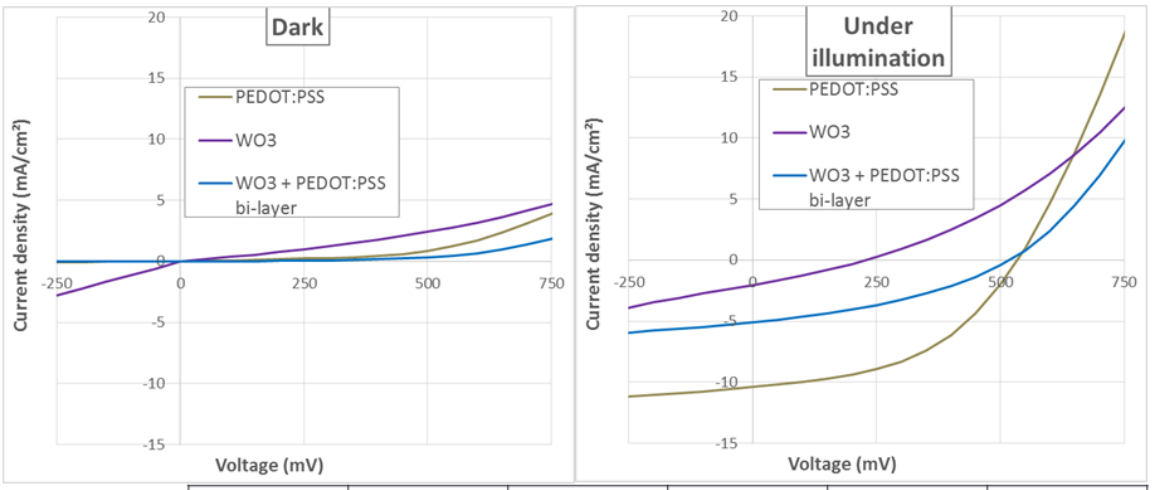

	Voc (mV)	Jsc (mA/cm²)	FF (%)	PCE (%)	Rs (ohm.cm2)	Rsh (ohm.cm2)
Reference PEDOT:PSS	533	10.4	47.1	2.60	13.5	2230
WO_3	227	2.0	29.2	0.13	34.2	100
WO_3 + PEDOT:PSS bilayer	516	5.1	37.4	0.98	24.7	2120

Figure 4.24: *J(V) curves in the dark or under illumination and extracted PV parameters of three representative cells with a PEDOT:PSS, WO_3 or bilayer WO_3 + PEDOT:PSS HTL.*

in the HTL layer allowing direct contact between the active layer and the electrodes or undesirable energy levels within the WO_3 layer allowing electrons to be transported.

WO_3 layers morphology In order to gain insight on the layers homogeneity, optical micrographs taken on PEDOT:PSS and WO_3 layers deposited on P3HT:PCBM and annealed for 10 minutes at 120 °C in a nitrogen atmosphere are shown in Fig.4.25. To reduce the amount of macroscopic aggregates observed on WO_3 layers in Fig.4.19, a 15 minutes indirect ultrasonic treatment of the WO_3 vials in a water bath and filtering through a 0.45 µmeter PTFE filter were performed.

On a macroscopic scale, the WO_3 layers show slightly less defects than PEDOT:PSS. Indeed, PEDOT:PSS often forms large aggregates easily visible with the bare eye. Macroscopic WO_3 aggregates observed in Fig.4.19 seemed to have been successfully eliminated by the ultrasonic and filtering procedures introduced.

In contrast, on the microscopic scale, the layers have a significantly different morphology. the PEDOT:PSS layer forms an homogeneous layer (the gray background) with numerous aggregates (the black dots). As observed previously, the WO_3 layer forms relatively homogeneous layers which crack upon thermal annealing at 120 °C. It is yet to be investigated if a direct contact between the active layer and the electrode is possible through such cracks and if the cells behave well without such cracks.

6 cells, two per condition, either with a PEDOT:PSS HTL layer annealed for 10 minutes at

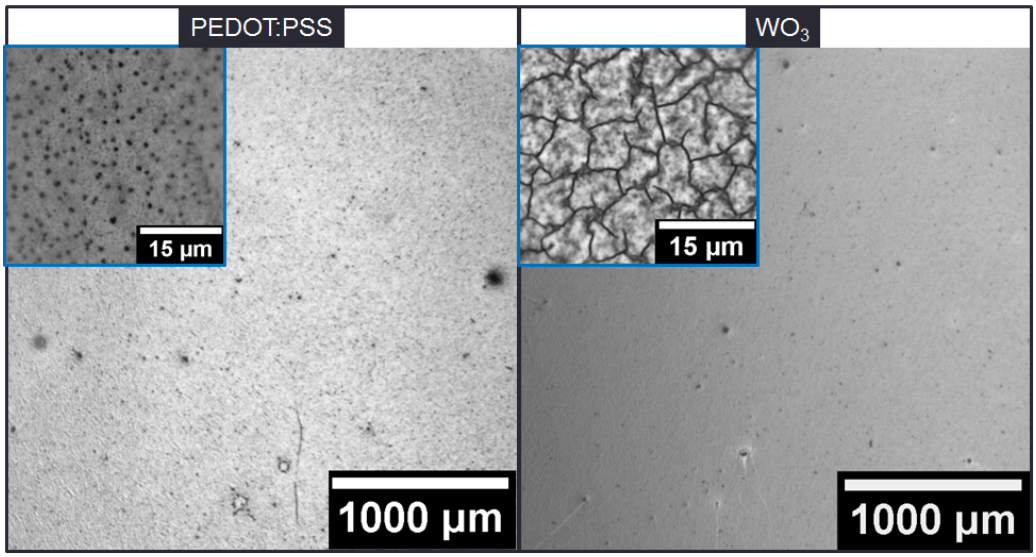

Figure 4.25: *1.25 times magnified optical micrographs of PEDOT:PSS and WO_3 layers deposited on P3HT:PCBM and annealed for 10 minutes at 120 °C in a nitrogen atmosphere. Insets were magnified 50 times.*

120 °C in a nitrogen atmosphere or with an as-prepared or annealed for 10 minutes at 120 °C WO_3 HTL layer were prepared. A reference silver electrode was deposited as back electrode layer.

Corresponding J(V) curves and PV parameters of 3 representative cells are shown in Fig.4.26.

The reduced number of samples does not allow us to be conclusive on the parameters values. However, such data allows us to identify parameters trends along the WO_3 annealing.

One can see that the shunt resistance R_{SH}, the FF and the V_{OC} are rapidly decreasing as a function of the annealing time of the WO_3 layers. As stated before, such parameters decrease is attributed to an increasing electron leakage through the HTL layer induced by the thermal annealing.

On one hand, the coinciding apparition of cracks in the WO_3 layer during thermal annealing suggest that the active layer and the top electrodes might be in contact through them.

On the other hand, cells with a pristine WO_3 layer without thermal annealing, which was observed to be dense and homogeneous in Fig.4.19, have a limited diode behavior compared to the reference PEDOT:PSS cell. **This suggests that the WO_3 dense layers feature unsuitable electronic properties even before annealing.**

WO_3 layers electronic properties Fig.4.27 recalls the energetic landscape in flat band representation of our cells according to the literature [64, 90], with our reference CPP105D PEDOT:PSS layer annealed for 10 minutes at 120 °C in a nitrogen atmosphere.

The PEDOT:PSS HTL provides energy levels between those of silver and P3HT to allow efficient hole transport between them. With its lack of available electron-transport states, it also prevents electrons to be transferred to the silver electrode. These properties partially explain why

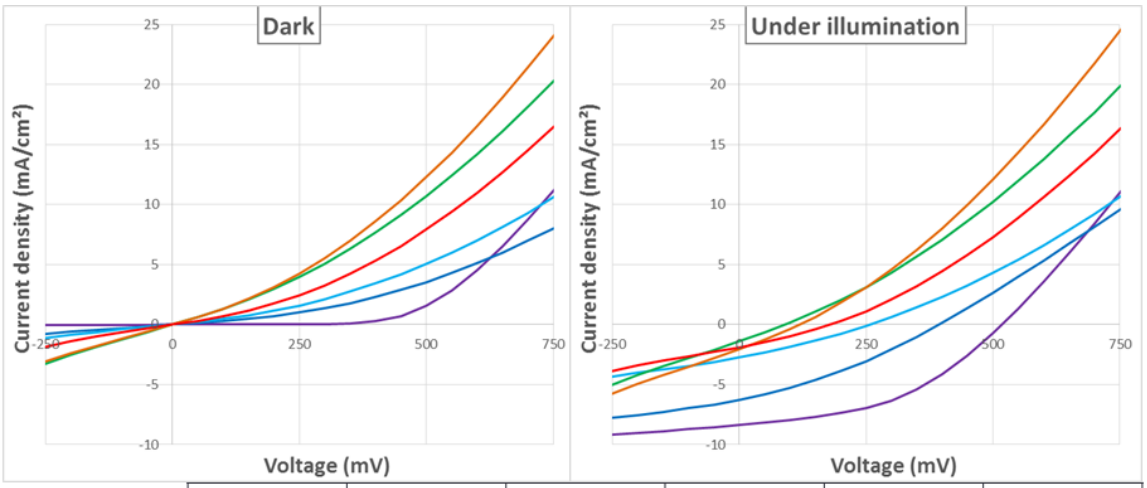

	Voc (mV)	Jsc (mA/cm²)	FF (%)	PCE (%)	Rs (ohm.cm²)	Rsh (ohm.cm²)
Reference PEDOT:PSS + 10' @120 °C	517	8.33	44.5	1.92	19	870
WO_3 without annealing	395	6.14	32.4	0.78	34	170
WO_3 + 2'30 @120 °C	255	2.65	30.1	0.20	34	120
WO_3 + 5' @120 °C	89	1.30	27.3	0.03	24	40
WO_3 + 7'30 @120 °C	117	1.94	28.8	0.07	18	40
WO_3 + 10' @120 °C	179	1.81	30.6	0.10	25	60

Figure 4.26: *PV parameters and J(V) curves of complete devices with a PEDOT:PSS or WO_3 HTL layers annealed at 120 °C in a nitrogen atmosphere. A reference silver electrode was used.*

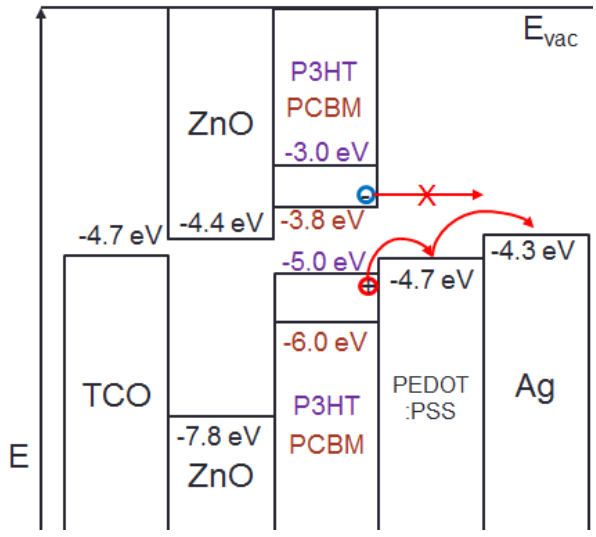

Figure 4.27: *Energy diagram of a complete inverted cell during photovoltaic operation. Energy levels were extracted from [90] at the exception of PEDOT:PSS which comes from [64].*

PEDOT:PSS is currently one of the most used HTL material in OPV devices.

Transition metal oxides such as WO_3 were long thought to be p-type semi-conductors with a conduction and valence bands both located above those respective of P3HT. However, more

recently, their valence band edges were found to be significantly deeper than expected and their Fermi levels were determined to be close ($\approx$ 0.2 eV) to their conduction band edges [290–292]; they are therefore referred to as n-type semi-conductors.

Their deep valence band edges (below -7.3 eV according to [293]), i.e. their hole-transport levels, does not allow direct hole transfer from the P3HT valence band. In addition, their conduction band edges are too low to allow them to be used as electron blockers.

In order to explain the good performances obtained from integration of transition metal oxides such as WO_3 as HTLs in OPV devices, another mechanism was proposed [294–296].

Fig.4.28 depicts the energy scheme of a P3HT / WO_3 interface of a device under illumination.

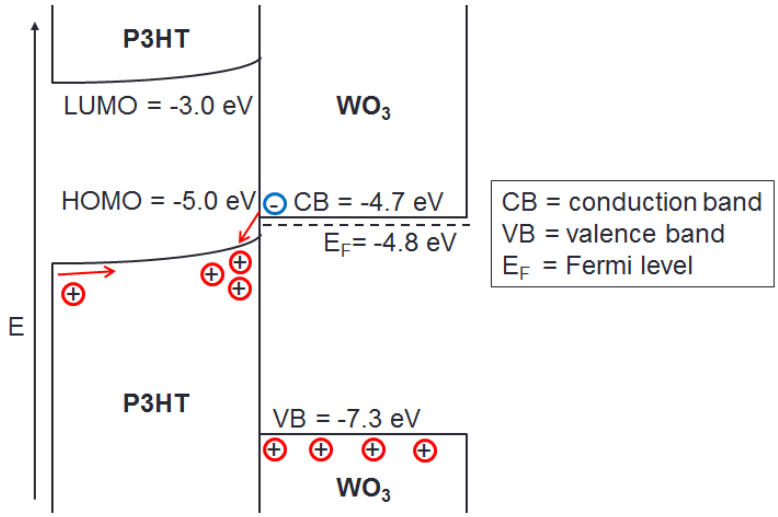

Figure 4.28: *Energy diagram of the P3HT/WO_3 interface. WO_3 energy levels were found in [90].*

During photovoltaic operation, photo-generated holes in the P3HT valence band recombine with electrons located in the WO_3 conduction band. This induces charge carrier concentration gradients in the P3HT, i.e. energy bands bending, favoring migration of holes and blocking of electrons at the interface. This can be viewed as an interfacial p-doping of P3HT. As electrons recombine at its interface with P3HT, the WO_3 layer is thus filled with holes that can be collected at the anode of the cell.

According to this mechanism, the valence band of P3HT at the interface is pinned at the Fermi level (E_F) of WO_3. In order to have good electronic properties, the WO_3 layer must have a Fermi energy level close to that of the P3HT valence band.

Fermi level measurements were performed with a Kelvin probe on the PEDOT:PSS or WO_3 layers of the cells whose J(V) curves are shown in Fig.4.26 just before the silver back electrode deposition. Such measurements are strongly dependent on the surface properties of the layer such as surface dipoles induced by atmospheric contamination for example.

Kelvin probe measurements were performed in air. However, as measurements times and conditions were kept similar between the samples, we assume that oxygen contamination does not have a significantly different effect on the measured E_F of each sample. Furthermore, although only the data point directly corresponding to the J(V) curves previously presented are shown, two samples were tested for each conditions; the absolute difference measured between

two similar samples was no more than 0.14 eV. The presented data is therefore thought to be representative of each sample. However, although the Kelvin probe measurements are consistent with themselves, significant discrepancies between E_F values measured by Kelvin probe or photoelectron spectroscopy are often observed [297].

Finally, the Fermi level of two freshly evaporated 100 nm thick reference silver layers were measured and scaled to tabulated value (-4.3 eV in [90]) in order to convert the experimental relative energy measured to absolute Fermi levels. Results are shown in Fig.4.29.

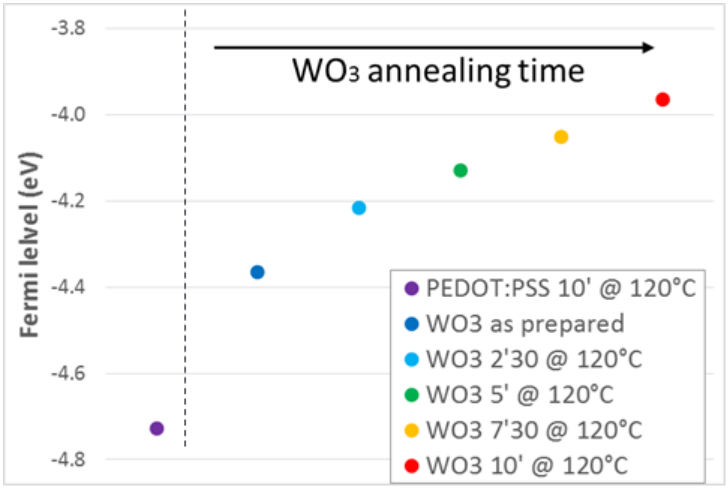

Figure 4.29: *Measured Fermi levels of a reference PEDOT:PSS sample annealed for 10 minutes at 120 °C and WO_3 layers annealed at 120 °C for several times. Samples correspond to those whose J(V) curves are shown in Fig.4.26. Relative values were scaled to two reference silver samples freshly prepared in order to yield absolute Fermi levels.*

The measured value of the PEDOT:PSS E_F of -4.73 eV is in excellent agreement with the literature (-4.7 eV in ref.[64]). This value is a good target value allowing the HTL to bridge both P3HT valence band maximum and silver Fermi level of -5.0 and -4.3 eV, respectively. According to the literature [189, 270], WO3 level is expected between -5.5 and -5.3 eV making it an interesting candidate as HTL material. However, our WO_3 layers feature higher Fermi levels further increasing as a function of the annealing time ranging from -4.37 eV for the pristine sample to -3.96 eV for the layer annealed for 10 minutes at 120 °C in a nitrogen atmosphere. Such observations are in agreement with others reported on MoO_3 and WO_3 HTL layers aged one week at 85 °C [94].

The work function is composed of two parts: the chemical work and the electrostatic work required to transport the electron through the surface [298]. Therefore, the observed WO_3 E_F increase as a function of the annealing time can be caused by several factors: a change of the surface chemical composition by reduction of tungsten oxide (although unexpected at 120 °C [270]), a possible organic shell degradation, the diffusion of the layers [299], a morphological change such as a roughness increase for example [298], the adsorption of oxygen during the measurement [300] or the creation of intra-gap states [301].

The Fermi level increase observed as a function of the 120 °C annealing time is coinciding with the cracking of the WO_3 layer observed by optical microscopy in Fig.4.19. The energy level

increase may be, at least partially, related to such morphological changes. In ref.[94], the Fermi level increase of WO_3 and MoO_3 during aging at 85 °C is proposed to be assigned to interfacial trap-states creation.

In order to assess the Fermi level evolution on the cells performances, scatter plots of the PV parameters of the 6 cells presented previously as a function of the HTL Fermi level measured just before the silver electrode deposition are shown in Fig.4.30.

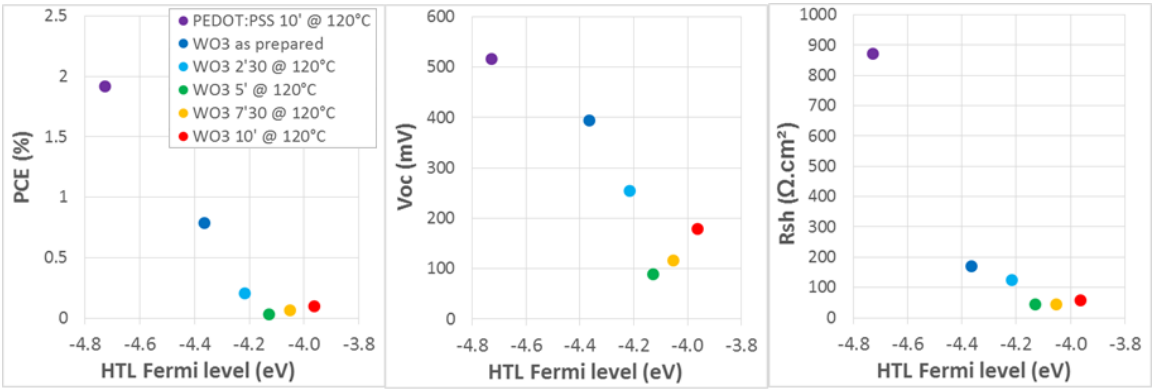

Figure 4.30: *PV parameters of complete cells as a function of the Fermi level measured on the HTL layer just before electrode deposition.*

Strong correlations are observed between the HTL Fermi levels and the R_{SH}, the V_{OC} and ultimately the PCE of the corresponding cells. Such correlations suggest that **an unexpectedly high Fermi level of the HTL is the main factor explaining the lower performances of cells made with the WO_3 HTL.** Similar correlations were made in ref.[94].

According to the V_{OC} versus E_F scatter plot, the relatively high energy levels of the WO_3 layer provides electron leakage paths across the HTL layer. A corresponding electron leakage mechanism is proposed in Fig.4.31.

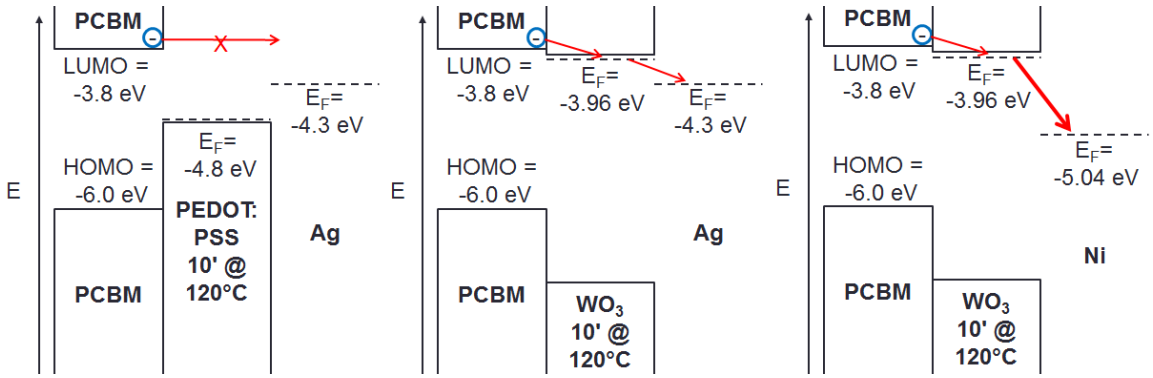

Figure 4.31: *Band diagram of the active layer / HTL / anode part of a cell. Because we focus on the electron leakage mechanism, we do not represent the P3HT levels. (left) reference device, (center) 10' annealed at 120 °C WO_3 HTL with an Ag anode (right) 10' annealed at 120 °C WO_3 HTL with a Ni anode. Ni Fermi level was found in ref[231].*

PEDOT:PSS does not provide any electron transport level available to the electrons incoming

from PCBM. As a consequence, the leakage current of electrons to the anode is strongly reduced by the PEDOT:PSS HTL layer.

WO_3 in contrast, provides such energetic levels, particularly once it is annealed for 10' at 120 °C. Thus the electrons can be transferred from the PCBM to the HTL.

The electrons in the HTL conduction band are then transferred to the anode thus generating an electron leakage current. In addition, as nickel Fermi level is lower than silver, such electron transfer is further favored in the former case which explains the additional shunting observed on Ni electrode cells compared to Ag electrode ones.

The increase of Fermi level during thermal annealing, described in the literature as trap-levels formation, and its unexpectedly high value just after deposition suggests that our WO_3 material is unsuitable for integration as HTL in our devices. Other material batches, with deeper Fermi levels according to the supplier should be tested in order to investigate further this material.

4.6 Conclusions and outlooks

In this chapter, the effect on OPV cells' initial performances of two encapsulation material/process pairs, the encapsulation by dual roll lamination of a pressure sensitive adhesive, named the PSA/R2R encapsulation and the vacuum lamination of a molten polyethylene encapsulant called the TP/S2S encapsulation, was studied.

Firstly, in Sec.4.1, the J(V) curves and parameters after encapsulation of relatively large batches of cells were compared to their performances before encapsulation.

We have shown that the TP/S2S encapsulation process had little to no effect on the cell's power conversion efficiency. Comparing the average performances after encapsulation to before, a 10 % J_{SC} decrease was counterbalanced by a comparable FF increase thus yielding cells with on average 104% normalized efficiency after encapsulation.

In contrast, the PSA/R2R encapsulated cells showed broadly decreased PCE values ranging from 15 to 91 % of initial efficiency. Such PCE decrease was shown to be correlated to strong J_{SC} (64% average) and FF (83% average) decreases themselves correlated with a doubled R_S value. The worst performing cells suffered an additional V_{OC} loss correlated to a R_{SH} decrease. By comparison to a hybrid PSA material/S2S encapsulation process, we deduced that such **losses were mostly related to the R2R process than the PSA material.**

Secondly, in Sec.4.2, the imaging techniques developed in Sec.3.1 were applied to the cells before and after their encapsulation.

On cells encapsulated with the TP/S2S pair, the only significant change observed was an average 28 % increase of their photo-luminescence (PL) emission. In agreement with the slight J_{SC} decrease observed on the J(V) curves, it is likely originating from an active layer morphological evolution induced by the 12 minutes heating process at 130 °C.

On the PSA/R2R encapsulated cells, strong contrasts were observed on the laser-beam-induced-current (LBIC) images of the most degraded cells. The degradation mechanism is

therefore a complete loss of contribution of some areas of the cells instead of an evenly distributed degradation. PL images showed little to no changes, which indicates that the active layer still performs its role after encapsulation. However, the biased PL images at -1 V compared to the OC images were strongly correlated to the LBIC images. Therefore, **we described the degradation of the PSA/R2R encapsulated cell as a photo-generated charge transport failure from the active layer to the terminals instead of a charge generation issue.** Consequently, we proposed mechanical degradation as a likely mechanism explaining the performance losses of cells during PSA/R2R encapsulation.

To assess this hypothesis, in Sec.4.3, we performed mechanical characterization developed in Sec.3.2on our devices. As a result, we found that **two interfaces were significantly weaker than the others: the TCO / ZnO A and the P3HT:PCBM / PEDOT:PSS** interfaces with measured peeling strength of 0.07 ± 0.07 and 0.17 ± 0.14 N/cm, respectively. These two mechanically weak interfaces were therefore thought to delaminate during the PSA/R2R encapsulation process.

As the PSA/R2R encapsulation process holds several advantages over the TP/S2S, we tried to strengthen the mechanically weak interfaces in order to enable the PSA/R2R process to be applied to the cells.

In the first place, in Sec.4.4 we addressed the TCO/ ZnO A interface. Alkyl compounds, known to be used as ZnO nanoparticles shells in order to stabilize their dispersions, were found remaining in the processed ZnO A films. By removing some, either by **applying an UVO_3 treatment or by replacing the dispersion by another one with different alkyl species, we improved the TCO / ZnO interface to yield peeling strength of more than 9.0 N/cm.**

The removal of the alkyl species from the ZnO A layers improved the cells as-prepared performances, with an average relative PCE increase of 12% compared to the untreated cells. This is originating from a slight J_{SC} and FF increase related to the removal of the relatively insulating alkyl species. Furthermore, the average relative PCE after encapsulation observed during the PSA/R2R encapsulation was found to be increased from 0.70 ± 0.15 to 0.81 ± 0.16 for reference devices and with an improved TCO/ETL interface, respectively. **This result strongly suggests that our proposed hypothesis of delamination during the PSA/R2R process was right. It is also encouraging as such mechanical degradations could be mitigated for mechanically resilient devices.**

Finally, in Sec.4.5, we addressed the P3HT:PCBM/PEDOT:PSS interface. Among several strategies tested, we eventually found that **replacing the PEDOT:PSS material by a WO_3, deposited via spin-coating, and annealed at 120 °C for 10 minutes yielded satisfying adhesion with the active layer with a peeling strength of at least 9.0 N/cm.** The thermal annealing was shown to be mandatory in order to achieve a good adhesion. Although we cannot conclude on the precise adhesion mechanism, the coincidental apparition of microscopic cracks in the WO_3 layer during thermal annealing suggests that interpenetration of active layer polymer chains into such cracks might play a prime role in the increased adhesion observed.

However, the PEDOT:PSS replacement by **WO_3 induces a low adhesion between the replaced HTL and the silver electrodes. A high (more than 9.0 N/cm) adhesion was observed with evaporated nickel electrodes.** A possible adhesion mechanism might be the introduction of nickel atoms into interstitial sites of the WO_3 crystalline lattice.

After such mechanical improvements, the measured peeling strength when testing our devices was 9.0 $\pm$ 0.5 N/cm. Rupture occurred at the Ni / PSA interface. **As a consequence, all the interfaces within the OPV devices are estimated to be stronger than 9.0 N/cm.**

However, integration of **WO_3 as HTL has proven to dramatically reduce the device performances from 2.60 $\pm$ 0.05 % to 0.66 $\pm$ 0.18 %.**

A strong R_S increase, inducing a significant J_{SC} loss was observed. This loss should be mitigated by decreasing the WO_3 layer thickness as advised in the literature.

In addition, a significant R_{SH} decrease inducing a strong V_{OC} loss was also observed. From further analysis, this loss was shown to be originating from an electron leakage from the active layer to the metallic anode. Two factors explaining such leakages were underlined : the contact between the active layer and the anode through the microscopic cracks developing during WO_3 annealing and the presence of parasitic, unexpected energy levels in the WO_3 layer allowing electron transport through it. Our layers showed unexpectedly high Fermi levels and poor PV performances before the thermal annealing which produces microscopic cracks. **Therefore, electron leakage is thought to be related to the high Fermi level observed on our layers. Other WO_3 batches, with Fermi levels more adapted to our use, according to suppliers, should be tested to conclude about the integration of such layers as HTLs in order to produce mechanically resilient OPV devices.**

The integration of nickel electrodes to the cells further decreased the performances. However, it is likely related to its stronger electron affinity compared to silver. Therefore, **improving the electron blocking properties of the WO_3 HTL would suppress such additional loss**. Finally, the electrode thickness will have to be increased in order to have a conductivity similar to the reference silver electrode.

Chapter 5

Aging of encapsulated OPV devices

Introduction

Stability of OPV devices over long operating times is a requirement for their commercialization.

In order to study their behavior during their lifetime in a convenient duration, devices are aged in extreme environments conditions (such as continuous full 1 sun illumination, with a high UV component, or at elevated temperature, under high relative humidity, or a combination thereof) and characterized regularly. The devices are required to reach certain standard lifetimes in such conditions which is expected to guarantee their stability in real-life environments.
In order to pass the thin-film PV modules European standards criteria [302], thin-film PV modules, organic or not, are required to reach several pass/fail criteria, for example a 90% relative efficiency after 1000 hours of aging in an 85 °C / 85% relative humidity (RH) climate chamber.

In order to study the permeation mechanisms relative to our encapsulation strategies, we studied cells aged in the harsh damp-heat standard conditions of 85 °C and 85%RH in the dark [87].
To decorrelate the effect of the atmospheric species, i.e. water and oxygen, and the temperature, additional cells were aged separately in vacuum at 85 °C and at room temperature in a nitrogen glove box.

In this chapter, the aging of encapsulated solar cells with the thermoplastic and the sheet-to-sheet (TP/S2S) material/process pair was investigated in the first place.
In addition to the performance monitoring by J(V) measurements, non-destructive imaging characterizations performed on devices along aging campaigns can yield valuable information on the cells degradation mechanisms [197, 198, 215, 216, 222, 248]. In our case, laser-beam induced current and photoluminescence (both biased and in open circuit) imaging characterizations were performed systematically thorough our aging campaigns.
From such characterizations, relevant parameters of degradation were then identified and treated statistically to yield an overall behavior for all studied cells.
The spatial information contained in the images was also investigated in order to study the

degradation heterogeneity and the permeation path of the oxidative species.
Finally, from all these data, degradation mechanisms were proposed.
In addition, a comparison with similar experiments performed on cells encapsulated with the pressure sensitive adhesive and the roll-to-roll process (PSA/R2R) was performed.

5.1 PV parameters over aging time

During the aging campaign of the cells encapsulated according to the TP/S2S process, nine samples were aged in 85 °C/85 %RH damp-heat conditions [1], Seven cells were aged at 85 °C in vacuum [2] and three cells were kept in a nitrogen glove box.

Due to a temporary S2S encapsulation equipment failure, cells underwent a J_{SC} degradation during encapsulation. As a consequence, cells studied in this chapter have encapsulated T0 performances lower than those studied in chapter 4 (where PCE = 2.41% and J_{SC} = 11.0 mA/cm^2).

Statistics of the PV parameters of the cells are shown as a function of their aging time for the three aging conditions in Fig.5.1.

Intrinsic stability at room temperature of the cells in an inert atmosphere was tested with 3 cells kept in a nitrogen glove box (GB). Such cells showed stable overall performances over 184 hours of storage.

Thermal stability of one cell under heat at 85 °C was also tested. After 521 hours of aging, the studied cell suffered a moderate PCE decrease from 1.62 to 1.44 % led by a J_{SC} decrease from 6.02 to 5.50 mA/cm^2 and a 1.6 fold R_S increase from 19 to 31 ohm.cm^2. The first performance decrease is observed between measurements at 42 and 87 hours. However, this cell performance decrease might be related to the same delamination events observed on the other samples of the batch. This degradation behavior should be confirmed by larger statistics on cells aged at 85 °C in a nitrogen glove box rather than in vacuum.

In stark contrast, cells aged in 85 °C/85 % RH climate chambers showed a strongly different behavior which can be broken down in three characteristic phases:

1. Firstly, within a 38 hours time frame, cells suffered PCE losses from 1.60 ± 0.21 % to 1.07 ± 0.27 % representing a 34 % loss of their initial performances. Such performances

1. During aging in 85 °C/85 %RH damp-heat conditions, some of the nine initial cells were randomly chosen for electroluminescence imaging characterization and were not reintroduced in the statistics due to the potentially destructive nature of this characterization technique (as shown in Sec.3.1.3). As a consequence, statistics of the parameters of such cells become poorer as a function of the aging time.

2. Among the seven cells aged at 85 °C under vacuum, all but one were immediately destroyed, showing an open-circuit behavior, after their introduction in the climate chamber. As shown in Sec.3.2.3, mechanical properties of cells encapsulated by the thermoplastic material were shown to be extremely poor due to the elastic behavior of the encapsulation. Therefore, the sudden death observed on most of the tested samples is thought to be related to delaminations within the cells induced by the vacuum application.

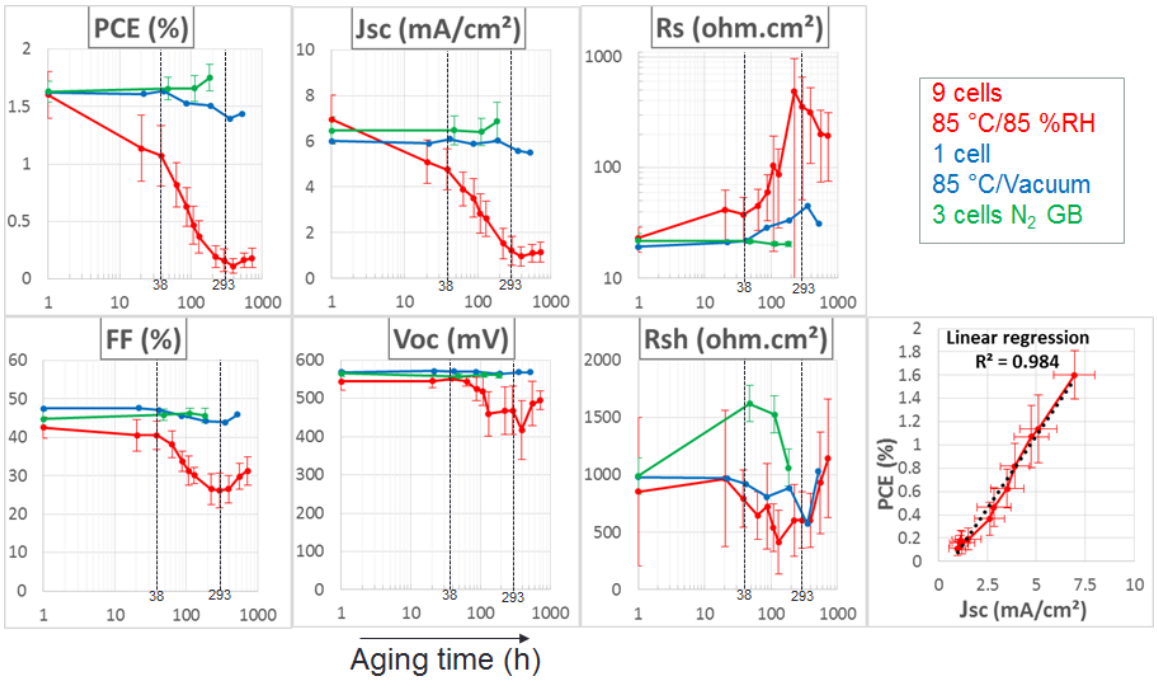

Figure 5.1: *PV parameters of cells encapsulated by the TP/S2S method as a function of their aging time in various conditions. Two aging times, 38 and 293 hours, are emphasized as particular frontier times for different aging phases of the 85 °C / 85% RH cells. For the cells aged at 85 °C/85 %RH, the PCE = f(J_{SC}) correlation was plotted in the bottom right of the graph.*

degradation was driven by a 31 % J_{SC} loss correlated to a 156 % increase of the series resistance.

2. Secondly, from 38 to 293 hours of aging, the cells performances decay accelerated from 1.07 ± 0.27 % to 0.10 ± 0.06 % of PCE. Both the J_{SC} decrease and the R_S increase observed on the previous phase occurred at a faster rate. In addition, FF and V_{OC} losses are observed, correlated with an overall R_{SH} decrease.

3. Finally, from 293 to 724 hours of aging, the performance of the cells, although very poor, remained stable between 0.10 ± 0.06 % % and 0.11 ± 0.06 % of PCE. All PV parameters showed a slight recovery of their initial values.

We have shown that the encapsulated cells were stable in inert atmosphere at room temperature. At 85 °C in vacuum, despite a lack of statistics, the tested cell showed a limited degradation of its initial performances. Once kept in an oxidative atmosphere with a 85 % relative humidity, the cells lost performance in less than 11 hours. Consequently, such losses can be ascribed to the permeation of external species, i.e. oxygen and/or water within the devices. This shows that the TP/S2S encapsulation system as it is, with a geometry emphasizing edge effects due to the small 5 mm rim, fails to prevent permeation of oxidizing species at 85 °C; it is however a useful system to emphasize the impact of moisture and oxygen ingress on the devices lifetime.

5.2 Imaging degradation along aging

To further study the degradation observed on the J(V) curves during aging in damp-heat conditions, we systematically performed non-destructive imaging characterizations, namely standard and voltage-biased photoluminescence imaging, on our samples during each stage of aging.

In a first place, the study of a single representative sample will be given as an example in order to present the evolutions observed during aging and to detail which parameters were extracted from the images to describe them statistically.
In a second place, such image parameters statistics will be correlated to their corresponding J(V) parameters in order to deepen our understanding of the degradation mechanisms along aging of the samples.
Finally, the spatial distribution of the degradation will be studied in order to propose permeation mechanisms of the oxidative species through the barrier and OPV layers.

5.2.1 Aging at 85 °C/85%RH - Parameters extracted from luminescence images

The study of a single cell representative of those aged in damp-heat conditions is presented here.

Fig.5.2 represents J(V) curves of the chosen cell aged at 85 °C/85% RH, each taken at a time representative of a particular aging phase.

This cell behave in a similar fashion than the complete batch statistically described in Fig.5.1. In a first phase, a J_{SC} decrease is observed with a moderate R_S increase. Then, in a second phase, a strong R_S increase is observed together with J_{SC} and FF decreases. Finally, the R_S and FF partially recover their original values.

In this work, PL images were acquired with a 875 nm high-pass filter. Therefore, only the band-tail of the PL emission is observed. Based on PL spectra recorded on unencapsulated cells aged 200 hours at 85 °C/ 85% RH, which show no spectral shifts, we assume that imaged PL intensity decays are only originating from global spectral decays instead of spectral shifts out of the imaging window.

Standard photoluminescence images. The classical open-circuit (OC) PL images taken at each aging time are shown in the top part of Fig.5.3. The corresponding histograms, extracted from the cell's active area labeled with a dashed red rectangle on the images and normalized to their maximum, are shown in the bottom left graph of Fig.5.3. The mean PL signal μ_{PL} and the relative standard deviation σ_{PL} calculated from such histograms is represented as a function of

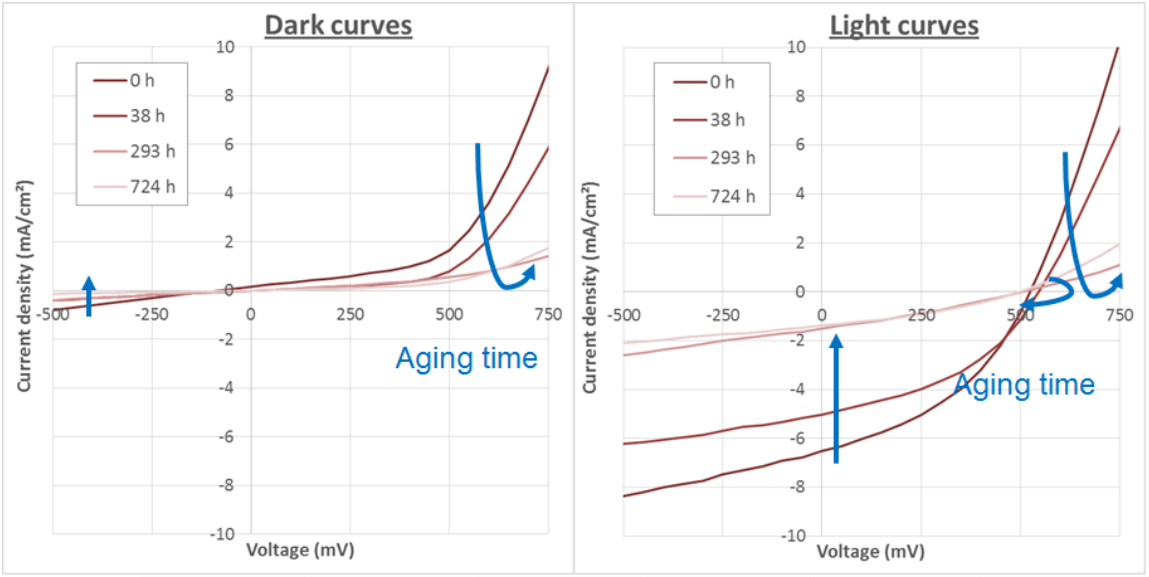

	Voc (mV)	Jsc (mA/cm²)	FF (%)	PCE (%)	Rs (ohm.cm2)	Rsh (ohm.cm2)
0 h	524	6.49	41.0	1.39	19	278
38 h	549	4.99	41.9	1.15	27	364
293 h	509	1.50	29.2	0.22	172	504
724 h	498	1.39	34.0	0.23	98	690

Figure 5.2: *J(V) curves in the dark or under illumination of a single cell at four aging times, each representing a separate aging phase. Blue arrows emphasize evolution of the parameters over time.*

the aging time in the bottom right graphs of Fig.5.3.

Voltage-biased photoluminescence images. Photoluminescence images taken at a -1 V reverse bias were divided by the corresponding open-circuit images for each aging time in the top part of Fig.5.4. Corresponding histograms, extracted from the dashed red area on the images and normalized to their maximum, are shown in the bottom left graphs of Fig.5.4. From such histograms, the mean signal μ_{vbPL} and its relative standard deviation σ_{vbPL} are shown on the bottom right graphs of Fig.5.4.

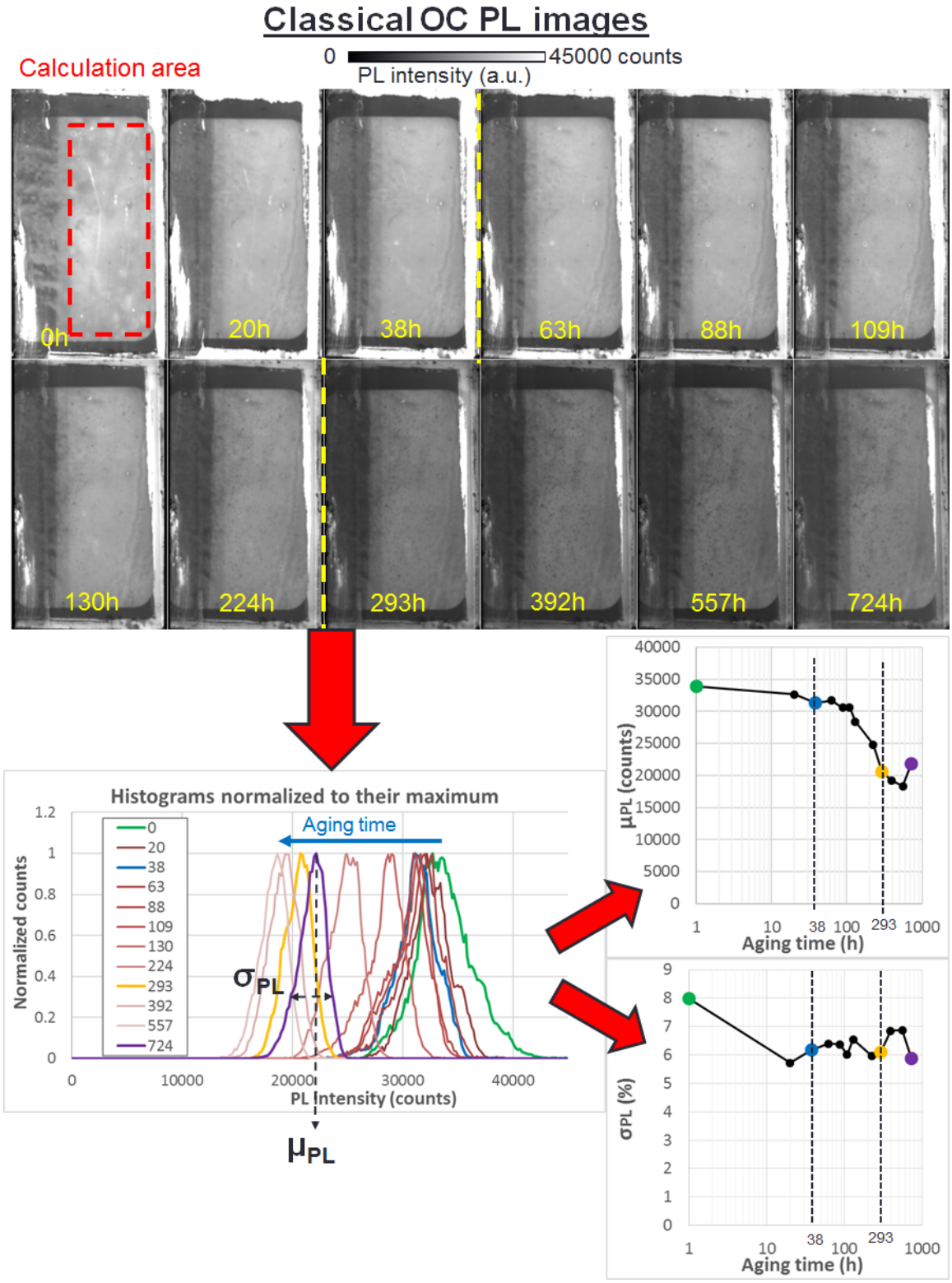

Figure 5.3: *(top images) Classical open-circuit photoluminescence images of a single cell aged at 85 °C/85 % RH for different times. Dashed yellow lines represent the three different phases observed on the J(V) curves. Statistics were calculated in the area surrounded by dashed red lines. (bottom left) Histograms, normalized to their maximum, extracted from the images in the red dashed area centered on the cell active area. (top right graph) Mean PL emission of the red dashed area μ_{PL} plotted as a function of the aging time. (bottom right graph) Relative standard deviation of the PL emission of the red dashed area σ_{PL} plotted as a function of the aging time. Histograms and extracted parameters at 0, 38, 293 and 724 hours of aging are drawn in particular colors.*

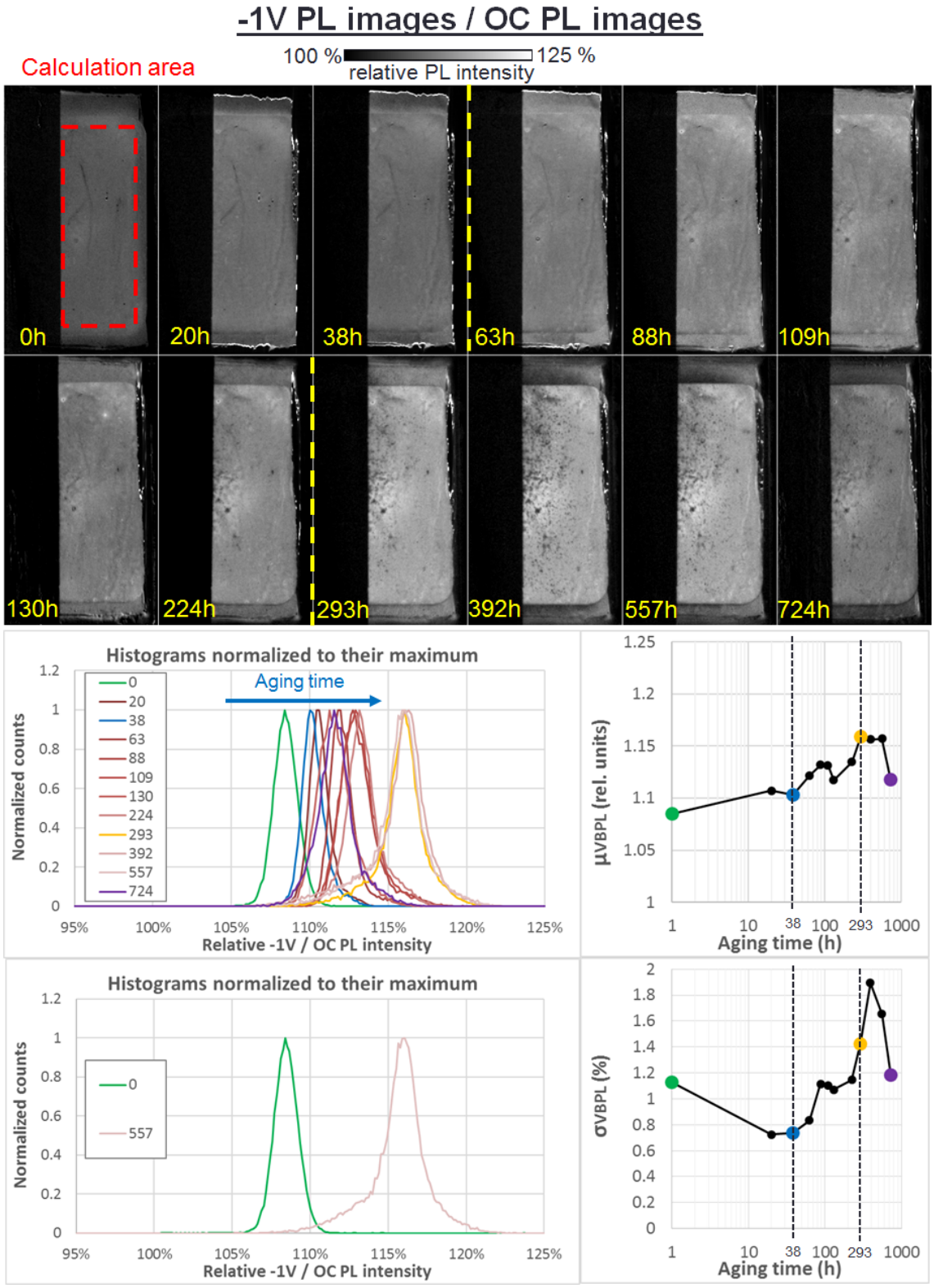

Figure 5.4: *(top images) Classical open-circuit photoluminescence images of a single cell aged at 85 °C/85 % RH for different times. Dashed yellow lines represent the three different phases observed on the J(V) curves. Statistics were calculated in the area surrounded by dashed red lines. (bottom left) Histograms, normalized to their maximum, extracted from the images in the red dashed area centered on the cell active area. (bottom right) Mean PL emission and its relative standard deviation of the red dashed area μ_{vbPL} and σ_{vbPL} plotted as a function of the aging time. Histograms and extracted parameters at 0, 38, 293 and 724 hours of aging are drawn in particular colors.*

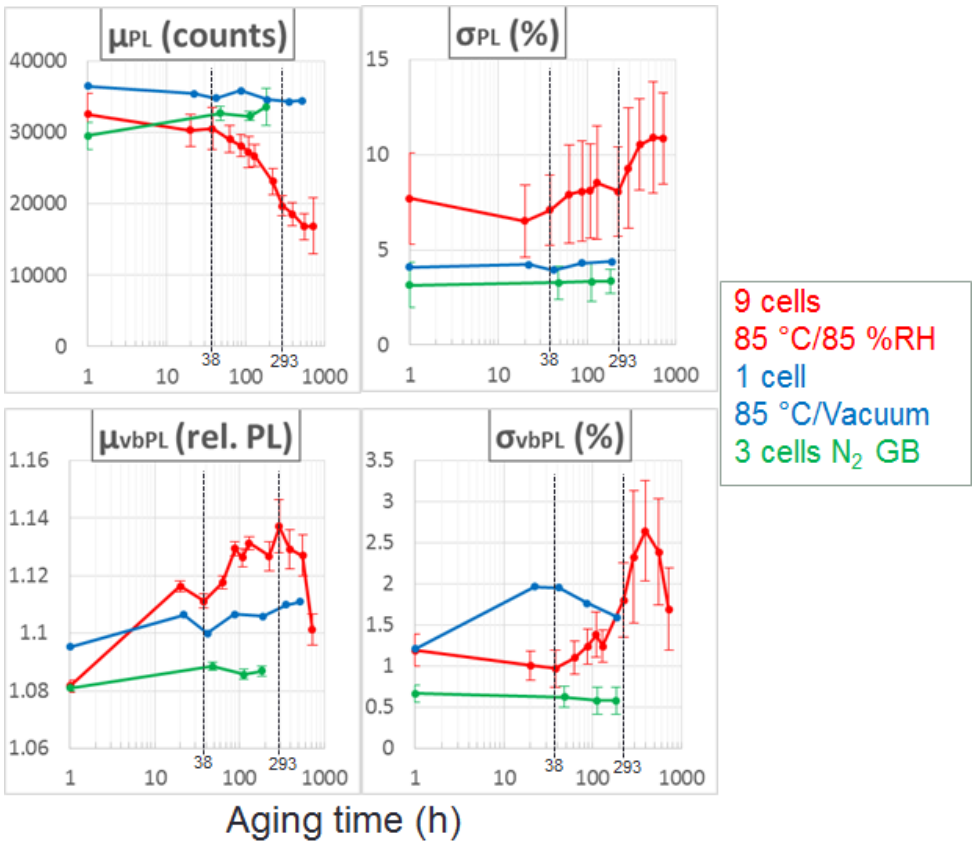

Figure 5.5: *Image parameters of cells encapsulated by the TP/S2S method as a function of their aging time in various conditions. Two aging times, 38 and 293 hours, are emphasized as particular frontier times for different aging phases of the 85 °C / 85% RH cells.*

Image parameters statistics. The mean (μ) and the relative standard deviation (σ) of both classical (PL) and biased PL (vbPL) images were calculated systematically during aging of all the cells presented in Sec.5.1. Their statistics are shown in Fig.5.5.

All image parameters of the glove box and 85 °C cells remain relatively stable over 184 and 521 hours of aging, respectively.

In strong contrast, parameters of cells aged under 85 °C and 85 %RH, strongly varied during aging. In the first phase of aging, between 0 and 38 hours, parameters remained fairly stable with the exception of μ_{vbPL} suggesting no strong degradation occurred during this time. In the second phase, between 38 and 293 hours of aging, the mean PL emission μ_{PL} significantly decreased to 60 % of its initial value. In the meantime, the voltage biased PL relative standard deviation σ_{vbPL}, which was initially stable, slightly increased showing the apparition of heterogeneities on the images. Finally during the last step, after 293 hours of aging, both classical and voltage-biased PL relative standard deviations showed a significant increase, meaning an increasingly localized degradation.

Due to their significant variations over time, the μ_{PL} and σ_{vbPL} parameters were shown to be representative of the images condition. They can be studied statistically in order to draw

information from a large volume of data.

5.2.2 Correlating images and J(V) parameters

Correlations of such image parameters and some J(V) parameters of cells aged at 85 °C/85 %RH are made in Fig.5.6.

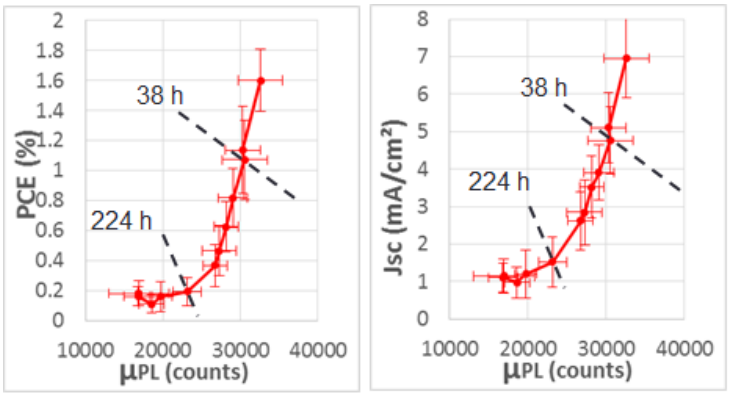

(a)

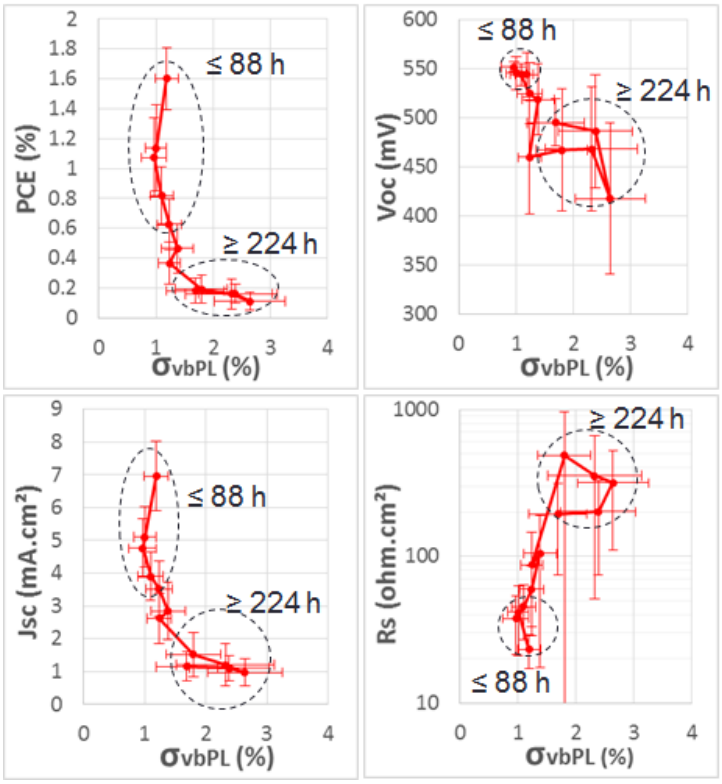

(b)

Figure 5.6: *Correlations between J(V) parameters and photoluminescence images parameters of cells aged at 85 °C/85 %RH. (a) PCE and J_{SC} as a function of the mean photoluminescence intensity μ_{PL}. (b) PCE, V_{OC}, J_{SC} and R_S as a function of the -1 V biased photoluminescence images relative standard deviation σ_{vbPL}.*

From the μ_{PL} graphs, one can see that the PL emission decrease is well correlated with the PCE and J_{SC} decreases observed during the first two phases of degradation, up to 224

hours of aging. Therefore, the first phase of performances degradation is related to a charge photo-generation decrease rather than a collection issue.

In contrast, the σ_{vbPL} parameter significantly increases only once the cells reached very low performances, above 224 hours of aging, during the third phase of aging. This brutal increase is correlated with low V_{OC} and J_{SC} and high R_S values. As a consequence, photo-generated charges collection issues are thought to occur in the later aging phases.

To further support such observations, laser-beam induced current (i.e. J_{SC}) images were taken before and after aging of the representative cell presented earlier. The LBIC images are first compared to the classical open-circuit PL images in Fig.5.7a and then to the voltage-biased PL images in 5.7b.

Both LBIC and PL imaging techniques applied to the aged sample show a decreased signal all over the sample active surface compared to the fresh cell images. A particularly dark area on the aged LBIC image is correlated with a darker PL area marked by numerous dark dots.

Comparing the LBIC to the voltage-biased PL images, one can see that their respective contrasted areas are well correlated. Therefore, dark spots on voltage-biased PL images correspond to particularly degraded areas.

5.2.3 Spatial distribution of degradation over time

In this subsection, we will focus on the degradation observed not only in the active area but on the whole cell surface.

From the classical PL images shown in Fig.5.3, the PL intensity profiles relative to T0 were measured as a function of the aging time of the cell. Profiles were plotted on the lateral and the vertical axis and averaged over the red and blue boxes, measuring 270 and 80 pixels wide, respectively. Saturated areas were eliminated prior to calculations. The frontiers between areas made of a different stack are shown with dashed lines and each different area is labeled with a colored circle number. From the intensity profiles, the mean PL intensity and the corresponding standard deviation of each area were calculated. Results are shown in Fig.5.8.

On the vertical axis, two distinct areas are identified: the first one corresponds to the complete OPV stack, i.e. the active area of the cell, and the second one is the same stack without the silver electrode. A third region, without ETL and HTL was saturated at initial time and was not studied quantitatively. One can see that region 2 without silver electrode shows a stronger short-time ($\leq$ 109 hours) PL decay than region 1 with silver. Between 109 and 224 hours the PL decay in the silver electrode area 1 accelerates and then stabilizes to intensity levels close to areas 2 without silver.

On the horizontal axis, three additional areas are shown here, from right to left: the first one

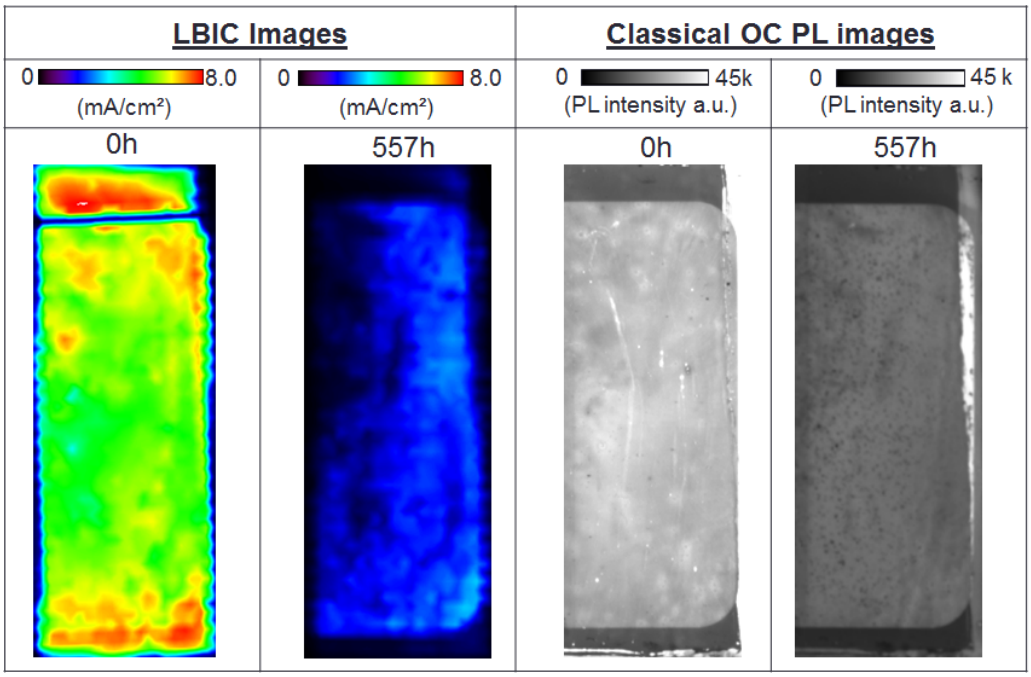

(a)

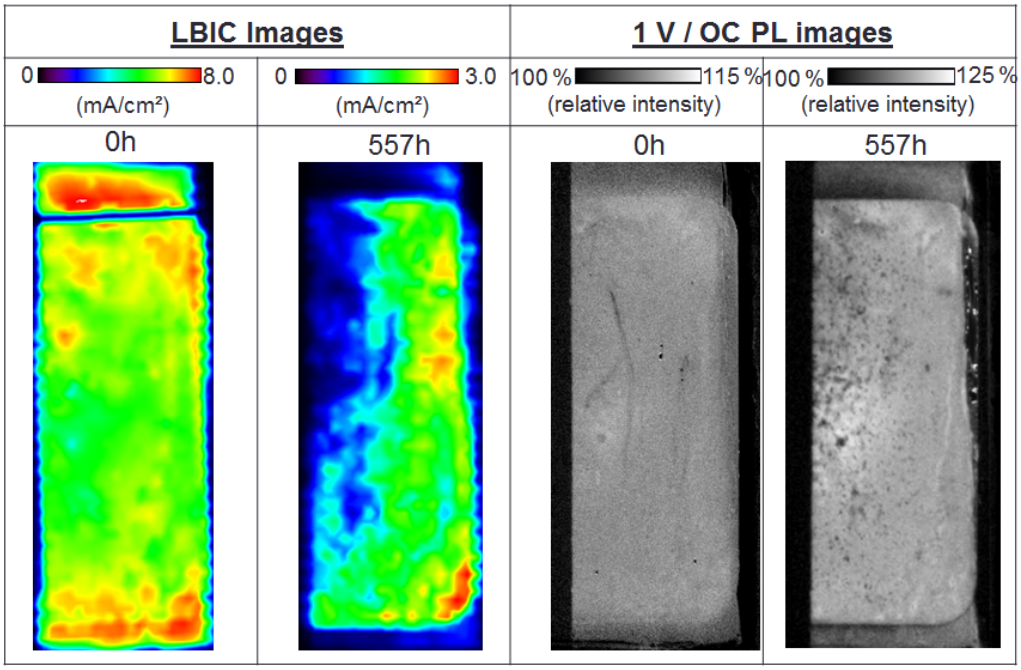

(b)

Figure 5.7: *(a) (left) LBIC images of the same cell before and after 557 hours of aging at 85 °C/85 %RH. (right) Corresponding classical PL images. Color scales were kept unchanged for both pairs of images. (b) (left) LBIC images of the same cell before and after 557 hours of aging at 85 °C/85 %RH. (right) Corresponding -1 V voltage-biased PL images divided by their OC counterparts. Color scales were adapted for each image in order to maximize contrast.*

is the complete active stack, the third one is without the TCO layer and the fourth one without TCO nor ETL layers.

The area 1' with the complete stack follows the same behavior as described with the vertical axis study (the measured areas are strongly overlapped). A slightly faster decay is observed in the area 3 without TCO. A significantly faster decay is observed in the area 4 without ETL.

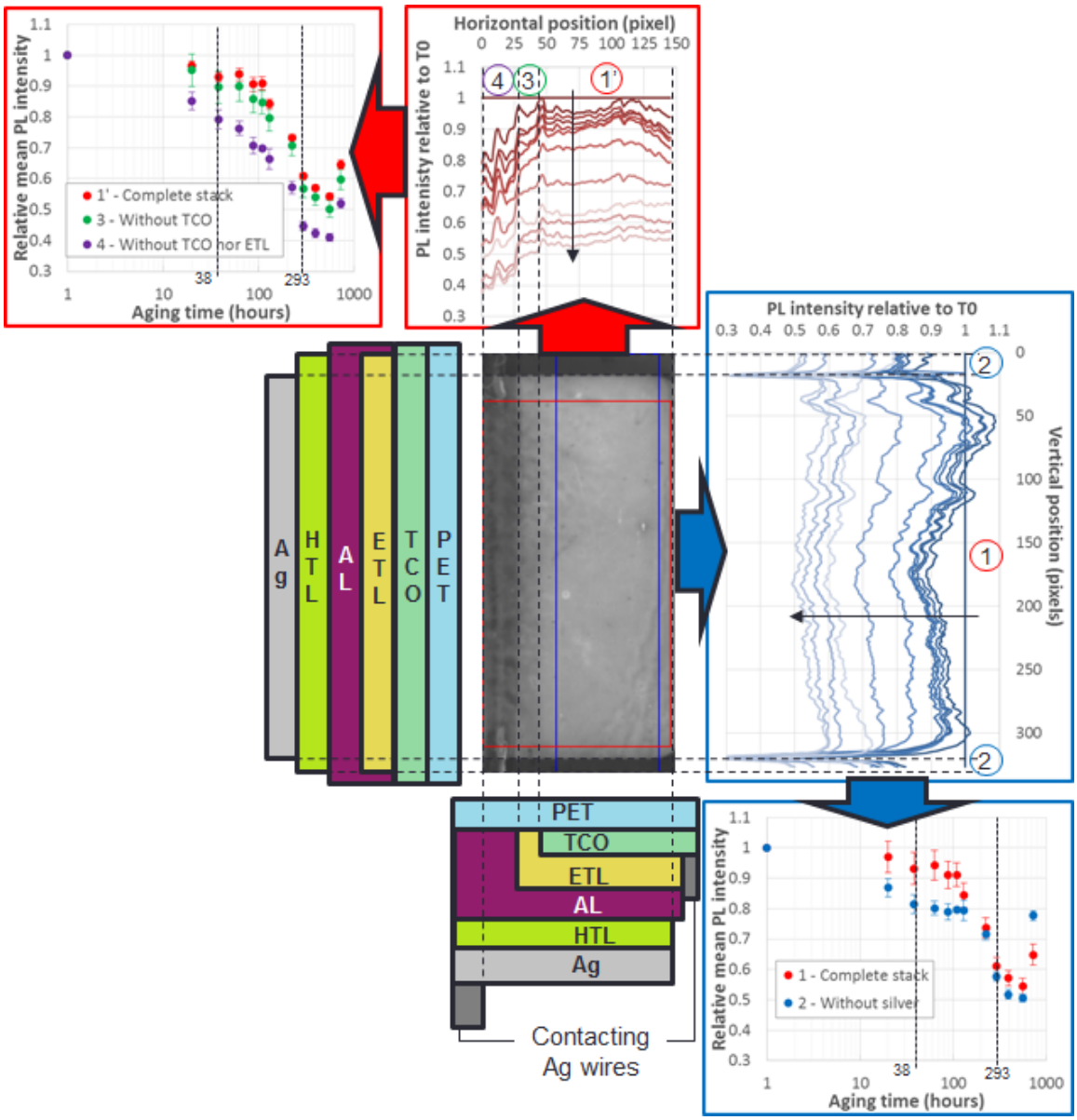

Figure 5.8: *PL intensity profiles relative to T0 as a function of the aging time under 85 °C and 85 %RH of a TP/S2S encapsulated cell. Profiles were averaged on the width of the blue and red boxes, measuring 270 and 80 pixels wide, respectively. Frontiers between different stack areas are shown as dashed lines and each stack is labeled with a colored circled number. The mean PL intensity of each area is shown next to the corresponding profiles.*

5.2.4 Permeation and degradation mechanisms discussion

Observations performed during 85°C/85% RH of the TP/S2S cells are summarized in Fig.5.9.

From the above observations, some hypotheses concerning the possible degradation mechanisms can be proposed:

PL intensity decay over aging. Classical open-circuit photoluminescence imaging shows that the PL emission of the cells decreased as a function of their aging time at 85 °C/85 %RH. Comparing the PL emission μ_{PL} of cells stored in vacuum or in oxidative 85 %RH atmosphere in Fig.5.5, it is evidenced that the samples PL emission is decreased by exposition to oxygen

Aging phase	J(V) Curves	Classical OC PLI	Voltage-biased PLI	PL emission profiles
Phase 1 0-38 hours	❖ PCE decrease ❖ J_{SC} decrease ❖ R_S increase	❖ Slight μ_{PL} decrease	❖ No significant changes	❖ Faster PL decay in areas without TCO nor ETL and in areas without silver
Phase 2 38-293 hours	❖ Faster PCE decrease ❖ Faster J_{SC} decrease ❖ Faster R_S increase ❖ V_{OC}, FF and R_{SH} decrease	❖ Faster μ_{PL} decrease ❖ Small darker spots apparition ➔ slight σ_{PL} increase	❖ μ_{vbPL} increase ❖ Small dark spots apparition➔ σ_{vbPL} increase ❖ Dark spots on LBIC and vbPL images are correlated	❖ Same observations ❖ PL decay in active area catch up with areas without silver at 130 hours
Phase 3 293-724 hours	❖ Slight recovery of all PV parameters	❖ PL emission decrease at a slower rate	❖ μ_{vbPL} and σ_{vbPL} decrease	❖ PL decay stabilization in all areas

Figure 5.9: *Summary of the characterization results obtained during each phase of the aging at 85°C/85 % RH of TP/S2S encapsulated cells.*

and/or water.

Generally, a PL emission decrease in oxidative conditions can be caused by several factors:

1) **Transmission/reflexion decrease of non-active layers**

Transmission losses of the layers located in the light path to the active layer (front side barrier, substrate, TCO and ETL) and reflection decrease of those located behind the active layer (HTL and in particular the silver reflecting electrode) may explain a decrease of PL as a function of time.

Furthermore, As shown in Fig.5.8, PL emission decreased on the whole cell surface and not in a particular region where the layers are patterned. Therefore, optical losses may have occurred on layers which cover the whole cell surface such as the front side barrier, the thermoplastic encapsulant, the PET substrate or the active layer.

In our case, visual inspection of the samples did not allowed us to see any significant decrease of such properties. UV-visible absorption measurements should be performed on each layer separately in order to rigorously discard this hypothesis.

2) **Excitation light absorption loss of P3HT itself induced by its degradation**

To our knowledge, the only PL decrease of OPV cells observed in oxidating atmosphere [215] was due to a coupled influence of both oxygen and illumination inducing photo-oxidation of the P3HT alkyl side chains [105]. However, our samples were aged in the dark and were only illuminated periodically in order to perform J(V) measurements or PL experiments. Therefore, we assume that the photo-assisted oxidation by oxygen of the polymer is unlikely.

Furthermore, as shown in photo oxidation studies [105, 133], chemical degradation of the

active layer is known to lead to a bleaching of the latter. From visual inspection of the aged samples, no bleaching was observed, even for advanced PL degradation where PL emission was halved as compared to the initial state. UV-visible absorption spectra should be recorded as a function of the aging time to further investigate this possibility. Such experiments were performed in the literature under 65 °C/85 %RH for 118 hours and no absorption losses were to be reported [216]. Therefore, the direct active layer oxidation hypothesis can be reasonably discarded.

3) **Radiative recombination rate decrease of photo-generated excitons**

Morphological evolution of the active layer

As shown in the litterature, exposing bulk heterojunction cells to a temperature above the polymer glass transition temperature, 56 °C for P3HT, can cause morphological evolutions in the active layer, i.e. donor/acceptor domain sizes change[88, 89]. Such domain size evolutions are expected to impact the excitons recombination/dissociation rate which is probed by the PL emission [303].

In Fig.5.5, we showed that PL emission of a cell aged at a 85 °C temperature does not show a significant decrease even for 521 hours aging. As a consequence, we assume that the temperature of 85 °C has no influence on the active layer morphology for such aging times.

To our knowledge, water and oxygen are not known to have an influence on the BHJ morphology. Therefore, we do not ascribe the PL decay over time as a consequence of a morphological evolution of our active layer.

Radiative recombinations shifting to non-radiative transitions

A decrease of PL signal could also be observed on images if the recombination mechanism changed. Such a change could cause the emission spectrum to shift towards undetected wavelengths or to decrease in intensity due to more non-radiative recombinations.

Based on PL spectra recorded on unencapsulated cells aged 200 hours at 85 °C/ 85% RH, we observed a global decrease of the PL emission spectrum rather than a significant spectral shift, at least in the visible range.

Therefore, the one hypothesis remaining to explain the PL decay would be an increase of the non-radiative recombination rate over the radiative one. This mechanism would take place by the creation of intra-gap states by degradation compounds. Such states behave as trapping centers for the photo-generated charges which could decrease J_{SC} [51].

Additional characterizations such assystematic spectral studies, variable illumination measurements [70, 304, 305], time dependent PL spectroscopy [306] or impedance spectroscopy [256, 307, 308] can be used in order to probe an increase of non-radiative recombinations over the aging time.

Independently of its precise origin, such PL emission decay is indirectly a marker for at least a part of the J_{SC} losses observed during aging at 85°C/85 % RH.

Additional J_{SC} losses induced by R_S increase. If the PL decrease may help to, at least partially, understand the J_{SC} decrease observed simultaneously, the series resistance R_S parameter was shown to increase over time, decreasing J_{SC} as well. However, such parameter is not sensible toward optical changes. Therefore, its increase over time is yet to be explained.

Regarding charge transport properties, PEDOT:PSS is known for its hygroscopic properties which accelerates aging of OPV cells [114, 115, 309–311]. It also shows reduced conductivity upon exposure to oxygen and water during a few hours [96, 311–313].
In addition, for longer aging times, a metal oxide layer may form between PEDOT:PSS and the silver electrode, thus increasing series resistance [120, 215, 222, 248]. Such R_S increase is generally much stronger than the one observed during PEDOT:PSS degradation and it may completely hinder charge transport between the active layer and the electrodes.

Metal-oxide related transport failures are expected to be strongly contrasting electroluminescence [248] and by analogy voltage-biased PL images, while PEDOT:PSS related slight R_S increase is not expected to significantly impact such images.

Dark spots apparition on voltage-biased PL images. VbPL images show an increasing number of small dark spots as a function of aging time of the samples.

The characteristic dot shape of such dark spots recall those observed on electroluminescence images of unencapsulated standard cells with an Al electrode aged in the dark in air[215, 222]. In these studies, PL images made on the same devices also showed reduced signal at the same locations where EL was degraded. Conclusions of the study was that water and oxygen permeated through pinholes in the evaporated aluminum electrode leading to oxide formation at the interface with the inner layers. This aluminum oxide then locally prevented charge transport from the active layer to the bulk electrode. Such electrode oxidation also caused a decrease of the reflection properties of the electrode which was noticeable on PL images due to the reduced reflection of both the excitation and the emission light. Despite being less sensitive than aluminum toward water and oxygen, evaporated silver was also shown to oxidize even when kept in room temperature-humidity conditions [120]. Inverted solar cells were also shown to yield similar EL images after aging in ambient conditions as well [222].

In addition, in the same study, for some of the inverted cells which showed degraded EL images and also suffered V_{OC} and R_{SH} losses, dark lock-in thermography images showed the formation of shunts paths during aging. This was ascribed to a possible silver migration through the PEDOT:PSS layer [222, 248].

The similarity of the symptoms observed both on the J(V) curves and our vbPL images suggests that similar degradation mechanisms take place during our aging experiment.
Complementary characterizations, such as dark lock-in thermography (DLIT) in order to locate potential shunting paths and time-of-flight secondary-ion mass spectroscopy (TOF-SIMS) experiments in order to investigate the chemical composition of the degraded cells may be useful in

order to complete such study.

PL emission decay profiles. The global PL decay rapidly observed on the whole active area suggests that permeation occurred either orthogonally through the barrier layer and/or laterally at a very fast rate.

Water vapor transmission rate (WVTR) of the barrier (3.10^{-4} g/m^2/day measured at 40 °C/90 % RH in 48 hours) was shown to be three orders of magnitude lower than the 150 µm thick polyethylene encapsulant (1.8 g/m^2/day measured at 40 °C/90 % RH). In other investigations in our laboratory, the barrier was shown to have a stable helium permeation rate before and after 1000 hours of storage at 85 °C /85 % RH. The polyethylene encapsulant, however, has not be tested. We therefore expect water permeation to primarily occur laterally from the edges of the devices rather than orthogonally through the barrier, particularly with small encapsulation rims of 5 mm.

Furthermore, in previous investigations in our laboratories [314], light transmission measurements were performed on a calcium layer encapsulated according to the PSA/R2R process and materials. The opaque calcium layer forms transparent calcium oxide when in contact with water. An overall whitening of the whole surface is assumed to be orthogonal permeation through the barrier and a completely white cropping of the edges is a sign of lateral permeation. The influence of contacting ribbons, piercing through the encapsulation, on the water ingress was investigated. Results are shown in Fig.5.10.

From the Ca test images of the PSA/R2R sample without contacting wires, orthogonal permeation could be observed on the 30 hours image with a slight edge cropping. On images of sample with silver wires, the area cropping was significantly stronger at 30 hours and almost reached the whole calcium area at 68 hours of aging. In contrast, compared to the PSA/R2R sample, the TP/S2S encapsulated sample showed a reduced edge cropping after 30 hours of aging. As a consequence, permeation of water through the contacting wires is likely to occur with both the PSA/R2R and TP/S2S encapsulation processes. However, TP/S2S encapsulation is thought to seal more efficiently such permeation path and can therefore bring a longer time lag before permeation than the PSA/R2R process.

It must be noted that the calcium tests were performed at 65 °C/85 %RH. Thus, the time lag prior to permeation is likely to be shortened during aging of cells at 85 °C/85 %RH.

However, on PL images, areas close to the contacting ribbons (located on the bottom right and left of the PL images) did not show significantly faster decay than areas located on the other side. This suggests that either contacting ribbons are not preferential permeation paths with the TP/S2S encapsulation or that permeation occurred too quickly to be localized on our images.

Furthermore, as shown in the vertical profile in Fig.5.8, areas under silver show less PL decay over time than those with the bare PEDOT:PSS in contact with the encapsulation system. This

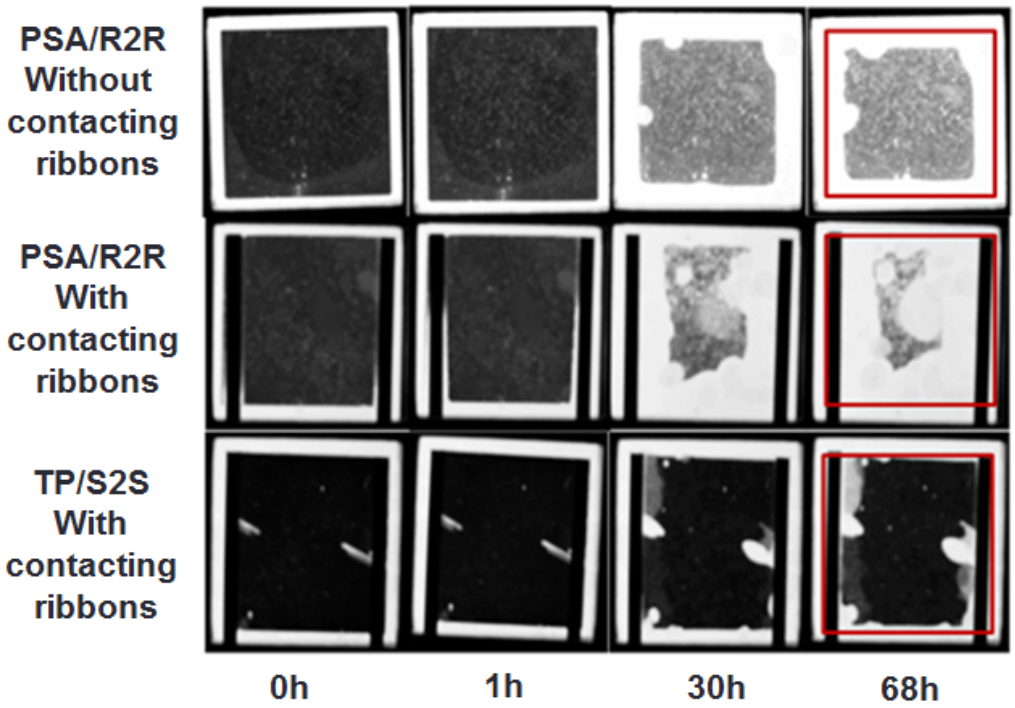

Figure 5.10: *Optical micrographs of a calcium layer (dimensions: 4.5 x 4.5 cm) encapsulated with the PSA/R2R or TP/S2S processes as a function of aging time at 65 °C /85%RH. A PSA/R2R sample without connecting ribbons was tested as well. Reproduced from [314].*

suggests that, in agreement with the litterature [222, 315], the metal electrode offers a degree of protection against permeation of water. However, no obvious degradation from bottom to top is observed. Therefore, permeation through the contacting silver wires located at the bottom of the cells is either not a dominant permeation path or on the opposite is occurring too fast to create an oxygen and moisture gradient.
Finally, as shown in the horizontal profile in Fig.5.8, areas without ETL shows an increased PL decay than those covered by this layer. This result would suggest that the ETL layer can prevent to a certain extent water permeation incoming from the front side of the cell, through the PET substrate and the TCO layer.

Finally, the most likely permeation paths and degradation mechanisms, according to our observations, are summarized in Fig.5.11 and discussed below.

First aging phase (0-38 hours). Comparing the J(V) curves of cells stored at 85 °C under vacuum or in a 85 % RH atmosphere, one can see that permeation of oxidative species occurs during this time frame inducing performances losses of the cells. Due to the much higher water vapor permeation resistance of the barrier compared to the thermoplastic, lateral permeation through the encapsulation rims is expected. However, from the PL degradation profiles, which allow us to track progressing degradation of the cells, no significant PL emission gradient was observed. As a consequence, permeation is though to occur very rapidly from the edges.

During this aging phase, the performance loss was driven by a J_{SC} loss correlated with a

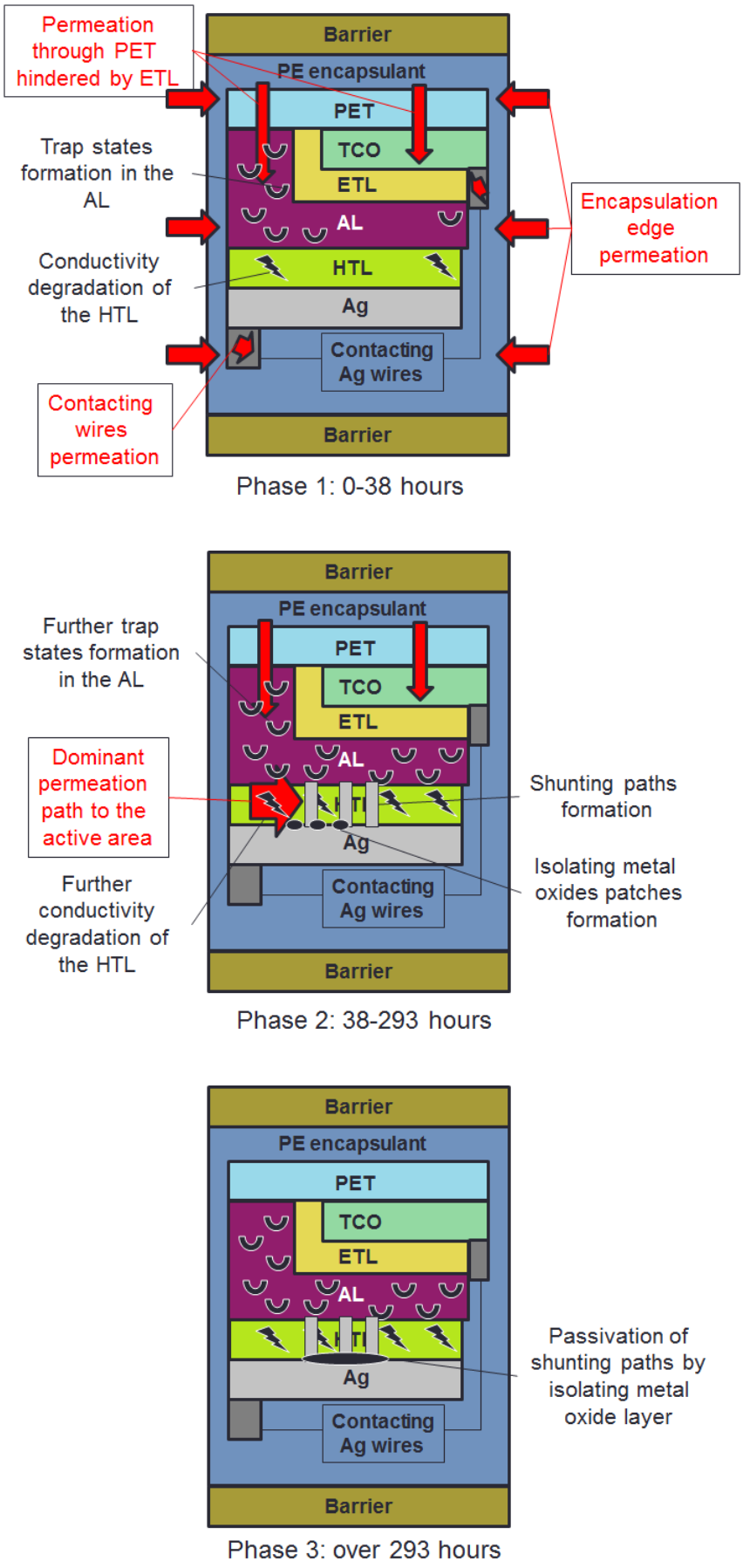

Figure 5.11: *Schematic representation of the most likely, according to our observations, permeation paths in red and degradation mechanisms in black of the TP/S2S cells during their three phases of aging at 85 °C/85 %RH conditions.*

PL emission decay and a limited R_S increase. No significant feature was observed on voltage-biased PL images. PL decay and a part of the J_{SC} loss may likely be related to an increase of non-radiative recombinations. The R_S increase and the other part of the J_{SC} loss may likely be induced by a PEDOT:PSS conductivity degradation after its absorption of water.

Second aging phase (38-293 hours). During this aging phase, performance and J_{SC} decrease rates were accelerated. R_S also increased at a much faster rate. As shown with the cell aged at 85 °C under vacuum, thermal degradation lead to a slight R_S increase which might be caused by the thermal degradation of PEDOT:PSS [96]. Such degradation are therefore expected at 85 °C/85 %RH. In addition, as suggested by the apparition of small dark spots on the voltage-biased PL images, isolating metal-oxide patches may likely be formed at the electrode/PEDOT:PSS interface after water permeation through pinholes in the metal electrode (as observed by electroluminescence imaging of cells with an aluminum electrode [222]).

Additional V_{OC} and R_{SH} decreases were observed on some samples wich may be caused by the migration of silver through the PEDOT:PSS layer.

As the PL emission profiles decrease faster in the outer border than in the center of the active area, water is thought to also permeate under the silver electrode within the hygroscopic PEDOT:PSS layer.

Third aging phase (over 293 hours). During this phase, a slight recovery of the J(V) parameters ,notably V_{OC} and R_{SH}, can be observed. This might be related to the passivation of shunted areas by the growing metal oxide patches.

5.3 Comparisons between the TP/S2S and PSA/R2R encapsulation systems

Cells encapsulated with the pressure-sensitive adhesive and the roll-to-roll process were studied in two different aging campaigns in the same aging conditions as the TP/S2S cells discussed previously. PV parameters and the mean classical PL emission observed on all cells are shown in Fig.5.12. During these aging experiments, the voltage-biased PL characterization technique was still in its early development stage and we can not provide any relevant data about the PSA/R2R encapsulated cells. Furthermore, aging experiments on PSA/R2R cells were not performed over more than 100 hours which corresponds to the phase 2 of TP-S2S cells degradation.

In comparison to TP/S2S cells, PCE of PSA/R2R samples decreases at a close rate. In a similar fashion as TP/S2S encapsulated samples, PCE decrease of the PSA/R2R cells is driven by a J_{SC} decrease. Such J_{SC} decrease was shown to be slightly faster for PSA/R2R cells. However, the PL emission decrease and the R_S increase was quite similar for both encapsulation strategies. This suggests that the J_{SC} decrease of the PSA/R2R cells may originate from additional degradation mechanisms than the TP/S2S cells.

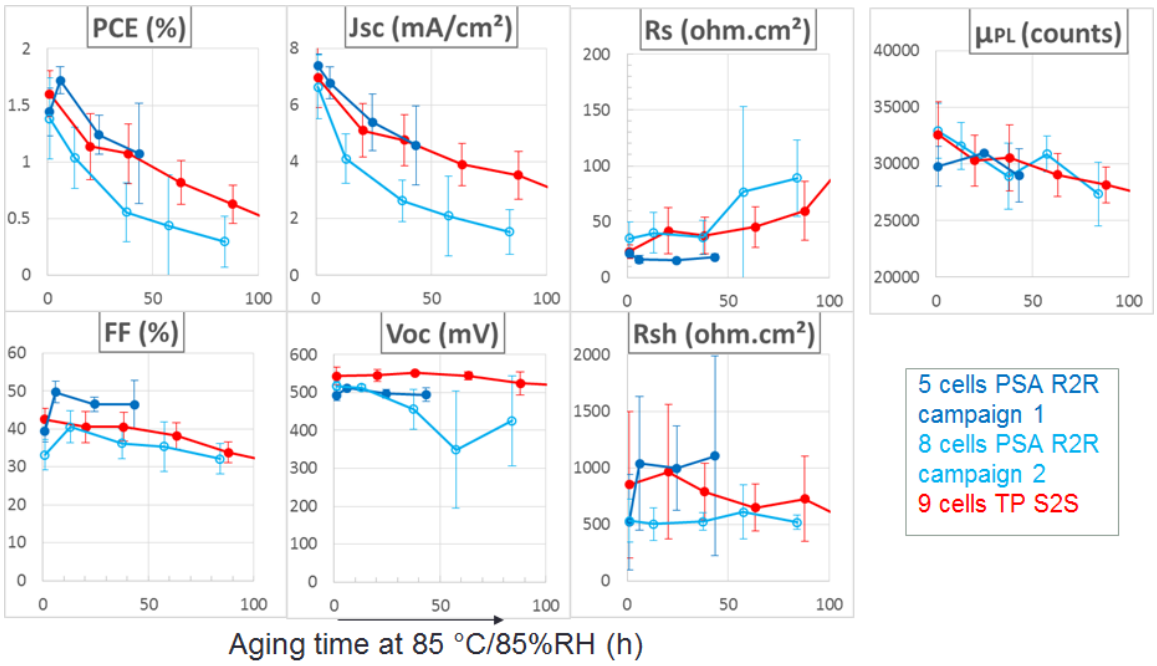

Figure 5.12: *PV parameters of cells encapsulated by the TP/S2S or the PSA/R2R methods as a function of their aging time at 85 °C/85 %RH.*

In addition, V_{OC} drops are observed in less than 50 hours for PSA/R2R cells which is much earlier than for TP/S2S which showed such behaviors after at least 100 hours of aging. No stabilization behavior of the PSA/R2R cells was observed as in phase 3 (after 293 hours of aging) of the TP/S2S cells aging.

Classical PL images and the corresponding PL intensity profiles of a single cell are shown in Fig.5.13a and Fig.5.13b, respectively.

In agreement with the observations made on the TP/S2S encapsulated samples, the mean PL intensity decrease as a function of the aging time in the 85 °C/85% RH chamber.
Similarly, as shown on the horizontal profile in Fig.5.13b, areas without ETL nor TCO have a significantly stronger PL decay than areas composing the active stack of the cell. Such similarity reinforce the hypothesis that, at 85 °C, permeation may occur from the front side of the sample through both the encapsulation and the substrate. Such permeation seems to be significantly impeded by the ETL ZnO nanoparticles layer.

In strong contrast to the aging of the TP/S2S encapsulated cell, gradual gas bubbles formation can be observed first on the cells contour and then on the whole cells surface within the PSA/R2R encapsulation. Such bubbles formation change the optical properties making such areas appear brighter on the PL images. In the example shown in fig.5.13a, such patterns are particularly observable on the edge of the cell for aging times as short as 13 hours. This causes the vertical PL profile in fig.5.13b to show a signal increase in edge regions without silver. For longer aging times, similar patterns can be observed in the central area as well. As such bubbles were not observed on samples aged at 85 °C under vacuum, they are likely formed of water and/or oxygen.

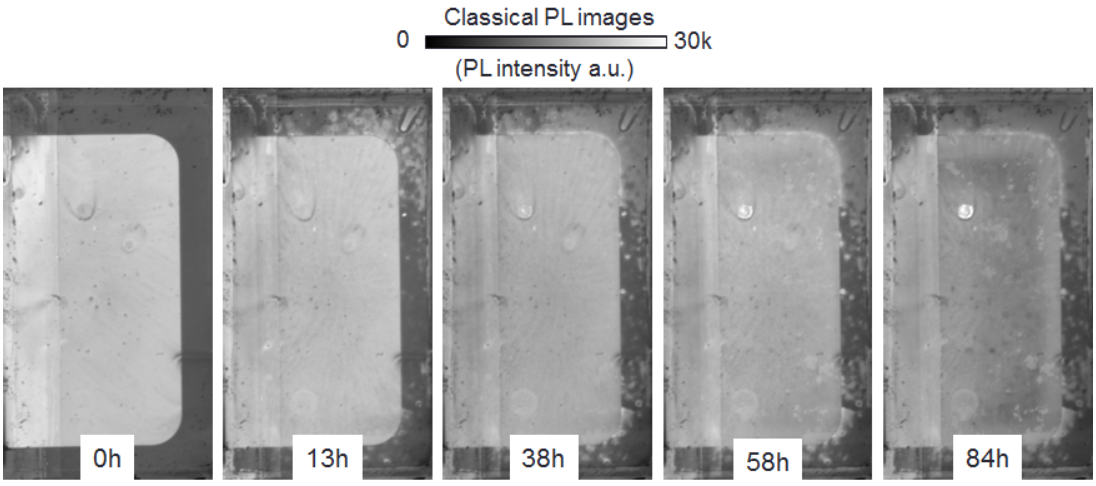

(a)

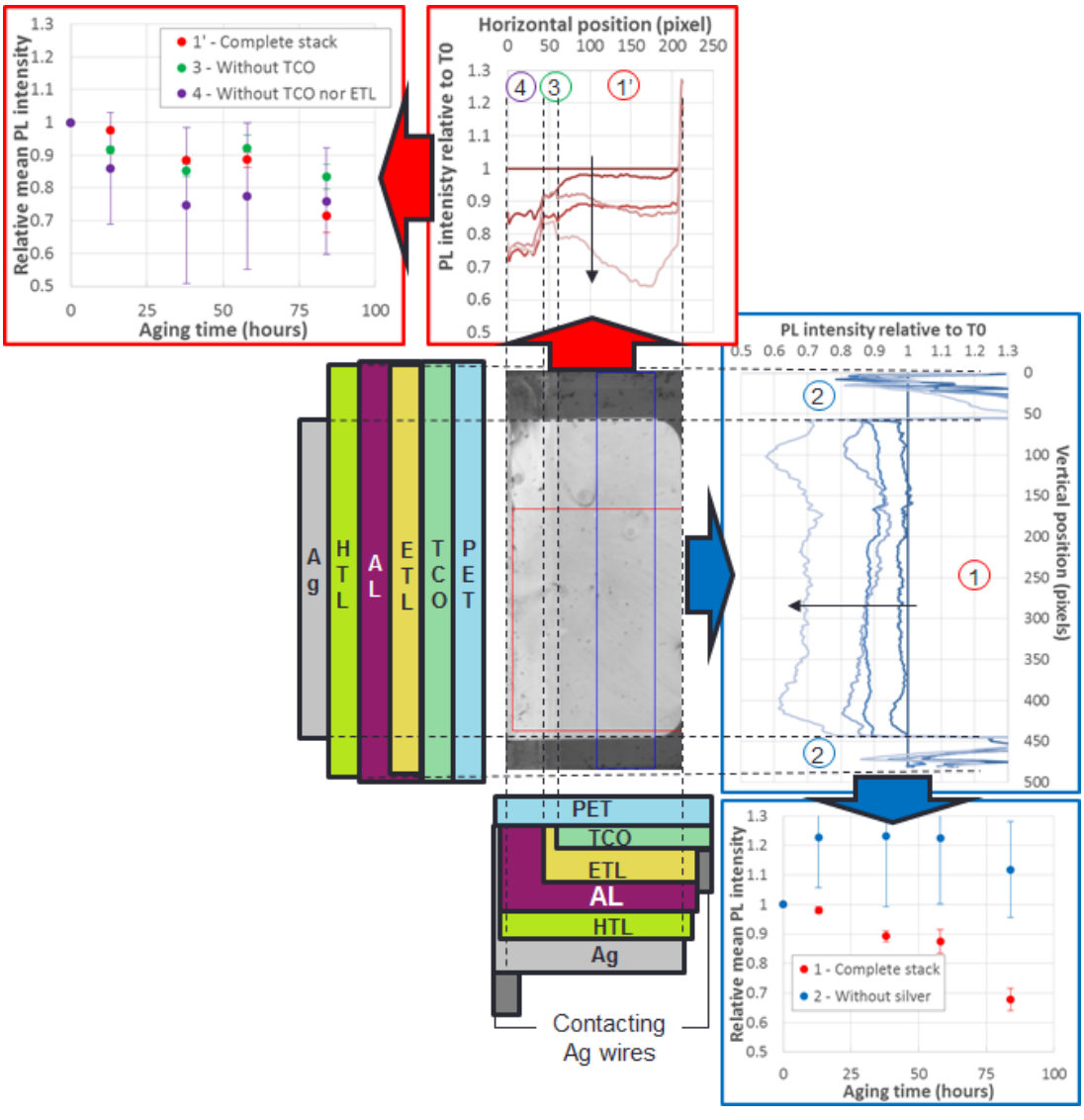

(b)

Figure 5.13: *(a) Classical PL images of a PSA/R2R encapsulated cell aged under 85 °C and 85 %RH. (b) PL intensity profiles relative to T0 as a function of the aging time under 85 °C and 85 %RH of a PSA/R2R encapsulated cell. Profiles were averaged in relatively homogeneous areas on the width of the blue and red boxes, respectively. Frontiers between different stack areas are shown as dashed lines and each stack is labeled with a colored circled number. The mean PL intensity of each area is shown next to the corresponding profiles.*

Finally, in order to investigate the permeation path relevant for the PSA/R2R cells, PL images were acquired on a half-encapsulated sample after 25 hours of aging at 85 °C /85%RH. Results are shown in Fig.5.14. Two vertical profiles are plotted: in the blue rectangle, the area without ETL nor TCO and in green the active area in an homogeneous region.

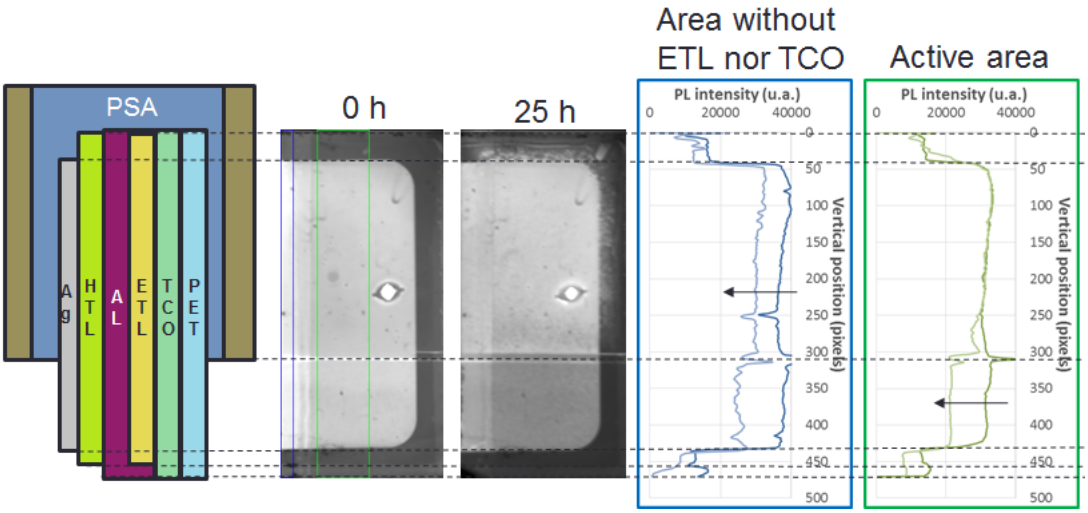

Figure 5.14: *Absolute PL intensity profiles as a function of the aging time under 85 °C and 85 %RH of a half-encapsulated PSA/R2R cell. Profiles were averaged in relatively homogeneous areas on the width of the blue and green boxes, respectively. Frontiers between different stack areas are shown as dashed lines.*

From the green graph representing the PL emission in the active area, one can see a strong PL decrease, from 32 000 to 22 500 counts in average, in the non-encapsulated half of the cell. In the meantime, PL emission of the encapsulated area only slightly decreased at the interface with the unencapsulated area evidencing a lateral permeation phenomenon. This result suggest that the PSA/R2R encapsulation strategy offers a degree of protection to the devices which would degrade even faster without. It also confirms the detrimental effect of moisture and/or oxygen on the PL emission.

In contrast, in the area without ETL nor TCO, the non-encapsulated area shows a similar strong PL decay than the complete stack area with a PL signal decreasing from 37 500 to 25 000 counts. The encapsulated area however, also decays, from 37 500 to 30 500 in average, but at a slower rate than the unencapsulated area. This result further shows that the area without ETL and TCO is a prime permeation path.

5.4 Conclusions and outlook

In this chapter, we studied the behavior of cells protected with either the PSA/R2R or the TP/S2S encapsulation strategies. By regularly recording their J(V) curves along their aging, we observed a significant degradation of the devices aged at 85 °C and /85 %RH. By comparing these data with those of cells aged without an oxidating atmosphere or elevated temperature,

we can conclude that degradation occurs mainly due to the permeation of such species in the encapsulated devices.

To further investigate the degradation mechanisms and the permeation paths followed by the aggressive species, we performed luminescence imaging characterization along aging in parallel to the J(V) curves recording.

Thanks to the imaging techniques, we also investigated the spatial evolution of degradation over time. We observed that the PSA/R2R encapsulation offers a degree of protection toward water to the cells. We also showed that the silver electrode and the TCO/ETL layers seem to also protect the active layer from the oxidant species. This further suggests that at 85 °C, permeation likely occurs very rapidly from the edges of the encapsulation system, crosses the encapsulation rim and then flow through the PET substrate.

From these data, we isolated three distinct degradation phases for the TP/S2S encapsulated cells:

First, an immediate J_{SC} decrease linked with a moderate R_S increase was observed. In the literature, such degradation behavior is often thought to be a degradation by water of the PEDOT:PSS layer. In addition, a gradual photoluminescence (PL) emission decay can be observed as a function of the aging time. To our knowledge, such PL decrease in damp heat conditions was not investigated in the literature and its exact cause is yet to be proven. Characterizations such as impedance spectroscopy or variable illumination J(V) measurements may help unravel the precise cause of such PL decay. However, its strong correlation with the PCE, the J_{SC} and the LBIC images make us think it can be harnessed as an indirect probe of the degradation of the active layer or the modification of optical properties of the cells.

Second, we observed a gradual apparition of small dark spots on voltage-biased PL images. Such dark spots are characteristic of a localized charge transport hindrance. In analogy with the electroluminescence literature, such dark spots may likely be originating from the formation of metal oxide at the metal electrode/PEDOT:PSS interface.
Finally, a last V_{OC} and R_{SH} degradation pattern could be observed. Such degradation is often interpreted as a shunting of the cell. The shunting origin however, is yet to be understood. In the case of the TP/S2S cells, such parameters losses could be partially recovered coincidentally with the dark spots formation on the vbPL images. This may be the sign of the electrical passivation of the shunt paths by metal-oxide patches.

Such characterizations already yield a global idea of the degradation mechanisms and the permeation paths for our devices. However, we also showed that the data need strong interpretation. In order to further improve our comprehension of the devices degradation, several complementary non-destructive imaging characterizations can be performed: UV-Vis absorption spectroscopy can consolidate data obtained by PL imaging and decorrelate absorption losses from other causes of PL decay, lock-in thermography [222, 245–248, 316] can yield additional

information on the resistive and the shunted areas of the encapsulated solar cells during their aging; Variable illumination J(V) measurements [70, 304, 305] and impedance spectroscopy [256, 307, 308] can track the presence of traps, which can be linked to the rate of non-radiative recombinations over time.

In parrallel to this work, the development and study of better encapsulation systems, reaching thousands hours of lifetime in damp-heat conditions for state of the art systems has been achieved [129, 196], and should be studied thanks to these techniques.

In addition, cells with adhesion-improved TCO/ETL interface may be studied in order to check if the oxidative species permeation within the cell can be delayed. Replacement of the PEDOT:PSS HTL by an other material may also yield interesting aging results which may be studied with such methods.

Finally, aging of partial stacks (without silver, ETL or TCO layers for example) may be useful in order to study the permeation hindrance and degradation resistance brought by each layer.

Chapter 6

Summary and outlook

Summary

Due to their sensitivity towards moisture and oxygen, organic photovoltaic (OPV) cells have to be protected from their environment by an encapsulation system. However, despite its potential cost and its importance on both the devices as-manufactured performances and lifetime, encapsulation is scarcely described in the literature. In this work, we focused on symmetrical encapsulation strategies where two barrier films, held by an encapsulant layer, sandwich the cells. **Two encapsulation processes were investigated: the roll-to-roll (R2R) lamination of a pressure sensitive adhesive (PSA) and the sheet-to-sheet (S2S) lamination under vacuum of a hotmelt thermoplastic (TP).**

In addition, the **mechanical stresses applied to the flexible devices during their manufacture, encapsulation and use are suspected to be important degradation factors.** Indeed, the literature reports several mechanically weak interfaces or layers within the OPV stacks. The literature also reports that mechanical properties of the devices can be a limiting factor of the devices lifetime, before their photo-chemical stability, and that the devices mean performances and reject rate can be improved by increasing mechanical properties of such weak interfaces.

Furthermore, gathering informations on the device degradation mechanims once encapsulated is challenging. As a result, most of the advanced studies investigating the devices aging are performed on unencapsulated devices or through post-mortem analysis. **Imaging characterizations offer both the assets to be non-destructive as well to be employable on encapsulated devices**. As such, they represent powerful tools to study both the devices processing and aging.

In a first part, **we developed several imaging methods: the laser-beam induced-current (LBIC) mapping, the electro-luminescence (EL) imaging and the photo-luminescence (PL) imaging. Such techniques allow to spatially resolve the local photo-current output, the charge transport ability and the active layer state, respectively.** However, the EL imaging technique was shown to be limited for imaging our poly-3-hexylthiophene (P3HT):phenyl-C61-butyric acid methyl ester (PCBM) OPV cells: imaging cells with relatively small series resistance in a convenient time was impossible and the technique could be destructive and therefore unsuitable for aging studies. As a consequence, **we developed a voltage-biased photoluminescence**

(vbPL) imaging technique which yields images with similar information to EL imaging, with the assets to be fast and non-destructive. The three above mentioned characterizations offer a detailed overview of a 17x25 mm cell properties with at least a 400 µm resolution in less than thirty minutes. **Such relatively fast and convenient techniques allowed us to analyze statistically-relevant batches of samples** which were then processed with a suitable data-analysis method.

We then adapted a classical adhesion characterization technique, the 180 °peeling test, to our flexible devices. Peeling was achieved by pulling the front-side encapsulation with one clamp and holding both the substrate and back-side encapsulation in the other one. The required strength needed to peel the samples was recorded in the same time. In order to attribute such peeling strength values to a debonded interface (in the event of adhesive rupture) or layer (for the case of a cohesive rupture), a combination of physico-chemical characterizations were performed systematically in order to locate each layer on the peeled devices and deduce the corresponding rupture path. **This allowed us to obtain quantitative peeling strengths from flexible devices, without using a sample preparation step foreign to the devices fabrication protocols.** Although the obtained peeling strengths are only comparable to other acquired in the same conditions, two particularly weak interfaces were identified in our reference devices.

In a second part, we investigated the influence of both our reference encapsulation protocols, the PSA/R2R and the TP/S2S protocols, on the devices initial performances.

With classical J(V) characterizations, **we showed that the TP/S2S encapsulation protocol had little to no effect on the cells performances while the PSA/R2R protocol induced significant and strongly dispersed performance losses.** The study of a mixed protocol, the encapsulation with the S2S process and a PSA material, suggested that such losses were more related to the R2R encapsulation process than the PSA material (or a synergistic effect of both).

Imaging characterization applied on the PSA/R2R encapsulated devices showed that the degraded samples exhibited a strongly localized, complete degradation rather than a spatially distributed, milder loss of performance. Because of the strong correlation between vbPL and LBIC images, **such degradation was proven to be originating from a charge-transport failure.**

Consequently, we proposed mechanical degradation occurring during the PSA/R2R encapsulation process to be responsible for the observed performance losses. We then applied our peeling test on partial and complete devices which allowed us to quantify the adhesion of each interface of the devices. In agreement with the literature, **two interfaces were shown to be significantly weaker than the others: the transparent electrode (TCO) / electron transport layer (ETL) interface and the active layer (AL) / hole transport layer (HTL) one.** In contrast with the literature, we did not observe any cohesive rupture, notably within the active layer. As a result, **such weak interfaces were thought to delaminate during the PSA/R2R encapsulation step.**

Thus, we addressed the TCO/ETL weak interface. In the literature, the zinc oxide (ZnO) nanoparticles ETL is often described as a ZnO core with an alkyl outer shell. Such alkyl shell is used to prevent aggregation of the particles in several commercial colloidal suspensions.

However, once the ETL layer is deposited and dried, such alkyl compounds are not useful anymore and are suspected to limit the layer conductivity and to decrease interaction with the TCO layer, which may ultimately prevent adhesion with the underlying layer. In order to assess this hypothesis, we tested two strategies: **the post-ETL-deposition partial removal of the alkyl compounds with a UV-O_3 treatment and the replacement of the ZnO solution by another one with a smaller amount of different alkyl species. As a result, both strategies showed to significantly increase by two orders of magnitude the peeling strength of the TCO/ETL interface.** Furthermore, series resistance of UV-O_3 treated devices were slightly lower than reference devices, which improved initial performances of the former. These results strongly suggest that a high amount of alkyl species as ZnO nanoparticles outer shell limits both its adhesion with the TCO layer and the cells performances. Finally, **UV-O_3 treated devices showed limited and less scattered performance losses after PSA/R2R encapsulation than reference ones.** This result supports our hypothesis of mechanical degradation during the PSA/R2R encapsulation. **It also suggests that performances losses induced by the PSA/R2R encapsulation protocol could be mitigated by improving the devices mechanical stability.**

Finally, the AL/HTL interface was addressed. Several mechanical improvement strategies were considered and **the replacement of the poly(3,4-ethylenedioxythiophene):polystyrene sulfonate (PEDOT:PSS) HTL material by a thick, thermally annealed tungsten trioxide (WO_3) layer was the only method which significantly increased the measured peeling strength measured at the AL/HTL interface.** Although the adhesion mechanism is yet to be precised, post-deposition thermal annealing was shown to be mandatory in order to obtain high peeling strengths. The coincidental apparition of microscopic cracks in the WO_3 layer during annealing suggests that interpenetration of active-layer polymer chains in such cracks may be an important factor for obtaining high peeling strength values between both. However, **cells with a WO_3 HTL layer showed significantly reduced PV efficiencies than the PEDOT:PSS references.** Such result had two origins: increased series resistance, most likely induced by the thick, relatively insulating metal oxide layer and a significantly degraded diode behavior attributed to the poor electron blocking properties of the annealed WO_3 layers as suggested by their relatively high Fermi levels (which were measured).

Finally, aging studies were led on cells encapsulated according to both our reference protocols. **Three aging conditions were studied: the storage in the dark in a glove box, the aging under vacuum at 85 °C and the aging at 85 °C and 85% of relative humidity (RH).** With J(V) characterizations, **we identified moisture and/or oxygen permeation as the main degradation factors of the cells performances.**

Then, previously developed imaging characterizations allowed us to study both the oxidants ingress and the associated degradation mechanisms. **We observed that, despite an almost immediate (less than 13 hours) decrease of performance at 85°C/85%RH, the PSA/R2R encapsulation partially protects the active layer from degradation. In addition, the silver electrode, the TCO and the ETL layers also seem to delay degradation** as PL emission from exposed areas of active layer decreased faster than those covered with such layers. Furthermore,

as no significant lateral PL emission gradient could be observed on any images, **permeation is thought to occur from the devices edges, through the encapsulant rim in less than eleven and twenty hours of aging at 85°C/85%RH for the PSA/R2R and the TP/S2S encapsulation protocols, respectively.**

Finally, **the degradation mechanisms occurring during aging at 85°C/85% RH of reference TP/S2S cells were explored. Such mechanisms were shown to happen in a three step process**: firstly, a short-circuit current degradation, a limited series resistance increase and a PL emission decrease are thought to be originating from a PEDOT:PSS and active layer degradation by water. Secondly, a harsher series resistance increase correlated with the apparition of dark spots on vbPL images is likely originating from the creation of a localized metal-oxide patches between the PEDOT:PSS and silver electrode. Finally, shunt resistance and open-circuit voltage drops were observed on a fraction of the samples. Such drops were shown to be partially reversible after longer aging times. A possible explanation would be the formation of shunting paths through the active layer followed by their passivation with metal oxide patches. The involved shunting mechanism is yet to be cleared, although some groups suggest a possible migration of silver through the PEDOT:PSS layer.

In conclusion, we addressed several degradation mechanisms occurring during encapsulation and aging of the flexible OPV devices. With the help of imaging characterization techniques, the charge transport and the absorption failure contribution on the performances degradation could be separated allowing us to better understand the degradation mechanisms occurring in several processing and aging conditions.

Outlook

This work could be followed in several directions: our characterization methodology could be improved allowing for a richer understanding of various degradation mechanisms.

EL imaging has been largely used in the literature and was proven to be a powerful technique to describe the cells electrical properties [197, 216, 222, 243, 317]. However, we experienced several issues, such as low signal-to-noise ratio or possible degradation of the samples, when we tried to apply it to our samples. Despite we chose to use the vbPL technique to bypass such issues, some enhancements could be brought to the former technique, notably the use of a better spectrally matched detector [47] or the use of the lock-in technique [216, 318].

Although the vbPL imaging characterization could be used to investigate the local charge transport ability of our P3HT:PCBM cells, such technique was not successfully applied on other more efficient donor:acceptor blends tested in our laboratory. In fact, the PL emission mechanism under a voltage bias is not clearly understood. Indeed, for our reference P3HT:PCBM samples, the evolution followed by the PL emission intensity once the cell is under a voltage bias is in opposition with what is generally reported in the OPV literature [37, 82, 205]. A better understanding of such PL mechanisms may enable the application of such technique on several

active layer blends or to extract quantitative parameters from such images, in analogy to what is developed with electro-luminescence imaging [211, 219, 220, 319–321].

Finally, the dark lock-in thermography (DLIT) characterization technique, complementary with our other characterizations, may be useful in order to complete the degradation picture obtained with our methodology. Such technique consists of visualizing the heat emission of a device subjected to a voltage bias in the dark. Its use in reverse or direct bias can yield valuable information on the localization of shunt and series resistances, respectively [245–247, 316]. Its use could notably confirm our hypothesis of shunts formation followed by their passivation during aging of our cells at 85°C/85% RH.

One of our more interesting result was that by improving the mechanical properties of the TCO/ETL interface, the PV performance losses suffered by our devices during PSA/R2R encapsulation could be at least partially mitigated. This result suggests that the improvement of the other weak AL/HTL interface may at least partially reduce such losses. However, the improvement of this interface was challenging and the only satisfactory answer we found, the replacement of the PEDOT:PSS layer by a thick, thermally annealed WO_3 layer, strongly decreased the devices performance. Nonetheless, the performance of WO_3 layers as HTLs may very likely be optimized as several articles report acceptable PV performances with such HTL materials [94, 118, 189, 269, 288]. Such optimization comprise the layers thickness, their post-deposition thermal annealing time and temperature and the Fermi level of the nanoparticles. However, as the adhesion mechanism between the active layer and the WO_3 layer is not understood, peeling tests should be performed in parallel of the tested performance improvement strategies. A similar process could be followed with the upper WO_3/electrode interface that might need mechanical optimization as well, as shown by our preliminary results.

The introduction of mechanical aging tests such as bending or torsion cycle experiments [139] could be performed on such mechanically resilient devices in order to study the influence of mechanical stability on their lifetime in realistic conditions for flexible devices.

Then, encapsulation and aging tests could be performed with other, more efficient encapsulation systems, notably with UV-cured epoxy encapsulants [133, 191, 314] and with a more favorable geometry (larger rim). Imaging characterization performed along aging tests could help to isolate the main degradation mechanisms and to design new encapsulation strategies accordingly. Additional absorption and emission spectra may be acquired in parallel in order to consolidate the imaging data.

The improvement of both the devices protection against atmospheric nocive species, assisted by imaging characterizations, and their intrinsic properties, such as mechanical resilience, should participate to the increase of the OPV modules lifetime.

Bibliography

1. International Energy Agency. Key world energy statistics 2017. <https://www.iea.org/publications/> (2017).
2. Perez, M. & Perez, R. A Fundamental Look At Supply Side Energy Reserves For The Planet. *The international Energy agency shc solar update,* 4 (2015).
3. Hunt, T. *The solar singularity is nigh* (ed media, G.) (2015).
4. International Energy Agency. World Energy Outlook 2017. <https://www.iea.org/publications/> (2017).
5. Becquerel, A. E. Decomposition de l eau par le moyen de deux lames de platine en communication chacune avec l un des elements d un couple voltaique ; procede de M. Grove. *Comptes rendus hebdomadaires des seances de l Academie des sciences* **8,** 497 (1839).
6. Weston, E. *pat.* US389124 (1888).
7. Shirakawa, H., Louis, E., MacDiarmid, A., Chiang, C. & Heeger, A. Synthesis of electrically conducting organic polymers: halogen derivatives of polyacetylene, (CH)x. *Journal of the Chemical Society, Chemical communications* **16,** 578–580 (1977).
8. Kaltenbrunner, M. *et al.* Ultrathin and lightweight organic solar cells with high flexibility. *Nature Communications* **3,** 770. ISSN: 2041-1723 (2012).
9. Wang, X., Ng, G.-M., Ho, J.-W., Tam, H.-L. & Zhu, F. Efficient Semitransparent Bulk-Heterojunction Organic Photovoltaic Cells With High-Performance Low Processing Temperature Indium Tin Oxide Top Electrode. *IEEE J. Select. Topics Quantum Electron.* **16,** 1685–1689. ISSN: 1558-4542 (2010).
10. Wen, L. *et al.* Theoretical design of multi-colored semi-transparent organic solar cells with both efficient color filtering and light harvesting. *Sci. Rep.* **4,** 7036. ISSN: 2045-2322 (2014).
11. Eggenhuisen, T. M. *et al.* High efficiency, fully inkjet printed organic solar cells with freedom of design. *Journal of Materials Chemistry A* **3,** 7255 (2015).
12. Sondergaard, R., Hosel, M., Angmo, D., Larsen-Olsen, T. T. & Krebs, F. C. Roll-to-roll fabrication of polymer solar cells. *materials today* **15,** 36 (2012).
13. *Dracula Technologies* <https://www.dracula-technologies.com/innovation-technology-OPV> (2018).
14. Davy, N. C. Near-UV Organic solar cells paired with electrochromic windows for smart management of the solar spectrum. *Nature Energy* **2** (2017).

15. Weinberger, B., Akhtar, M. & Gau, S. Polyacetylene photovoltaic devices. *Synthetic Metals* **4,** 187–197 (1982).
16. GmbH, H. *Heliatek sets new Organic Photovoltaic world record efficiency of 13.2%* (ed GmbH, H.) <http://www.heliatek.com/en/press/press-releases/details/heliatek-sets-new-organic-photovoltaic-world-record-efficiency-of-13-2> (2016).
17. *Fraunhofer Institute for Solar Energy Systems* <https://www.ise.fraunhofer.de/en.html>.
18. NREL. *NREL efficiency chart* <https://www.nrel.gov> (2018).
19. Grossiord, N., Kroon, J. M., Andriessen, R. & W.M., B. P. Degradation mechanisms in organic photovoltaic devices. *Organic Electronics,* 432–456 (2012).
20. Gevorgyan, S. A. *et al.* Baselines for Lifetime of Organic Solar Cells. *Advanced Energy Materials* **6,** 1600910. ISSN: 1614-6832 (2016).
21. Konarka Technologies, NREL and University of Delaware. *Low Cost, Lightweight Solar Modules Based on Organic Photovoltaic Technology* (2010).
22. Chittibabu, K., Estes, R., Gaudiana, R., Kreger, M. & Zeira, E. *pat.* WO2011112701A1. WO Patent App. PCT/US2011/027,722. <https://www.google.com/patents/WO2011112701A1?cl=en>(2011).
23. Yan, F., Noble, J., Peltola, J., Wicks, S. & Balasubramanian, S. Semitransparent OPV modules pass environmental chamber test requirements. *Solar Energy Materials & Solar Cells,* 214–218 (114 2013).
24. commision, I. E. <http://www.iec.ch/>.
25. Krebs, F. C., Espinosa, N., Hosel, M., Sondergaard, R. R. & Jorgensen, M. 25th Anniversary Article: Rise to Power - OPV-Based Solar Parks. *Advanced Materials* **26,** 29–39. ISSN: 0935-9648 (2013).
26. Krebs, F. C., Nielsen, T. D., Fyenbo, J., Wadstrom, M. & Pedersen, M. S. Manufacture, integration and demonstration of polymer solar cells in a lamp for the "Lighting Africa" initiative. *Energy & Environmental Science* **3,** 512. ISSN: 1754-5706 (2010).
27. Hu, B. *Workshop on Key Scientific and Technological Issues for Development of Next-Generation Organic Solar Cells* tech. rep. (National Science Foundation and Office of Naval Research, 2012).
28. Blom, P. W. M., Mihailetchi, V. D., Koster, L. J. A. & Markov, D. E. Device Physics of Polymer:Fullerene Bulk Heterojunction Solar Cells. *Advanced Materials* **19,** 1551–1566. ISSN: 1521-4095 (2007).
29. Goswami, D. Y. *Advances in Solar Energy : An Annual Review of Research and Development* (2007).
30. Scharber, M. & Sariciftci, N. Efficiency of bulk-heterojunction organic solar cells. *Progress in Polymer Science* **38,** 1929–1940. ISSN: 0079-6700 (Apr. 2013).
31. Tang, C. W. Two layer organic photovoltaic cell. *Applied Physics Letters* **48,** 183–185. ISSN: 1077-3118 (1986).

32. Halls, J. J. M. *et al.* Charge- and energy-transfer processes at polymer/polymer interfaces: A joint experimental and theoretical study. *Physical Review B* **60,** 5721–5727 (1999).
33. Melianas, A. *et al.* Photo-generated carriers lose energy during extraction from polymer-fullerene solar cells. *Nature Communications* **6,** 8778. ISSN: 2041-1723 (2015).
34. Muller, J. G. *et al.* Ultrafast dynamics of charge carrier photogeneration and geminate recombination in conjugated polymer:fullerene solar cells. *Physical Review B* **72.** ISSN: 1550-235X. doi:10.1103/physrevb.72.195208. <http://dx.doi.org/10.1103/PhysRevB.72.195208> (2005).
35. Banerji, N., Cowan, S., Vauthey, E. & Heeger, A. J. Ultrafast Relaxation of the Poly(3-hexylthiophene) Emission Spectrum. *The Journal of Physical Chemistry C* **115,** 9726–9739. ISSN: 1932-7455 (2011).
36. Loi, M. A. *et al.* Charge Transfer Excitons in Bulk Heterojunctions of a Polyfluorene Copolymer and a Fullerene Derivative. *Advanced Functional Materials* **17,** 2111–2116. ISSN: 1616-3028 (2007).
37. Tvingstedt, K., Vandewal, K., Zhang, F. & Inganas, O. On the Dissociation Efficiency of Charge Transfer Excitons and Frenkel Excitons in Organic Solar Cells: A Luminescence Quenching Study. *The Journal of Physical Chemistry C* **114,** 21824–21832. ISSN: 1932-7455 (2010).
38. Lee, J. *et al.* Charge Transfer State Versus Hot Exciton Dissociation in Polymer-Fullerene Blended Solar Cells. *Journal of the American Chemical Society* **132,** 11878–11880. ISSN: 1520-5126 (2010).
39. Vandewal, K. *et al.* Efficient charge generation by relaxed charge-transfer states at organic interfaces. *Nature Materials* **13,** 63–68. ISSN: 1476-4660 (2013).
40. Kniepert, J., Schubert, M., Blakesley, J. C. & Neher, D. Photogeneration and Recombination in P3HT/PCBM Solar Cells Probed by Time-Delayed Collection Field Experiments. *The Journal of Physical Chemistry Letters* **2,** 700–705. ISSN: 1948-7185 (2011).
41. Cowan, S. R., Street, R. A., Cho, S. & Heeger, A. J. Transient photoconductivity in polymer bulk heterojunction solar cells: Competition between sweep-out and recombination. *Physical Review B* **83,** 035205. ISSN: 1550-235X (2011).
42. Grancini, G. *et al.* Hot exciton dissociation in polymer solar cells. *Nature Materials* **12,** 29–33. ISSN: 1476-4660 (2012).
43. Tamura, H. & Burghardt, I. Ultrafast Charge Separation in Organic Photovoltaics Enhanced by Charge Delocalization and Vibronically Hot Exciton Dissociation. *Journal of the American Chemical Society* **135,** 16364–16367. ISSN: 1520-5126 (2013).
44. Chen, W. *et al.* Hierarchical Nanomorphologies Promote Exciton Dissociation in Polymer/Fullerene Bulk Heterojunction Solar Cells. *Nano Letters* **11,** 3707–3713. ISSN: 1530-6992 (2011).
45. Bansal, N. *et al.* Influence of Crystallinity and Energetics on Charge Separation in Polymer-Inorganic Nanocomposite Films for Solar Cells. *Scientific Reports* **3,** 1–8. ISSN: 2045-2322 (2013).

46. Kastner, C., Vandewal, K., Egbe, D. A. M. & Hoppe, H. Revelation of Interfacial Energetics in Organic Multiheterojunctions. *Advanced Science,* 1600331. ISSN: 2198-3844 (2017).
47. Tvingstedt, K. *et al.* Electroluminescence from Charge Transfer States in Polymer Solar Cells. *Journal of the American Chemical Society* **131,** 11819–11824. ISSN: 1520-5126 (2009).
48. Kirchartz, T., Pieters, B. E., Kirkpatrick, J., Rau, U. & Nelson, J. Recombination via tail states in polythiophene:fullerene solar cells. *Physical Review B* **83.** ISSN: 1550-235X. doi:10.1103/physrevb.83.115209. <http://dx.doi.org/10.1103/PhysRevB.83.115209> (2011).
49. Hawks, S. A., Li, G., Yang, Y. & Street, R. A. Band tail recombination in polymer:fullerene organic solar cells. *Journal of Applied Physics* **116,** 074503. ISSN: 1089-7550 (2014).
50. Street, R. A., Northrup, J. E. & Krusor, B. S. Radiation induced recombination centers in organic solar cells. *Physical Review B* **85,** 043305. ISSN: 1550-235X (2012).
51. Street, R. A., Krakaris, A. & Sarah.R., C. Recombination Through Different Types of Localized States in Organic Solar Cells. *Adv. Funct. Mater.* **22,** 4608–4619 (2012).
52. Street, R. A. & Davies, D. M. Kinetics of light induced defect creation in organic solar cells. *Applied Physics Letters* **102,** 043305. ISSN: 1077-3118 (2013).
53. Tamai, Y., Ohkita, H., Benten, H. & Ito, S. Exciton Diffusion in Conjugated Polymers: From Fundamental Understanding to Improvement in Photovoltaic Conversion Efficiency. *The Journal of Physical Chemistry Letters* **6,** 3417–3428. ISSN: 1948-7185 (2015).
54. Halls, J. J. M. *et al.* Efficient photodiodes from interpenetrating polymer networks. *Nature* **376,** 498–500 (1995).
55. Yu, G., Gao, J., Hummelen, J. C., Wudi, F. & Heeger, A. J. Polymer Photovoltaic Cells: Enhanced Efficiencies via a Network of Internal Donor-Acceptor Heterojunctions. *Science* **270,** 1789 (1995).
56. Hoppe, H. & Sariciftci, N. S. Morphology of polymer/fullerene bulk heterojunction solar cells. *Journal of Materials Chemistry* **16,** 45–61 (2006).
57. Hoppe, H. *et al.* Efficiency limiting morphological factors of MDMO-PPV:PCBM plastic solar cells. *Thin Solid Films* **511,** 587–592 (2006).
58. Huang, Y.-C. *et al.* Study of the effect of annealing process on the performance of P3HT/PCBM photovoltaic devices using scanning-probe microscopy. *Solar energy Materials & Solar Cells* **93,** 288–292 (2009).
59. Krantz, J. *et al.* Printing high performance reflective electrodes for organic solar cells. *Organic Electronics* **17,** 334–339. ISSN: 1566-1199 (2015).
60. Steim, R., Kogler, F. R. & Brabec, C. J. Interface materials for organic solar cells. *Journal of Materials Chemistry* **20,** 2499. ISSN: 1364-5501 (2010).
61. Lattante, S. Electron and Hole Transport Layers: Their Use in Inverted Bulk Heterojunction Polymer Solar Cells. *Electronics* **3,** 132–164. ISSN: 2079-9292 (2014).

62. Kanwat, A. & Jang, J. Extremely stable organic photovoltaic incorporated with WOxdoped PEDOT:PSS anode buffer layer. *J. Mater. Chem. C* **2,** 901–907. ISSN: 2050-7534 (2014).
63. Reese, M. O. *et al.* Pathways for the degradation of organic photovoltaic P3HT:PCBM based devices. *Solar Energy Materials and Solar Cells* **92,** 746–752. ISSN: 0927-0248 (2008).
64. Glatthaar, M. *et al.* Organic solar cells using inverted layer sequence. *Thin Solid Films* **491,** 298–300. ISSN: 0040-6090 (2005).
65. Zhang, F. *et al.* Recent development of the inverted configuration organic solar cells. *Solar Energy Materials and Solar Cells* **95,** 1785–1799. ISSN: 0927-0248 (2011).
66. Gevorgyan, S. A. *et al.* Lifetime of Organic Photovoltaics: Status and Predictions. *Adv. Energy. Mater.* **6,** 1501208 (2015).
67. Shockley, W. The theory of p-n junctions in semiconductors and p-n junction transistors. *The Bell System technical Journal* **28,** 435–489 (1949).
68. Cuevas, A. The recombination parameter J0. *Energy Procedia* **55,** 53–62 (2014).
69. Sah, C.-t., Noyce, R. N. & William, S. Carrier Generation and Recombination in P-N Junctions and P-N Junction Characteristics. *Proceedings of the IRE* **September,** 1228 (1957).
70. Tvingstedt, K. & Deibel, C. Temperature Dependence of Ideality Factors in Organic Solar Cells and the Relation to Radiative Efficiency. *Advanced Energy Materials* **6,** 1502230. ISSN: 1614-6832 (2016).
71. Hawks, S. A. *et al.* Relating Recombination, Density of States, and Device Performance in an Efficient Polymer:Fullerene Organic Solar Cell Blend. *Advanced Energy Materials* **3,** 1201–1209. ISSN: 1614-6832 (2013).
72. Wetzelaer, G.-J. A. H., Kuik, M. & Blom, P. W. M. Identifying the Nature of Charge Recombination in Organic Solar Cells from Charge-Transfer State Electroluminescence. *Adv. Energy Mater.* **2,** 1232–1237 (2012).
73. Servaites, J. D., Ratner, M. A. & Marks, T. J. Organic solar cells: A new look at traditional models. *Energy Environ. Sci.* **4,** 4410. ISSN: 1754-5706 (2011).
74. Banwell, T. & Jayakumar, A. Exact analytical solution for current flow through diode with series resistance. *Electronics letters* **36,** 291–292 (2000).
75. Kumar, P., Jain, S. C., Kumar, V., Chand, S. & Tandon, R. P. A model for the J-V characteristics of P3HT:PCBM solar cells. *Journal of Applied Physics* **105,** 104507. ISSN: 1089-7550 (2009).
76. Kumar, P. & Gaur, A. Model for the J-V characteristics of degraded polymer solar cells. *Journal of Applied Physics* **113,** 094505. ISSN: 1089-7550 (2013).
77. Krebs, F. C., Tromholt, T. & Jorgensen, M. Upscaling of polymer solar cell fabrication using full roll-to-roll processing. *Nanoscale* **2,** 873. ISSN: 2040-3372 (2010).
78. Bird, R., Hulstrom, R. & Lewis, L. Terrestrial Solar Spectral Data Sets. *Solar Energy* **30,** 563 (1983).

79. Vandewal, K., Tvingstedt, K., Gadisa, A., Inganas, O. & Manca, J. V. On the origin of the open-circuit voltage of polymer-fullerene solar cells. *Nat Mater* **8,** 904–909. ISSN: 1476-4660 (2009).

80. Vandewal, K., Tvingstedt, K., Gadisa, A., Inganas, O. & Manca, J. V. Relating the open-circuit voltage to interface molecular properties of donor:acceptor bulk heterojunction solar cells. *Physical Review B* **81.** ISSN: 1550-235X. doi:10.1103/physrevb.81.125204. <http://dx.doi.org/10.1103/PhysRevB.81.125204> (2010).

81. Manor, A. & Katz, E. A. Open-circuit voltage of organic photovoltaics: Implications of the generalized Einstein relation for disordered semiconductors. *Solar Energy Materials and Solar Cells* **97,** 132–138. ISSN: 0927-0248 (2012).

82. Spies, A., List, M., Sarkar, T. & Wurfel, U. On the Impact of Contact Selectivity and Charge Transport on the Open-Circuit Voltage of Organic Solar Cells. *Advanced Energy Materials,* 1601750. ISSN: 1614-6832 (2016).

83. Blakesley, J. C. & Neher, D. Relationship between energetic disorder and open-circuit voltage in bulk heterojunction organic solar cells. *Physical Review B* **84,** 075210. ISSN: 1550-235X (2011).

84. Street, R. A. Electronic Structure and Properties of Organic Bulk-Heterojunction Interfaces. *Advanced Materials* **28,** 3814–3830. ISSN: 0935-9648 (2016).

85. Shuttle, C. G. *et al.* Experimental determination of the rate law for charge carrier decay in a polythiophene: Fullerene solar cell. *Applied Physics Letters* **92,** 093311. ISSN: 1077-3118 (2008).

86. Mateker, W. R. & McGehee, M. D. Progress in Understanding Degradation Mechanisms and Improving Stability in Organic Photovoltaics. *Advanced Materials* **29,** 1603940. ISSN: 0935-9648 (2017).

87. Reese, M. O. *et al.* Consensus stability testing protocols for organic photovoltaic materials and devices. *Solar Energy Materials and Solar Cells* **95,** 1253–1267. ISSN: 0927-0248 (2011).

88. Sachs-Quintana, I. T. *et al.* Electron Barrier Formation at the Organic-Back Contact Interface is the First Step in Thermal Degradation of Polymer Solar Cells. *Advanced Functional Materials* **24,** 3978–3985. ISSN: 1616-301X (2014).

89. Muller, C. On the Glass Transition of Polymer Semiconductors and Its Impact on Polymer Solar Cell Stability. *Chemistry of Materials* **27,** 2740–2754. ISSN: 1520-5002 (2015).

90. Yip, H.-L. & Jen, A. K.-Y. Recent advances in solution-processed interfacial materials for efficient and stable polymer solar cells. *Energy & Environmental Science* **5,** 5994. ISSN: 1754-5706 (2012).

91. Dupont, S. R., Voroshazi, E., Nordlund, D., Vandewal, K. & Dauskardt, R. H. Controlling Interdiffusion, Interfacial Composition, and Adhesion in Polymer Solar Cells. *Advanced Materials Interfaces* **1.** ISSN: 2196-7350. doi:10.1002/admi.201400135. <http://dx.doi.org/10.1002/admi.201400135> (2014).

92. Bhowmik, R., Berry, R. J., Varshney, V., Durstock, M. F. & Leever, B. J. Molecular Modeling of Interfaces between Hole Transport and Active Layers in Flexible Organic

Electronic Devices. *The Journal of Physical Chemistry C* **119,** 27909–27918. ISSN: 1932-7455 (2015).

93. Greenbank, W., Hirsch, L., Wantz, G. & Chambon, S. Interfacial thermal degradation in inverted organic solar cells. *Applied Physics Letters* **107,** 263301. ISSN: 1077-3118 (2015).
94. Greenbank, W. *et al.* Improved mechanical adhesion and electronic stability of organic solar cells with thermal ageing: the role of diffusion at the hole extraction interface. *J. Mater. Chem. A* **5,** 2911–2919. ISSN: 2050-7496 (2017).
95. Hermerschmidt, F. *et al.* Influence of the Hole Transporting Layer on the Thermal Stability of Inverted Organic Photovoltaics Using Accelerated-Heat Lifetime Protocols. *ACS Applied Materials & Interfaces.* ISSN: 1944-8252. doi:10.1021/acsami.7b01183. <http://dx.doi.org/10.1021/acsami.7b01183> (2017).
96. Vitoratos, E. *et al.* Thermal degradation mechanisms of PEDOT:PSS. *Organic Electronics* **10,** 61–66. ISSN: 1566-1199 (2009).
97. Voroshazi, E., Cardinaletti, I., Conard, T. & Rand, B. P. Light-Induced Degradation of Polymer:Fullerene Photovoltaic Devices: An Intrinsic or Material-Dependent Failure Mechanism? *Adv. Energy Mater.* **4,** 1400848. ISSN: 1614-6832 (2014).
98. Heumueller, T. *et al.* Morphological and electrical control of fullerene dimerization determines organic photovoltaic stability. *Energy Environ. Sci.* **9,** 247–256. ISSN: 1754-5706 (2016).
99. Schwenn, P. E. *et al.* A Small Molecule and Non-fullerene Electron acceptor and Organic Solar and Cells. *Adv.Energy Mater.* **1,** 73–81 (2011).
100. Yan, L. *et al.* External load-dependent degradation of P3HT:PC61BM solar cells: behavior, mechanism, and method of suppression. *J. Mater. Chem. A* **5,** 10010–10020 (20 2017).
101. Krebs, F. *Stability and degradation of organic and polymer solar cells* (2012).
102. Lilliedal, M. R., Medford, A. J., Madsen, M. V., Norrman, K. & Krebs, F. C. The effect of post-processing treatments on inflection points in currentvoltage curves of roll-to-roll processed polymer photovoltaics. *Solar Energy Materials and Solar Cells* **94,** 2018–2031. ISSN: 0927-0248 (2010).
103. Manor, A., Katz, E. A., Tromholt, T. & Krebs, F. C. Enhancing functionality of ZnO hole blocking layer in organic photovoltaics. *Solar Energy Materials and Solar Cells* **98,** 491–493. ISSN: 0927-0248 (2012).
104. Wilken, S., Parisi, J. & Borchert, H. Role of Oxygen Adsorption in Nanocrystalline ZnO Interfacial Layers for Polymer:Fullerene Bulk Heterojunction Solar Cells. *The Journal of Physical Chemistry C* **118,** 19672–19682. ISSN: 1932-7455 (2014).
105. Manceau, M. *et al.* Effects of long-term UV-visible light irradiation in the absence of oxygen on P3HT and P3HT:PCBM blend. *Solar Energy Materials and Solar Cells* **94,** 1572–1577. ISSN: 0927-0248 (2010).

106. Kroon, J., Wienk, M., Verhees, W. & J.C., H. Accurate efficiency determination and stability studies of conjugated and polymer-fullerene solar cells. *Thin Solid Films* **403-404,** 223–228 (2002).

107. Manceau, M. *et al.* Photochemical stability of pi-conjugated polymers for polymer solar cells: a rule of thumb. *Journal of Materials Chemistry* **21,** 4132. ISSN: 1364-5501 (2011).

108. Manceau, M., Helgesen, M. & Krebs, F. C. Thermo-cleavable polymers: Materials with enhanced photochemical stability. *Polymer Degradation and Stability* **95,** 2666–2669. ISSN: 0141-3910 (2010).

109. Cros, S., Firon, M., Lenfant, S., Trouslard, P. & Beck, L. Study of thin calcium electrode degradation by ion beam analysis. *Nuclear Instruments and Methods in Physics Research Section B: Beam Interactions with Materials and Atoms* **251,** 257–260. ISSN: 0168-583X (2006).

110. Hermenau, M. *et al.* Water and oxygen induced degradation of small molecule organic solar cells. *Solar Energy Materials and Solar Cells* **95,** 1268–1277. ISSN: 0927-0248 (2011).

111. Norrman, K., Gevorgyan, S. A. & Krebs, F. C. Water-Induced Degradation of Polymer Solar Cells Studied by H218O Labeling. *ACS Applied Materials & Interfaces* **1,** 102–112. ISSN: 1944-8252 (2009).

112. Madogni, V. I. *et al.* Comparison of degradation mechanisms in organic photovoltaic devices upon exposure to a temperate and a subequatorial climate. *Chemical Physics Letters* **640,** 201–214. ISSN: 0009-2614 (2015).

113. Jorgensen, M. *et al.* Stability of Polymer Solar Cells. *Advanced Materials* **24,** 580–612. ISSN: 0935-9648 (2012).

114. Voroshazi, E. *et al.* Influence of cathode oxidation via the hole extraction layer in polymer:fullerene solar cells. *Organic Electronics* **12,** 736–744. ISSN: 1566-1199 (2011).

115. Girotto, C., Voroshazi, E., Cheyns, D., Heremans, P. & Rand, B. P. Solution-Processed MoO3 Thin Films As a Hole-Injection Layer for Organic Solar Cells. *ACS Applied Materials & Interfaces* **3,** 3244–3247. ISSN: 1944-8252 (2011).

116. Betancur, R., Maymo, M., Elias, X., Vuong, L. T. & Martorell, J. Sputtered NiO as electron blocking layer in P3HT:PCBM solar cells fabricated in ambient air. *Solar Energy Materials and Solar Cells* **95,** 735–739. ISSN: 0927-0248 (2011).

117. Huang, J.-S., Chou, C.-Y. & Lin, C.-F. Efficient and Air-Stable Polymer Photovoltaic Devices With WO_3-V_2O_5 Mixed Oxides as Anodic Modification. *IEEE Electron Device Letters* **31,** 332–334. ISSN: 1558-0563 (2010).

118. Espinosa, N. *et al.* Roll-to-Roll Processing of Inverted Polymer Solar Cells using Hydrated Vanadium(V)Oxide as a PEDOT:PSS Replacement. *Materials* **4,** 169–182. ISSN: 1996-1944 (2011).

119. Abdulrazzaq, O. *et al.* Comparative Aging Study of Organic Solar Cells Utilizing Polyaniline and PEDOT:PSS as Hole Transport Layers. *ACS Applied Materials & Interfaces* **7,** 27667–27675. ISSN: 1944-8252 (2015).

120. Savva, A., Burgues-Ceballos, I., Papazoglou, G. & Choulis, S. A. High-Performance Inverted Organic Photovoltaics Without Hole-Selective Contact. *ACS Applied Materials & Interfaces* **7,** 24608–24615. ISSN: 1944-8252 (2015).

121. Czanderna, A. & Pern, F. Encapsulation of PV modules using ethylene vinyl acetate copolymer as a pottant: A critical review. *Solar Energy Materials and Solar Cells* **43,** 101–181 (1996).

122. Koontz, J. D. *Ice sphere impact testing of photovoltaic solar panels* in. 27 th RCI International Convention and Trade show (2012).

123. Manceau, M., Matheron, M., Lemaitre, N., Cros, S. & Berson, S. *Lifetime study of flexible encapsulated organic photovoltaic modules: optimization of device architecture and selection of encapsulation materials* in. Flex Europe Conference 2016 (2016).

124. Mulligan, C. J. *et al.* A projection of commercial-scale organic photovoltaic module costs. *Solar Energy Materials and Solar Cells* **120,** 9 –17. ISSN: 0927-0248 (2014).

125. Machui, F. *et al.* Cost analysis of roll-to-roll fabricated ITO free single and tandem organic solar modules based on data from manufacture. *Energy & Environmental Science* **7,** 2792 (2014).

126. Espinosa, N. *et al.* OPV for mobile applications: an evaluation of roll-to-roll processed indium and silver free polymer solar cells through analysis of life cycle, cost and layer quality using inline optical and functional inspection tools. *Journal of Materials Chemistry A* **1,** 7037 (2013).

127. Cros, S. *et al.* Definition of encapsulation barrier requirements: A method applied to organic solar cells. *Solar Energy Materials and Solar Cells* **95,** S65–S69. ISSN: 0927-0248 (2011).

128. Delo. *Delo Katiobond LP655 UV-curable epoxy adhesive data sheet* tech. rep. (). <https://www.delo-adhesives.com/fileadmin/datasheet/DELO%20KATIOBOND_LP655_%28TIDB-GB%29.pdf>.

129. Weerasinghe, H. C., Rolston, N., Vak, D., Scully, A. D. & Dauskardt, R. H. A stability study of roll-to-roll processed organic photovoltaic modules containing a polymeric electron-selective layer. *Solar Energy Materials & Solar Cells* **152,** 133–140 (2016).

130. Tanenbaum, D. M. *et al.* Edge sealing for low cost stability enhancement of roll-to-roll processed flexible polymer solar cell modules. *Solar Energy Materials and Solar Cells* **97,** 157–163. ISSN: 0927-0248 (2012).

131. PSA tapes enhance the capabilities and performance of photovoltaic modules. *Sealing Technology* **2012,** 1. ISSN: 1350-4789 (2012).

132. Cros, S. & Maindron, T. *Technologies d'encapsulation avancees pour l'electronique organique* ed. by de l'ingenieur, T. (2014).

133. Hosel, M., Sondergaard, R. R., Jorgensen, M. & Krebs, F. C. Comparison of UV-Curing, Hotmelt, and Pressure Sensitive Adhesive as Roll-to-Roll Encapsulation Methods for Polymer Solar Cells. *Adv. Eng. Mater.* **15,** 1068–1075. ISSN: 1438-1656 (2013).

134. Angmo, D. *et al.* Scalability and stability of very thin, roll-to-roll processed, large area, indium-tin-oxide free polymer solar cell modules. *Organic Electronics* **14,** 984–994. ISSN: 1566-1199 (2013).

135. Gevorgyan, S. & Madsen, M. V. <http://plasticphotovoltaics.org/lc/chara\-cterization/lc-isos.html>.

136. Norrman, K., Madsen, M. V., Gevorgyan, S. A. & Krebs, F. C. Degradation Patterns in Water and Oxygen of an Inverted Polymer Solar Cell. *Journal of the American Chemical Society* **132,** 16883–16892. ISSN: 1520-5126 (2010).

137. Lipomi, D. J. & Bao, Z. Stretchable, elastic materials and devices for solar energy conversion. *Energy & Environmental Science* **4,** 3314. ISSN: 1754-5706 (2011).

138. Savagatrup, S., Printz, A. D., OConnor, T. F., Zaretski, A. V. & Lipomi, D. J. Molecularly Stretchable Electronics. *Chemistry of Materials* **26,** 3028–3041. ISSN: 1520-5002 (2014).

139. Finn, M. *et al.* Mechanical stability of roll-to-roll printed solar cells under cyclic bending and torsion. *Solar Energy Materials and Solar Cells* **174,** 7 –15. ISSN: 0927-0248 (2018).

140. Savagatrup, S. *et al.* Mechanical degradation and stability of organic solar cells: molecular and microstructural determinants. *Energy Environ. Sci.* **8,** 55–80. ISSN: 1754-5706 (2015).

141. Da Silva, L. F. M., Ochsner, A. & Adams, R. D. *Handbook of Adhesion Technology* (2011).

142. Tong, Q.-Y. & Gosele, U. *SemiConductor Wafer Bonding: Science and Technology* (ed electrochemical society, T.) (Wiley, 1998).

143. Hobart, K. D. *Semiconductor Wafer Bonding VIII : Science, Technology, and Applications* (ed electrochemical society, T.) (ECS, 2005).

144. Adamson, A. W. *Physical chemistry of surfaces* (eds Wiley, J. & Sons) (John Wiley and Sons, 1990).

145. Licari, J. J. & Swanson, D. W. *Adhesives Technology for Electronic Applications: Materials, Processing, Reliabilty* (William Andrew, 2011).

146. Kinloch, A. *Adhesion and Adhesives: Science and Technology* (ed Media, S. S. . B.) (Springer Science & Business Media, 2012).

147. Benedek, I. *Pressure-Sensitive Adhesives and Applications, Second Edition* (ed Press, C.) (Marcel-Decker.Inc, 2004).

148. Oliver, J. F. *Adhesion in Cellulosic and Wood-Based Composites* (ed Oliver, J. F.) (Plenum Press, 2013).

149. Dupont, S. R., Voroshazi, E., Heremans, P. & Dauskardt, R. H. Adhesion properties of inverted polymer solarcells: Processing and film structure parameters. *Organic Electronics* **14,** 1262–1270. ISSN: 1566-1199 (2013).

150. Huang, D. M. *et al.* The Consequences of Interface Mixing on Organic Photovoltaic Device Characteristics. *Adv. Funct. Mater* **21,** 1657–1665 (2011).

151. Mueller, C., Capaccio, G., Hiltner, A. & Baer, E. Heat Sealing of LLDPE: Relationships to Melting and Interdiffusion. *Journal of applied polymer science* **70,** 2021 (1998).

152. Planes, E. & Flandin, S. M. . L. Optimizing the heat sealing parameters of multilayers polymeric films. *J Mater Sci* **46,** 5948–5958 (2011).

153. Strobhand, S. & Dauskardt, R. Interface Separation in Residually-Stressed Thin-Film Structures. *Interface science* **11,** 309–317 (2003).

154. Mittal, K. Adhesion measurements of thin films. *Electrocomponent Science and Technology* **3,** 21–42 (1976).

155. Kleinbichler, A., Bartosik, M., Volker, B. & Cordill, M. J. Thin Film Adhesion of Flexible Electronics Influenced by Interlayers. *Advanced Engineering Materials* (2016).

156. Dauskardt, R., Lane, M., Mab, Q. & Krishna, N. Adhesion and debonding of multi-layer thin film structures. *Engineering Fracture Mechanics* **61,** 141–162 (1998).

157. Lane, M. & Dauskardt, R. H. Plasticity contributions to interface adhesion in thin-film interconnect structures. *J. Mater. Res* **15,** 2758 (2000).

158. Hakeem, M. I. & Phillips, M. G. Unstable crack propagation - A fractographic study using PMMA in liquid environments. *Journal of material science* **14,** 2901–2905 (1979).

159. Bruner, C. & Dauskardt, R. Role of Molecular Weight on the Mechanical Device Properties of Organic Polymer Solar Cells. *Macromolecules* **47,** 1117–1121. ISSN: 1520-5835 (2014).

160. Gledhill, R. A., Kinloch, A. J., Yamini, S. & Young, R. J. Relationship between mechanical properties and crack propagation in epoxy resin adhesives. *Polymer* **19,** 574–582 (1978).

161. Lang, U., Nicola, N. & Dual, J. Mechanical characterization of PEDOT:PSS thin films. *Synthetic Metals* **159,** 473 (2009).

162. Tummala, N. R., Bruner, C., Risko, C., Bredas, J.-L. & Dauskardt, R. H. Molecular-Scale Understanding of Cohesion and Fracture in P3HT:Fullerene Blends. *ACS Applied Materials & Interfaces* **7,** 9957–9964. ISSN: 1944-8252 (2015).

163. Dupont, S. R., Voroshazi, E., Nordlund, D. & Dauskardt, R. H. Morphology and interdiffusion control to improve adhesion and cohesion properties in inverted polymer solar cells. *Solar Energy Materials and Solar Cells* **132,** 443–449. ISSN: 0927-0248 (2015).

164. Balcaen, V., Rolston, N., Dupont, S. R., Voroshazi, E. & Dauskardt, R. H. Thermal cycling effect on mechanical integrity of inverted polymer solar cells. *Solar Energy Materials and Solar Cells* **143,** 418–423. ISSN: 0927-0248 (2015).

165. Dupont, S. R., Novoa, F., Voroshazi, E. & Dauskardt, R. H. Decohesion Kinetics of PEDOT:PSS Conducting Polymer Films. *Adv. Funct. Mater.* **24,** 1325–1332. ISSN: 1616-301X (2013).

166. Tummala, N. R., Risko, C., Bruner, C., Dauskardt, R. H. & Bredas, J.-L. Entanglements in P3HT and Their Influence on Thin-Film Mechanical Properties: Insights from Molecular Dynamics Simulations. *Journal of polymer science* **53,** 934 (2015).

167. Dupont, S. R., Oliver, M., Krebs, F. C. & Dauskardt, R. H. Interlayer adhesion in roll-to-roll processed flexible inverted polymer solar cells. *Solar Energy Materials and Solar Cells* **97,** 171–175. ISSN: 0927-0248 (2012).

168. Corazza, M. *et al.* Role of Stress Factors on the Adhesion of Interfaces in R2R Fabricated Organic Photovoltaics. *Adv. Enrgy Mater.* 1501927 (2016).

169. Bruner, C., Miller, N. C., McGehee, M. D. & Dauskardt, R. H. Molecular Intercalation and Cohesion of Organic and Bulk and Heterojunction Photovoltaic and Devices. *Adv. Funct. Mater* **23,** 2863–2871 (2013).

170. Bruner, C., Novoa, F., Dupont, S. & Dauskardt, R. Decohesion Kinetics in Polymer Organic Solar Cells. *Applied materials and interfaces* **6,** 21474 (2014).

171. Brand, V., Bruner, C. & Dauskardt, R. H. Cohesion and device reliability in organic bulk heterojunction photovoltaic cells. *Solar Energy Materials and Solar Cells* **99,** 182–189. ISSN: 0927-0248 (2012).

172. Dupont, S. R., Voroshazi, E., Heremans, P. & Dauskardt, R. H. The effect of anneal, solar irradiation and humidity on the adhesion/cohesion properties of P3HT:PCBM based inverted polymer. *IEEE* **12,** 003259 (2011).

173. Davidson, P. & Waas, A. M. Non-smooth mode I fracture of fibre-reinforced composites: an experimental, numerical and analytical study. *Philosophical Transactions of the Royal Society A: Mathematical, Physical and Engineering Sciences* **370,** 1942–1965. ISSN: 1471-2962 (2012).

174. Vasilak, L. *et al.* Statistical Paradigm for Organic Optoelectronic Devices: Normal Force Testing for Adhesion of Organic Photovoltaics and Organic Light-Emitting Diodes. *ACS Applied Materials & Interfaces.* ISSN: 1944-8252. doi:10.1021/acsami.6b15618. <http://dx.doi.org/10.1021/acsami.6b15618> (2017).

175. Gregori, A. *Synthesis of Conjugated Polymers and Adhesive Properties of Thin Films in OPV Devices* PhD thesis (Universite de Pau et des pays de l'Adour, 2015).

176. Gregori, A. *et al.* The role of donor polymer and PEDOT:PSS formulation on adhesion processes in inverted organic solar cells. *Solar Energy Materials and Solar Cells* **174,** 25–33 (2018).

177. Luber, E. J. & Buriak, J. M. Reporting Performance in Organic Photovoltaic Devices. *ACS Nano* **7,** 4708–4714. ISSN: 1936-086X (2013).

178. Dong, Q. *et al.* All-spin-coating vacuum-free processed semi-transparent inverted polymer solar cells with PEDOT:PSS anode and PAH-D interfacial layer. *Organic Electronics* **11,** 1327–1331. ISSN: 1566-1199 (2010).

179. Xie, J., Zhang, A. & Cao, J. *pat.* 20110263842 A1 (2011).

180. Stevenson, J. P., Rogers, M. E. & Topasna, D. M. *pat.* 7018709 B2 (2006).

181. KG, H. D. G. . C. *pat.* (WO2014154360) (2014).

182. Zhou, Y. *et al.* Investigation on polymer anode design for flexible polymer solar cells. *Applied Physics Letters* **92,** 233308. ISSN: 0003-6951 (2008).

183. Senghor, M., Berson, S. & Manceau, M. *pat.* EP2763203 A2 (2014).

184. Kang, D. J. *et al.* Enhancing Mechanical Properties of Highly Efficient Polymer Solar Cells Using Size-Tuned Polymer Nanoparticles. *ACS Applied Materials & Interfaces* **7,** 2668–2676. ISSN: 1944-8252 (2015).

185. Larsen-Olsen, T. T. *et al.* Roll-to-roll processed polymer tandem solar cells partially processed from water. *Solar Energy Materials & Solar Cells* **97,** 43–49 (2012).

186. Vilkman, M. *et al.* Gravure-Printed ZnO in Fully Roll-to-Roll Printed Inverted Organic Solar Cells: Optimization of Adhesion and Performance. *Energy Technology* **3,** 407–413. ISSN: 2194-4288 (2015).

187. Krebs, F. C., Thomann, Y., Thomann, R. & Andreasen, J. W. A simple nanostructured polymer/ZnO hybrid solar cell preparation and operation in air. *Nanotechnology* **19,** 424013 (2008).

188. Kahn, M. L. *et al.* Size- and Shape-Control of Crystalline Zinc Oxide Nanoparticles: A new Organometallic Synthetic Method. *Adv. Funct. Mater* **15,** 458–468 (2005).

189. Stubhan, T. *et al.* High Fill Factor Polymer Solar Cells Incorporating a Low Temperature Solution Processed WO_3 Hole Extraction Layer. *Adv. Energy Mater.* **2,** 1433–1438 (2012).

190. Sakohara, S., Ishida, M. & Anderson, M. A. Visible Luminescence and Surface Properties of Nanosized ZnO Colloids Prepared by Hydrolyzing Zinc Acetate. *J. Phys. Chem. B* **102,** 10169–10175. ISSN: 1520-5207 (1998).

191. Ahmad, J., Bazaka, K., Anderson, L. J., White, R. D. & Jacob, M. V. Materials and methods for encapsulation of OPV: A review. *Renewable and Sustainable Energy Reviews* **27,** 104–117. ISSN: 1364-0321 (2013).

192. Sapkota, S. B., Fischer, M., Zimmermann, B. & Wurfel, U. Analysis of the degradation mechanism of ITO-free organic solar cells under UV radiation. *Solar Energy Materials and Solar Cells* **121,** 43–48. ISSN: 0927-0248 (2014).

193. Kastner, C., Seeland, M., Egbe, D. A. M. & Hoppe, H. Locally resolved large scale phase separation in polymer:fullerene blends. *J. Mater. Chem. A* **4,** 1244–1250. ISSN: 2050-7496 (2016).

194. Jeranko, T, Tributsch, H, Sariciftci, N. & Hummelen, J. Patterns of efficiency and degradation of composite polymer solar cells. *Solar Energy Materials and Solar Cells* **83,** 247–262. ISSN: 0927-0248 (2004).

195. Feron, K., Nagle, T. J., Rozanski, L. J., Gong, B. B. & Fell, C. J. Spatially resolved photocurrent measurements of organic solar cells: Tracking water ingress at edges and pinholes. *Solar Energy Materials and Solar Cells* **109,** 169–177. ISSN: 0927-0248 (2013).

196. Angmo, D. *et al.* Outdoor Operational Stability of Indium-Free Flexible Polymer Solar Modules Over 1 Year Studied in India, Holland, and Denmark. *Advanced Engineering Materials* **16,** 976–987. ISSN: 1438-1656 (2014).

197. Hoyer, U. *et al.* Comparison of Electroluminescence Intensity and Photocurrent of Polymer Based Solar Cells. *Adv. Energy Mater.* **1,** 1097–1100. ISSN: 1614-6832 (2011).

198. Bergqvist, J., Tholen, E. A. & Inganas, O. LED array scanner for inline characterization of thin film photovoltaic modules. *Solar Energy Materials and Solar Cells* **157,** 1057–1064. ISSN: 0927-0248 (2016).

199. Krebs, F. C. & Jorgensen, M. 2D Characterization of OPV from Single and Tandem Cells to Fully Roll-to-Roll Processed Modules with and without Electrical Contact. *Advanced Optical Materials* **2,** 465–477. ISSN: 2195-1071 (2014).

200. Reinhardt, J., Apilo, P., Zimmermann, B., Rousu, S. & Wurfel, U. Determining the photocurrent of individual cells within an organic solar module by LBIC and the filtering approach: Experiments and simulations. *Solar Energy Materials and Solar Cells* **134,** 157–164. ISSN: 0927-0248 (2015).

201. Planck, M. *Theorie Der Warmestrahlung* (1906).

202. Wurfel, P. The chemical potential of radiation. *J. Phys. C: Solid State Phys.* **15,** 3967–3985 (1982).

203. Rau, U. Reciprocity relation between photovoltaic quantum efficiency and electroluminescent emission of solar cells. *Physical Review B* **76.** ISSN: 1550-235X. doi:10.1103/physrevb.76.085303. <http://dx.doi.org/10.1103/PhysRevB.76.085303> (2007).

204. Baran, D. *et al.* Qualitative Analysis of Bulk-Heterojunction Solar Cells without Device Fabrication: An Elegant and Contactless Method. *Journal of the American Chemical Society* **136,** 10949–10955. ISSN: 1520-5126 (2014).

205. Veldman, D. *et al.* Compositional and Electric Field Dependence of the Dissociation of Charge Transfer Excitons in Alternating Polyfluorene Copolymer/Fullerene Blends. *Journal of the American Chemical Society* **130,** 7721–7735. ISSN: 1520-5126 (2008).

206. Hallermann, M., Haneder, S. & Da Como, E. Charge-transfer states in conjugated polymer/fullerene blends: Below-gap weakly bound excitons for polymer photovoltaics. *Applied Physics Letters* **93,** 053307. ISSN: 0003-6951 (2008).

207. Hallermann, M. *et al.* Correlation between charge transfer exciton recombination and photocurrent in polymer/fullerene solar cells. *Applied Physics Letters* **97,** 023301. ISSN: 1077-3118 (2010).

208. Goutam, P. J., Singh, D. K. & Iyer, P. K. Photoluminescence Quenching of Poly(3-hexylthiophene) by Carbon Nanotubes. *The Journal of Physical Chemistry C* **116,** 8196–8201. ISSN: 1932-7455 (2012).

209. Kim, H. *et al.* Electroluminescence in polymer-fullerene photovoltaic cells. *Applied Physics Letters* **86,** 183502. ISSN: 0003-6951 (2005).

210. Van Reenen, S., Vitorino, M. V., Meskers, S. C. J., Janssen, R. A. J. & Kemerink, M. Photoluminescence quenching in films of conjugated polymers by electrochemical doping. *Physical Review B* **89.** ISSN: 1550-235X. doi:10.1103/physrevb.89.205206. <http://dx.doi.org/10.1103/PhysRevB.89.205206> (2014).

211. Seeland, M., Kastner, C. & Hoppe, H. Quantitative evaluation of inhomogeneous device operation in thin film solar cells by luminescence imaging. *Applied Physics Letters* **107,** 073302. ISSN: 1077-3118 (2015).

212. Hodgkiss, J. M. *et al.* Exciton-Charge Annihilation in Organic and Semiconductor Films. *Adv. Funct. Mater* **22,** 1567 (2012).

213. Liang, Z. & Gregg, B. A. Compensating Poly(3-hexylthiophene) Reveals Its Doping Density and Its Strong Exciton Quenching by Free Carriers. *Advanced Materials* **24,** 3258–3262 (2012).

214. Yu, J., Song, N. W., McNeill, J. D. & Barbara, P. F. Efficient Exciton Quenching by Hole Polarons in the Conjugated Polymer MEH-PPV. *Israel journal of chemistry* **44,** 127–132 (2004).

215. Seeland, M., Rosch, R. & Hoppe, H. Luminescence imaging of polymer solar cells: Visualization of progressing degradation. *Journal of Applied Physics* **109,** 064513. ISSN: 0021-8979 (2011).

216. Adams, J. *et al.* Water Ingress in Encapsulated Inverted Organic Solar Cells: Correlating Infrared Imaging and Photovoltaic Performance. *Adv. Energy Mater.* 1501065. ISSN: 1614-6832 (2015).

217. Shen, C. *et al.* Improved local efficiency imaging via photoluminescence for silicon solar cells. *Solar Energy Materials and Solar Cells* **123,** 41–46. ISSN: 0927-0248 (2014).

218. Hoffler, H., Al-Mohtaseb, H., Haunschild, J., Michl, B. & Kasemann, M. Voltage calibration of luminescence images of silicon solar cells. *Journal of Applied Physics* **115,** 034508. ISSN: 1089-7550 (2014).

219. Glatthaar, M. *et al.* Spatially resolved determination of dark saturation current and series resistance of silicon solar cells. *physica status solidi (RRL) - Rapid Research Letters* **4,** 13–15. ISSN: 1862-6270 (2010).

220. Glatthaar, M. *et al.* Evaluating luminescence based voltage images of silicon solar cells. *Journal of Applied Physics* **108,** 014501. ISSN: 1089-7550 (2010).

221. Hameiri, Z. *et al.* Photoluminescence and electroluminescence imaging of perovskite solar cells. *Progress in photovoltaics : research and applications* **23,** 1697 (2015).

222. Rosch, R. *et al.* Investigation of the degradation mechanisms of a variety of organic photovoltaic devices by combination of imaging techniques-the ISOS-3 inter-laboratory collaboration. *Energy & Environmental Science* **5,** 6521. ISSN: 1754-5706 (2012).

223. Perkins, J. *et al. Optimization of conductivity and transparency in amorphous In-Zn-O transparent conductors* in *Preprint 33rd IEEE Photovoltaic Specialists Conference* (2008).

224. Perkins, J., Gennett, T., Galante, M., Gillaspie, D. & Ginley, D. *Amorphous Indium-Zinc-Oxide Transparent Conductors for Thin Film PV Preprint J. Perkins, T. Gennett, M. Galante, D. Gillaspie, and D. Ginley* in *37th IEEE Photovoltaic Specialists Conference* (IEEE, 2011).

225. Sigala, J. J. O. *et al.* Structural and Optical Characterization of Indium Zinc Oxynitride Thin Films. *Journal of Materials Science and Engineering A* **4,** 91 (2014).

226. Acton, Q. A. *Zinc Compounds - Advances in Research and Application: 2013 Edition* (ed ScholarlyEditions) (ScholarlyEditions, 2013).

227. Tao, X. *Systemes intelligents integres aux structures textiles* PhD thesis (Universite de sciences et technologies de Lille, 2010).

228. Jonsson, S. *et al.* The effects of solvents on the morphology and sheet resistance in poly(3,4-ethylenedioxythiophene):polystyrenesulfonic acid (PEDOT:PSS) films. *Synthetic Metals* **139,** 1–10. ISSN: 0379-6779 (2003).

229. ASTM. in *Standard Specification for Solar Simulation for Terrestrial Photovoltaic Testing (ref. E927 - 10)* (2015).
230. *ImageJ software homepage* <https://imagej.nih.gov/ij/>.
231. Lide, D. R. *Handbook of chemistry and physics* (2009).
232. Sani, E. & Dell'Oro, A. Spectral optical constants of ethanol and isopropanol from ultraviolet to far infrared. *Optical Materials* **60,** 137 –141. ISSN: 0925-3467 (2016).
233. Novinrooz, A., Sharbatdaran, M. & Noorkojouri, H. Structural and optical properties of WO3 electrochromic layers prepared by the sol-gel method. *Open Physics* **3,** 456–466 (2005).
234. Rao, M. & Hussain, O. Optical Properties of Vacuum Evaporated WO3 Thin Films. *Research Journal of Chemical Sciences* **1,** 76–80 (Jan. 2011).
235. Yu, S. *Polymer interface and adhesion* (ed Dekker, M.) 151 (1982).
236. *Prof. Fengling Zhang academic personal page* <https://www.ifm.liu.se/applphys/biorgel/staff/dr.-fengling-zhang/>.
237. *Website of the Department of physics, chemistry and biology of Linkoping Univesity* <https://www.ifm.liu.se/>.
238. *COST program website* <http://www.cost.eu/>.
239. *Stable Next-generation photovoltaics Website* <MP1307>.
240. *Nanocharacterization Platform (PFNC) Website* <https://www.minatec.org/en/research/minatec-dedicated-research-platforms/nanocharacterization-platform-pfnc/>.
241. Baikie, I. D., Mackenzie, S., Estrup, P. J. Z. & Meyer, J. A. Noise and the Kelvin method. *Review of Scientific Instruments* **62,** 1326–1332 (1991).
242. Baikie, I. D., Peterman, U., Lagel, B. & Dirscherl, K. Study of high- and low-work-function surfaces for hyperthermal surface ionization using an absolute Kelvin probe. *Journal of Vacuum Science & Technology A: Vacuum, Surfaces, and Films* **19,** 1460–1466 (2001).
243. Seeland, M., Roesch, R. & Hoppe, H. Quantitative analysis of electroluminescence images from polymer solar cells. *Journal of Applied Physics* **111,** 024505. ISSN: 0021-8979 (2012).
244. Seeland, M. & Hoppe, H. Comparison of distributed vs. lumped series resistance modeling of thin-film solar cells and modules: Influence on the geometry-dependent efficiency. *Phys. Status Solidi A* **212,** 1991–2000 (2015).
245. Bachmann, J. *et al.* Organic solar cells characterized by dark lock-in thermography. *Solar Energy Materials and Solar Cells* **94,** 642–647. ISSN: 0927-0248 (2010).
246. Hoppe, H. *et al.* Quality control of polymer solar modules by lock-in thermography. *Journal of Applied Physics* **107,** 014505. ISSN: 0021-8979 (2010).
247. Besold, S. *et al.* Quantitative imaging of shunts in organic photovoltaic modules using lock-in thermography. *Solar Energy Materials and Solar Cells* **124,** 133–137. ISSN: 0927-0248 (2014).

248. Rosch, R., Krebs, F. C., Tanenbaum, D. M. & Hoppe, H. Quality control of roll-to-roll processed polymer solar modules by complementary imaging methods. *Solar Energy Materials and Solar Cells* **97,** 176–180. ISSN: 0927-0248 (2012).

249. Krebs, F. C., Sondergaard, R. & Jorgensen, M. Printed metal back electrodes for R2R fabricated polymer solar cells studied using the LBIC technique. *Solar Energy Materials and Solar Cells* **95,** 1348–1353. ISSN: 0927-0248 (2011).

250. *InfinityPV Website* <https://www.infinitypv.com/products/hardware/lbic> (2017).

251. *LEPMI laboratory website* <http://lepmi.grenoble-inp.fr/about-lepmi/lepmi-presentation-754430.kjsp>.

252. Foundation, P. S. <https://www.python.org/> (2001-2017).

253. Goncalves, G. *et al.* UV and ozone influence on the conductivity of ZnO thin films. *Journal of Non-Crystalline* **352,** 1444–1447 (2006).

254. Tenery, D. & Gesquiere, A. J. Effect of PCBM Concentration on Photoluminescence Properties of Composite MEH-PPV:PCBM Nanoparticles Investigated by a Franck-Condon Analysis of Single-Particle Emission Spectra. *ChemPhysChem* **10,** 2449–2457 (2009).

255. Ehrenreich, P. *et al.* H-aggregate analysis of P3HT thin films - Capability and limitation of photoluminescence and UV-Vis spectroscopy. *Scientific reports* **6,** 32000 (2016).

256. Garcia-Belmonte, G. *et al.* Charge carrier mobility and lifetime of organic bulk heterojunctions analyzed by impedance spectroscopy. *Organic Electronics* **9,** 847–851 (2008).

257. Carle, J. E., Helgesen, M., Madsen, M. V., Bundgaard, E. & Krebs, F. C. Upscaling from single cells to modules - fabrication of vacuum and ITO-free polymer solar cells on flexible substrates with long lifetime. *Journal of Materials Chemistry C* **2,** 1290 (2014).

258. Livi, F. *et al.* Round-Robin Studies on Roll-Processed ITO-free Organic Tandem Solar Cells Combined with Inter-Laboratory Stability Studies. *Energy Technology* **3,** 423–427 (2015).

259. Hosel, M. *et al.* High-Volume Processed ITO-Free Superstrates and Substrates for Roll-to-Roll Development of Organic Electronics. *Advanced Science* **1,** 1400002 (2014).

260. Hogg, R. V. & Craig, A. T. *Introduction to Mathematical Statistics* (1978).

261. Mirabella, F. J. *Internal reflection spectroscopy: Theory and applications* 17–52 (1992).

262. McMahon, T. Accelerated Testing and Failure of Thin-film PV Modules. *Progress in photovoltaic: research and applications* **12,** 235–248 (2004).

263. Uysal, I., Severcan, F. & Evis, Z. Characterization by Fourier transform infrared spectroscopy of hydroxyapatite co-doped with zinc and fluoride. *Ceramics International* **39,** 7727–7733 (2013).

264. Kammori, O., Yamaguchi, N. & Sato, K. Infrared absorption of metal oxides. *BUNSEKI KAGAKU* **16,** 1050–1055 (1967).

265. Hook, D. A., Olhausen, J. A., Krim, J. & Dugger, M. T. Evaluation of Oxygen Plasma and UV Ozone Methods for Cleaning of Occluded Areas in MEMS Devices. *J. Microelectromech. Syst.* **19,** 1292–1298. ISSN: 1941-0158 (2010).

266. Vig, J. R. UV/ozone cleaning of surfaces. *J. Vac. Sci. Technol. A* **3,** 1027–1034 (1985).

267. Stalder, A., Kulik, G., Sage, D., Barbieri, L. & Hoffmann, P. A Snake-Based Approach to Accurate Determination of Both Contact Points and Contact Angles. *Colloids And Surfaces A: Physicochemical And Engineering Aspects* **286,** 92–103 (2006).

268. Karge, H. G. & Weitkamp, J. *Characterization II* (2006).

269. Wang, Y. *et al.* Solution-Processed MoO_3:PEDOT:PSS Hybrid Hole Transporting Layer for Inverted Polymer Solar Cells. *ACS Applied Materials & Interfaces* **7,** 7170–7179. ISSN: 1944-8252 (2015).

270. Greiner, M. T., Chai, L., Helander, M. G., Tang, W.-M. & Lu, Z.-H. Transition Metal Oxide Work Functions: The Influence of Cation Oxidation State and Oxygen Vacancies. *Advanced Functional Materials* **22,** 4557–4568. ISSN: 1616-3028 (2012).

271. Meyer, J. *et al.* Highly efficient simplified organic light emitting diodes. *Applied Physics Letters* **91,** 113506 (2007).

272. Shtern, Y., Shtern, M., Mironov, R., Sherchenkov, A. & Rogachev, M. Technology of Thin Film Fabrication on Porous Metal Oxide Substrates. *Acta Physica Polonica A* **129,** 776 (2016).

273. Schossberger, F. & Franson, K. D. Adhesion of evaporated metal films. *Vacuum* **9,** 28–35 (1959).

274. Karnowsky, M. M. & Estill, W. B. Scratch Test for Measuring Adherence of Thin Films to Oxide Substrates. *Review of Scientific Instruments* **35,** 1324 (1964).

275. Huang, T., Sundaram, V., Raj, P. M., Sharma, H. & Tummala, R. Adhesion and Reliability of Direct Cu Metallization of Through-Package Vias in Glass Interposers. *Electronic Components & Technology Conference,* 2266 (2014).

276. Lee, L. *Fundamentals of Adhesion* (2013).

277. Sotiropoulou, D. & Nikolopoulos, P. Work of adhesion in ZrO2-1iquid metal systems. *Journal of material science* **28,** 356 (1993).

278. Peden, C. H. F., Kidd, K. B. & Shinn, N. D. Metal/metal-oxide interfaces: A surface science approach to the study of adhesion. *Journal of Vacuum Science & Technology A: Vacuum, Surfaces, and Films* **9,** 1518 (1991).

279. Khan, T. H., Zhou, Y., Dindar, A., Shim, C. J. W. anf Fuentes-Hernandez & Kippelen, B. Organic Photovoltaic Cells with Stable Top Metal Electrodes Modified with Polyethylenimine. *ACS Appl. Mater. Interfaces* **6,** 6202–6207 (2014).

280. Elsaka, S. E., Hamouda, I. M., Elewady, Y. A., Abouelatta, O. B. & Swain, M. V. Influence of chromium interlayer on the adhesion of porcelain to machined titanium as determined by the strain energy release rate. *Journal of Dentistry* **38,** 648 –654. ISSN: 0300-5712 (2010).

281. Xiao, X., Sheldon, B., Konca, E., Lev, L. & Lukitsch, M. The failure mechanism of chromium as the interlayer to enhance the adhesion of nanocrystalline diamond coatings on cemented carbide. *Diamond and Related Materials* **18,** 1114 –1117. ISSN: 0925-9635 (2009).

282. Ali, N, Ahmed, W, Rego, C. & Fan, Q. Chromium interlayers as a tool for enhancing diamond adhesion on copper. *Diamond and Related Materials* **9,** 1464 –1470. ISSN: 0925-9635 (2000).

283. Zimmermann, B., Wurfel, U. & Niggemann, M. Longterm stability of efficient inverted P3HT:PCBM solar cells. *Solar Energy Materials and Solar Cells* **93.** Processing and Preparation of Polymer and Organic Solar Cells, 491 –496. ISSN: 0927-0248 (2009).

284. Lassner, E. & Schubert, W.-D. *Tungsten: Properties, Chemistry, Technology of the Element, Alloys, and Chemical Compounds* (2012).

285. Kim, Y. H. *et al.* Highly Conductive PEDOT:PSS Electrode with Optimized Solvent and Thermal Post-Treatment for ITO-Free Organic Solar Cells. *Advanced Functional Materials* **21,** 1076–1081. ISSN: 1616-3028 (2011).

286. Hirose, T., Kawano, I. & Niino, M. Electrical Conductivity of Tungsten Trioxide (WO3). *Journal of the Physical Society of Japan* **33,** 272–272 (1972).

287. Gillet, M., Aguir, K., Lemire, C., Gillet, E. & Schierbaum, K. The structure and electrical conductivity of vacuum-annealed WO3 thin films. *Thin Solid Films* **467,** 239 –246. ISSN: 0040-6090 (2004).

288. Shrotriya, V., Li, G., Yao, Y., Chu, W. & Yang, Y. Transition metal oxides as the buffer layer for polymer photovoltaic cells. *Applied physics Letters* **88,** 073508 (2006).

289. Chen, K.-J., Hung, F.-Y., Lui, T.-S., Chang, S.-P. & Wang, W.-L. The inter-metallic oxide of ZnO/ITO/ZnO tri-layer films using a heat-induced diffusion mechanism. *Applied Surface Science* **273,** 598–602 (May 2013).

290. Meyer, J. *et al.* Charge generation layers comprising transition metal-oxide/organic interfaces: Electronic structure and charge generation mechanism. *Applied Physics Letters* **96,** 193302 (2010).

291. Meyer, J. *et al.* Transition Metal Oxides for Organic Electronics: Energetics, Device Physics and Applications. *Advanced materials* **24,** 5408–5427 (2012).

292. Gerling, L. G., Mahato, S., Voz, C., Alcubilla, R. & Puigdollers, J. Characterization of Transition Metal Oxide/Silicon Heterojunctions for Solar Cell Applications. *Applied sciences* **5,** 695 (2015).

293. Gratzel, M. Photoelectrochemical cells. *Nature* **414,** 338 (2001).

294. Kim, D. Y. *et al.* The effect of molybdenum oxide interlayer on organic photovoltaic cells. *Applied Physics Letters* **95,** 093304 (2009).

295. Choy, W. C. H. & Zhang, D. Solution-Processed Metal Oxides as Efficient Carrier Transport Layers for Organic Photovoltaics. *Small* **12,** 461 (2016).

296. Greiner, M. T. *et al.* Universal energy-level alignment of molecules on metal oxides. *Nature Materials* **11,** 76 (2011).

297. Davis, R. J. *et al.* Determination of energy level alignment at interfaces of hybrid and organic solar cells under ambient environment. *J. Mater. Chem.* **21,** 1721–1729 (6 2011).

298. Xue, M. *et al.* Understanding of the correlation between work function and surface morphology of metals and alloys. *Journal of Alloys and Compounds* **577,** 1 –5. ISSN: 0925-8388 (2013).

299. Wang, X.-R. *et al.* Annealing effect on the metal gate effective work function modulation for the Al/TiN/SiO2/p-Si structure. *Microelectronic Engineering* **88.** The 2010 International workshop on Materials for Advanced Metallization, 573 –577. ISSN: 0167-9317 (2011).

300. Petermann, U., Baikie, I. & Lagel, B. Kelvin probe study of metastable states during initial oxygen adsorption dynamics on Si(111). *Thin Solid Films* **343,** 492 –494. ISSN: 0040-6090 (1999).

301. Hancox, I. *et al.* The effect of a MoOx hole-extracting layer on the performance of organic photovoltaic cells based on small molecule planar heterojunctions. *Organic Electronics* **11,** 2019 –2025. ISSN: 1566-1199 (2010).

302. *Thin-film terrestrial photovoltaic (PV) modules - Design qualification and type approval* (European comittee for electrotechnical standardization, 2008).

303. Bertho, S. *et al.* Effect of temperature on the morphological and photovoltaic stability of bulk heterojunction polymer:fullerene solar cells. *Solar Energy and Materials and Solar Cells* **9,** 753–760 (2008).

304. Mauer, R., Howard, I. A. & Laquai, F. Effect of Nongeminate Recombination on Fill Factor in Polythiophene/Methanofullerene Organic Solar Cells. *The Journal of Physical Chemistry Letters* **1,** 3500–3505 (2010).

305. Sharma, A. *et al.* Revealing the correlation between charge carrier recombination and extraction in an organic solar cell under varying illumination intensity. *Phys. Chem. Chem. Phys.* **19,** 26169–26178 (38 2017).

306. Hameiri, Z. & McIntosh, K. R. *On the use of local ideality factor obtained from effective carrier lifetime measurements* in *2013 IEEE 39th Photovoltaic Specialists Conference (PVSC)* (2013), 1412–1416. doi:10.1109/PVSC.2013.6744408.

307. Fabregat-Santiago, F., Garcia-Belmonte, G., Mora-Sero, I. & Bisquert, J. Characterization of nanostructured hybrid and organic solar cells by impedance spectroscopy. *Phys. Chem. Chem. Phys.* **13,** 9083–9118 (20 2011).

308. Germa, G.-B. Carrier recombination flux in bulk heterojunction polymer:fullerene solar cells: Effect of energy disorder on ideality factor. *Solid-State Electronics* **79,** 201 –205. ISSN: 0038-1101 (2013).

309. Nardes, A. M. *On the conductivity of PEDOT:PSS thin films* (ed Universiteit, E. T.) (2007).

310. Son, H. J., Kim, S. H. & Kim, D. H. Critical Impact of Hole Transporting Layers and Back Electrode on the Stability of Flexible Organic Photovoltaic Module. *Advanced Energy Materials* **7.** 1601289, 1601289. ISSN: 1614-6840 (2017).

311. Vitoratos, E., Sakkopoulos, S., Paliatsas, N., Konstantinos, E. & Choulis, S. A. Conductivity Degradation Study of PEDOT: PSS Films under Heat Treatment in Helium and Atmospheric Air. *Open Journal of Organic Polymer Materials* **2,** 7–11 (2012).

312. Kawano, K. *et al.* Degradation of organic solar cells due to air exposure. *Solar Energy Materials and Solar Cells* **90,** 3520 –3530. ISSN: 0927-0248 (2006).

313. Drakonakis, V. M., Savva, A., Kokonou, M. & Choulis, S. A. Investigating electrodes degradation in organic photovoltaics through reverse engineering under accelerated humidity lifetime conditions. *Solar Energy Materials and Solar Cells* **130,** 544 –550. ISSN: 0927-0248 (2014).

314. Matheron, M. *et al. Lifetime Study of Flexible Encapsulated Organic Photovoltaic Modules: Optimization of Device Architecture and Selection of Encapsulation Materials* in *Oral presentation, ISOS 9* (2016).

315. Lloyd, M. T. *et al.* Influence of the hole-transport layer on the initial behavior and lifetime of inverted organic photovoltaics. *Solar Energy Materials and Solar Cells* **95,** 1382–1388. ISSN: 0927-0248 (2011).

316. Vetter, A. *et al.* Visualizing the performance loss of solar cells by IR thermography - an evaluation study on CIGS with artificially induced defects. *Progress in Photovoltaics: Research and Applications* **24,** 1001–1008. ISSN: 1062-7995 (2016).

317. Hoyer, U. *et al.* Electroluminescence imaging of organic photovoltaic modules. *Applied Physics Letters* **97,** 233303. ISSN: 0003-6951 (2010).

318. Adams, J. *Failure Analysis and Long Term Stability of Thin Film Solar Cells and Modules* PhD thesis (2015).

319. Trupke, T. *et al.* Photoluminescence Imaging for Photovoltaic Applications. *Energy Procedia* **15,** 135–146. ISSN: 1876-6102 (2012).

320. Breitenstein, O., Hoffler, H. & Haunschild, J. Photoluminescence image evaluation of solar cells based on implied voltage distribution. *Solar Energy Materials and Solar Cells* **128,** 296–299. ISSN: 0927-0248 (2014).

321. Haunschild, J., Glatthaar, M., Kasemann, M., Rein, S. & Weber, E. R. Fast series resistance imaging for silicon solar cells using electroluminescence. *physica status solidi (RRL) - Rapid Research Letters* **3,** 227–229. ISSN: 1862-6270 (2009).

List of Figures

List of Tables

Appendices

Scientific production

- Oral talk
  Sacha JUILLARD, Muriel MATHERON, Emilie PLANES, Solenn BERSON, Lionel FLANDIN
  Encapsulation impact on initial performance of organic photovoltaic (OPV) devices: Influence of mechanical stability and strategies for improvement
  10th International Symposium on Flexible Organic Electronics (ISFOE) 3-6 July 2017, Thessaloniki, Greece.

- Oral talk + Poster presentation
  Sacha JUILLARD, Muriel MATHERON, Emilie PLANES, Solenn BERSON, Lionel FLANDIN
  Complementary Imaging Techniques for Tracking Degradation of Flexible Encapsulated Organic Photovoltaic Devices Along Processing and Aging
  ILMAGING 2016, 9-12 November 2016, Ilmenau, Germany.

- Poster presentation
  Sacha JUILLARD, Muriel MATHERON, Emilie PLANES, Solenn BERSON, Lionel FLANDIN
  Complementary Imaging Techniques for Tracking Degradation of Flexible Encapsulated Organic Photovoltaic Devices Along Processing and Aging
  Journee nationales du photovoltaique 29 November-2 December 2016, Dourdan, France.

- Poster presentation
  Sacha JUILLARD, Muriel MATHERON, Emilie PLANES, Solenn BERSON, Lionel FLANDIN
  Optimization of the Performance of Encapsulated Organic Photovoltaic Devices. Coupling of Mechanical, Morphological, Physico-chemical and Optoelectronic Characterizations
  French-American Doctoral Exchange (FADEx), 23-24 March 2015, Le-Bourget-du-Lac, France.

Abstract

In order to limit the flexible organic photovoltaic devices degradation induced by moisture and oxygen, the solar cells are encapsulated between two gas-barrier films. Despite the importance of the encapsulation processes and their potential influence on the initial performances as well as during aging of the devices, they are scarcely described in the literature. Furthermore, several field aging studies showed that mechanical degradation could limit the devices lifetime before their photo-chemical stability became an issue. Thus, adhesion between the different layers composing the devices is a critical factor in order to develop flexible OPV devices reliable after their manufacturing and during their use.

In this work, two encapsulation protocols were studied: the roll-to-roll lamination of a pressure sensitive adhesive and the vacuum lamination of a hotmelt thermoplastic. In order to quantify the adhesion strength of every interface comprised in the samples, the 180° peeling test mechanical characterization was adapted for and then applied to the flexible devices. In addition, non-destructive imaging characterization techniques were developed: the laser-beam induced-current mapping and the luminescence emission imaging under optical and electrical excitation. Thank to these techniques, the hypothesis of a mechanical degradation occurring during the roll-to-roll lamination process was made. Answers allowing for the improvement of the interfaces identified as weak were searched for and evaluated with respect to the photovoltaic performances of the reference devices. The imaging techniques previously developed were also applied along the accelerated aging of encapsulated cells. A mechanism was proposed, which allows one to explain the localization of the degradation but also the failure type, either optical or electrical, occurring during each aging step.

Résumé

En vue de limiter la dégradation par l'humidité et l'oxygène des dispositifs photovoltaïques organiques flexibles, les cellules solaires sont encapsulées entre des films barrières aux gaz. Malgré l'importance des procédés d'encapsulation et leur potentiel impact sur les performances initiales et lors du vieillissement des dispositifs, ils sont rarement étudiés dans la littérature. En outre, plusieurs études de vieillissement sur le terrain ont montré que la détérioration mécanique limitait la durée de vie des échantillons bien avant que leur stabilité photochimique ne soit mise en cause. L'adhésion entre les différentes couches composant les cellules est donc un facteur critique afin d'obtenir des dispositifs flexibles fiables après leur mise en œuvre et lors de leur utilisation.

Dans ce travail, deux procédés d'encapsulation ont été étudiés : la lamination à rouleaux d'un adhésif sensible à la pression et la lamination sous vide d'un thermoplastique. Afin de quantifier l'adhésion de chacune des interfaces comprises dans les échantillons, la technique de caractérisation mécanique par pelage à 180° a été adaptée et ensuite appliquée aux dispositifs flexibles. De plus, des techniques de caractérisation des dispositifs par imagerie non-destructive ont été développées : la cartographie du courant induit par faisceau laser (plus couramment connu sous l'acronyme anglais « LBIC ») et l'imagerie de luminescence sous excitation optique et électrique. Grace à ces techniques, l'hypothèse d'une dégradation mécanique des dispositifs durant le procédé d'encapsulation par lamination à rouleaux a été émise. Des solutions permettant l'amélioration des interfaces identifiées comme mécaniquement faibles ont été recherchées et ensuite évaluées par rapport aux performances photovoltaïques des dispositifs de référence. Les techniques d'imagerie développées précédemment ont également été appliquées durant le vieillissement en condition accélérées des cellules encapsulées. Un mécanisme a été proposé, qui permet d'expliquer la localisation spatiale de la dégradation mais également le type de dégradation, optique ou électrique, survenu à chaque étape du vieillissement.